**Astrophysics and Space Science Proceedings** 

Andrea Miglio Josefina Montalbán Arlette Noels *Editors* 

# Red Giants as Probes of the Structure and Evolution of the Milky Way





Astrophysics and Space Science Proceedings

# Red Giants as Probes of the Structure and Evolution of the Milky Way

**Editors** 

Andrea Miglio Josefina Montalbán Arlette Noels







Editors
Andrea Miglio
Université de Liège
Inst. d'Astrophysique et de Géophysique
Liége, Belgium
and
School of Physics and Astronomy
University of Birmingham
Birmingham, UK

Josefina Montalbán Arlette Noels Université de Liège Inst. d'Astrophysique et de Géophysique Liége, Belgium

ISSN 1570-6591 e-ISSN 1570-6605 ISBN 978-3-642-18417-8 e-ISBN 978-3-642-18418-5 DOI 10.1007/978-3-642-18418-5 Springer Heidelberg Dordrecht London New York

Library of Congress Control Number: 2012930406

#### © Springer-Verlag Berlin Heidelberg 2012

This work is subject to copyright. All rights are reserved, whether the whole or part of the material is concerned, specifically the rights of translation, reprinting, reuse of illustrations, recitation, broadcasting, reproduction on microfilm or in any other way, and storage in data banks. Duplication of this publication or parts thereof is permitted only under the provisions of the German Copyright Law of September 9, 1965, in its current version, and permission for use must always be obtained from Springer. Violations are liable to prosecution under the German Copyright Law.

The use of general descriptive names, registered names, trademarks, etc. in this publication does not imply, even in the absence of a specific statement, that such names are exempt from the relevant protective laws and regulations and therefore free for general use.

Printed on acid-free paper

Springer is part of Springer Science+Business Media (www.springer.com)

# **Preface**

Red giants are cool, highly luminous stars, covering a rather wide domain in mass, age, chemical composition, and evolutionary state. They have an extended convective envelope which can, as in solar-like stars, stochastically excite p-modes of oscillation. During its first long run (150 days) of observation, the CoRoT satellite launched in December 2006 has observed a large number of red giants and has detected these oscillations in about 900 of them. Not only radial but also nonradial modes of oscillation were detected. It was indeed the first clear detection of nonradial modes in such stars. Moreover, for the very first time, the large number of observed stars (it amounts now to thousands and many more to come) allows the statistical analysis of red giants based on their pulsation properties.

- The first striking result of this statistical analysis has shown that the distribution of frequency at maximum power  $(v_{max})$  among all the observed red giants presents a rather narrow peak centered on about 35 µHz. This has to bear the print of the evolution of our Galaxy since these red giants of different masses and ages are representative of all the successive generations of stars in the Galaxy. A first theoretical study made using synthetic stellar population models shows that the actual distribution of red giants in the CoRoT field is indeed highly dominated by stars in a narrow range of stellar masses from 0.8 to  $2.5 M_{\odot}$ . The computed distribution of the frequency at maximum power for such stars, which is determined by their mass, radius, and effective temperature does indeed present a peak near 35 µHz, excitingly close to the observed value. These stars  $(0.8-2.5\,M_{\odot})$  are "red clump" stars. They have undergone a helium flash, with a common critical mass of their helium core of about 0.5  $M_{\odot}$ ; their luminosities and their radii are thus almost the same. Observations of red giants in clusters show indeed an accumulation of stars in this region of the HR diagram. Moreover, as shown by Hipparcos data, the bulk of giant stars in the solar neighborhood consist indeed of red clump stars.
- This can have a very important impact on our vision of the Galaxy. If  $\nu_{max}$  of a red giant, whose parallax is unknown, is derived from asteroseismic observations together with the so-called large frequency separation, its radius can be estimated

vi Preface

and its distance derived. Solar-like oscillating red giants can thus become new distance indicators.

A spectroscopic analysis of these stars coupled with this new distance indicator
could provide an unprecedented tool to measure the radial and vertical metallicity
gradient in our Galaxy. These gradients would be representative of the metallicity
distribution at an early phase of the galactic evolution, typical of the time of
birth of clump stars. Moreover, thanks to the estimate of stellar mass through
seismic constraints, we can potentially characterize the age distributions and agemetallicity relations of the observed populations of giants.

These results are so promising that further analyses are urgently needed. Future CoRoT long runs pointed on different galactic longitudes will bring new red giant asteroseismic data. The *Kepler* mission will also observe red giants at a higher galactic latitude compared to that of CoRoT's fields. The PLATO mission will hopefully add some important data to this harvest. This could indeed reveal secondary peaks in the distribution of the frequency at maximum power, indicative of different stellar populations or different stellar formation episodes. The pulsation properties now available for thousands of red giants promise to add valuable and independent constraints to current models of structure and evolution of our Galaxy. Such a close connection between stellar evolution, galactic evolution, and asteroseismology opens a new very promising gate in our understanding of stars and galaxies. It needs, however, a collaboration between researchers of different expertise. The aim of this workshop was thus to put together for a 3-day meeting,

- Expert researchers in galactic evolution
- Expert researchers in stellar structure
- Asteroseismologists from the Red Giant Team of the CoRoT and Kepler missions

in order to allow a broad discussion on the physical aspects involved in red giant modeling such as convection, rotation, conditions prevailing at the onset and during the helium flash, as well as on the parameters involved in galactic evolution and stellar population synthesis, e.g., Stellar Formation Rate, Age-Metallicity Relation, Initial Mass Function.

We are happy to say that due to the dedication and the enthusiasm of the participants, this workshop was a great success. All of us learned a lot, discussed a lot, ate a lot, drank a lot, and went back to their home university with their head full of new ideas and plans for future collaborations.

Liège, Belgium

Andrea Miglio Josefina Montalbán Arlette Noels

# Acknowledgements

We would like to heartily thank our sponsors:

- Université de Liège
- Fonds National de la Recherche Scientifique Communauté Française de Belgique
- CSL Centre Spatial de Liège
- AMOS Advanced Mechanical and Optical Systems
- Academia Belgica, Roma
- And, last but not least, PRODEX Office Belgium, which is financing most of the asteroseismology research in Belgium and, in particular, is covering the printing costs of this volume.

We are extremely grateful to Mr Geerts, director of the Academia Belgica, which hosted this workshop. Everything was done to help us feel at home and forget about the local organization and catering. Thanks also to Mrs Geerts, Mrs Michiels, and Rocco, who is a master in preparing and serving Italian buffets.

Thank you Maria Pia for kindly proposing the efficient and smiling help of your secretary, Catia Spalletta, and for having organized a musical interlude which helped everybody relax before the reception given by Mr Geerts.

Many, many thanks to the participants. They were not only experts in their research fields but also cheerful companions, and the ambiance was really highly stimulating throughout the workshop. They prepared splendid presentations with an emphasis on the general idea of bringing together different domains for this brainstorming meeting. Moreover, they agreed to publish their talks in this volume which will hopefully become a landmark as well as a new starting point in the knowledge of red giants.

Liège, Belgium

Andrea Miglio Josefina Montalbán Arlette Noels viii Acknowledgements

#### Scientific organizing committe:

- Andrea Miglio (Université de Liège) chairperson
- Josefina Montalbán (Université de Liège) co-chairperson
- Joris De Ridder (Katholieke Universiteit Leuven)
- Marc-Antoine Dupret (Université de Liège)
- Fabien Carrier (Katholieke Universiteit Leuven)
- Léo Girardi (INAF, Osservatorio Astronomico di Padova)
- Francesca D'Antona (INAF, Osservatorio Astronomico di Roma)
- Arlette Noels (Université de Liège)

# **Contents**

# Part I Asteroseismology of Red Giants

Aspects of Observational Red Giant Population Seismology  Joris De Ridder	3		
Asteroseismology of Red Giants as a Tool for Studying Stellar  Populations: First Steps  Andrea Miglio	11		
Adiabatic Solar-Like Oscillations in Red Giant Stars  Josefina Montalbán, Andrea Miglio, Arlette Noels, Richard Scuflaire, Paolo Ventura, and Francesca D'Antona			
Energetic Aspects of Non-Radial Solar-Like Oscillations in Red Giants	33		
Part II Internal Structure, Atmosphere, and Evolution of Red Giants: Current Models and Their Uncertainties			
Evolution and Internal Structure of Red Giants	45		
Uncertainties and Systematics in Stellar Evolution Models of Red Giant Stars Santi Cassisi	57		
Convection Modelling and the Morphology of RGBs in Stellar Clusters	69		
Helium Burning in Moderate-Mass Stars	77		

x Contents

<b>Hydrodynamic Simulations of Shell Convection in Stellar Cores</b> Miroslav Mocák, Ewald Müller, and Lionel Siess	87
Impact of Rotational Mixing on the Global and Asteroseismic Properties of Red Giants Patrick Eggenberger, Nadège Lagarde, and Corinne Charbonnel	95
3D Picture of the Convective Envelope of a Rotating RGB Star	105
Effects of Rotation and Thermohaline Mixing in Red Giant Stars  Corinne Charbonnel, Nadège Lagarde, and Patrick Eggenberger	115
3D Model Atmospheres of Red Giant Stars	125
Part III Stellar Populations in the Milky Way	
Structure and Evolution of the Milky Way	137
Red Giant Stars: Probing the Milky Way Chemical Enrichment	147
Chemical Abundances of Giants in Globular Clusters	155
TRILEGAL, a TRIdimensional modeL of thE GALaxy: Status and Future  Léo Girardi, Mauro Barbieri, Martin A.T. Groenewegen, Paola Marigo, Alessandro Bressan, Helio J. Rocha-Pinto, Basílio X. Santiago, Julio I.B. Camargo, and Luiz N. da Costa	166
The Besançon Model of Stellar Population Synthesis of the Galaxy  Annie C. Robin, Céline Reylé, Douglas J. Marshall, and Mathias Schultheis	171
Index	181

# **Contributors**

Mauro Barbieri Observatoire Côte d'Azur, Nice, France, mauro, barbieri@oca.eu

Paul Beck K.U. Leuven, Leuven, Belgium, Paul.Beck@ster.kuleuven.be

Serena Benatti INAF Osservatorio di Padova, Padova, Italy, serena.benatti@oapd.inaf.it

Kévin Belkacem IAS, 91405 Orsay, Cedex, France, kevin.belkacem@ias.u-psud. fr

**Angela Bragaglia** INAF – Osservatorio Astronomico di Padova, Vicolo dell'Osservatorio 5, 35122 Padova, Italy, angela.bragaglia@oabo.inaf.it

**Alessandro Bressan** SISSA-ISAS, International School for Advanced Studies, Trieste, Italy, alessandro.bressan@sissa.it

Vittoria Caloi IASF Roma, Roma, Italy, vittoria.caloi@iasf-roma.inaf.it

**Julio I.B. Camargo** Universidade Federal do Rio Grande do Sul, Porto Alegre, RS, Brazil, camargo@on.br

**Roberta Carini** INAF – Osservatorio Astronomico di Roma, via Frascati 33, 00040 Monte Porzio Catone (RM), Italy, roberta.carini@oa-roma.inaf.it

**Fabien Carrier** K.U. Leuven, Leuven, Belgium, fabien@ster.kuleuven.be

**Eugenio Carretta** INAF – Osservatorio Astronomico di Padova, Vicolo dell'Osservatorio 5, 35122 Padova, Italy, eugenio.carretta@oabo.inaf.it

**Santi Cassisi** INAF – Astronomical Observatory of Collurania, Via M. Maggini, 64100 Teramo, Italy, cassisi@te.astro.it

**Corinne Charbonnel** Observatoire de Genève, Université, de Genève, 51 ch. des Maillettes, 1290 Sauverny, Switzerland

Laboratoire d'Astrophysique de Toulouse-Tarbes, CNRS UMR 5572, Université de Toulouse, 14 av. E. Belin 31400 Toulouse, France, corinne.charbonnel@unige.ch

xii Contributors

**Cristina Chiappini** Leibniz-Institut fur Astrophysik Potsdam (AIP), An der Sternwarte 16 14482, Potsdam, Germany, cristina.chiappini@aip.de

Riccardo Claudi INAF Osservatorio di Padova, Padova, Italy, riccardo.claudi@oapd.inaf.it

Luiz N. da Costa Observatorio Nacional, Rio de Janeiro, RJ, Brazil

Laboratorio Interinstitucional de e-Astronomia LIneA, Rio de Janeiro, RJ, Brazil, ldacosta@eso.org

**Francesca D'Antona** INAF – Roma, Via Frascati, 33, Monteporzio Catone, Rome, Italy, franca.dantona@oa-roma.inaf.it

**Valentina D'Orazi** INAF – Osservatorio Astronomico di Padova, Vicolo dell'Osservatorio 5, 35122 Padova, Italy, valentina.dorazi@oapd.inaf.it

**Joris De Ridder** Instituut voor Sterrenkunde, K.U.Leuven, Celestijnenlaan 200D, 3001 Leuven, Belgium, joris@ster.kuleuven.ac.be

Marcella Di Criscienzo INAF – Osservatorio Astronomico di Roma, via Frascati 33, 00040 Monte Porzio Catone (RM), Italy, marcella.dicriscienzo@oa-roma.inaf.it

Maria Pia Di Mauro IASF Roma, Roma, Italy, mariapia.dimauro@iasf-roma.inaf.it

**Marc-Antoine Dupret** Institut d'Astrophysique et Géophysique, University of Liège, 4000 Liège, Belgium, MA.Dupret@ulg.ac.be

**Wojtek Dziembowski** Nicolaus Copernicus Astronomical Center, Warsaw, Poland, wd@astrouw.edu.pl

**Patrick Eggenberger** Observatoire de Genève, Université de Genève, 51 ch. des Maillettes, 1290 Sauverny, Switzerland, patrick.eggenberger@unige.ch

**Ken Freeman** Australian National University, Canberra, ACT 0200, Australia, kcf@mso.anu.edu.au

Léo Girardi Osservatorio Astronomico di Padova INAF, Padova, Italy

Laboratorio Interinstitucional de e-Astronomia LIneA, Rio de Janeiro, RJ, Brazil, leo.girardi@oapd.inaf.it

**Raffaele Gratton** INAF-Osservatorio Astronomico di Padova, Vicolo dell'Osservatorio 5, 35122 Padova, Italy, raffaele.gratton@oapd.inaf.it

**Martin A.T. Groenewegen** Koninklijke Sterrenwacht van Belgium, Brussels, Belgium, marting@oma.be

**Nicolas Grevesse** Université de Liège, Liège, Belgium, Nicolas.Grevesse@ulg.ac. be

Contributors xiii

**Nadège Lagarde** Observatoire de Genève, Université de Genève, 51 ch. des Maillettes, 1290 Versoix, Switzerland, lagarde.nadege@unige.ch

**Sara Lucatello** INAF-Osservatorio Astronomico di Padova, Vicolo dell'Osservatorio 5, 35122 Padova, Italy, sara.lucatello@oapd.inaf.it

**Hans-Günter Ludwig** Zentrum für Astronomie der Universität Heidelberg, Landessternwarte, Königstuhl 12, 69117 Heidelberg, Germany, H.Ludwig@lsw. uni-heidelberg.de

Carla Maceroni INAF Osservatorio di Roma, Monte Porzio Catone (RM), Italy, carla maceroni@oa-roma inaf.it

Paola Marigo Dipartimento di Astronomia, Università di Padova, Padova, Italy, paola.marigo@unipd.it

**Douglas J. Marshall** Université de Toulouse, UPS-OMP, IRAP, 31028 Toulouse cedex 4. France

CNRS, Institut de Recherche en Astrophysique et Planétologie, 9 Av. colonel Roche, BP 44346, 31028 Toulousecedex 4, France, douglas.marshall@cesr.fr

**Andrea Miglio** School of Physics and Astronomy, University of Birmingham, Birmingham B15 2TT, UK

Institut d'Astrophysique et de Géophysique de l'Université de Liège, 4000 Liège, Belgium, miglioa@bison.ph.bham.ac.uk

**Miroslav Mocák** Institute of Astronomy and Astrophysics at the Université Libre de Bruxelles, 1050 Bruxelles, Belgium, mmocak@ulb.ac.be

**Josefina Montalbán** Institut d'Astrophysique et Geophysique, Université de Liège, allée du 6 Août 17, 4000 Liège, Belgium, j.montalban@ulg.ac.be

**Benôit Mosser** Observatoire de Paris-Meudon, Meudon, France, benoit.mosser@obspm.fr

**Ewald Müller** Max-Planck-Institut für Astrophysik, 85748 Garching bei München, Germany, ewald@mpa-garching.mpg.de

Ulisse Munari INAF Osservatorio di Padova, Padova, Italy, munari@pd.astro.it

**Arlette Noels** Institut d'Astrophysique et Geophysique, Université de Liège, allée du 6 Août 17, 4000 Liège, Belgium, a.noels@ulg.ac.be

**Ana Palacios** LUPM, Université Montpellier 2 cc 72 – Place Eugène Bataillon – 34095 Montpellier cedex, France

CEA/DSM/IRFU/SAp, L'Orme des Merisiers bât 709, 91191 Gif-sur-Yvette, France, ana.palacios@univ-montp2.fr

**Bertrand Plez** Université de Montpellier, Montpellier cedex, France, bertrand. plez@univ-montp2.fr

xiv Contributors

**Céline Reylé** Institut Utinam, CNRS UMR6213, Université de Franche-Comté, Observatoire de Besançon, Besançon, France, celine@obs-besancon.fr

**Annie C. Robin** Institut Utinam, CNRS UMR6213, Université de Franche-Comté, Observatoire de Besançon, Besançon, France, annie.robin@obs-besancon.fr

**Helio J. Rocha-Pinto** Universidade Federal do Rio de Janeiro, Observatório do Valongo, Rio de Janeiro, RJ, Brazil, helio@iagusp.usp.br

**Maurizio Salaris** Astrophysics Research Institute, Liverpool John Moores University, 12 Quays House, Birkenhead, UK, ms@astro.livjm.ac.uk

**Basílio X. Santiago** Universidade Federal do Rio Grande do Sul, Porto Alegre, RS, Brazil, santiago@if.ufrgs.br

Laboratório Interinstitucional de e-Astronomia LIneA, Rio de Janeiro, RJ, Brazil

**Richard Scuffaire** Institut d'Astrophysique et Geophysique, Université de Liège, allée du 6 Août 17, 4000 Liège, Belgium, r.scuffaire@ulg.ac.be

Mathias Schultheis Institut Utinam, CNRS UMR6213, Université de Franche-Comté, Observatoire de Besançon, Besançon, France, mathias@obs-besancon.fr

**Lionel Siess** Institute of Astronomy and Astrophysics at the Université Libre de Bruxelles, 1050 Bruxelles, Belgium, siess@astro.ulb.ac.be

**Matthias Steffen** Astrophysikalisches Institut Potsdam, An der Sternwarte 16, 14482 Potsdam, Germany, msteffen@aip.de

Marica Valentini Université de Liège, Liège, Belgium, valentini@astro.ulg.ac.be

**Paolo Ventura** INAF – Osservatorio Astronomico di Roma, via Frascati 33, 00040 Monte Porzio Catone (RM), Italy, paolo.ventura@oa-roma.inaf.it

**Achim Weiss** Max-Planck-Institut für Astrophysik, Karl-Schwarzschild-Str. 1, 85748 Garching, Germany, aweiss@mpa-garching.mpg.de

# Part I Asteroseismology of Red Giants

# **Aspects of Observational Red Giant Population Seismology**

Joris De Ridder

**Abstract** The space missions CoRoT and *Kepler* provide us with large samples of red giant stars wherein non-radial solar-like oscillations can be detected. This leads to the exciting opportunity to do population seismology. In this paper we give a short overview of some relevant technical aspects of the two satellites, we list and comment on some important target selection biases relevant for population seismology, and we make a case to use kernel density estimates as an alternative for histograms to characterize population characteristics.

#### 1 Introduction

Population seismology uses oscillation properties of a population of variables of a particular type to extract information about their stellar interior, or about the spatial structure, history, and future evolution of the population. In case of a homogenous population such as often assumed inside stellar clusters, population seismology is often referred to as *ensemble seismology*. In case of a heterogenous population, such as the collection of red giants in a certain field of view, it is assumed that the population is sufficiently representative to extract information about our Galaxy as a whole.

Basically four ingredients are needed for population seismology: (1) seismic observables for a fairly large population, (2) a proper understanding of the selection biases that were involved in selecting the population members, (3) theoretical population models, and (4) a quantitative method to compare observations with theory to derive information. None of these ingredients are trivial and usually require an extensive amount of work. In this paper we will touch upon topics (1),

Instituut voor Sterrenkunde, K.U.Leuven, Celestijnenlaan 200D, 3001 Leuven, Belgium e-mail: joris@ster.kuleuven.ac.be

J. De Ridder (⊠)

4 J. De Ridder

(2), and (4), and we refer for the theoretical population models to the contribution of Miglio in this volume.

Requiring a set of seismic observables of a fairly-sized sample of variables implies gathering high-quality time series for a large number of stars. From the ground this turns out to be very challenging. The better large time-resolved databases are currently surveys such as OGLE (Udalski et al. 1997), and ASAS (Pojmanski 2002). Unfortunately, these datasets are not good enough to detect the really low-amplitude solar-like oscillations in red giants. In addition, these surveys are done with small telescopes observing relatively bright and therefore relatively near giants. This limits the possibility to deeply probe our galaxy.

Dedicated extensive spectroscopic campaigns of very bright giants (e.g. Frandsen et al. 2002; De Ridder et al. 2006) show that it is possible to detect unambiguously low-amplitude solar-like oscillations in red giants. However, it was not until the arrival of the satellite CoRoT that it was possible to convincingly prove the existence of non-radial oscillations in giants (De Ridder et al. 2009). Although CoRoT was capable of making a giant leap forward in red giant seismology, even this satellite is not sensitive enough to detect oscillations in all types of red giants. Giants with a frequency  $\nu_{\rm max}$  (at maximum oscillation power) larger than 120  $\mu$ Hz are often out of reach for CoRoT, which includes the rare but important low-mass low-luminosity giants. It took an even larger space telescope, *Kepler*, to also detect this type of giants (Bedding et al. 2010). Currently CoRoT and *Kepler* are the only two instruments which allow red giant population seismology.

## 2 CoRoT and Kepler in a Nutshell

In this section we give a brief overview of the technical aspects of CoRoT and *Kepler* relevant for population seismology.

The CoRoT spacecraft (see e.g. Baglin et al. 2009) was successfully launched on 27 December 2006 into a circular polar orbit around Earth. Using its 27 cm sized pupil, it was designed to continuously monitor the brightness of stars in a field of view of about  $2.7^{\circ} \times 3.05^{\circ}$  somewhere inside two circular parts of the sky, called the eyes of CoRoT near the galactic plane at  $\alpha \approx 6h50$  and  $\alpha \approx 18h50$ . As the satellite orbits Earth, it is forced to regularly interrupt its observation runs to repoint in another direction to avoid the sunlight. This leads to two 150 run periods per year (so called long runs, LRs), and two short runs of about 30 days (SRs). The first two long runs were chosen in the constellations of Monoceros and Aquila. From the beginning it was made clear that CoRoT had two goals: (1) finding exoplanets, and (2) asteroseismology. This led to a technical design of 4 CCDs of 2,046×4,096 pixels each: 2 seismofield CCDs (A1 and A2) and 2 exoplanet field CCDS (E1 and E2). The former are meant to observe relatively few but bright targets of asteroseismological interest, while the latter aim to observe together about 12,000 relatively faint targets to detect exoplanet transits. The exoplanet field targets have visual magnitudes between 12 and 16, and are observed with an exposure time of 512 s. A significant fraction of these targets are red giants, which make up a population excellently suited for population seismology. More information about the CoRoT mission can be found in ESA SP-1306 (2006).

NASA's *Kepler* mission (see e.g. Borucki et al. 2009) was launched almost 3 years after CoRoT on 7 March 2009. The spacecraft is in a heliocentric orbit which allows it to stare for at least 3.5 years at the same field of view in the Cygnus constellation. It's aperture is about 95 cm, and it features 42 CCDs covering about 105 square degrees of the sky. Roughly 130,000 targets within a dynamic magnitude range of  $9 \le m_V \le 16$ , are continuously monitored, and also here a significant fraction turn out to be red giants, which are observed with an exposure time of about 30 min (long cadence) or of about 1 min (short cadence).

How do these satellites compare for a population seismologist? CoRoT had the advantage of being first, which led to the first population seismology paper relying on non-radial oscillations in red giants observed by CoRoT (Miglio et al. 2009). However, the performance of *Kepler* in terms of S/N or in terms of the length of the time series goes beyond anything what CoRoT can provide. This allows for more accurate seismic observables, and an evolutionary stage coverage that includes red giants with  $\nu_{max} \geq 120\,\mu\text{Hz}$  (cf. Sect. 1). CoRoT, on the other hand, changes its field of view regularly, which allows to probe different directions in our galaxy to study, for example, possible spatial metallicity gradients. In this sense, the two missions are complementary.

#### 3 Selection Biases

Comparing observations with theory usually involves comparing observational and theoretical histograms (or equivalent) of some seismic observable. A difficult aspect of population seismology is to investigate if there are any selection biases that may have caused some of the bins to be less populated than they should be. Failing to identify these selection biases, or failing to make a proper impact analysis of them will likely result into an erroneous interpretation of the data.

There can be basically four reasons why a red giant was selected to be observed by CoRoT or *Kepler*. First, by selection on scientific grounds by, for example, the red giant analysis team. Secondly, simply because there were roughly the same number of targets in the field as available slots on the CCDs, so that every target is observed. Thirdly, failure to avoid red giants by planet hunters. And fourthly, as astrometric targets. Each of these reasons may have different (although overlapping) selection criteria and biases.

In what follows we list and comment on some of the common selection criteria.

• The most obvious selection criteria are based on observationally derived stellar parameters. For example, every *Kepler* astrometric giant satisfies the criteria  $T_{\rm eff} < 5,400$  K,  $R/R_{\odot} > 2$ , and  $\log g < 3.8$ . It's important to realize, however, that the derivation of stellar parameters for the databases of targets of CoRoT

and *Kepler* are for the largest part not based on spectroscopic data, but rather on fitting a small set of photometric measurements. As a result, both the parameters and their quoted uncertainties are not always reliable, especially for the hotter and the cooler stars. To what extend this affects a histogram of the observed giant population remains to be investigated, however.

- The allowed magnitude range of the targets is determined by the dynamic range of the instrument, but may be limited for specific purposes. The astrometric giants of the *Kepler* mission, for example, have a rather narrow magnitude range of 11–12.5. The fainter the target, the lower the S/N ratio will be, and the more difficult it will be to extract useful asteroseismic information. While this is unlikely an issue for *Kepler*, it could be for CoRoT, depending on what type of asteroseismic information one is looking for. As the signal strength may vary because of the stochastic nature of the oscillations, the upper magnitude boundary of the sample of useful red giants can be rather fuzzy, in contrast with the lower magnitude boundary which is set to avoid saturation.
- It is not only the saturation risk of a potential red giant target that matters. Even if the target is sufficiently faint, it may still be rejected if a neighboring star on the CCD would likely saturate and bleed upon it.
- Red giants suffering too much from crowding (i.e. from background objects contributing more than e.g. 5% of the flux in the mask) are rejected to avoid a decrease in S/N, a signal contamination, or inaccurate centroiding in the case of astrometric giants.
- Astrometric giants also require a small parallax and a small proper motion, for obvious reasons.
- The effective field of view (FOV) is a bit smaller than the quoted instrumental FOV. The reason is that the silicon edge is usually avoided for target selection. This is especially the case for *Kepler*, where the exact position on the CCD depends on the season, and where one requires that a giant star is observable in all seasons.
- The appearance of instrumental peaks in the power spectrum can have a large effect on the final red giant sample. In the case of the CoRoT sample, for example, there appear to be hardly any giants with a a  $\nu_{\text{max}} \geq 120\,\mu\text{Hz}$  for which reliable seismic observables can be derived. This is not only due to S/N limitations, but also due to the occurrence of peaks coming from a mixture of orbital and diurnal frequencies at  $(161.7 \pm k \cdot 11.6)\,\mu\text{Hz}$ , with k an integer (Mosser et al. 2010) which make the data reduction and analysis a lot more difficult.
- The limited number of available slots on the CCD can also introduce a selection bias for specific types of giants. In the case of *Kepler* the long cadence (LC) time series have a Nyquist frequency of about  $\nu_{\rm Nyq} \approx 280\,\mu{\rm Hz}$ . Red giants with a  $\nu_{\rm max} \geq \nu_{\rm Nyq}$  therefore need to be observed in short cadence (SC). The SC slots are, however, mainly used for main sequence stars and subgiants to fulfill the space mission's main science objective. The number of low-luminosity low-mass giants will therefore be underrepresented in the *Kepler* red giant sample. Although much less, there is also an over-demand for the LC slots. Usually a selection is made to ensure a large variety of giants ( $\nu_{\rm max}$ , magnitude, metallicity, etc).

The list above is not exhaustive, and it should be clear that it would be rather challenging (if not impossible) for a theoretician to reproduce all selection criteria to produce a suitable synthetic population. Some of the criteria may not even be formulated in the form of hard constraints. However, one usually does know the observational data that were available to make the selection. A better alternative may therefore consist of Monte Carlo resampling the corresponding synthetic data to produce an optimal distribution of synthetic populations with the observed characteristics. All statistical inferences can then be made in a Bayesian way which makes it easy to include this distribution.

## 4 Comparing Population Characteristics

Visualizing seismic population characteristics is often done using a histogram (e.g. Miglio et al. 2009). In this section, we would like to advocate using a better alternative: kernel density estimates (KDE). Histograms depend on two free parameters both of which can have a rather large impact on its shape and appearance: the origin, and the bin width h. Varying these parameter may change the appearance of a peak in the histogram from symmetric to skewed, or vice versa, and may cause small features to appear or disappear. The problem of the histogram origin can in principle be solved by averaging histograms made with different bin grids. Choosing a good bin width, however, remains difficult if the shape of the true distribution is unknown. If we choose the bin width too small, we're under-smoothing and suffer a large variance. A too large bin width, on the other hand, leads to over-smoothing and a large bias.

A useful alternative would be a non-parametric density estimate using a kernel function K. Given a set of n observed values  $\{X_i\}$ , the probability density function f(x) of the corresponding quantity is estimated by

$$\hat{f}_h(x) = \frac{1}{nh} \sum_{i=1}^n K\left(\frac{x - X_i}{h}\right) \tag{1}$$

where K is a kernel function and h the bandwidth. Often used Kernels are the Gaussian kernel  $K(u) \equiv exp(-u^2/2)/\sqrt{2\pi}$  or the Epanechnikov kernel  $K(u) \equiv 0.75 (1 - u^2) I(|u| \le 1)$  where I is the indicator function.

At first sight, not much seems to be gained. There is still a bandwidth h to choose, which can be seen as the analogue of the bin width of a histogram, and now we also have to choose which kernel is best suited. In practice, however, the latter is not a problem because it usually makes very little difference which kernel is exactly used. An important reason to choose KDEs is that they have better asymptotic properties than a histogram. Quantifying the performance of a density esimator can be done by looking at the bias  $E[\hat{f}_h(x)] - f(x)$ , the variance  $Var[\hat{f}_h(x)]$ , and the mean integrated

8 J. De Ridder

squared error (MISE):

$$MISE[\hat{f}_h] \equiv E \left[ \int_{-\infty}^{+\infty} (\hat{f}_h(x) - f(x))^2 dx \right]$$
 (2)

The latter quantity can used to derive the optimal bandwidth  $h_{\rm opt}$  that minimizes the MISE. Table 1 (adapted from Härdle 1990) compares the results for histograms and KDEs. Clearly, both the bias and the MISE of the KDE have a higher convergence rate than those of histograms.

Although the optimal bandwidth  $h_{\rm opt}$  derived from the MISE is handy to derive theoretical results, it has no practical use if the shape of the true distribution is not known. It can be shown, however (see e.g. Härdle et al. 2004) that using the integrated squared error (ISE)

$$ISE[\hat{f_h}] \equiv \int_{-\infty}^{+\infty} (\hat{f_h}(x) - f(x))^2 dx$$
 (3)

**Table 1** Asymptotic properties of the histogram and the kernel density estimator (KDE). Using the mean integrated squared error (MISE) as a measure, the KDE proves to have a better convergence rate compared to the histogram

	Bias	Variance	$h_{\mathrm{opt}}$ (MISE)	$\mathrm{MISE}(f_h)$
	$(h \to 0)$	$(nh \to \infty)$	$(nh \to \infty)$	$(nh \to \infty)$
Histogram	$\sim h$	$\sim (nh)^{-1}$	$\sim n^{-1/3}$	$\sim n^{-2/3}$
Kernel	$\sim h^2$	$\sim (nh)^{-1}$	$\sim n^{-1/5}$	$\sim n^{-4/5}$

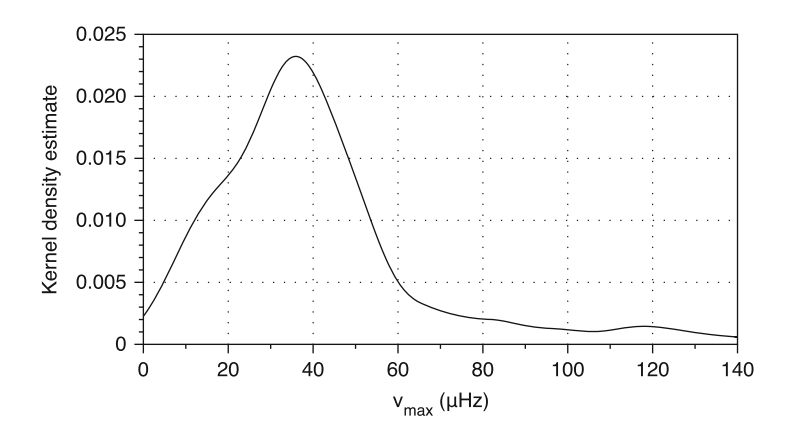


Fig. 1 Kernel density estimate of the distribution of the frequency  $\nu_{max}$  of maximum power of a sample of CoRoT giants in the first anti-center field (LRa1). Seismic data from Mosser et al. (2010)

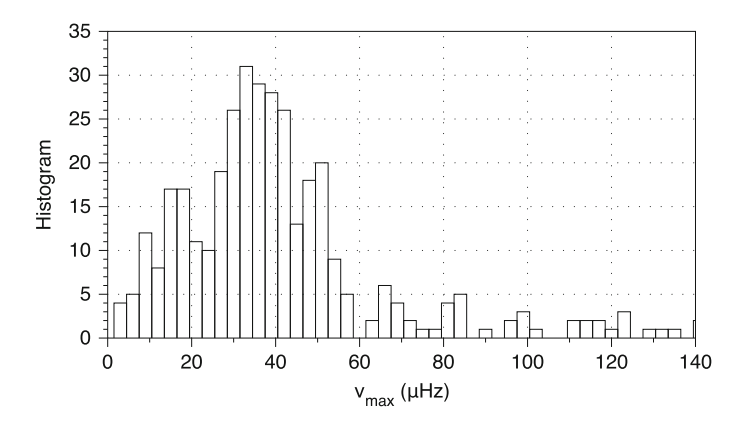


Fig. 2 Kernel density estimate of the distribution of the frequency  $v_{\text{max}}$  of maximum power of a sample of CoRoT giants in the first anti-center field (LRa1). Seismic data from Mosser et al. (2010)

together with cross-validation can be used to compute an optimal value for the bandwidth. This method, as well as alternative statistically justified methods are readily available in the statistical package R. In addition, we refer to Härdle et al. (2004) on how to compute confidence intervals and confidence bands for the KDEs, something which is not easily available for histograms. As a final illustration, we show the KDE of the frequency of maximum power of a sample of CoRoT giants in the LRa1 field in Fig. 1, and a histogram of the same sample in Fig. 2. We hope this short introduction will convince population seismologists of the benefits of using KDEs.

#### References

Baglin, A., Auvergne, M., Barge, P., et al.: Proceedings of the International Astronomical Union, vol. 253, Transiting Planets, pp. 71–81 (2009)

Bedding, T.R., Huber, D., Stello, D., et al.: ApJ**713**, L176 (2010)

Borucki, W., Koch, D., Batalha, N., et al.: Proceedings of the International Astronomical Union, vol. 253, Transiting Planets, pp. 289–299 (2009)

De Ridder, J., Barban, C., Carrier, F., et al.: A&A448, 689 (2006)

De Ridder, J., Barban, C., Baudin, F., et al.: Nature 459, 398 (2009)

Frandsen, S., Carrier, F., Aerts, C., et al.: A&A394, L5 (2002)

Härdle, W.: Smoothing Techniques: With Implementation in S. Springer Series in Statistics. Springer, Berlin (1990)

Härdle, W., Müller, M., Sperlich, S., Werwatz, A.: Nonparametric and semiparametric models. Springer Series in Statistics. Springer, Berlin (2004)

Miglio, A., Montalbán, J., Baudin, F., et al.: A&A503, L21 (2009)

Mosser, B., Belkacem, K., Goupil, M., et al.: A&A517, A22 (2010)

Pojmanski, G.: Acta Astron. 52, 397 (2002)

Udalski, A., Kubiak, M., Szymanski, M.: Acta Astron. 47, 319 (1997)

# Asteroseismology of Red Giants as a Tool for Studying Stellar Populations: First Steps

Andrea Miglio

**Abstract** The detection of solar-like oscillations in G and K giants with the CoRoT and *Kepler* space-based satellites allows robust constraints to be set on the mass and radius of such stars. The availability of these constraints for thousands of giants sampling different regions of the Galaxy promises to enrich our understanding on the Milky Way's constituents. In this contribution we briefly recall which are the relevant constraints that red-giant seismology can currently provide to the study of stellar populations. We then present, for a few nearby stars, the comparison between radius and mass determined using seismic scaling relations and those obtained by other methods.

#### 1 Introduction

Since the data from the first CoRoT observational runs were analysed, and solar-like oscillations were detected in thousands of red giant stars (De Ridder et al. 2009; Hekker et al. 2009; Mosser et al. 2010; Kallinger et al. 2010), it has become clear that the newly available observational constraints will allow novel approaches in the study of so far poorly constrained galactic stellar populations (Miglio et al. 2009).

While CoRoT continues to monitor giants in different regions of the Milky Way, *Kepler* is contributing significantly to the characterisation not only of redgiant populations (see De Ridder, this volume for a review) but it has also opened the way for "ensemble seismology" of solar-like stars. The detection of solar-like oscillations in about 500 F and G dwarfs allowed Chaplin et al. (2011) to perform a

12 A. Miglio

first quantitative comparison between the distributions of observed masses and radii of these stars with predictions from models of synthetic populations in the Galaxy.

We outline in Sect. 2 the innovative aspects of seismic constraints, highlighting the importance of being able to determine the mass of giant stars, while we will discuss in detail the implications of the radius (hence distance) estimates in a future paper. In Sect. 3 we first review how mass and radius of giants are estimated using the average seismic parameters  $\Delta\nu$  (average large frequency separation) and  $\nu_{max}$  (frequency corresponding to the maximum observed oscillation power), and then present, for a few nearby stars, the comparison between radius and mass determined using seismic and non-seismic observational constraints.

## 2 New Constraints on Stellar Populations

Once they reach the red-giant phase of their evolution, stars of significantly different age end up sharing similar photospheric properties. As a consequence, field giants belonging to the composite galactic-disk population were so far considered poor tracers of age. However, the possibility of determining with asteroseismology the masses of thousands of these objects has unexpectedly reversed this picture.

As is well known, the age of RGB and red-clump (RC) stars is largely determined by their main-sequence lifetime and hence, to a first approximation, by their mass and metallicity. The age-mass relation of giant stars predicted by stellar models is illustrated in Fig. 1, where it is compared with that of stars on the main sequence. For the purposes of this comparison, a crude criterion based on the surface gravity g was used to separate giants ( $\log g < 3.5$ ) from main-sequence stars ( $\log g > 3.5$ ). The synthetic population shown in the figure was computed with the code TRILEGAL (Girardi et al. 2005; Girardi et al., this volume), and is representative of thin-disk stars monitored by CoRoT in the LRc01 field. The tight age-mass relation shown in the lower panel of Fig. 1 clearly shows that adding the mass among the observational constraints enables us to use giants as potentially very precise age indicators.

From a closer inspection of Fig. 1, it is worth noticing that for stars with  $M \lesssim 1.5$   $M_{\odot}$  the age-mass relation bifurcates due to the significant mass loss ( $\sim 0.1$ – $0.2 \, M_{\odot}$ ) experienced by low-mass stars near the tip of the RGB. Consequently, RC stars are younger than stars on the RGB with the same actual mass (and metallicitiy). We can, however, remove this degeneracy in the age-mass relation thanks to additional seismic constraints. It is indeed excellent news in this context that the detailed properties of dipolar oscillation modes allow us to clearly distinguish RGB from RC stars (Montalbán et al. 2010; Bedding et al. 2011; Mosser et al. 2011; Montalbán et al. this volume). When applied to the characterisation of stellar populations this

<sup>&</sup>lt;sup>1</sup>In the models used in Fig. 1, RGB mass loss is implemented adopting the Reimers (1975) prescription (see Girardi et al. 2000 for more details).

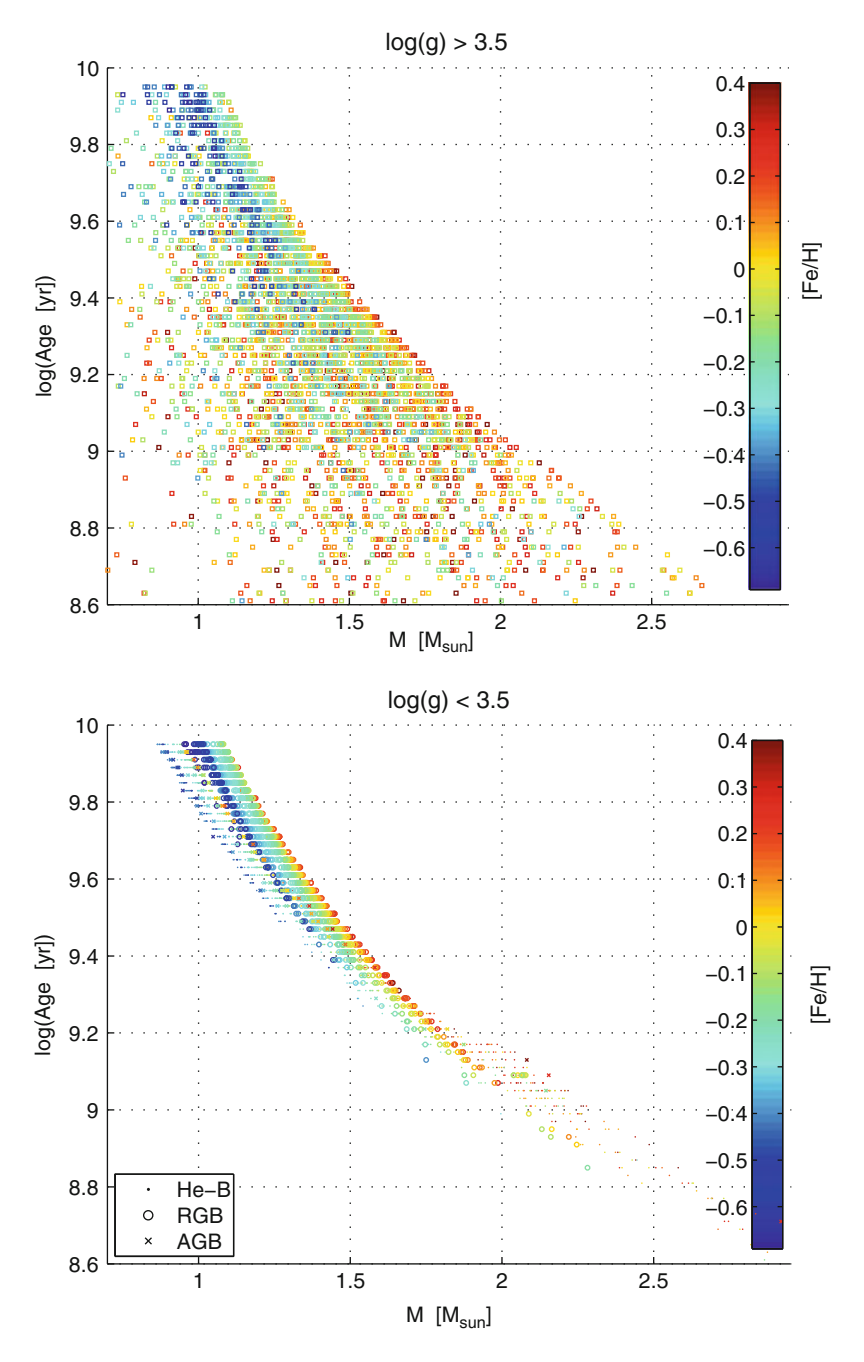


**Fig. 1** Age-mass-metallicity relation for main-sequence stars (*upper panel*) and red giants (*lower panel*) in a synthetic population representative of thin-disk stars observed by CoRoT in the LRc01 field. The evolutionary state of giants is marked with a different symbol: *dots* (stars in the core-Helium-burning phase), *crosses* (Asymptotic-Giant-Branch stars), and *open circles* (stars on the Red Giant Branch). The fraction of AGB stars in the population of giants shown here is ~4%

14 A. Miglio

result can potentially lead to age estimates independent of the uncertain RGB massloss rates.

As a word of caution we should recall, however, that these age estimates are inherently model dependent, being affected by uncertainties in predicting, e.g. main-sequence lifetimes. On the other hand, the potential of asteroseismology goes well beyond the determination of global stellar parameters using scaling relations. As frequencies of individual pulsation modes become available, detailed comparisons between observed and theoretical oscillation spectra promise to improve both the precision of age estimates (see e.g. Di Mauro et al. 2011), along with their accuracy, by providing stringent constraints on models of the internal structure of both main-sequence and in giant stars.

As a relevant additional constraint that seismology could potentially provide to the study of stellar populations, we recall that investigations are currently underway to assess under which conditions a reliable indication of the envelope-helium abundance can be derived from the seismic signature of helium ionisation detected in CoRoT and *Kepler* giants (see Miglio et al. 2010; Montalbán et al. this volume).

Finally, as discussed during this meeting, it is worth mentioning that (2) below provides a potentially very accurate way of determining the surface gravities of stars, which could be then used as an input to refine spectroscopic analyses (see e.g. Morel et al. 2011) and, eventually, to test model atmospheres of giant stars (Plez this meeting).

# 3 Scaling Relations

Radii and masses of solar-like oscillating stars can be estimated from the average seismic parameters that characterise their oscillation spectra: the so-called average large frequency separation ( $\Delta \nu$ ), and the frequency corresponding to the maximum observed oscillation power ( $\nu_{max}$ ).

The large frequency separation is predicted by theory to scale as the square root of the mean density of the star (see e.g. Vandakurov 1967; Tassoul 1980):

$$\Delta v \simeq \sqrt{\frac{M/M_{\odot}}{(R/R_{\odot})^3}} \Delta v_{\odot},$$
 (1)

where  $\Delta \nu_{\odot} = 135\,\mu\text{Hz}$ . The frequency of maximum power is expected to be proportional to the acoustic cutoff frequency (Brown et al. 1991; Kjeldsen and Bedding 1995; Mosser et al. 2010; Belkacem et al. 2011), and therefore:

$$u_{\rm max} \simeq \frac{M/M_{\odot}}{(R/R_{\odot})^2 \sqrt{T_{\rm eff}/T_{\rm eff,\odot}}} \nu_{\rm max,\odot},$$
(2)

where  $\nu_{\text{max},\odot} = 3$ , 100  $\mu$ Hz and  $T_{\text{eff},\odot} = 5$ , 777 K.

Depending on the observational constraints available, we may derive mass estimates from (1) and (2) alone, or via their combination with other available information from non-seismic observations. When no information on distance/luminosity is available, which is the case for the vast majority of field stars observed by CoRoT and Kepler, (1) and (2) may be solved to derive M and R (see e.g. Kallinger et al. 2010; Mosser et al. 2010):

$$\frac{M}{M_{\odot}} \simeq \left(\frac{\nu_{\text{max}}}{\nu_{\text{max},\odot}}\right)^{3} \left(\frac{\Delta \nu}{\Delta \nu_{\odot}}\right)^{-4} \left(\frac{T_{\text{eff}}}{T_{\text{eff},\odot}}\right)^{3/2} \tag{3}$$

$$\frac{R}{R_{\odot}} \simeq \left(\frac{\nu_{\text{max}}}{\nu_{\text{max},\odot}}\right) \left(\frac{\Delta \nu}{\Delta \nu_{\odot}}\right)^{-2} \left(\frac{T_{\text{eff}}}{T_{\text{eff},\odot}}\right)^{1/2}.$$
 (4)

However, when additional constraints on the distance/luminosity of stars are available, M can also be estimated also from (1) or (2) alone:

$$\frac{M}{M_{\odot}} \simeq \left(\frac{\Delta \nu}{\Delta \nu_{\odot}}\right)^{2} \left(\frac{L}{L_{\odot}}\right)^{3/2} \left(\frac{T_{\rm eff}}{T_{\rm eff,\odot}}\right)^{-6} \tag{5}$$

$$\frac{M}{M_{\odot}} \simeq \left(\frac{\nu_{\text{max}}}{\nu_{\text{max},\odot}}\right) \left(\frac{L}{L_{\odot}}\right) \left(\frac{T_{\text{eff}}}{T_{\text{eff},\odot}}\right)^{-7/2} \tag{6}$$

These scaling relations have been widely adopted to estimate masses and radii of red giants (see e.g. Stello et al. 2008; Kallinger et al. 2010; Mosser et al. 2010), but they are based on simplifying assumptions which must be checked against independent fundamental measurements. Recent advances have been made on providing a theoretical basis for the relation between the acoustic cut-off frequency and  $\nu_{\text{max}}$  (Belkacem et al. 2011), and preliminary investigations with stellar models (Stello et al. 2009) indicate that the scaling relations hold to within  $\sim 3\%$  on the main sequence and RGB (see also the Supporting Online Material in Chaplin et al. 2011).

# 3.1 Empirical Tests of the $v_{max}$ and $\Delta v$ Scaling Relations

To assess the accuracy of the scaling relations, ongoing studies based on models of stars in different evolutionary phases, and covering a wide range of parameters (see e.g. White et al. 2011; Miglio et al. 2012), must be complemented by calibration of the  $\nu_{max}$  and  $\Delta\nu$  relations with independent determinations of masses and radii. As a very first step in this process, we present here a simple comparison between radii and masses determined via seismic constraints with those obtained by other methods (combination of parallax, bolometric flux, effective temperature, angular radius, mass derived from the orbital solution of binary systems).

We include in this comparison nearby stars with available seismic constraints, along the lines of the work presented by Bruntt et al. (2010). We consider a total of

16 A. Miglio

27 stars with published values of both  $\nu_{max}$  and  $\Delta\nu$ . The quality of the seismic data available for the stars in this sample is highly heterogeneous, ranging from nearly 6-months long space-based photometric observations with the CoRoT satellite, to few days' single-site radial-velocity monitoring. The methods used to estimate  $\nu_{max}$  and  $\Delta\nu$  are also not uniform. We therefore decided to adopt a 2 and 5% uncertainty in  $\Delta\nu$  and  $\nu_{max}$ , respectively, as also suggested in Bruntt et al. (2010).

Asteroseismic, spectroscopic, interferometric, and photometric constraints were either taken from the Bruntt et al. (2010) compilation (to which we refer for the original references), or collected from the papers by Ballot et al. (2011), Barban et al. (2009), Bazot et al. (2011), Bruntt (2009), Carrier and Eggenberger (2006), Carrier et al. (2010), Deheuvels et al. (2010), Eggenberger et al. (2008), Gillon and Magain (2006), Kallinger et al. (2010), Mathur et al. (2010), Mazumdar et al. (2009), Mérand et al. (2010), Mosser et al. (2008, 2009, 2010) and Quirion et al. (2010). Parallaxes are taken from van Leeuwen (2007) and bolometric corrections from Flower (1996). When available, we used  $T_{\rm eff}$  determined from the bolometric fluxes and interferometric angular radii, in which case we considered the value quoted in Bruntt et al. (2010). Otherwise, we adopted spectroscopic  $T_{\rm eff}$  with uncertainties of 100 K, unless the uncertainty was larger in the original reference. As in Bruntt (2009) we excluded from the sample HD175726 since its estimated large separation shows an unexplained large modulation with frequency (see Mosser et al. 2009).

We then determined radii using (4) and masses via (3) or by including constraints on the luminosity, using (5) and (6). The comparisons between different (not always independent) determinations of radius and mass are presented in Figs. 2 and 3.

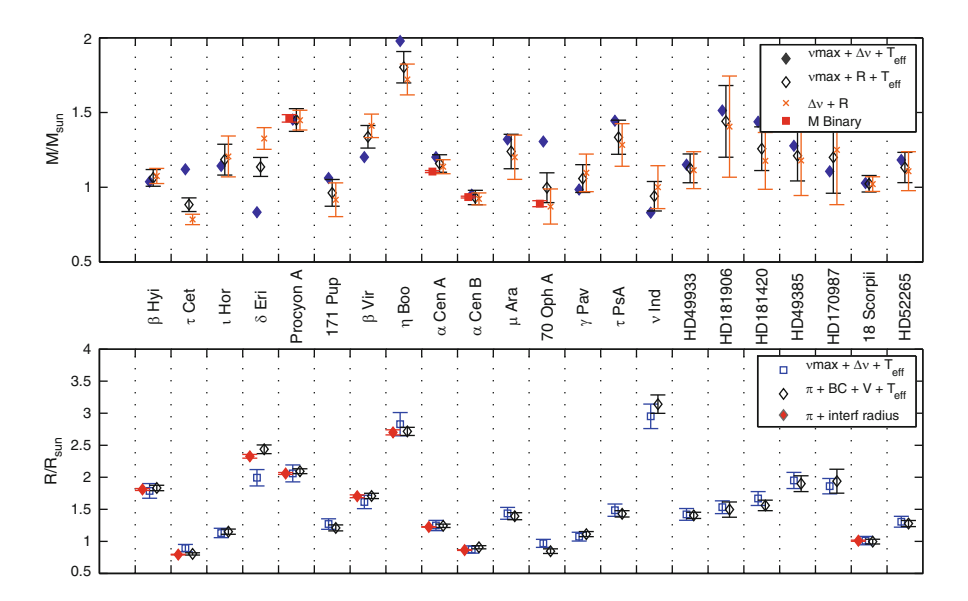


Fig. 2 Comparison between masses (*upper panel*) and radii (*lower panel*) determined by different combinations of the observational constraints available

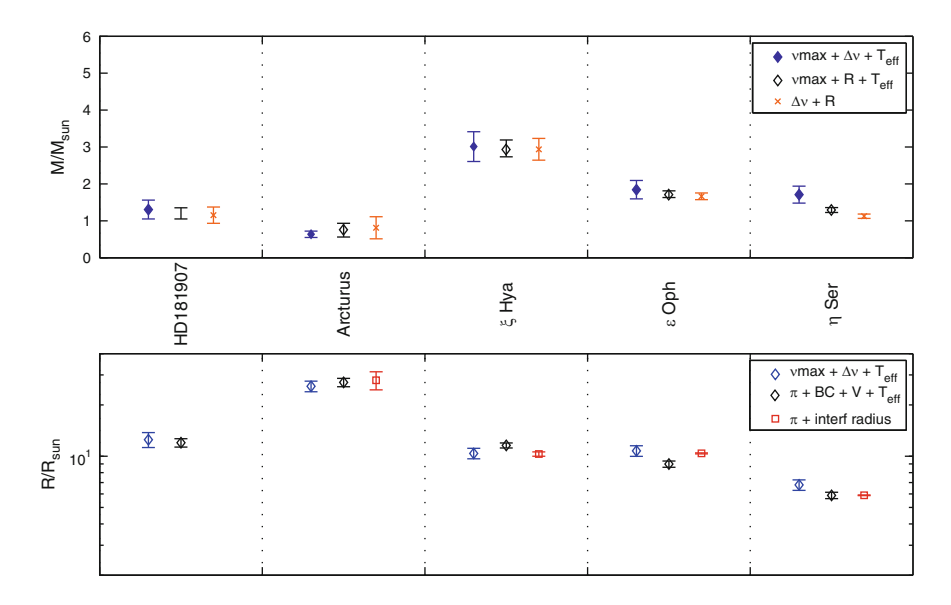


Fig. 3 Same as Fig. 2, but considering giants with published seismic analysis

The targets considered span a large domain in radius: from sub-solar radii ( $\tau$  Cet, 70 Oph A, and  $\alpha$  Cen B) to the  $\sim$  30  $R_{\odot}$  of the metal-poor giant Arcturus. The overall agreement found between values determined via (4) and using classical constraints is remarkable (see Figs. 4 and 5), and the two determinations agree within 1- $\sigma$  ( $\sim$ 7%) in most cases (see Fig. 5). Weighting the differences according to their errors, we find a mean difference ( $R_{\rm seismo}-R$ ) and standard deviation of -1.5% and 6%, respectively. A significantly larger number of stars (especially giants) should be included to investigate possible trends with stellar properties. This comparison is indeed encouraging and adds strong support to the use of solar-like oscillators as distance indicators, also when compared to results obtained using accurate determinations of radii in eclipsing binaries, as presented in the recent review by Torres et al. (2009) (see e.g. their Fig. 1).

The expected uncertainty in the mass determined using (3) and the available data is  $\sim 10-15\%$ . Besides noting a good agreement when comparing different (but correlated) expressions to estimate the mass (see Figs. 2 and 3), only for few visual binary systems ( $\alpha$  Cen A and B, Procyon A, and 70 Oph A) could we test the mass determined using  $\nu_{\rm max}$  and/or  $\Delta\nu$  with the independent estimate based on the orbital solution. In these cases we find a 1- $\sigma$  agreement, except for 70 Oph A which has an observed  $\nu_{\rm max}$  larger than expected (still within 2  $\sigma$  of the predicted value). This is clear from the direct comparison between  $\nu_{\rm max}$  and  $\Delta\nu$  observed and predicted by scaling relations is shown in Fig. 6.

The quality of seismic constraints obtained from space-based data exceeds that available for most of the stars considered in this comparison. Consequently, while radii and masses can be estimated with greater precision, this demands more

18 A. Miglio

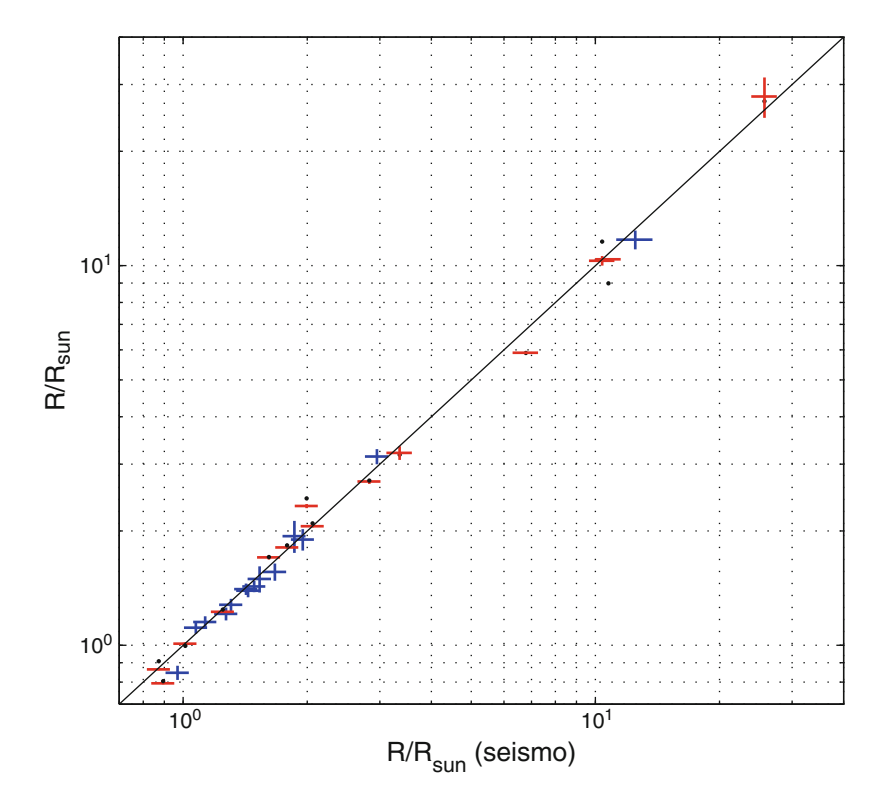


Fig. 4 Radii determined using seismic constraints (4) vs. radii determined from parallax and angular interferometric radius (red), and from apparent magnitude, parallax, BC and  $T_{\rm eff}$  (blue). For targets where interferometric measurements are available we also report the comparison with radii determined from apparent magnitude+ parallax+ BC +  $T_{\rm eff}$  ( $black\ dots$ )

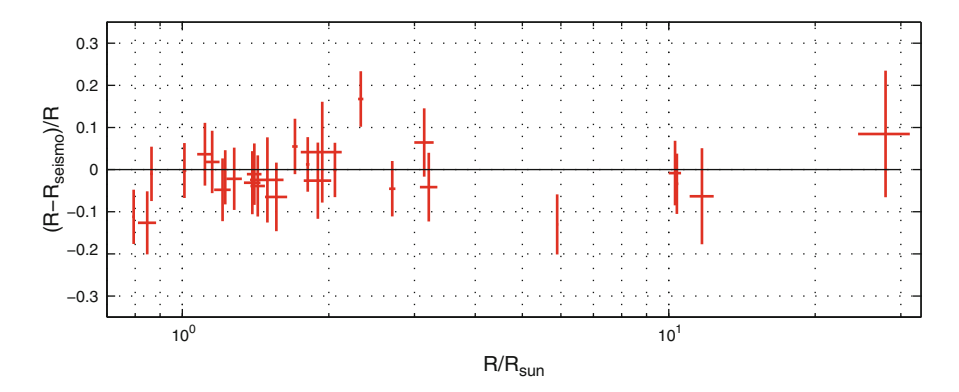


Fig. 5 Percentage difference between radii determined using seismic constraints (4) and those derived from the parallax and interferometric angular radius (if available) or the the estimated bolometric luminosity and  $T_{\rm eff}$ 

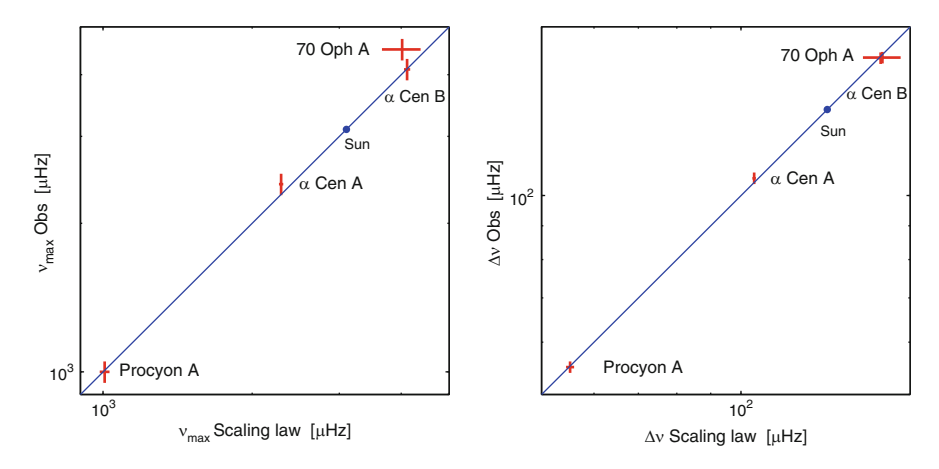


Fig. 6 Left panel: Comparison between  $\nu_{\text{max}}$  observed vs.  $\nu_{\text{max}}$  predicted using independent measurements of mass and radius. Right panel: as left panel, but for  $\Delta \nu$ 

stringent tests of the accuracy of the scaling relations. In this respect nearby *Kepler* and CoRoT targets, and in particular high-duty cycle ground-based observations (e.g. with SONG, see Grundahl et al. 2009) will play a crucial role in testing  $\nu_{\text{max}}$  and  $\Delta\nu$  in well constrained systems. Moreover, the detection with *Kepler* of solar-like oscillations in red giants members of open clusters provides additional means for testing the accuracy of scaling relations, particularly when largely model-independent constraints are available for cluster members (see the encouraging results reported in Stello et al. 2010; Basu et al. 2011; Miglio et al. 2011). Eclipsing binaries with solar-like pulsating components observed by *Kepler* and CoRoT are also promising and privileged targets for this purpose (see e.g. Hekker et al. 2010).

# 4 Summary and Outlook

Thanks to the interpretation of solar-like oscillation spectra detected by CoRoT and *Kepler*, we can now determine the mass and radius of thousands of stars belonging to the composite population of the Milky Way's disk. These truly innovative constraints will allow precise age estimates for giants, and will inform studies of galactic formation and evolution with observational constraints which were not available prior to asteroseismology. To fully exploit the potential of these observations, however, it will be crucial to combine them with spectroscopic constraints, which should become available in the near future thanks to large spectroscopic surveys such as SDSS-APOGEE and the GAIA-ESO spectroscopic survey. Further efforts should also be devoted to assess the validity of the  $\nu_{\rm max}$  and  $\Delta\nu$  scaling relations, both in terms of their theoretical foundation, and through calibration with independent measurements of radius and mass.

20 A. Miglio

In the future, the pioneering observations of CoRoT and *Kepler* could be extended to significantly wider areas of the sky by the candidate ESA mission PLATO,<sup>2</sup> providing observational constraints that will be complementary to the accurate distance and proper motions measured by GAIA<sup>3</sup> in the coming years.

**Acknowledgements** The author acknowledges FNRS for financial support, M. Barbieri, L. Girardi, J. Montalbán, T. Morel, B. Mosser, and A. Noels for enlightening discussions about seismology and stellar populations. Additional thanks are due to M. Barbieri and L. Girardi for their kind help with the code TRILEGAL, and to W. J. Chaplin for reading the manuscript.

#### References

```
Ballot, J., Gizon, L., Samadi, R., et al.: A&A 530, A97 (2011)
```

Barban, C., Deheuvels, S., Baudin, F., et al.: A&A 506, 51 (2009)

Basu, S., Grundahl, F., Stello, D., et al.: ApJ 729, L10 (2011)

Bazot, M., Ireland, M.J., Huber, D., et al.: A&A 526, L4 (2011)

Bedding, T.R., Mosser, B., Huber, D., et al.: Nature 471, 608 (2011)

Belkacem, K., Goupil, M.J., Dupret, M.A., et al.: A&A 530, A142 (2011)

Brown, T.M., Gilliland, R.L., Noyes, R.W., Ramsey, L.W.: ApJ 368, 599 (1991)

Bruntt, H.: A&A 506, 235 (2009)

Bruntt, H., Bedding, T.R., Quirion, P.-O., et al.: MNRAS 405, 1907 (2010)

Carrier, F., Eggenberger, P.: A&A 450, 695 (2006)

Carrier, F., De Ridder, J., Baudin, F., et al.: A&A 509, A73 (2010)

Chaplin, W.J., Kjeldsen, H., Christensen-Dalsgaard, J., et al.: Science 332, 213 (2011)

De Ridder, J., Barban, C., Baudin, F., et al.: Nature 459, 398 (2009)

Deheuvels, S., Bruntt, H., Michel, E., et al.: A&A 515, A87 (2010)

Di Mauro, M.P., Cardini, D., Catanzaro, G., et al.: MNRAS 1166 (2011)

Eggenberger, P., Miglio, A., Carrier, F., Fernandes, J., Santos, N.C.: A&A 482, 631 (2008)

Flower, P.J.: ApJ 469, 355 (1996)

Gillon, M., Magain, P.: A&A 448, 341 (2006)

Girardi, L., Bressan, A., Bertelli, G., Chiosi, C.: A&AS 141, 371 (2000)

Girardi, L., Groenewegen, M.A.T., Hatziminaoglou, E., da Costa, L.: A&A 436, 895 (2005)

Grundahl, F., Christensen-Dalsgaard, J., Arentoft, T., et al.: CoAst 158, 345 (2009)

Hekker, S., Kallinger, T., Baudin, F., et al.: A&A 506, 465 (2009)

Hekker, S., Debosscher, J., Huber, D., et al.: ApJ 713, L187 (2010)

Kallinger, T., Weiss, W.W., Barban, C., et al.: A&A 509, A77 (2010)

Kjeldsen, H., Bedding, T.R.: A&A 293, 87 (1995)

Mathur, S., García, R.A., Catala, C., et al.: A&A 518, A53 (2010)

Mazumdar, A., Mérand, A., Demarque, P., et al.: A&A **503**, 521 (2009)

Mérand, A., Kervella, P., Barban, C., et al.: A&A 517, A64 (2010)

Miglio, A., Montalbán, J., Baudin, F., et al.: A&A 503, L21 (2009)

Miglio, A., Montalbán, J., Carrier, F., et al.: A&A 520, L6 (2010)

Miglio, A., Brogaard, K., Stello, D., et al.: MNRAS (submitted 2011)

Miglio, A., Brogaard, K., Stello, D., et al.: MNRAS, in press (2012)

<sup>&</sup>lt;sup>2</sup>http://sci.esa.int/plato.

<sup>3</sup>http://gaia.esa.int/.

Montalbán, J., Miglio, A., Noels, A., Scuflaire, R., Ventura, P.: ApJ 721, L182 (2010)

Morel, T., Miglio, A., Valentini, M.: J. Phys. Conf. Ser. 328, 012010 (2011)

Mosser, B., Deheuvels, S., Michel, E., et al.: A&A 488, 635 (2008)

Mosser, B., Michel, E., Appourchaux, T., et al.: A&A 506, 33 (2009)

Mosser, B., Belkacem, K., Goupil, M.-J., et al.: A&A 517, A22 (2010)

Mosser, B., Barban, C., Montalbán, J., et al.: A&A 532, 86 (2011)

Quirion, P.-O., Christensen-Dalsgaard, J., Arentoft, T.: ApJ 725, 2176 (2010)

Reimers, D.: Mem. Soc. R. Sci. Liege 8, 369 (1975)

Stello, D., Bruntt, H., Preston, H., Buzasi, D.: ApJ 674, L53 (2008)

Stello, D., Chaplin, W.J., Basu, S., Elsworth, Y., Bedding, T.R.: MNRAS 400, L80 (2009)

Stello, D., Basu, S., Bruntt, H., et al.: ApJ **713**, L182 (2010)

Tassoul, M.: ApJS 43, 469 (1980)

Torres, G., Andersen, J., Giménez, A.: A&A Rev. 18, 67 (2009)

van Leeuwen, F.: A&A **474**, 653 (2007)

Vandakurov, Y.V.: AZh 44, 786 (1967)

White, T. R., Bedding, T., Stello, D., et al.: ApJ 743, 161 (2011)

# Adiabatic Solar-Like Oscillations in Red Giant Stars

Josefina Montalbán, Andrea Miglio, Arlette Noels, Richard Scuflaire, Paolo Ventura, and Francesca D'Antona

**Abstract** Since the detection of non-radial solar-like oscillation modes in red giants with the CoRoT satellite, the interest in the asteroseismic properties of red giants and the link with their global properties and internal structure is substantially increasing. Moreover, more and more precise data are being collected with the space-based telescopes CoRoT and *Kepler*. In this paper we present a survey of the most relevant theoretical and observational results obtained up to now concerning the potential of solar-like oscillations in red giants.

## 1 Structure and Oscillation Spectra of Red Giant Models

Red giants are cool stars with an extended and diluted convective envelope surrounding a dense core, which makes their structure and therefore their pulsation properties very different from those of the Sun. As in solar-like stars, however, their convective envelope can stochastically excite oscillation modes. The properties of oscillation modes depend on the behavior of the Brunt-Väisälä (N) and Lamb  $(S_\ell)$  frequencies. In a first approximation we can describe the radial displacement due to

J. Montalbán ( $\boxtimes$ ) · A. Noels · R. Scuflaire

Institut d'Astrophysique et Geophysique, Université de Liège,

allée du 6 Août 17, 4000 Liège, Belgium

e-mail: j.montalban@ulg.ac.be; a.noels@ulg.ac.be; r.scuflaire@ulg.ac.be

A. Miglio

School of Physics and Astronomy, University of Birmingham, Edgbaston,

Birmingham B15 2TT, UK

e-mail: miglioa@bison.ph.bham.ac.uk

P. Ventura · F. D'Antona

INAF-Roma, Via Frascati, 33, Monteporzio Catone, Rome, Italy e-mail: paolo.ventura@oa-roma.inaf.it; franca.dantona@oa-roma.inaf.it

24 J. Montalbán et al.

the perturbation as:

$$\frac{d^2\xi_r}{dr^2} = -K_s(r)\,\xi_r\tag{1}$$

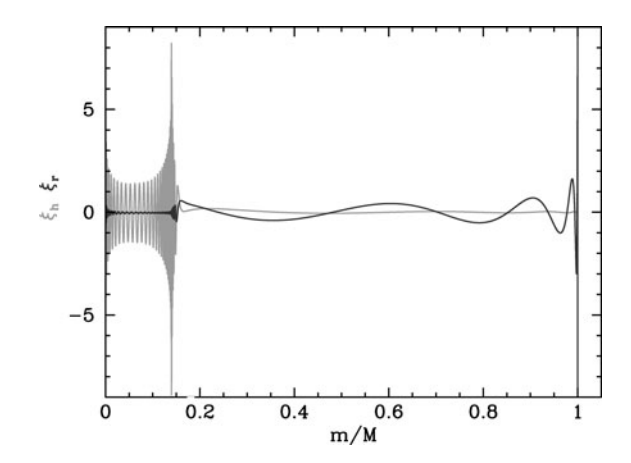
with  $K_s(r) = \frac{\omega^2}{c_s^2} \left( \frac{N^2}{\omega^2} - 1 \right) \left( \frac{S_\ell^2}{\omega^2} - 1 \right)$ ,  $\omega$  is the oscillation frequency and  $c_s$  the sound speed. From this expression we identify two propagation domains or cavities where the motion has an oscillatory character:  $\omega^2 > N^2$ ,  $S_\ell^2$  and  $\omega^2 < N^2$ ,  $S_\ell^2$ , while the regions where these conditions are not satisfied are evanescent regions with the amplitude of motion exponentially increasing or decreasing. In the limit cases in which  $\omega^2 \gg N^2$ ,  $S_\ell^2$  or  $\omega^2 \ll N^2$ ,  $S_\ell^2$  we deal with pure acoustic (p modes) and pure gravity modes (g modes) respectively. Because of the contraction of stellar central regions during the post-main sequence evolution, N reaches huge values  $(>10^4 \,\mu\text{Hz})$  in the central regions of red giant models. As a consequence, the frequency of g modes ( $\omega_g \sim \int N/r dr$ , see Tassoul 1980) increases with respect to main-sequence models. On the other hand, the drop of mean density resulting from the expansion of the hydrogen rich envelope makes the frequency of pressure modes  $(\omega_p \sim \left(\int_0^R dr/c\right)^{-1})$  decrease. All that leads to an oscillation spectrum for red giants where in addition to radial modes, one finds a large number of non-radial modes with mixed g-p properties, that is, for a given frequency  $\omega$  the mode can propagate in the envelope ( $\omega^2 > S^2$ ,  $N^2$ , see Fig. 2) as a pressure mode and also in the central region ( $\omega^2 < S^2$ ,  $N^2$ ) as a g mode. In Fig. 1 we plot the horizontal and radial components of the displacement corresponding to one of these g-p mixed modes propagating in a 1.4  $M_{\odot}$  model with a radius of 5  $R_{\odot}$ .

The dominant p or g character of these non-radial modes depends on the coupling between gravity and acoustic cavities and may be estimated from the value of the normalized mode inertia (E, see e.g. Christensen-Dalsgaard 2004, and references therein):

$$E = \frac{\int_{V} \rho |\boldsymbol{\xi}|^{2} dV}{M |\boldsymbol{\xi}|_{ph}^{2}},\tag{2}$$

Figure 2 shows the propagation diagrams for dipole and quadrupole modes corresponding to a 1.5  $M_{\odot}$  red giant on the red giant branch (upper panel) and in the

Fig. 1 Horizontal (*grey*) and radial (*black*) components of displacement corresponding to a mixed mode as a function of the relative mass for a  $1.4~M_{\odot}$  model with  $5~R_{\odot}$ . g modes are predominantly horizontal while acoustic ones are radial. This mixed mode behaves as a g mode in the central region (m/M < 0.15) and as a p mode in the envelope



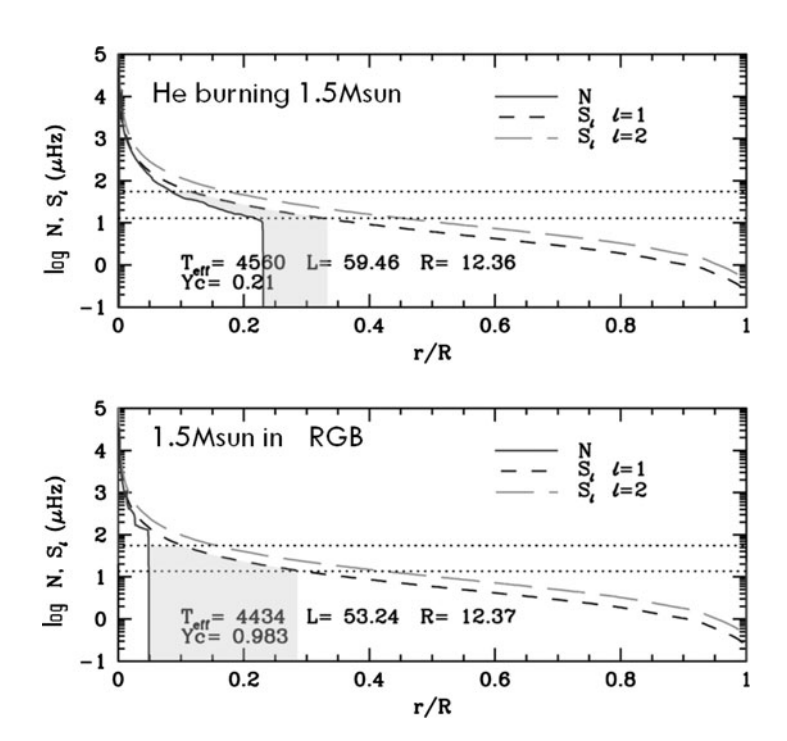


Fig. 2 Propagation diagrams for a 1.5  $M_{\odot}$  star in two different evolutionary phases. Upper panel: central He burning phase, with central He mass fraction Yc=0.21, and lower panel, RGB phase, both with the same stellar radius ( $R=12.35~R_{\odot}$ ). Horizontal lines indicate the solar-like frequency domain, and shadowed regions highlight the potential barrier that separates the acoustic and gravity cavities for modes in that domain. Brunt-Väisälä and Lamb frequencies for dipole and quadrupole modes as a function of the relative radius correspond to solid, dashed and long-dashed lines respectively

26 J. Montalbán et al.

central He burning phase (lower panel). The horizontal lines indicate the frequency domain where we expect solar-like oscillations (see Kjeldsen and Bedding 1995). From these diagrams we observe that: (1) the evanescent region is smaller for dipole modes than for quadrupole ones; (2) the importance of the evanescent region  $(\int K_s dr)$ , or the potential barrier that separates the two cavities, depends on the evolutionary state. As a consequence, the interaction between the two cavities is more important for  $\ell = 1$  modes, and their mixed character changes with the evolutionary state. The number of g modes by frequency interval can be estimated from the asymptotic theory (Tassoul 1980) as:

$$n_g \propto (\ell (\ell+1))^{1/2} \int \frac{N}{r} dr.$$
 (3)

So, the density of oscillation modes is larger for quadrupole modes and its value also changes with the evolutionary state.

The amplitude of modes at different frequencies in the oscillation spectrum results from the balance between excitation and damping rates (Dziembowski et al. 2001; Dupret et al. 2009, and Dupret in these proceedings), nevertheless, an estimation of the relative amplitude of different modes can be provided by the normalized mode inertia (Houdek et al. 1999). In this framework, the amplitude is inversely proportional to  $E^{1/2}$  (see e.g. Christensen-Dalsgaard 2004, and references therein).

Figure 3 (panels A–D) presents the inertia of the oscillation modes as a function of frequency for radial, dipole and quadrupole modes for models of red giant stars in different evolutionary states. The corresponding models are indicated in the HR diagram (Fig. 3 left-top panel). Radial modes have the lowest inertia, and between two consecutive radial modes there is large number of non-radial modes with an inertia that can vary by several orders of magnitude. Between two radial modes there is always an  $\ell=2$  mode with an inertia close to that of the adjacent radial mode. The inertia of dipole modes  $(E_{\ell=1})$  presents as well a minimum between two consecutive radial modes but, depending on the evolutionary state, that minimum is not always well defined, and the difference between the value of  $E_{\ell=1}$  and that corresponding to the radial mode varies. The central density of the He burning (He-B hereafter) model is 10 times smaller than that of a RGB model with the same radius and mass. Consequently, in the RGB phase, the high potential barrier between the acoustic and the gravity cavities reduces the interaction between p and g modes, and dipole modes with  $E_{\ell=1} \sim E_{\ell=0}$  behave as pure p modes and show a regular frequency spacing. For He-B models, the coupling between these cavities is more important and  $\ell = 1$  modes are mixed modes with  $E_{\ell=1} > E_{\ell=0}$ . Nevertheless,  $E_{\ell=1}$  still presents a minimum and even if  $E_{\ell=1} > E_{\ell=0}$ , the modes can be still considered, based on the value of E, as observable modes. If E is a good proxy of the amplitudes, the results presented in Fig. 3 suggest that, contrarily to pure p-mode oscillation spectra of main sequence solar-like pulsators, the number of non-radial modes potentially observable in the frequency interval between two consecutive

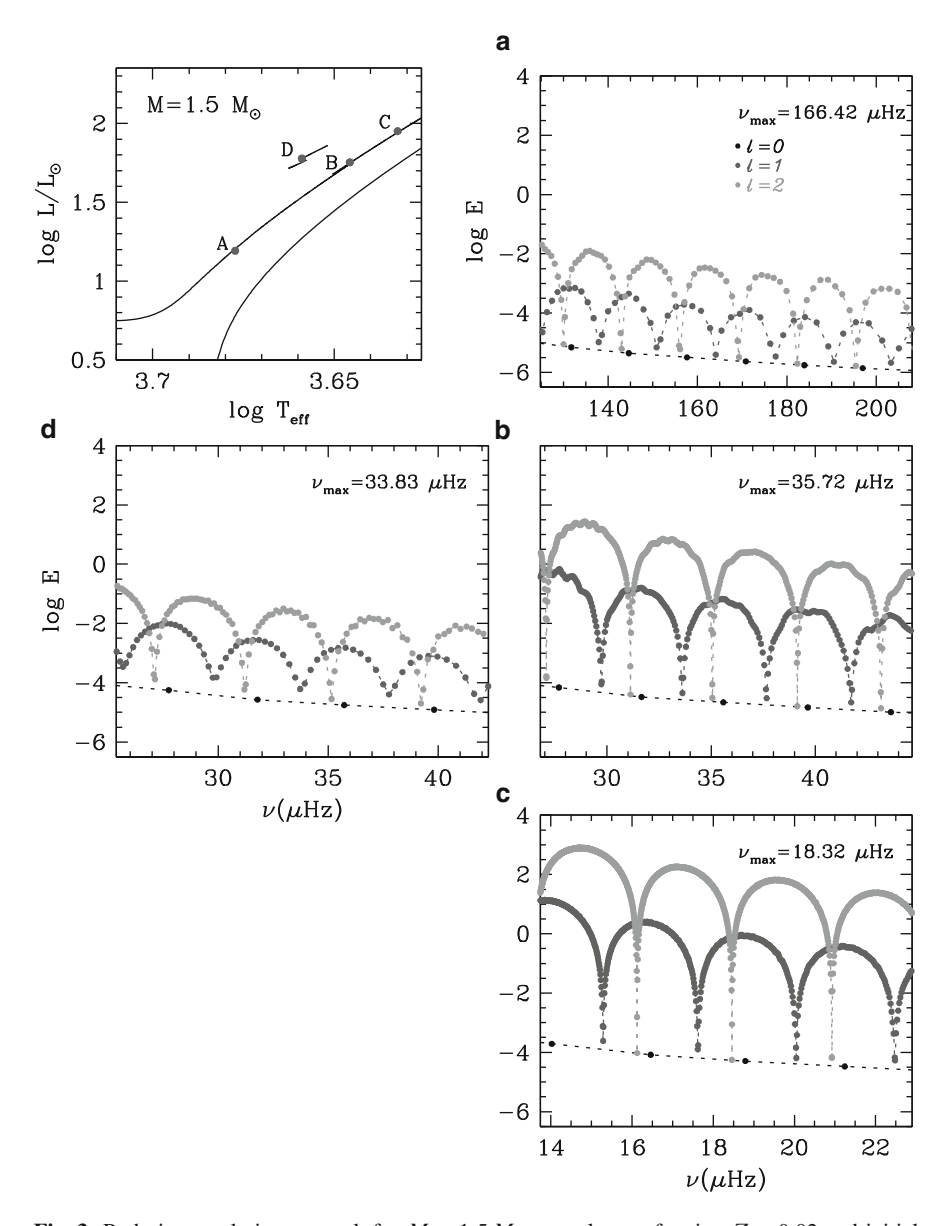


Fig. 3 Red giant evolutionary track for  $M=1.5\,M_\odot$ , metal mass fraction Z=0.02 and initial helium mass fraction Y=0.278. Labels from A to D indicate the models whose spectra are shown in the corresponding panels. A–D *panels*: Inertia as a function of frequency for radial (*black*), dipole (*light gray*) and quadrupole (*dark grey*) modes.  $\nu_{\rm max}$  is the frequency at the maximum amplitude as expected from scaling laws (Kjeldsen and Bedding 1995)

28 J. Montalbán et al.

radial modes depends on  $\ell$ , on the evolutionary state, and on the precision of the time series, both in sensitivity and in frequency resolution.

# 2 Diagnostic Power of Red Giant Oscillation Spectra

In the framework of the asymptotic theory for p modes (Vandakurov 1967; Tassoul 1980; Gough 1986) the frequencies of two modes of same degree and consecutive order are separated by a constant value  $\langle \Delta \nu \rangle$  which is approximately independent of  $\ell$  for low degree modes. The asymptotic theory is no longer valid for mixed modes or in regions with rapid varying physical quantities, nevertheless, the modes partially or well trapped in the acoustic cavity (hence with a dominant p character) show such a regular pattern. These modes have been used to compute the large and small frequency separations and to analyse their behavior with stellar parameters and evolutionary state, both in recent theoretical (Montalbán et al. 2010a,b) and observational works based on CoRoT and *Kepler* satellite data (Bedding et al. 2010; Huber et al. 2010; Mosser et al. 2010; Carrier et al. 2010).

In the domain of validity of the asymptotic approximation for pressure modes, the spectrum of p modes can be described by (e.g. Tassoul 1980):

$$\nu_{n\ell} = (n + \frac{\ell}{2} + \varepsilon) \, \Delta \nu - \frac{\ell \, (\ell+1)}{4\ell + 6} \delta \nu_{\ell} \tag{4}$$

where  $\Delta v = v_{n \ell} - v_{n-1 \ell}$  is the inverse of twice the sound travel time between the surface and the center, and is thus proportional to the square root of the mean density of the star.  $\delta v_{n\ell} = v_{n\ell} - v_{n-1\ell+2}$  on the other hand, reflects the behaviour of the sound speed mostly in the central regions, and hence is linked to the central density and to the stellar evolutionary state. The dependence of  $\delta \nu$  and  $\Delta \nu$  on stellar mass and evolution is usually adopted as a good seismic diagnostic allowing to derive, if the chemical composition is known, the stellar mass and age for main sequence solar-like pulsators (see e.g. Christensen-Dalsgaard 1988). For red giants, however,  $\delta v_{02}$  does not seem to provide much more information than  $\Delta v$ . Predictions from RGB models suggest a linear dependence on  $\Delta \nu$ , with a slope that slightly increases as the mass decreases. Chemical composition and convection treatment do not strongly affect this linear dependence that is mainly dominated by the mass and radius of the star (Montalbán et al. 2010a,b). The observational results obtained from the first 34 days of *Kepler* operations that covered stars with  $\Delta v > 8 \,\mu\text{Hz}$ were well fitted by the linear relation  $\delta_{02} \sim 0.125 \Delta \nu$  (Bedding et al. 2010). The comparison with theoretical models suggests that the observed sample is dominated by RGB stars with masses around 1.3  $M_{\odot}$ . The extension of these observations to 134d allowed us to consider stars with  $\Delta \nu$  as low as 2  $\mu$ Hz and to show that the slope of the relation and the scatter increase for  $\Delta \nu < 6 \,\mu\text{Hz}$  (Huber et al. 2010). In fact, at  $\Delta v \sim 4 \mu$ Hz the red giant population is dominated by red clump stars (Miglio et al. 2009) that, as shown in Fig. 4, follow a different trend. The comparison between this

Fig. 4 Normalized small separation vs large separation of radial modes for models in the RGB phase (cross) with masses 1.0 and 1.5  $M_{\odot}$ chemical composition Z = 0.006, 0.01, 0.02, 0.03,Y = 0.25 and 0.278, and three different treatments of convection. Dots correspond to models burning He in the center, with masses between 0.7 and 2.3  $M_{\odot}(\Delta M = 0.1)$ and between 2.5 and 4.0  $M_{\odot}$  $(\Delta M = 0.5)$  and chemical composition Z = 0.02, Y = 0.278

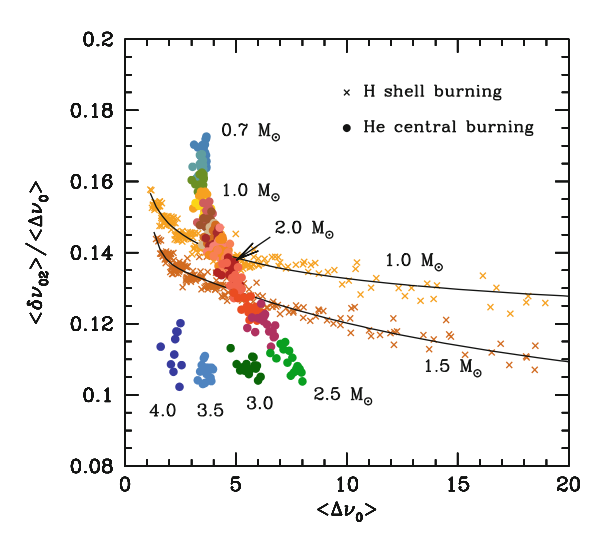


figure and Fig. 10 in Huber et al. (2010) indicates that predictions from theory are in good agreement with the observed behavior of  $\delta \nu_{02}$  in RGB and red clump stars.

For main sequence stars, the frequency separation  $\delta \nu_{01} = (\nu_{n,0} - 2 \nu_{n1} + \nu_{n+1,0})/2$  has also been suggested as a good indicator of the evolutionary state (e.g. Roxburgh and Vorontsov 2003), and in the framework of asymptotic approximation of p modes,  $\delta \nu_{01} = 1/3\delta \nu_{02}$ . This relation is neither matched by theoretical models of red giants nor by the observational data obtained with *Kepler* and CoRoT. Nevertheless, the value of  $\delta \nu_{01}$  may contain relevant information. In fact the sample of red giants studied in Bedding et al. (2010), that corresponds to low luminosity RGB stars ( $L < 30L_{\odot}$ ) and the CoRoT sismo target HR7349 (Carrier et al. 2010) show values of  $\delta \nu_{01}$  close to zero or negative. Theoretical studies (Montalbán et al. 2010a,b) on the other hand, predict that models in the RGB present values of  $\delta \nu_{01}$  close to zero or negative, while more massive stars in the He-B phase have positive values. Moreover, those studies show that the value of  $\delta \nu_{01}$  seems correlated with the distance between the  $\ell = 1$  turning point and the bottom of the convective envelope, thus, models with the turning point inside the convective envelope present negative or very small value of  $\delta \nu_{01}$ .

# 2.1 Deviation from Asymptotic Approximation: Evolutionary State

The mean value of the large frequency separation decreases as the star ascends the RGB with a denser and denser core and a more and more diffuse envelope. On the basis of  $\langle \Delta \nu \rangle$  alone, however, it is not possible to distinguish among different evolutionary states, i.e. ascending RGB, descending RGB, or core-He

burning. From the asymptotic theory  $\Delta v$  should be constant and  $\ell$ -independent, however, we are out of its validity domain and  $\Delta \nu$  varies with frequency and with  $\ell$ . A measurement of how far we are from the asymptotic behaviour could be the scatter of  $\Delta \nu$  values  $(\sigma(\Delta \nu_{\ell}))$  with respect to its average value in the domain of frequency where solar-like oscillations are expected. The computation of these quantities for models with stellar masses between 1 and 5  $M_{\odot}$  from the bottom of the RGB until the exhaustion of He in the center shows that  $\sigma(\Delta \nu_{\ell})$  depends on  $\ell$ : while its value is very small for  $\ell = 0$  and 2, it is generally larger for  $\ell = 1$  and its value depends strongly on the evolutionary state: (1) the scatter in the  $\ell = 1$  ridge in an échelle diagram representation of the oscillation spectra (e.g. Grec et al. 1983) decreases as luminosity  $(\Delta v)$  increases (decreases) during the RGB phase, since the increase of density contrast leads to decoupling the acoustic and gravity cavities and modes more likely observed behave as pure p modes. (2) For models in the He-B phase, the central density decreases leading to a spectrum of dipole modes dominated by p-g mixed modes. As a consequence, the width of the  $\ell = 1$  ridge will be more larger for those models than for the RGB ones at the same luminosity (Montalbán et al. 2010a). This result is very important because it suggests that the aspect of the  $\ell=1$  oscillation spectrum is able to reveal the evolutionary state of red giant stars otherwise very close un their global properties (Montalbán et al. 2010a,b).

From the observational point of view, the population of red giants studied by Bedding et al. (2010) is dominated by stars at the bottom of the RGB with masses between 1. and 1.5  $M_{\odot}$  and showed a folded échelle diagram with a larger dispersion in the ridge corresponding to dipole modes than in those for radial and quadrupole ones. On the other hand, the sample of red giants observed by CoRoT during the first two runs is dominated by red clump stars (Miglio et al. 2009; Mosser et al. 2010) and the analysis of their oscillation properties by Mosser et al. (2011b) showed that all the modes are arranged in almost vertical lines corresponding to different radial orders, and that a large dispersion is found for dipole modes at  $\Delta \nu \sim 4 \,\mu$ Hz, that is the value of the large separation corresponding to the red-clump luminosity. The comparison between these observational results and the theoretical predictions for the same stellar population (Montalbán et al. 2010b) is noteworthy.

As can be seen in Fig. 3, around the minima of inertia, there may be several dipole modes with close values of the inertia and, therefore, with expected similar amplitudes. As the observation time of red giants has increased, the frequency resolution has been noticeably improved and it has been possible not only to detect in the spectra of red giant stars the acoustic modes, but also to distinguish around those a forest of mixed modes. The frequency (or period) separation between these modes around to the minimum of inertia, also depends on the evolution state and the mass of the model. Models with a large density contrast show a frequency difference between consecutive modes that is much smaller than for models at the bottom of the RGB or in the He-B phase. These properties have been measured by Bedding et al. (2011) in the spectra of red giants observed by *Kepler* and also in those of CoRoT red giants (Mosser et al. 2011a). At a given  $\Delta \nu$  (that of the red clump) the difference of period ( $\Delta P$ ) between consecutive modes gathers the stars in two groups: one characterized by targets with  $\Delta P > 100 \, \mathrm{s}$  and one with  $\Delta P < 60 \, \mathrm{s}$ .

The comparison with theoretical computations allows us to identify these two groups with stars that are burning He at the center, for the first group, and with stars that are still burning H in a shell during the ascending RGB for the second one, and then to lift the degeneracy between RGB and He-B models with the same  $\Delta \nu$  and  $\nu_{\rm max}$ .

# 2.2 Deviation from Asymptotic Approximation: Glitch Associated to HeII Ionization Region

In the asymptotic approximation it is assumed that the physical quantities describing the equilibrium structure of the star present variations with a characteristic scale larger than the wavelength of the mode. Any localized region of sharp variation of the sound speed (so-called acoustic glitches) induce in the frequencies an oscillatory component with a periodicity related to the sound-travel time measured from that region to the surface of the star (acoustic depth) (Vorontsov 1988; Gough 1990). The amplitude of this oscillatory component depends on the sharpness of the glitch and decreases with frequency because, as v increases, the wavelength of the mode becomes comparable with or less than the extent of the glitch. These sharp variations of the structure are found in regions of rapidly changing chemical composition, in ionization zones of major chemical elements, or in regions where the energy transport switches from radiative to convective. The analysis of periodic variations in the frequencies,  $\Delta v$ , or second frequency differences, allowed the derivation of the depth of the solar convective envelope and its He content with a hight precision (see Christensen-Dalsgaard 2002, for a review). In the case of red giants, the acoustic depth of the boundary of the convective envelope is very high and therefore the modulation of the frequency is not easily seen in the solarlike frequency domain. On the other hand, the variation of the adiabatic index  $\Gamma_1$ due to the second ionization of He is located at  $\sim 0.5$  of the total acoustic radius and its signal is clearly separated from that of the bottom of the convective zone making the extraction of its signal much more easy than for solar-like main sequence pulsators. The first detection and characterization of the HeII signal for a red giant was obtained for the CoRoT sismo target HR7349 (Miglio et al. 2010), but this signal has also been detected in numerous exofield CoRoT red giants (Mosser et al. 2010) and it is expected that the red giants that Kepler will observe during three years will provide very precise characterization of their HeII signal. The relevance of the detection and characterization of the acoustic glitch associated with the HeII region in red giant stars is enormous: while global features of the spectra such as  $\Delta \nu$ and  $\nu_{\rm max}$  will provide us with the mass and radius of the star, the HeII feature will allow potentially to derive the abundance of He in its convective envelope, allowing finally to answer questions about simple or multiple stellar populations to explain stellar cluster morphology, and to eliminate one of the main sources of degeneracy in the study of evolved stars (see Gratton in this volume).

J. Montalbán et al.

## 3 Conclusions

We have summarized here some aspects of the enormous potential of solar like oscillations in red giants. These stars, intrinsically highly luminous, take up a small range of colors in the HR diagram for a large domain of masses, chemical composition and evolutionary state. A simple and adiabatic analysis of its stochastically excited oscillations allow us to derive their fundamental parameters such as mass and radius (see Miglio in this volume), but also their evolutionary state, and potentially the abundance of He in their convective envelope. The agreement between observation and theoretical prediction is up to now remarkable, allowing to explain observations in the framework of standard stellar models. In a near future, when individual frequencies will be extracted, their study will allow us to go deeper into the study of stellar structure of red giants and their precursors. It is worthwhile to stress here that with only the global features of these spectra and a simple analysis we have already taken a giant step in the study of stellar evolution.

### References

Bedding, T.R., Huber, D., Stello, D., et al.: ApJ 713, L176 (2010)

Bedding, T.R., Mosser, B., Huber, D., et al.: Nature 471, 608 (2011)

Carrier, F., De Ridder, J., Baudin, F., et al.: A&A 509, A73 (2010)

Christensen-Dalsgaard, J.: IAU Symposium. In: Christensen-Dalsgaard, J., Frandsen, S. (eds.) Advances in Helio- and Asteroseismology, vol. 123, p. 295 (1988)

Christensen-Dalsgaard, J.: Rev. Modern Phys. 74, 1073 (2002)

Christensen-Dalsgaard, J.: Sol. Phys. 220, 137 (2004)

Dupret, M.-A., Belkacem, K., Samadi, R., et al.: A&A 506, 57 (2009)

Dziembowski, W.A., Gough, D.O., Houdek, G., Sienkiewicz, R.: MNRAS 328, 601 (2001)

Gough, D.O.: In: Osaki, Y. (ed.) Hydrodynamic and Magnetodynamic Problems in the Sun and Stars, vol. 117 (1986)

Gough, D.O.: Lecture Notes in Physics. In: Osaki, Y., Shibahashi, H. (eds.) Progress of Seismology of the Sun and Stars, vol. 367, p. 283. Springer, Berlin (1990)

Grec, G., Fossat, E., Pomerantz, M.A.: Sol. Phys. 82, 55 (1983)

Houdek, G., Balmforth, N.J., Christensen-Dalsgaard, J., Gough, D.O.: A&A 351, 582 (1999)

Huber, D., Bedding, T.R., Stello, D., et al.: ApJ 723, 1607 (2010)

Kjeldsen, H., Bedding, T.R.: A&A 293, 87 (1995)

Miglio, A., Montalbán, J., Baudin, F., et al.: A&A 503, L21 (2009)

Miglio, A., Montalbán, J., Carrier, F., et al.: A&A 520, L6 (2010)

Montalbán, J., Miglio, A., Noels, A., Scuflaire, R., Ventura, P.: Astron. Nachr. 331, 1010 (2010a)

Montalbán, J., Miglio, A., Noels, A., Scuffaire, R., Ventura, P.: ApJ 721, L182 (2010b)

Mosser, B., Belkacem, K., Goupil, M.-J., et al.: A&A 517, A22 (2010)

Mosser, B., Barban, C., Montalbán, J., et al.: A&A 532, 86 (2011)

Mosser, B., Belkacem, K., Goupil, M.J., et al.: A&A 525, L9 (2011b)

Roxburgh, I.W., Vorontsov, S.V.: A&A 411, 215 (2003)

Tassoul, M.: ApJS 43, 469 (1980)

Vandakurov, Y.V.: AZh 44, 786 (1967)

Vorontsov, S.V.: IAU Symposium. In: Christensen-Dalsgaard, J., Frandsen, S. Advances in Helioand Asteroseismology, vol. 123, p. 151 (1988)

# **Energetic Aspects of Non-Radial Solar-Like Oscillations in Red Giants**

Marc-Antoine Dupret and Kévin Belkacem

**Abstract** The non-radial oscillations discovered by CoRoT (see e.g. de Ridder et al. (2009)) and by *Kepler* (see e.g. Bedding et al. (2010)) in thousands of red giants constitute a wonderful mine of information to determine their global characteristics and probe their internal structure. A. Miglio and J. Montalbán have presented in detail in this conference the seismic structure of red giants, the information hold by their oscillation frequencies, and how it can be used. An adiabatic analysis of the oscillations was sufficient at this level as the frequencies are mainly determined by the deep layers were the oscillations are quasi-adiabatic. We consider here energetic aspects of non-radial oscillations in red-giants. Non-adiabatic models of solar-like oscillations are required to determine the theoretical amplitude and lifetimes of the modes. These parameters allow us to determine how power spectra are expected to look like, depending on the structure of the red giant. Comparison with the observed measures gives thus additional constraints on the models.

### 1 Seismic Structure of Red Giants

Details on the seismic structure of red giants are given e.g. in Montalbán et al. (these proceedings), Montalbán et al. (2010a,b). We recall here the most important aspects required for the forthcoming discussion. The two basic physical quantities which determine the mode physics in the deep regions of stars are the Brunt-Väisälä (BV) and Lamb frequencies. In a main-sequence solar-like star, the oscillation frequencies

M.-A. Dupret (⊠)

Institut d'Astrophysique et Géophysique, University of Liège, 4000 Liège, Belgium

e-mail: MA.Dupret@ulg.ac.be

K. Belkacem

IAS, 91405 Orsay, Cedex, France e-mail: kevin.belkacem@ias.u-psud.fr

of p-modes are larger than these two frequencies in most of the star. In addition, the frequencies are high enough to present more or less a regular structure, as expected in the asymptotic limit. This regularity allows us to build *échelle diagrams*, a very useful tool to identify the modes.

Because of the large density contrast between the core and the envelope, the BV frequency is very large in the core of a red giant compared to its envelope. As a consequence, non-radial modes have a mixed character in these stars. In their large envelope, the observed frequencies are larger than the BV and Lamb frequencies. Hence, the modes behave like usual acoustic p-modes in these layers, with the pressure gradient as main restoring force. We call this region the p-cavity. But in the dense core of the red giant, the oscillation frequencies are smaller than the BV and Lamb frequencies. Hence, the same modes behave in the core as gravity modes with the buoyancy acting as restoring force. We call this region the g-cavity. Between these two cavities, there is an evanescent zone, whose size depends on the frequency and the degree  $\ell$  of the modes.

# 2 Mode Trapping

Mode trapping always occurs when two oscillation cavities are connected. We may understand this as follows. If the two cavities were perfectly separated, the oscillation spectrum of the full star would be simply the sum of the spectra corresponding to the g- and p-cavities.

In the asymptotic limit, a constant *period spacing* is predicted between consecutive g-modes:  $P_{n,\ell} - P_{n-1,\ell} \simeq 2\pi^2/\left(\sqrt{\ell(\ell+1)}\int_{g-cavity}(N/r)\,\mathrm{d}r\right)$  and an equidistance in frequency called the large separation is expected between consecutive p-modes:  $\Delta\nu_n = \nu_{n,\ell} - \nu_{n-1,\ell} \simeq 1/(2\int_{n-cavity}\mathrm{d}r/c)$ .

When the two cavities are connected, all modes propagate in both cavities. But we can still separate the spectrum in two: some modes have most of their energy in the core (in red-giants we propose to call them g-like modes) and others have most of their energy in the envelope (we call them p-like modes). The period spectrum of g-like modes has a structure similar to the spectrum of pure g-modes, and the frequency spectrum of p-like modes has a structure similar to the spectrum of pure p-modes. However, the regularities in the spectrum expected in the asymptotic limit can be significantly perturbed by the the so-called *avoided crossings* which result from the coupling between the two cavities.

In the case of red giants, it is important to note that the evanescent zone is the smallest for  $\ell=1$  modes. The two cavities are thus strongly connected and mode trapping is less efficient for these modes. In particular,  $\ell=1$  p-like modes have a non-negligible energy in the core. This can be seen by considering the dimensionless mode inertia, also called often the mode mass:

$$I = \int_0^M |\xi|^2 \, \mathrm{d}m \, / \, (M \, |\xi_r(R)|^2), \tag{1}$$

where M is the total mass, R the radius and  $\xi$  is the displacement vector. Figures of mode inertia as a function of frequency in red giants can be seen e.g. in Dziembowski et al. (2001), Christensen-Dalsgaard (2004), Dupret et al. (2009), and Montalbán et al. (2010b). The local minima in these figures correspond to the p-like modes. The frequency separation between consecutive local minima of same  $\ell$  is more or less the large separation. The inertia of  $\ell=1$  p-like modes is larger than the one of  $\ell=2$  p-like modes. This has several consequences. The first concerns the frequency spectrum: it is less regular for  $\ell=1$  modes than for other modes, as discussed in details by Montalbán et al. (2010a,b). The other consequences concern the amplitudes and lifetimes of the modes, as will be discussed in the forthcoming sections.

## 3 Non-Adiabatic Oscillation Models

Solar-like modes are damped. This is shown by the Lorentzian profile of the individual modes in the power spectrum. This observational proof is evident for the Sun thanks to the quality of the data. For red giants, resolving the modes is not always evident as we will see. But we can be fairly sure that their modes are damped. Indeed, unstable modes with positive growth rates would reach much larger amplitudes than those observed in red giants solar-like oscillations.

In damped modes, the time dependence is given by a decreasing exponential  $\exp(-\eta t) = \exp(-t/\tau)$  where  $\eta$  is the damping rate and  $\tau$  the mode lifetime. From an observational point of view, a measure of the damping rate is given by the linewidth of the Loretzian profile corresponding to the mode. From a theoretical point of view, the damping rate is given by:

$$\eta = -\frac{W_e + W_c}{2\,\sigma I\,|\mathcal{E}_r(R)|^2 M}\,,\tag{2}$$

where  $\pi W_e$  and  $\pi W_c$  are the work performed by the envelope and the core of the star during one pulsation cycle and  $\sigma$  is the angular frequency. Neglecting the non-diagonal components of the Reynolds stress and the horizontal component of the flux vector, the local work performed per unit mass  $\pi dW/dm$  is such that:

$$\frac{dW}{dm} = -\Im\left\{\frac{\delta\rho^*}{\rho}\frac{\delta p}{\rho}\right\} = -\Im\left\{\frac{\delta\rho^*}{\rho}\frac{\delta p_t}{\rho}\right\} - \Im\left\{\delta T^*\delta s\right\} 
= -\Im\left\{\frac{\delta\rho^*}{\rho}\frac{\delta p_t}{\rho}\right\} - \Re\left\{\frac{\delta T^*}{T\sigma}\left[\frac{d(\delta L_R + \delta L_C)}{dm} - \delta\epsilon_K\right]\right\},$$
(3)

where  $\delta$  denotes lagrangian variations,  $p_t$  is the turbulent pressure,  $L_R$  and  $L_C$  are the radiative and convective luminosity and  $\epsilon_K$  is the dissipation rate of kinetic energy of turbulence into heat. This shows that the damping comes from phase

shifts between the pressure and density variations and is intrinsically related to the non-adiabaticity of the oscillations ( $\delta s \neq 0$ ). Non-adiabatic models which solve simultaneously the dynamical and energy equations of the problem are thus required to determine these quantities. In red giants, two distinct regions can contribute significantly to the negative work and thus the damping of the modes.

# 3.1 Time-Dependent Convection

The first of these regions is the outermost part of the convective envelope. There, the time-scale related to most energetic convective motions is of the same order as the oscillation periods. This means that the coherent interaction between convection and oscillations is very strong. We can understand qualitatively which processes are hidden behind this coherent interaction: the oscillations imply time-variations of the buoyancy force, which implies time-variations of the convective flux and turbulent pressure with loss of heat at the hot phase and thus damping (see the corresponding terms in (3)). However, to model this process is difficult.

Only a few time-dependent convection theories have been proposed for linear oscillations and all present significant uncertainties. Two of them make use of a Mixing-Length formalism. The first approach by Gabriel (1996), further developed by Grigahcène et al. (2005), follows the original ideas of Unno (1967), where a turbulent viscous term opposite to the buoyancy is introduced. This treatment implemented in our non-radial non-adiabatic pulsation code MAD is used for the results presented here. The second theory was developed by Gough (1977b) and follows the "kinetic of gas" picture of the MLT. Both theories can include a non-local treatment (Spiegel 1963; Gough 1977a; Balmforth 1992; Dupret et al. 2006b). A third formulation, no longer based on a mixing-length approach but on a Reynolds stress one was also proposed by Xiong et al. (1997). These theories encountered some successes, for example they obtain the red edge of the classical instability strip (Houdek 2000; Xiong and Deng 2001; Dupret et al. 2004). The reproduction of the solar mode lifetimes is also possible but not easy (Balmforth 1992; Xiong et al. 2000; Dupret et al. 2006a).

It is important to remark that  $W_e/|\xi_r(R)|^2$ , which is mainly produced by the time-dependent interaction between convection and oscillations, only depends on the eigenfunctions in the outer part of the convective envelope. It is thus not affected by the mode trapping.

# 3.2 Radiative Damping

The second source of damping occurs in the core of the red giant, mainly around the hydrogen burning shell. In this region, the BV frequency is very high, so that the eigenfunctions show very short wavelength oscillations. This implies significant variations of the temperature gradient during the oscillations, with radiative loss of heat at the hot phase and thus damping. In the asymptotic limit, this radiative damping is approximately given by the following integral (see Dziembowski 1977b; Van Hoolst et al. 1998; Godart et al. 2009):

$$-W_c \simeq \frac{K \left[\ell(\ell+1)\right]^{3/2}}{2\sigma^3} \int_{g-cavity} \frac{\nabla_{\rm ad} - \nabla}{\nabla} \frac{\nabla_{\rm ad} NgL}{pr^5} \, \mathrm{d}r \,, \tag{4}$$

In this equation, K is a constant proportional to the square of the amplitude of the eigenfunctions at the bottom of the envelope. Throughout this constant, the radiative damping is strongly affected by mode trapping: modes trapped in the core suffer more radiative loss than modes trapped in the envelope.

The importance of radiative damping compared to the convective damping depends on the evolutionary stage of the red giant, as will be discussed later.

## 4 Stochastic Excitation Models

Red giant solar-like oscillations are understood as stochastically excited modes. Convective motions act as a forcing term in the oscillation equation, supplying stochastically energy to the modes. The resulting amplitude is a balance between this stochastic energy supply and the mode damping. More precisely, the local squared amplitude of velocity variation at the layer where it is measured is given by (e.g., Baudin et al. 2005; Belkacem et al. 2006):

$$V^2 = \frac{P}{2nMI} = \frac{\Pi}{2nMI^2}.$$
 (5)

P is here the power stochastically supplied to the modes:

$$P = \frac{1}{8MI}(C_R^2 + C_S^2),\tag{6}$$

where  $C_R^2$  and  $C_S^2$  are the turbulent Reynolds stress and entropy contributions, respectively (see Samadi and Goupil 2001; Belkacem et al. 2006, for details). Both play a significant role in red giants and are included in the results presented here. To isolate the effect of inertia in (5), we introduce the product  $\Pi = PI$  which is, according to (6), independent of inertia.

We also introduce the maximum height of the mode profile in the power spectrum (PS), which is an observable and will permit us to draw conclusions about the mode detectability. To this end, one has to distinguish between two cases, namely resolved and unresolved modes. The resolved modes are typically the p-like modes trapped in the envelope. They present a Lorentzian profile in the PS and their heights are

given by (see e.g. Chaplin et al. 2005; Belkacem et al. 2006):

$$H = \frac{V^2(R)}{\eta} = \frac{\Pi}{2\eta^2 M I^2} = \frac{\Pi \tau^2}{2M I^2}$$
 (7)

where  $\tau = 1/\eta$  is the mode lifetime.

As we will see, g-like modes trapped in the core can have very long lifetime due to their large inertia (see (2)). When  $\tau \gtrsim T_{\rm obs}/2$  ( $T_{\rm obs}$  being the duration of observations), the modes are not resolved. In the limit  $\tau \to \infty$ , the heights in the PS tend to behave like (see e.g. Berthomieu et al. 2001; Lochard et al. 2005):

$$H_{\infty} = \frac{T_{\text{obs}}}{2} V^2(R) = \frac{\Pi T_{\text{obs}} \tau}{4 M I^2}.$$
 (8)

In the theoretical predictions of the heights presented in this paper, we choose the very favorable case of the CoRoT long runs with  $T_{\rm obs}=150$  days. We use (7) when  $\tau \leq T_{\rm obs}/2=75$  days and (8) when  $\tau > T_{\rm obs}/2=75$  days, so that H is a continuous function of  $\tau$ .

Finally, the observed velocity amplitudes are obtained by integration of the projected local velocity over the visible stellar disk (Dziembowski 1977a). This introduces a visibility factor depending on the inclination angle of the star (through the factor  $P_{\ell}^{m}(\cos i)$ ). We do not include this factor in the results discussed here.

### 5 Results

I present here a summary of results presented in details in Dupret et al. (2009). The red giant models were computed with the code ATON (Ventura et al. 2008). More details on the physical prescriptions adopted for the models used here are given in Dupret et al. (2009).

# 5.1 Case A: Low Luminosity Subgiants

In subgiants, the density contrast between the core and the envelope is not yet very large. Non-radial modes already have a mixed g-p character, but the number of nodes of the eigenfunctions in the g-cavity is not much larger than the number of nodes in the p-cavity. This happens essentially for  $\ell=1$  modes, since the local wave-number is given by  $k=\sqrt{\ell(\ell+1)}N/r$  in the g-cavity. The frequency spectrum loses its regularity in such situation.

We consider now the damping of the modes. Since the BV frequency is not yet very high in the core of these models, the radiative damping plays a negligible role (see (4)), even for modes trapped in the core. Dupret et al. (2009), top panel of

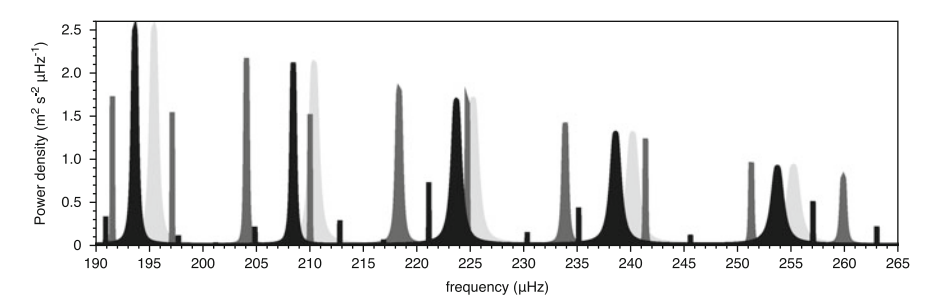


**Fig. 1** Theoretical power spectrum for model A of Dupret et al. (2009). Light gray corresponds to  $\ell=0$  modes, dark gray for  $\ell=1$  modes and black for  $\ell=2$  modes

Fig. 5 show the lifetimes of the modes as a function of frequency for a typical low luminosity red giant of 2 solar masses. According to (2), the lifetimes are proportional to the inertia and are thus modulated by the mode trapping: modes trapped in the envelope have short lifetimes and modes trapped in the core have very long lifetimes.

We consider now the predicted heights of the modes in the power spectrum. First, it is useful to consider the ratio  $\tau/I$ , since (7) indicates that the height is proportional to the square of this ratio for resolved modes. Dupret et al. (2009), panel 2 of Fig. 5 show that this ratio is not affected by mode trapping. Indeed, the normalized work is not affected by mode trapping because the radiative damping in the core is negligible compared to the convective damping in the envelope (we mentioned above that the latter is never affected by mode trapping). But this result would apply for the heights if all modes are resolved and this is not the case. Dupret et al. (2009) show that modes trapped in the core have typical lifetimes larger than 100 days and cannot be resolved. Hence, their heights are smaller in the power spectrum compared to other modes.

As an illustration, we give in Fig. 1 the theoretical power spectrum for model A of Dupret et al. (2009). We see that the power spectrum is regular for the short lifetime  $\ell=0$  and  $\ell=2$  modes. On the contrary, the spectrum of  $\ell=1$  modes is very irregular and many have long lifetimes.

# 5.2 Case B: Intermediate Luminosity Red Giants

In intermediate luminosity red giants, the density contrast between the core and the envelope is larger. The number of nodes of the eigenfunctions in the g-cavity is significantly larger than in the p-cavity. This implies that the frequency separation between consecutive g-like modes is smaller than the frequency separation between consecutive p-like modes (the large separation).

We consider now the damping of the modes. Radiative damping appears to be negligible for p-like modes, moderate for  $\ell=1$  g-like modes and large for  $\ell=2$ 

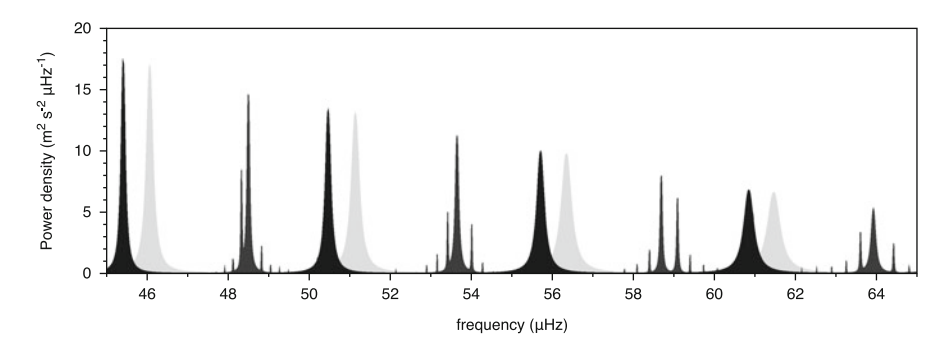


**Fig. 2** Theoretical power spectrum for model B of Dupret et al. (2009). Light gray corresponds to  $\ell=0$  modes, dark gray for  $\ell=1$  modes and black for  $\ell=2$  modes

g-like modes. Dupret et al. (2009), top panel of Fig. 7 show the lifetimes of the modes as a function of frequency for a typical intermediate luminosity red giant of 2 solar masses. As for model A, the lifetimes are proportional to the inertia and are thus modulated by the mode trapping.

We consider now the predicted heights of the modes in the power spectrum. In this purpose, we first consider the ratio  $\tau/I$ . Dupret et al. (2009), second panel of Fig. 7 show that this ratio is modulated by mode trapping, particularly for  $\ell=2$  modes. This is a direct consequence of the increasing importance of radiative damping for g-like modes.

The predicted heights (Dupret et al. 2009, bottom panel of Fig. 7) indicate that the detectable modes are on the one hand the p-like modes trapped in the envelope and on the other hand groups of  $\ell=1$  mixed modes between the radial modes.

As an illustration, we give in Fig. 2 the theoretical power spectrum for model B of Dupret et al. (2009). Concerning  $\ell=2$  modes, we note that only the p-like modes trapped in the envelope are detectable, they have short lifetimes and their location with respect to the radial modes allows to define a small separation like in main sequence solar-like stars. Even more interesting are the predictions for  $\ell=1$  modes. Instead of having individual  $\ell=1$  p-like modes between the radial ones, the  $\ell=1$  modes appear as groups of mixed modes. This is a very important prediction in full agreement with recent detection of these groups of  $\ell=1$  mixed modes by *Kepler* (Beck et al. 2011; Bedding et al. 2011) and by CoRoT (Mosser et al. 2011).

# 5.3 Case C: High Luminosity Red Giants

In high luminosity red giants, the density contrast between the core and the envelope is huge. This has several consequences. First, nearly a continuum of non-radial modes is predicted. Second, the mode trapping is very efficient: the energy of p-like modes is fully located in the envelope and the energy of g-like modes is fully located in the core. This implies that the radiative damping is very strong for

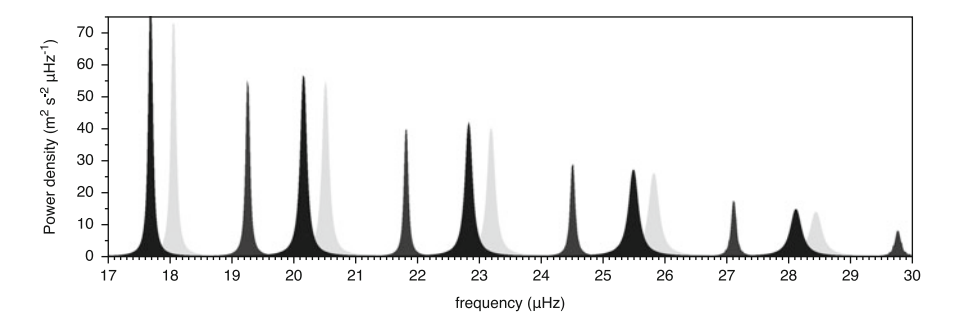


Fig. 3 Theoretical power spectrum for model C of Dupret et al. (2009). Light gray corresponds to  $\ell=0$  modes, dark gray for  $\ell=1$  modes and black for  $\ell=2$  modes

the "continuum" of g-like modes. As shown by Dupret et al. (2009), the predicted heights and amplitudes of these g-like modes is negligible because of this radiative damping. As a consequence, only the p-like modes fully trapped in the envelope are predicted to be detectable.

An illustration of the predicted power spectrum (model C of Dupret et al. 2009) is given in Fig. 3. In this case, the regular structure of the spectrum is very similar to main sequence stars.

## 6 Conclusions

Non-adiabatic oscillation models including a time-dependent treatment of convection allow to determine the theoretical amplitude and lifetimes of the modes. From these parameters and the frequencies, we can see how power spectra are expected to look like, depending on the structure of the red giant. For low-luminosity subgiants, the density contrast between the core and the envelope is not yet very high. The corresponding power spectra are predicted to be irregular, particularly for the  $\ell=1$  modes (Fig. 1). For intermediate luminosity red giants, the spectrum is more regular and  $\ell=1$  mixed modes more or less equaly spaced in periods are predicted (see Dupret et al. 2009 and Fig. 2) and observed (Beck et al. 2011; Bedding et al. 2011; Mosser et al. 2011). Finally, in high luminosity red giants, the trapping is very efficient, radiative damping is very strong for all g-like modes and the predicted spectrum is similar to main sequence stars (Fig. 3).

Acknowledgements We thank Joris de Ridder who made the figures.

### References

Balmforth, N.J.: MNRAS **255**, 603 (1992) Baudin, F., Samadi, R., Goupil, M.-J., et al.: A&A **433**, 349 (2005) Beck, P., Bedding, T., Mosser, B., et al.: Science 332, 205 (2011)

Bedding, T.R., Huber, D., Stello, D., et al.: ApJ 713, L176 (2010)

Bedding, T.R., Mosser, B., Huber, D., et al.: Nature 471, 608 (2011)

Belkacem, K., Samadi, R., Goupil, M.J., Kupka, F., Baudin, F.: A&A 460, 183 (2006)

Berthomieu, G., Toutain, T., Gonczi, G., et al.: ESA Special Publication, In: Wilson, A., Pallé, P.L. (eds.) SOHO 10/GONG 2000 Workshop: Helio- and Asteroseismology at the Dawn of the Millennium, vol. 464, pp. 411–414 (2001)

Chaplin, W.J., Houdek, G., Elsworth, Y., et al.: MNRAS 360, 859 (2005)

Christensen-Dalsgaard, J.: Sol. Phys. 220, 137 (2004)

de Ridder, J., Barban, C., Baudin, F., et al.: Nature 459, 398 (2009)

Dupret, M.-A., Grigahcène, A., Garrido, R., Gabriel, M., Scuffaire, R.: A&A 414, L17 (2004)

Dupret, M. A., Barban, C., Goupil, M.-J., et al.: ESA Special Publication, vol. 624. Proceedings of SOHO 18/GONG 2006/HELAS I, Beyond the spherical Sun (2006a)

Dupret, M.-A., Samadi, R., Grigahcene, A., Goupil, M.-J., Gabriel, M.: Commun. Asteroseismology 147, 85 (2006b)

Dupret, M., Belkacem, K., Samadi, R., et al.: A&A 506, 57 (2009)

Dziembowski, W.: Acta Astronom. 27, 203 (1977a)

Dziembowski, W.: Acta Astronom. 27, 95 (1977b)

Dziembowski, W.A., Gough, D.O., Houdek, G., Sienkiewicz, R.: MNRAS 328, 601 (2001)

Gabriel, M.: Bull. Astron. Soc. India 24, 233 (1996)

Godart, M., Noels, A., Dupret, M., Lebreton, Y.: MNRAS 396, 1833 (2009)

Gough, D.O.: Lecture Notes in Physics. In: Spiegel, E.A., Zahn, J.-P. (eds.) Problems of Stellar Convection, vol. 71, pp. 15–56. Springer, Berlin (1977a)

Gough, D.O.: ApJ 214, 196 (1977b)

Grigahcène, A., Dupret, M.-A., Gabriel, M., Garrido, R., Scuflaire, R.: A&A 434, 1055 (2005)

Houdek, G.: Astronomical Society of the Pacific Conference Series. In: Breger, M., Montgomery, M. (eds.) Delta Scuti and Related Stars, vol. 210, p. 454 (2000)

Lochard, J., Samadi, R., Goupil, M.J.: A&A 438, 939 (2005)

Montalbán, J., Miglio, A., Noels, A., Scuflaire, R., Ventura, P.: Astron. Nachr. 331, 1010 (2010a)

Montalbán, J., Miglio, A., Noels, A., Scuffaire, R., Ventura, P.: ApJ 721, L182 (2010b)

Mosser, B., Barban, C., Montalbán, J., Beck, P., et al.: A&A 532, A86 (2011)

Samadi, R., Goupil, M.: A&A 370, 136 (2001)

Spiegel, E.A.: ApJ 138, 216 (1963)

Unno, W.: PASJ 19, 140 (1967)

Van Hoolst, T., Dziembowski, W.A., Kawaler, S.D.: MNRAS 297, 536 (1998)

Ventura, P., D'Antona, F., Mazzitelli, I.: Ap&SS 316, 93 (2008)

Xiong, D.R., Deng, L.: MNRAS 324, 243 (2001)

Xiong, D.R., Cheng, O.L., Deng, L.: ApJS 108, 529 (1997)

Xiong, D.R., Cheng, Q.L., Deng, L.: MNRAS 319, 1079 (2000)

# Part II Internal Structure, Atmosphere, and Evolution of Red Giants: Current Models and Their Uncertainties

# **Evolution and Internal Structure of Red Giants**

Maurizio Salaris

**Abstract** The asteroseismic data obtained by the CoRoT and *Kepler* satellites have recently provided pulsation properties for thousands of red giants, that can add new important constraints to the evolutionary models of this important class of stellar objects. A brief review of the structure and evolution of red giant stars is presented, with emphasis on the major open problems.

#### 1 Introduction

Red giant stars, i.e., objects with extended convective envelopes inhabiting the bright, red side of observational colour-magnitude-diagrams (CMDs), play a fundamental role in our understanding of the evolution of old and intermediate-age Galactic and extragalactic stellar populations. The three main classes of red giants (Red Giant Branch, Red Clump and Asymptotic Giant Branch stars—see Sect. 2) provide a set of distance (Lee et al. 1993; Pulone 1992), metallicity (Sarajedini 1994) and star formation history (Girardi and Salaris 2001; Salaris and Girardi 2002; Maness et al. 2007) diagnostics from photometric observations of resolved, old and intermediate-age stellar populations. In case of extragalactic unresolved populations, red giant stars are the main contributors to the integrated light in the IR, a crucial spectral range to break the age-metallicity degeneracy (Salaris and Cassisi 2005), give a major contribution to metallicity-sensitive absorption feature indices, and affect also age-sensitive Balmer line indices (Schiavon et al. 2002).

The unprecedented asteroseismic data obtained by the CoRoT and Kepler satellites (see, i.e., De Ridder et al. 2009; Huber et al. 2010; Kallinger et al. 2010) have recently provided pulsation properties for thousands of red giant stars in the

M. Salaris (⊠)

Astrophysics Research Institute, Liverpool John Moores University, 12 Quays House, Birkenhead, UK

e-mail: ms@astro.livjm.ac.uk

46 M. Salaris

local Disk, that promise to add new important constraints to the evolutionary models of this important class of stars.

A survey of the structure and evolution of red giants is presented below. The main focus is on the evolutionary properties related to the use of red giants as probes of galaxy structure and evolution, and the associated theoretical uncertainties.

### 2 Three Classes of Red Giant Stars

The region of the CMD sampled by current asteroseismic observations of red giants is displayed schematically in Fig. 1. One can divide the whole red giant sample into the sequence of single-shell burning red giant branch (RGB) stars, the core He-burning red clump (RC) stars and the double shell-burning asymptotic giant branch (AGB) stars. The structure and evolution of these three evolutionary stages is discussed below.

### 2.1 Red Giant Branch Stars

RGB stars are objects with initial mass below  $\sim 2.0$ – $2.3~M_{\odot}$  (the precise value depending on the initial chemical composition), made of a nearly isothermal electron degenerate He-core (produced by central H-burning during the main sequence phase) sorrounded by a thin (in mass) H-burning shell that, in turn, is surrounded by a massive and extended convective envelope. RGB stars evolve towards increasing luminosities, due to the steady increase of the degenerate

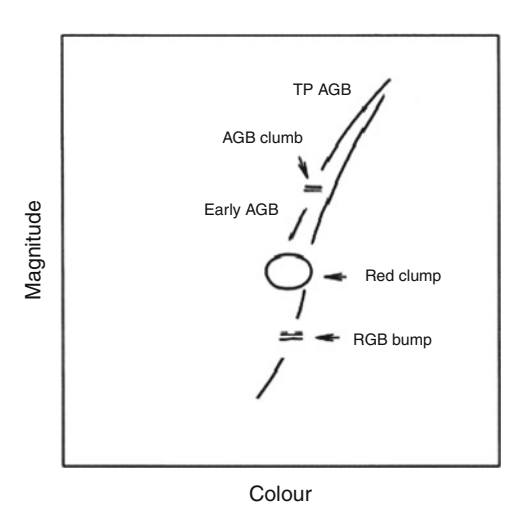


**Fig. 1** Schematic CMD of the red giants sampled by asteroseismic observations

 $M_{core}^{He}$ —and the existence of a well defined  $M_{core}^{He}$ -luminosity relationship (Kippenhahn and Weigert 1990)—caused by the fresh He produced by the H-burning (CNO-cycle) shell. The value of T<sub>eff</sub> moderately decreases along the evolution, and the lower boundary of the deep envelope convection steadily retreats towards the surface due to the outward displacement of the H-burning shell. The He-flash terminates the RGB evolution (at the so called RGB-tip) when  $M_{core}^{He} \sim 0.5 M_{\odot}$ . At solar metallicity RGB timescales are of order 10<sup>9</sup> year for a 1.0M<sub>☉</sub> star, decreasing to  $\approx 10^8$  year for a 2.0M<sub> $\odot$ </sub> star. A representative RGB evolutionary track (1M<sub> $\odot$ </sub>, solar metallicity) is displayed in Fig. 2. One can notice at  $\log(L/L_{\odot}) \sim 1.4$  a temporary drop of the surface luminosity, followed by a return to the steady increase with time. This feature is produced when the H-burning shell—until now advancing across layers of increasing H-abundance, partially processed during the main sequence phase—crosses the H-abundance discontinuity left over by convection, when it reached its maximum extension at the beginning of the RGB phase. When the shell crosses this chemical discontinuity, its efficiency is altered and the luminosity drops. As soon as the shell reaches the region beyond the discontinuity, with a flat Habundance profile, the luminosity starts again to increase monotonically. This phase manifests itself as a "bump" in the RGB differential luminosity function, given that the same luminosity range is crossed three times.

RGB stars lose mass from their convective envelope, and the value of the RGB mass at the He-flash is typically lower by  $0.1-0.2M_{\odot}$  compared to the initial value on the main sequence. There are no firm theoretical prescriptions for RGB mass loss rates, and observations (see, i.e., Origlia et al. 2002; Boyer et al. 2008) are limited to a few GCs. The amount of mass lost along the RGB is critical to predict the  $T_{\rm eff}$  of stars along the following He-burning phase.

# 2.2 Red Clump Stars

RC stars are typically metal rich objects with mass around the transition from degenerate to non-degenerate He-ignition—or metal rich low mass stars that have lost small amounts of mass along the RGB phase—in their central He-burning phase. RC stars are made of a central convective He-burning region nested within the He-core built during the previous RGB phase. A radiative H-burning (CNO-cycle) shell surrounds the He-core, and above the H-shell lies a massive, extended convective envelope, like in RGB stars. Representative red clump evolutionary tracks (1.0 and  $2.4 M_{\odot}$ , solar metallicity) are displayed in Fig. 2. The path in the CMD or Hertzsprung-Russell diagram is determined by the relative contribution to the total energy output by the central- and shell burning. Whenever the shell burning dominates the energy output, the RC track moves towards increasing  $T_{\rm eff}$ ; the opposite is true when the central burning dominates. At solar metallicity RC timescales are of order  $10^8$  year for all masses.

48 M. Salaris

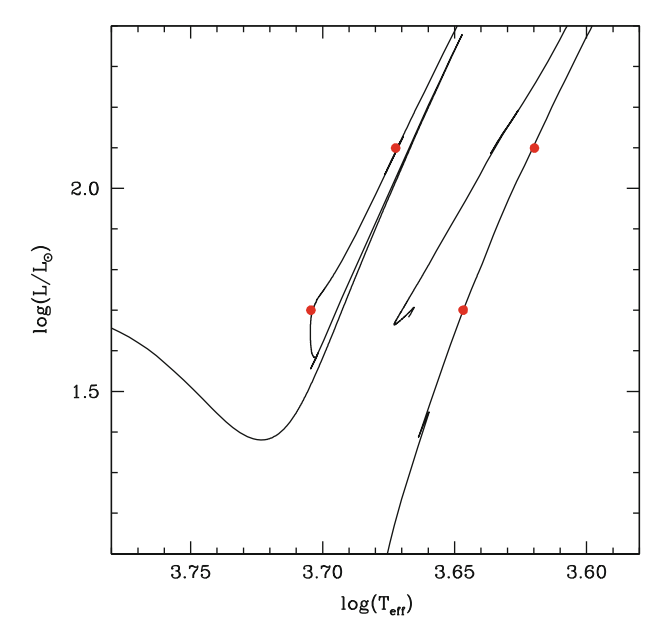


Fig. 2 Representative  $1M_{\odot}$  and  $2.4M_{\odot}$ , solar metallicity tracks, that cover the red giant evolutionary stages sampled by asteroseismic observations. Selected models discussed in the text are marked with filled circles.

# 2.3 Asymptotic Giant Branch Stars

Early-AGB stars are objects with an electron degenerate CO-core embedded within the original He-core at He-ignition. A H-burning shell is efficient above the He-core boundary, surrounded by a convective envelope. The evolution is similar to RGB stars. The early-AGB ends with the ignition of the He-burning shell, that produces the AGB clump (a feature similar to the case of the RGB bump, whereby the surface luminosity displays a temporary decrease before starting to increase again monotonically) at  $\log(L/L_{\odot}) \sim 2.1$  in the  $2.4 M_{\odot}$  track of Fig. 2. Timescales are  $\approx 10^7$  year. At higher luminosities AGB stars undergo thermal pulses, i.e., a phase whereby H- and He-burning shells are activated alternately. The increase with time of the CO mass together with efficient mass loss from the surface reduce the envelope to values of the order of  $0.01-0.001 M_{\odot}$ , at which point the models move fast (at constant luminosity) towards their final white dwarf cooling sequence.

### 3 Internal Structure of Red Giants

Figure 3 displays the contribution of the different energy generation (and losses) mechanisms inside a  $1M_{\odot}$  RGB model at  $\log(L/L_{\odot}) = 1.7$  (marked in Fig. 2). One can notice the narrowness of the nuclear energy generation region

Fig. 3 Energy generation coefficients due to nuclear reactions, gravitational energy and neutrino losses, in the inner layers of the labelled RGB model. The three coefficients are normalized to the maximum value of the nuclear energy generation

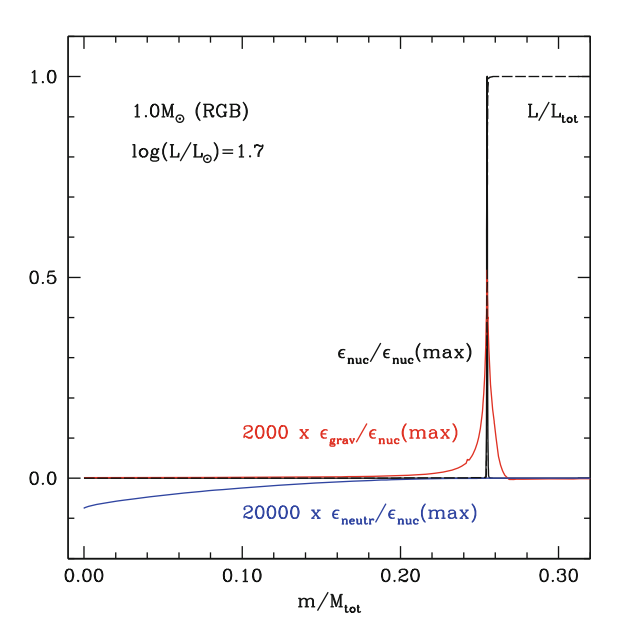
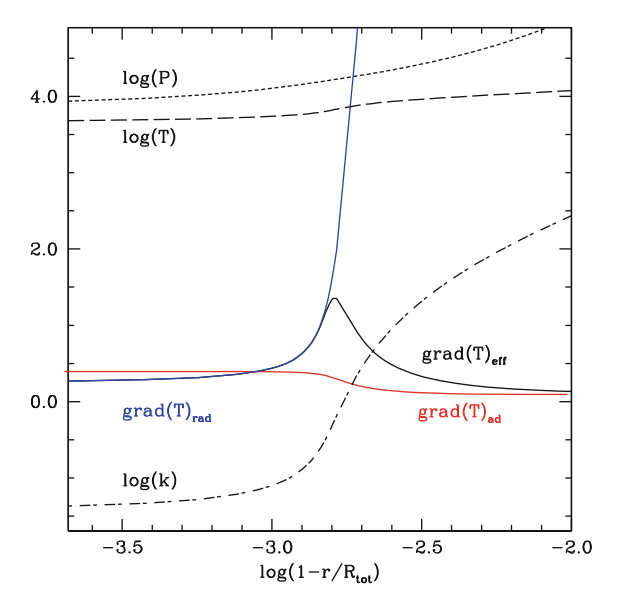


Fig. 4 Opacity, pressure, temperature and temperature gradients  $((\partial \ln T/\partial \ln P))$  in the envelope layers of the model displayed in Fig. 3



(the H-burning shell), the efficiency of neutrino energy losses (mainly plasmaneutrino emission) in the electron degenerate core, and the gravitational energy released by the contraction of the H-burning shell and neighbouring layers. Figure 4 displays the thermodynamical stratification of the external layers close to the photosphere. Moving down from the photosphere (in radiative equilibrium 50 M. Salaris

according to the Schwarzschild criterion) convection sets in due to the increase of the Rosseland opacity with depth. At the upper end of surface convection a superadiabatic region develops, whose (uncertain) temperature stratification is usually calculated employing the mixing length theory (MLT, see Böhm-Vitense 1958). The MLT is the most widely used formalism to calculate the superadiabatic temperature gradient, and needs the calibration of the free parameter related to the scale length of convective elements (Salaris and Cassisi 2008). An alternative formalism is the full spectrum theory of turbulence (Canuto et al. 1996). It is important to realize that for a given mass and initial chemical composition, it is the combined effect of the superadiabatic gradient and the surface boundary condition (pressure at the photosphere, coming from the integration of the atmospheric layers) that determine the T<sub>eff</sub> of the RGB models (Salaris et al. 2002).

As for RC stars, Figs. 5 and 6 display the energy generation contributions, and internal chemical structure of the RC model marked in Fig. 2. One can clearly see the double nuclear energy generation sources (core and H-shell), the expansion of the He-core and contraction of the H-shell. The nuclear reactions at this stage of the He-burning phase produce mainly carbon, as shown by Fig. 6. Moving from the centre outwards, one encounters first a convective region, followed by "semiconvective" layers, where adiabatic and radiative temperature gradients are equal. The onset of semiconvection is caused by the increasing opacity in the core due to the production of C (and O) at the expenses of He (Salaris and Cassisi 2005). The treatment of the semiconvective mixing, especially in the late stages of central He-burning—where it is most problematic, due to the uncertainties related to the treatment/suppression of the so-called "breathing pulses" (Salaris and Cassisi 2005)—is crucial to determine

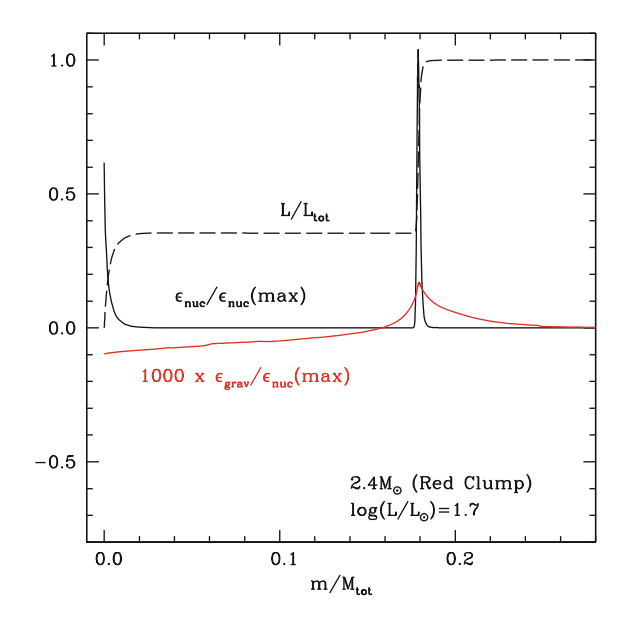


**Fig. 5** As in Fig. 3 but for the labelled RC model

Fig. 6 Chemical and temperature gradient stratifications in the inner layers of the model in Fig. 5

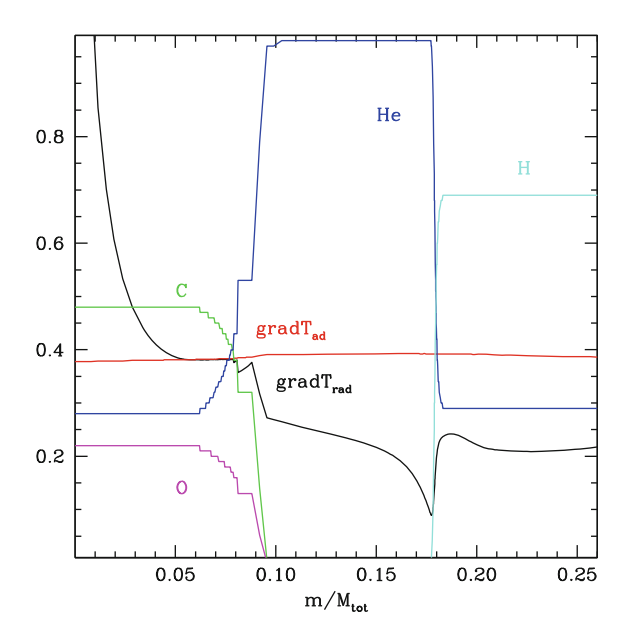
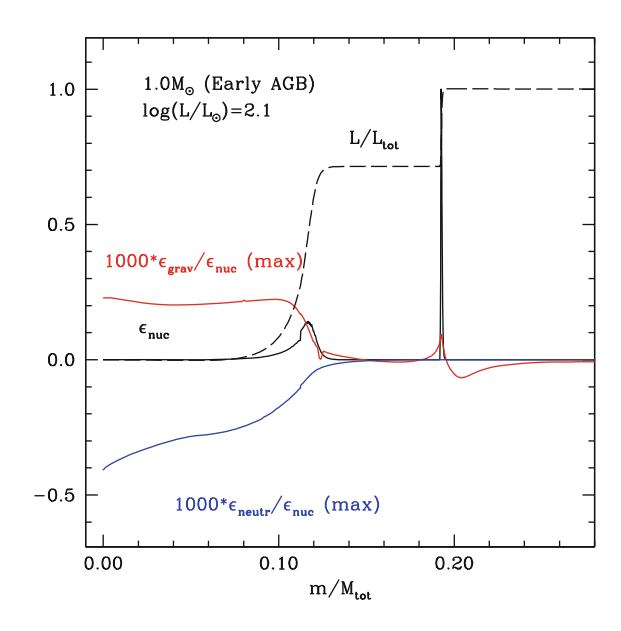


**Fig. 7** As in Fig. 5 but for the labelled early-AGB model

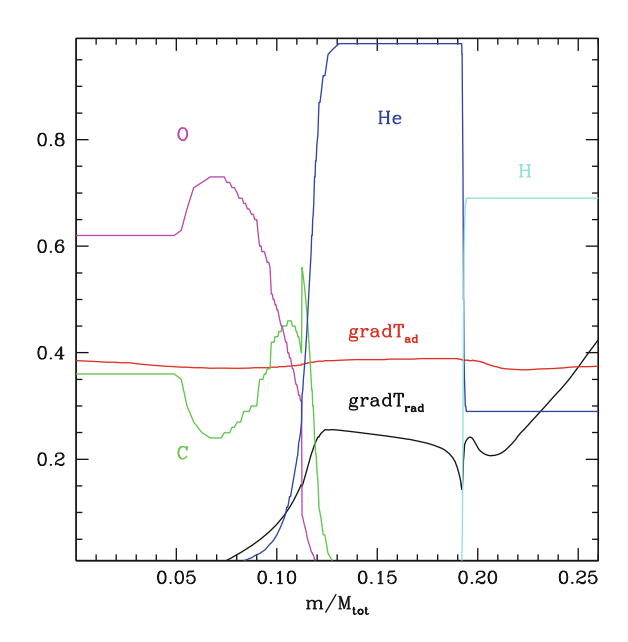


the central CO profiles of the electron degenerate core in the final white dwarf stage, and the total He-burning timescales (Salaris et al. 2010).

The internal structure of the early-AGB model marked in Fig. 2 is displayed in Figs. 7 and 8. The model is caught during the AGB clump phase, when the

52 M. Salaris

**Fig. 8** As in Fig. 6 but for the labelled early-AGB model



He-burning shell is starting to become active. Notice the efficiency of neutrino energy losses from the CO core that is becoming electron degenerate, and the final CO profile, with central oxygen abundance higher than the carbon one, due to the larger efficiency of the  $^{12}\text{C}(\alpha,\gamma)^{16}\text{O}$  reaction during the late stages of central Heburning.

From the point of view of asteroseismic studies, the important differences between the RGB, RC and early-AGB models marked in Fig. 2 are the chemical and (P, T,  $\rho$ ) stratifications. Figures 9 and 10 display the the T and  $\rho$  stratifications inside the RGB, RC and early-AGB models marked in Fig. 2. Notice the differences between different evolutionary phases at the same luminosity.

The RGB model in Fig. 9 has a much higher density throughout the He-core, compared to the RC counterpart, due to the effect of electron degeneracy. The differences between the central density of the RGB and early-AGB models of Fig. 10 are negligible, due to the onset of electron degeneracy in the CO core of the early-AGB object. Figure 11 shows the corresponding, well separated sound speed profiles for the four models of Figs. 9 and 10.

### 4 Additional Processes

Standard models for red giant stars are non-rotating, spherically symmetric and usually include only convection as element transport mechanism. Spectroscopic observations of surface chemical abundances in field Halo RGB stars (Gratton et al. 2000) have however convincingly demonstrated the need to include additional

**Fig. 9** T and  $\rho$  stratification inside the RGB and RC models at  $\log(L/L_{\odot}) = 1.7$  marked in Fig. 2

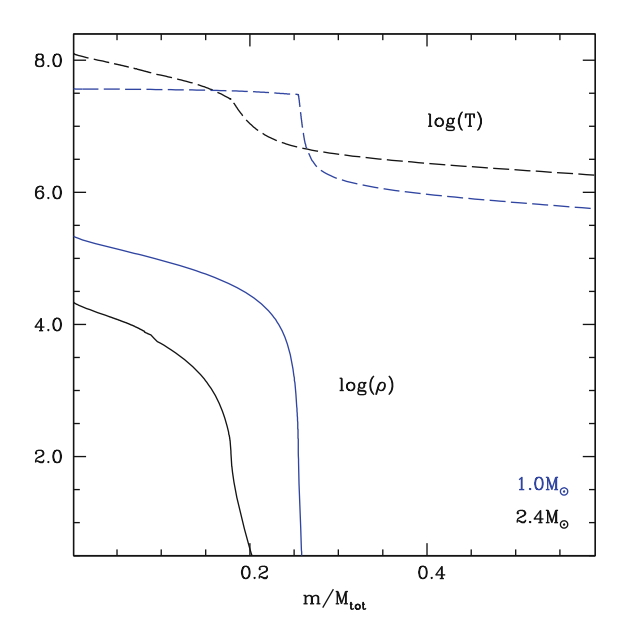
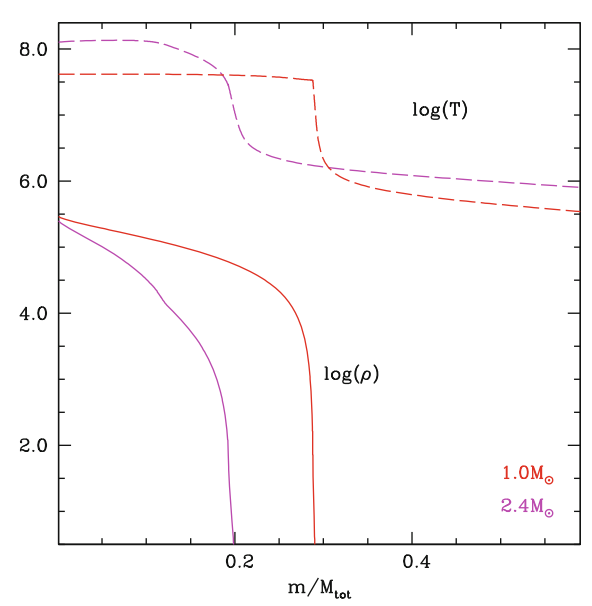


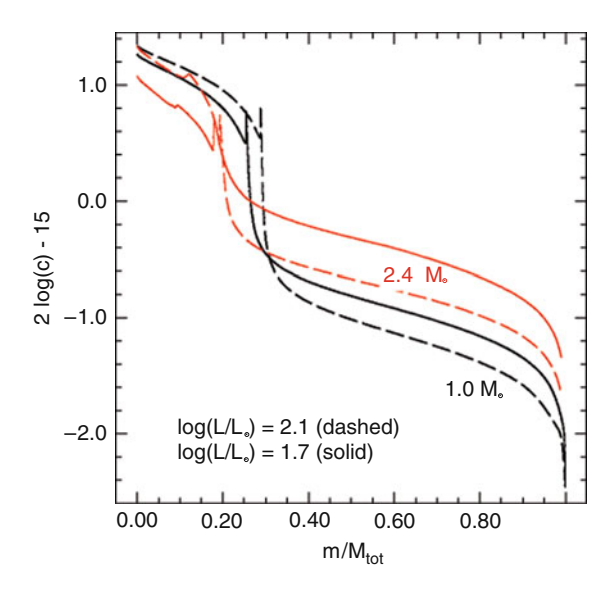
Fig. 10 As in Fig. 10, but for the RGB and early-AGB models at  $\log(L/L_{\odot}) = 2.1$  marked in Fig. 2



transport mechanisms. Standard RGB models predict that after the first dredge-up, happening approximately at the base of the RGB, the surface  $^{12}\text{C}/^{13}\text{C}$  ratio drops from  $\sim\!90$  to  $\sim\!25$ ,  $^{14}\text{N}$  increases by a factor  $\sim\!2$ ,  $^{12}\text{C}$  decreases by a factor  $\sim\!30$  and  $^{7}\text{Li}$  decreases by a factor  $\sim\!20$ . Observations show that right after the RGB bump luminosity,  $^{12}\text{C}$ ,  $^{7}\text{Li}$  and the  $^{12}\text{C}/^{13}\text{C}$  ratio drop again, and  $^{14}\text{N}$  displays another

54 M. Salaris

**Fig. 11** Sound speed profiles for the four models marked in Fig. 2



increase, due to some additional transport process that brings to the surface matter processed by layers below the Schwarzschild convective boundary. The additional mechanism that is being widely investigated is related to the so-called thermohaline instability. This instability occurs in a stable stratification that satisfies the Ledoux criterion for convective instability:

$$\nabla_{\rm ad} - \nabla + \left(\frac{\varphi}{\delta}\right) \nabla_{\mu} > 0 \tag{1}$$

but where the molecular weight decreases with depth ( $\nabla_{\mu} \equiv \frac{d \ln \mu}{d \ln P} < 0$ ). We denote here,  $\nabla = (\partial \ln T/\partial \ln P)$ ,  $\varphi = (\partial \ln \rho/\partial \ln \mu)_{P,T}$  and  $\delta = -(\partial \ln \rho/\partial \ln T)_{P,\mu}$ ,  $\nabla_{ad}$  being the adiabatic gradient. When these conditions are satisfied, the associated element transport is treated as a diffusion process, with diffusion coefficient (that multiplies the local chemical abundance gradients) given by:

$$D_{t} = C_{t} K \left(\frac{\varphi}{\delta}\right) \frac{-\nabla_{\mu}}{(\nabla_{ad} - \nabla)}$$
 (2)

for  $\nabla_{\mu}<0$ , where K is the thermal diffusivity, and  $C_t=\frac{8}{3}\pi^2\alpha^2$ , with  $\alpha$  being a free parameter that fixes the value of the coefficient  $C_t$ . For example, calculations by Charbonnel and Lagarde (2010) employ  $C_t=1,000$ . As discussed, i.e., in Eggleton et al. (2006), when the H-burning front moves outwards, preceding the H-burning region proper is a narrow region, in which  $^3$ He burns with the reaction  $^3$ He( $^3$ He, 2p) $^4$ He. Given that two nuclei become three nuclei, this  $^3$ He burning leads to a small local inversion of the  $\mu$  gradient (a local minimum) of order  $10^{-4}$ , when the shell moves across the flat H-profile beyond the discontinuity that produces

the RGB bump. The thermohaline instability caused by this  $\mu$  inversion triggers a transport of elements that can reproduce (for a suitable choice of  $C_t$ ) the observed extra-mixing observed at luminosities above the RGB bump. The reason why this transport is not activated before the bump, is because at that stage the H-shell is crossing a region with a strong H-abundance gradient (decreasing towards the centre) and the variation of  $\mu$  produced by the  $^3\text{He}(^3\text{He}, 2p)^4\text{He}$  reaction does not lead to a local  $\mu$  inversion.

Atomic diffusion, another transport mechanism expected to be efficient in stellar interiors, does not affect appreciably the structure and evolution of RGB stars (Michaud et al. 2010), while it contributes to the growth of the convective core in RC stars, mimicking the effect of convective overshooting (Michaud et al. 2007).

None of these additional transport mechanisms is able to eliminate the discrepancy between predicted and observed luminosities of the RGB bump along the giant branches of Galactic GCs (Cassisi et al. 2011), i.e., the fact that the predicted bump luminosities are too high compared to observations, by  $\sim 0.2$  mag. A possible solution to this discrepancy is to include convective overshooting of the order of 0.25 H<sub>p</sub> below the Schwarzschild boundary of the convective envelope, or some turbulent process that causes a smoothing of the H-profile discontinuity over a length of  $\sim 0.8$ H<sub>p</sub>.

Finally, the effect of rotation, when included in low-mass stellar models, is mainly to alter the internal chemical profiles during the main sequence phase. The effect is revealed later in the evolution, when the first dredge-up occurs (and may have some impact on the problem of the RGB bump luminosity). According to the models by Charbonnel and Lagarde (2010), rotational mixing favours the occurrence of the thermohaline instability in RGB stars, for masses between  $\sim 1.5$  and  $\sim 2.2 M_{\odot}$ .

### 5 Conclusions

The previous sections have presented a brief summary of the evolution of red giants, and an analysis of their chemical and physical structure. Below, is a list of open problems in red giant modelling, several of which can be addressed by a synergy between stellar evolution theory and asteroseismic studies:

- 1. Predictions of the temperature gradient in the superadiabatic region of red giant convective envelopes. This gradient affects the predicted T<sub>eff</sub> of the models.
- 2. Determination of the surface boundary conditions for stellar modelling (pressure at the layers near the photosphere). They affect the  $T_{\rm eff}$  of the models.
- 3. Prediction of RGB mass loss rates. They affect mainly the  $T_{\rm eff}$  of the following He-burning evolution.
- 4. Efficiency of thermohaline mixing (and rotational mixing), that affect the surface chemical abundances of RGB stars and later evolutionary phases.

56 M. Salaris

5. Efficiency of overshooting and/or additional turbulent transport mechanisms that decrease the predicted luminosity of the RGB bump.

6. Treatment of the semiconvective region in RC stars, especially during the late stages of central He-burning. This affects model luminosities, loops in the CMD and evolutionary timescales of both RC and early AGB models, CO stratification of the models for the final white dwarf stage.

**Acknowledgements** I wish to thank the organizers for their invitation and financial support, Santi Cassisi and Achim Weiss for numerous enlightening discussions and collaborative work on red giant stellar models.

### References

Böhm-Vitense, E.: ZAp 46, 108 (1958)

Boyer, M.L., McDonald, I., Loon, J.T., et al.: AJ 135, 1395 (2008)

Canuto, V.M., Goldman, I., Mazzitelli, I.: ApJ 473, 550 (1996)

Cassisi, S., Marin-Franch, A., Salaris, M., et al.: A&A 527, A59 (2011)

Charbonnel, C., Lagarde, N.: A&A 522, A10 (2010)

De Ridder, J., Barban, C., Baudin, F., et al.: Nature 459, 398 (2009)

Eggleton, P.P., Dearborn, D.S.P., Lattanzio, J.C.: Science 314, 1580 (2006)

Girardi, L., Salaris, M.: MNRAS 323, 109 (2001)

Gratton, R.G., Sneden, C., Carretta, E., Bragaglia, A.: A&A 354, 169 (2000)

Huber, D., Bedding, T.R., Stello, D., et al.: ApJ 723, 1607 (2010)

Kallinger, T., Mosser, B., Hekker, S., et al.: A&A 522, A1 (2010)

Kippenhahn, R., Weigert, A.: In: Kippenhahn, R., Weigert, A. (eds.) Stellar Structure and Evolution, XVI, 468 pp. 192 (1990)

Lee, M.G., Freedman, W.L., Madore, B.F.: ApJ 417, 553 (1993)

Maness, H., Martins, F., Trippe, S., et al.: ApJ 669, 1024 (2007)

Michaud, G., Richer, J., Richard, O.: ApJ 670, 1178 (2007)

Michaud, G., Richer, J., Richard, O.: A&A 510, A104 (2010)

Origlia, L., Ferraro, F.R., Fusi Pecci, F., Rood, R.T.: ApJ 571, 458 (2002)

Pulone, L.: Mem. Soc. Astron. Italiana 63, 485 (1992)

Salaris, M., Cassisi, S.: In: Salaris, M., Cassisi, S. (eds.) Evolution of Stars and Stellar Populations, pp. 400. ISBN 0-470-09220-3. Wiley-VCH (2005)

Salaris, M., Cassisi, S.: A&A 487, 1075 (2008)

Salaris, M., Girardi, L.: MNRAS 337, 332 (2002)

Salaris, M., Cassisi, S., Weiss, A.: PASP 114, 375 (2002)

Salaris, M., Cassisi, S., Pietrinferni, A., Kowalski, P.M., Isern, J.: ApJ 716, 1241 (2010)

Sarajedini, A.: AJ **107**, 618 (1994)

Schiavon, R.P., Faber, S.M., Rose, J.A., Castilho, B.V.: ApJ 580, 873 (2002)

# **Uncertainties and Systematics in Stellar Evolution Models of Red Giant Stars**

Santi Cassisi

**Abstract** In this last decade, our knowledge of evolutionary and structural properties of stars of different mass and chemical composition has significantly improved. This notwithstanding, updated stellar models are still affected by significant and, usually, not negligible uncertainties. These uncertainties are related to our poor knowledge of some physical processes occurring in the real stars such as the efficiency of mixing processes. These drawbacks of stellar models have to be properly taken into account when comparing theory with observations. In this paper we briefly review current uncertainties affecting low-mass stellar models, i.e. those structures with mass in the range between  $0.6 M_{\odot}$  and  $\sim 1.4 M_{\odot}$ , during the Red Giant Branch stage.

### 1 Introduction

During the second half of last century, stellar evolution theory has allowed us to understand the Color Magnitude Diagram (CMD) of both galactic globular clusters (GGCs) and open clusters, so that now we can explain the distribution of stars in the observed CMDs in terms of the nuclear evolution of stellar structures and, thus, in terms of cluster age and chemical composition. In recent years, however, the impressive improvements achieved for both photometric and spectroscopic observations as well as asteroseismological measurements, has allowed us to collect data of an un-precedent accuracy, which provide at the same time a stringent test and a challenge for the accuracy of the models.

On the theoretical side, significant improvements have been achieved in the determination of the Equation of State (EOS) of the stellar matter, opacities, nuclear

S. Cassisi (⊠)

INAF – Astronomical Observatory of Collurania, Via M. Maggini, 64100 Teramo, Italy e-mail: cassisi@te.astro.it

58 S. Cassisi

cross sections, neutrino emission rates, that are, the physical inputs needed in order to solve the equations of stellar structure.

The capability of current stellar models to account for all the observed evolutionary phases is undoubtedly an exciting achievement which crowns with success the development of stellar evolutionary theories as pursued all along the second half of the last century. Following such a success, one is often tempted to use evolutionary results in an uncritical way, i.e., taking these results at their face values without accounting for theoretical uncertainties. However, these uncertainties do exist, as it is clearly shown by the not negligible differences still existing among evolutionary results provided by different research groups (see the discussion in Chaboyer 1995; Cassisi et al. 1998, 1999; Castellani and degl'Innocenti 1999; Cassisi 2004).

We will discuss the main "ingredients" necessary for computing stellar models and show how the uncertainties on these inputs affect theoretical predictions of the evolutionary properties of Red Giant Branch (RGB) low-mass stars.

# 2 Stellar Evolution: The Ingredients

The stellar structure equations are well known since long time, and a clear description of the physical meaning of each one of them can be found in several books (as, for instance, Kippenhahn and Weigert 1990).

The (accurate) numerical solution of these differential equations is no longer a problem and it can be easily and quickly achieved when using modern numerical solution schemes and current generation of powerful computers. This notwithstanding, in order to solve these equations, boundary conditions have to be provided: the boundary condition at the stellar centre are trivial (see Salaris and Cassisi 2005); however the same does not apply for those at the stellar surface, i.e., the values of temperature and pressure at the base of the atmosphere. These boundary conditions can be obtained either by adopting an empirical relation for the thermal stratification like that provided by Krishna Swamy (1966) or a theoretical approximation as the so-called Eddington approximation. A more rigorous procedure is to use results from model atmosphere computations (VandenBerg et al. 2008).

In order to compute a stellar structure, it is fundamental to have an accurate description of the physical behaviour of the matter in the thermal conditions characteristics of the stellar interiors and atmospheres. This means that we need to know several physical inputs as: opacity, EOS, nuclear cross-sections, neutrino energy losses. A rich literature exists describing the improvements which have been achieved in this last decade concerning our knowledge of these physical inputs (Catelan 2009; Cassisi et al. 1998, 1999; Salaris et al. 2002, and references therein).

Some important assumptions have also to be made concerning the efficiency of those mechanisms, such as atomic diffusion and radiative levitation, which can modify the chemical stratification in the interiors and atmosphere. Until few years ago, all these non-canonical processes were usually ignored in stellar models computations. However, helioseismology has clearly shown how important is to

include atomic diffusion in the computation of the so-called Standard Solar Model (SSM), in order to obtain a good agreement between the observed and the predicted frequencies of the non-radial p-modes (Christensen-Dalsgaard et al. 1993). In the meantime, quite recent spectroscopical measurements for low-mass, metal-poor stars in GGCs strongly point out the importance of including radiative levitation in stellar computations in order to put in better agreement empirical estimates with the predictions provided by diffusive models.

When dealing with stellar model computations, one has also to account for the occurrence of mixing. Due to the poor knowledge of how to manage the mixing processes in a stellar evolutionary code, the efficiency of convection is commonly treated by adopting some approximate theory. In this context, it has to be noticed that when treating a region where convection is stable, one has to face with two problems: (1) What is the "right" temperature gradient in such region?, (2) What is the "real" extension of the convective region?

The first question is really important only when considering the outer convective regions such as the convective envelopes of cool stars. This occurrence is due to the evidence that, in the stellar interiors as a consequence of the high densities and, in turn, of the high efficiency of energy transport by convective motions, the "real" temperature gradient has to be equal to the adiabatic one. This consideration does not apply when considering the outer, low-density, stellar regions, where the correct temperature gradient has to be larger than the adiabatic one: the so-called *superadiabatic gradient*. One of the main problem in computing star models is related to the correct estimate of this superadiabatic gradient.

Almost all evolutionary computations available in literature rely on the mixing length theory (MLT Böhm-Vitense 1958). It contains a number of free parameters, whose numerical values affect the model  $T_{\rm eff}$ ; one of them is  $\alpha_{\rm MLT}$ , the ratio of the mixing length to the pressure scale height, which provides the scale length of the convective motions. There exist different versions of the MLT, each one assuming different values for these parameters. However, as demonstrated by Pedersen et al. (1990) and Salaris and Cassisi (2008), the  $T_{\rm eff}$  values obtained from the different formalisms can be made consistent, provided that a suitable value of  $\alpha_{MLT}$  is selected. Therefore, at least for the evaluation of  $T_{\rm eff}$ , the MLT is basically a oneparameter theory. The value of  $\alpha_{MLT}$  is usually calibrated by reproducing the solar  $T_{\rm eff}$ , and this solar-calibrated value is then used for computing models of stars very different from the Sun (e.g. metal poor giants). It is worth recalling that there exists also an alternative formalism for the computation of the superadiabatic gradient: the so-called Full-Spectrum-Turbulence theory (FST Canuto et al. 1996), a MLTlike formalism with a more sophisticated expression for the convective flux, and the scale-length of the convective motion fixed a priori.

For low-mass stars, the problem of the real extension of a convective region really affects only the convective envelope. In the canonical framework it is assumed that the border of a convective region is fixed by the condition—according to the classical Schwarzschild criterion—that the radiative gradient is equal to the adiabatic one. However, it is clear that this condition fixes the point where the acceleration of the convective cells is equal to zero, so it is realistic to predict that

60 S. Cassisi

the convective elements can move beyond, entering and, in turn, mixing the region surrounding the classical convective boundary. This process is commonly referred to as convective overshoot. Convective envelope overshoot could be important for RGB low-mass stars, since these structures have large convective envelope.

### 3 The Red Giant Branch

The possibility to apply RGB stellar models to fundamental astrophysical problems crucially relies on our capability to predict correctly: (1) the CMD location (in  $T_{\rm eff}$  and color) and extension (in brightness) of the RGB as a function of the initial chemical composition and age; (2) the evolutionary timescales all along the RGB; (3) the physical and chemical structure of RGB stars.

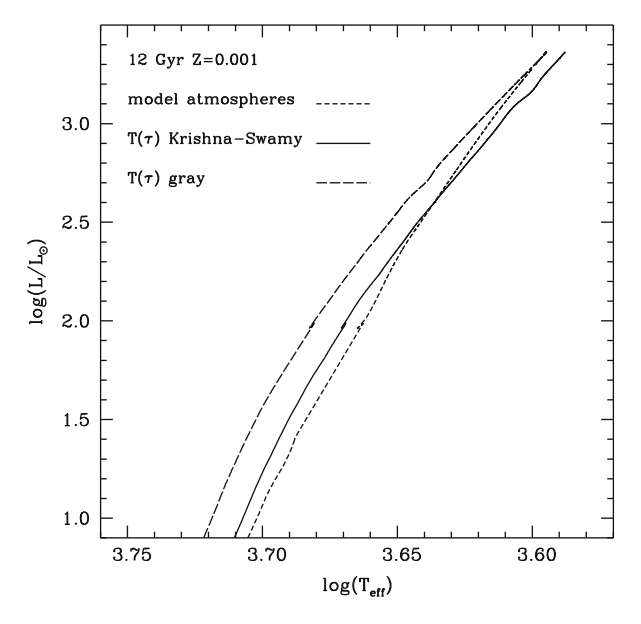
# 3.1 The Location and the Slope of the RGB

The main physical inputs used in model computation which affect the RGB location and slope are: the EOS, the low-temperature opacity, the efficiency of superadiabatic convection, and the choice about the outer boundary conditions.

EOS: The most recent stellar models rely on updated EOS tabulations, such as the OPAL EOS (Rogers and Nayfonov 2002) and the FreeEOS (Irwin 2005; Cassisi et al. 2003), which allow to properly "cover" the whole evolutionary stages. Low-mass RGB models computed by adopting these EOSs are in very good agreement, but the difference increase when comparing also models based on less updated EOS. In this case, one can easily found differences of the the order of  $\sim 100 \, \mathrm{K}$ .

Radiative opacity: Low-T opacities mainly determine the  $T_{\rm eff}$  location of theoretical RGB models, while the high-T ones—in particular those for temperature around  $10^6$  K—determine the extension of the convective envelope. Current generations of stellar models employ mainly the low-T opacity calculations by Alexander and Ferguson (1994) and by Ferguson et al. (2005), which are the most up-to-date computations suitable for stellar modeling. The main difference between these sets of data and the previous ones is the treatment of molecular absorption, most notably the fact that the latest opacity tables include the effect of the several molecules (among which the  $H_2O$  that is very important for metal rich RGB stars) and accounts also for the presence of grains. Although significant improvements are still possible as a consequence of a better treatment of the various molecular opacity sources, we do not expect dramatic changes in the temperature regime where the contribution of atoms and molecules dominate. Huge variation can be foreseen in the regime  $(T < 2,000 \, \text{K})$  where grains dominates the interaction between radiation and matter.

Fig. 1 The RGB loci of an isochrone computed by adopting different prescriptions for the outer boundary conditions. All other parameters, as for instance the  $\alpha_{MLT}$  parameter, have been kept fixed



When comparing, at different initial metallicities, stellar models<sup>1</sup> produced with these two sets of opacities with those based on previous estimates as the Kurucz (1993) (K92) ones, one finds that a very good agreement exists when  $T_{\rm eff}$  is larger than  $\sim$ 4,000 K. As soon as the RGB  $T_{\rm eff}$  goes below this limit (when the models approach the TRGB and/or their initial metallicity is increased), the most recent opacity evaluations by Ferguson et al. (2005) produce progressively cooler models (differences reaching values of  $\approx$ 100 K or more), due to the effect of the H<sub>2</sub>O molecule which contributes substantially to the opacity in this temperature range.

The outer boundary conditions: The procedure commonly used in the current generation of stellar models is the integration of the atmosphere by using a functional (semi-empirical or theoretical) relation between the temperature and the optical depth  $(T(\tau))$ . Recent studies of the effect of using boundary conditions from model atmospheres are in Montalbán et al. (2001) and VandenBerg et al. (2008). In Fig. 1 it is shown the effects on RGB stellar models of different  $T(\tau)$  relations, namely, the Krishna Swamy (1966) solar  $T(\tau)$  relationship, and the gray one. One notices that RGBs computed with a gray  $T(\tau)$  are systematically hotter by  $\sim 100 \, \text{K}$ . In the same Fig. 1, we show also a RGB computed using boundary conditions from the K92 model atmospheres, taken at  $\tau = 10$ . The three displayed RGBs, for consistency, have been computed by employing the same low-T opacities, namely the ones provided by K92, in order to be homogeneous with the model atmospheres. The model atmosphere RGB shows a slightly different slope, crossing

<sup>&</sup>lt;sup>1</sup>These stellar models are always based on a solar-calibrated mixing length.

over the track of the models computed with the Krishna Swamy (1966) solar  $T(\tau)$ , but the difference with respect to the latter stays always within  $\sim \pm 50$  K.

Even if it is, in principle, more rigorous the use of boundary conditions provided by model atmospheres, one has also to bear in mind that the convection treatment in the adopted model atmospheres (Montalbán et al. 2001) is usually not the same as in the underlying stellar models (i.e., a different mixing length formalism is used).

Superadiabatic convection: We already noticed that the value of  $\alpha_{MLT}$  is usually calibrated by reproducing the solar  $T_{\rm eff}$ , and this solar-calibrated value is then used for stellar models of different masses and along different evolutionary phases, including the RGB one. The adopted procedure guarantees that the models always predict correctly the  $T_{\rm eff}$  of at least solar type stars. However, the RGB location is much more sensitive to the value of  $\alpha_{MLT}$  than the main sequence. This is due to the evidence that along the RGB the extension (in radius) of the superadiabatic layers is quite larger when compared with the MS evolutionary phase. Therefore, it is important to verify that a solar  $\alpha_{\text{MLT}}$  is always suitable also for RGB stars of various metallicities. An independent way of calibrating  $\alpha_{MLT}$  for RGB stars is to compare empirically determined RGB T<sub>eff</sub> values for GGCs with RGB models of the appropriate chemical composition. This kind of comparison has been performed for many of the most updated stellar models databases, and the obtained results usually seem to suggest that the solar  $\alpha_{\rm MLT}$  value is adequate also for RGB stars. This notwithstanding, a source of concern about an a priori assumption of a solar  $\alpha_{\rm MLT}$ for RGB computations comes from the fact that recent models from various authors, all using a suitably calibrated solar value of  $\alpha_{MIT}$ , do not show the same RGB temperatures. This means that—for a fixed RGB temperature scale—the calibration of  $\alpha_{\rm MLT}$  on the empirical  $T_{\rm eff}$  values would not provide always the solar value (see the discussion in Salaris et al. 2002). Figure 2 displays several isochrones produced by different groups, all computed with the same initial chemical composition, same opacities, and the appropriate solar calibrated values of  $\alpha_{MLT}$ : the VandenBerg et al. (2000) and Salaris and Weiss (1998) models are identical, the Padua ones (Girardi et al. 2000) are systematically hotter by  $\sim 200 \,\mathrm{K}$ , while the  $Y^2$  ones (Yi et al. 2001) have a different shape. This comparison shows clearly that if one set of MLT solar calibrated RGBs can reproduce a set of empirical RGB temperatures, the others cannot, and therefore in some case a solar calibrated  $\alpha_{\rm MLT}$  value may not be adequate. The reason for these discrepancies must be due to some difference in the adopted input physics which is not compensated by the solar recalibration of  $\alpha_{\rm MLT}$ .

### 3.2 The Bump of the RGB Luminosity Function

The RGB luminosity function (LF) of GGCs is an important tool to test the chemical stratification inside the stellar envelopes (Renzini and Fusi Pecci 1988). The most interesting feature of the RGB LF is the occurrence of a local maximum in the luminosity distribution of RGB stars, which appears as a bump in the differential LF.

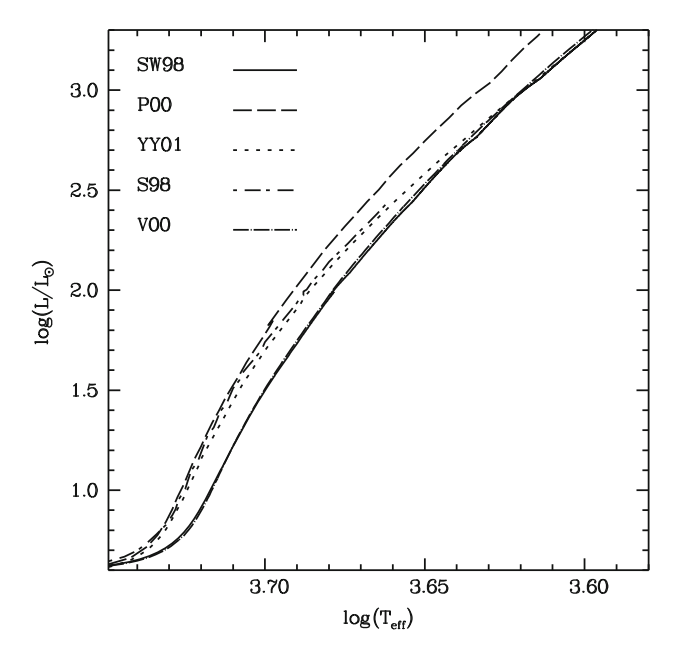


Fig. 2 As Fig. 1, but provided by various authors: Girardi et al. (2000, POO), Yi et al. (2001, YY01), VandenBerg et al. (2000, V00), Salaris and Weiss (1998, SW98), and Silvestri et al. (1998, S98)

This feature is caused by the sudden increase of H-abundance left over by the surface convection upon reaching its maximum inward extension at the base of the RGB (first dredge up) (see Thomas 1967). When the advancing H-burning shell encounters this discontinuity, its efficiency is affected, causing a temporary drop of the surface luminosity. After some time the thermal equilibrium is restored and the surface luminosity starts to increase again. As a consequence, the stars cross the same luminosity interval three times, and this occurrence shows up as a characteristic peak in the differential LF of RGB stars.

The brightness of the RGB bump is therefore related to the location of this H-abundance discontinuity, in the sense that the deeper the chemical discontinuity is located, the fainter is the bump luminosity. As a consequence, any physical inputs and/or numerical assumption adopted in the computations, which affects the maximum extension of the convective envelope strongly affects the bump brightness. A detailed analysis of this issue can be found in Cassisi and Salaris (1997) and Cassisi et al. (1997). A comparison between the predicted bump luminosity and observations allows a direct check of how well theoretical models predict the extension of convective envelope and, then provide a benchmark for the evolutionary framework.

The parameter routinely adopted to compare observations with theory is the quantity  $\Delta V_{\rm HB}^{\rm Bump} = V_{Bump} - V_{HB}$ , that is, the V-magnitude difference between the RGB-bump and the horizontal branch (HB) at the RR Lyrae instability strip level.

64 S. Cassisi

The most recent comparisons between  $\Delta V_{\rm HB}^{\rm Bump}$  models and observations (see Fig. 10 in Di Cecco et al. 2010) seem to confirm a discrepancy at the level of  $\sim$ 0.20 mag or possibly more for GCs with total metallicity [M/H] below  $\sim -1.5$ , in the sense that the predicted RGB-bump luminosity is too high; the exact quantitative estimate of the discrepancy depending on the adopted metallicity scale. At the upper end of the GC metallicity range, the existence of a discrepancy depends on the adopted metallicity scale. One drawback of using  $\Delta V_{\rm HB}^{\rm Bump}$  as a diagnostic is that uncertainties in the determination of the observed HB level for GCs with blue HB morphologies and in theoretical predictions of the HB luminosity hamper any interpretation of discrepancies between theory and observations.

An alternative avenue is offered by measuring the magnitude difference between the main sequence (MS) turn-off (TO) and the RGB-bump brightness  $\Delta V_{\text{TO}}^{\text{Bump}} = V_{TO} - V_{bump}$ , which bypasses the HB. This approach has been recently adopted by Cassisi et al. (2011) by adopting a small sample of GGCs. Although, an extension of this analysis to a larger, homogeneous sample of GCs is desirable; their results already provide clear evidence of a real "over-luminosity" of the predicted absolute magnitude of the RGB-bump, irrespective of problems with HB modeling and placement of the reference HB level in clusters with only blue HB stars.

We wish also to note that the RGB LF bump provides other important constraints for checking the accuracy of theoretical RGB models. In fact, both the shape and the location of the bump along the RGB LF can be used for investigating on the efficiency of a non-canonical mixing at the border of the convective envelope (Cassisi et al. 2002) able to partially smooth the chemical discontinuity.

# 3.3 The Brightness of the RGB Tip

The observational and evolutionary properties of stars at the Tip of the RGB (TRGB) play a pivotal role in current stellar astrophysical research. The reasons are manifold: (1) the mass size of the He core at the He flash fixes not only the TRGB brightness but also the luminosity of the HB, (2) the TRGB brightness is one of the most important primary distance indicators.

As for the uncertainties affecting theoretical predictions about the TRGB brightness, it is clear that, being this quantity fixed by the He core mass, any uncertainty affecting the predictions of  $M_{core}^{He}$  immediately translates into an error on  $M_{bol}^{TRGB}$ . An exhaustive analysis of the physical parameters that affect the estimate of  $M_{core}^{He}$  can be found in Salaris et al. (2002). Let us remember here that the physical inputs that have the largest impact in the estimate of  $M_{core}^{He}$  are the efficiency of atomic diffusion and the conductive opacity. Unfortunately, no updates are available concerning a more realistic estimate of the real efficiency of diffusion in low-mass stars, apart from the Sun. On the contrary, concerning the conductive opacity, large improvements have been obtained by (Potekhin 1999, P09), and lately by (Cassisi et al. 2007, C07). This new set represents a significant improvement (both in the accuracy and in the range of validity) with respect to previous estimates.

We show in Fig. 3 the comparison of the most recent results (Bertelli et al. 2008—Padua, Pietrinferni et al. 2004—BaSTI, Vandenberg et al. 2000—Victoria, Dotter et al. 2007—Dartmouth, Yi et al. 2001—Yonsei-Yale) concerning the TRGB bolometric magnitude and  $M_{core}^{He}$  at the He-flash; the displayed quantities refer to a  $0.8M_{\odot}$  model and various initial metallicities. When excluding the Padua models, there exists a fair agreement among the various predictions about  $M_{core}^{He}$ : at fixed metallicity the spread among the various sets of models is at the level of  $0.003 M_{\odot}$ . For the Padua models, we show the results corresponding to the two different initial He contents adopted by the authors: we have no clear explanation for the fact that the Padua models predict the lowest values for  $M_{core}^{He}$ , as well as for the presence of an "erratic" behavior of the values corresponding to the different He abundances: for a fixed total mass and metallicity, the  $M_{core}^{He}$  value is expected to be a monotonic function of the initial He abundance. Concerning the trend of M<sub>bol</sub><sup>TRGB</sup>, all model predictions at a given metallicity are in agreement within  $\sim 0.15$  mag, with the exception of the Padua models that appear to be brighter, at odds with the fact that they predict the lowest  $M_{core}^{He}$  values. In case of the Yonsei-Yale models, the result is also surprising since the fainter TRGB luminosity cannot be explained by much smaller  $M_{core}^{He}$  values, because this quantity is very similar to, for instance, the results given by VandenBerg et al. (2000). When neglecting the Padua and Yonsei-Yale models, the  $\sim$ 0.1 mag spread among the different TRGB brightness estimates can be interpreted in terms of differences in the adopted physical inputs.

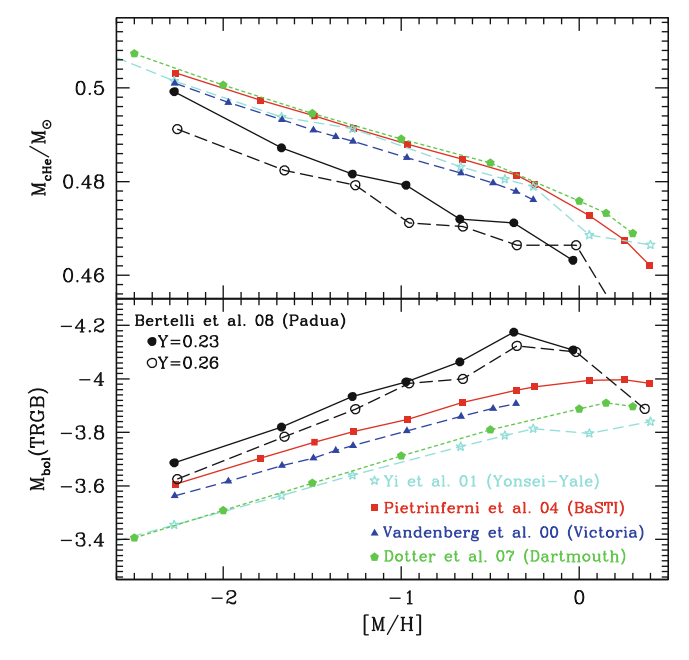


**Fig. 3** The trends of  $M_{core}^{He}$  and  $M_{bol}^{TRGB}$  as a function of the metallicity as provided by the most recent stellar model libraries (see text for more details)

S. Cassisi

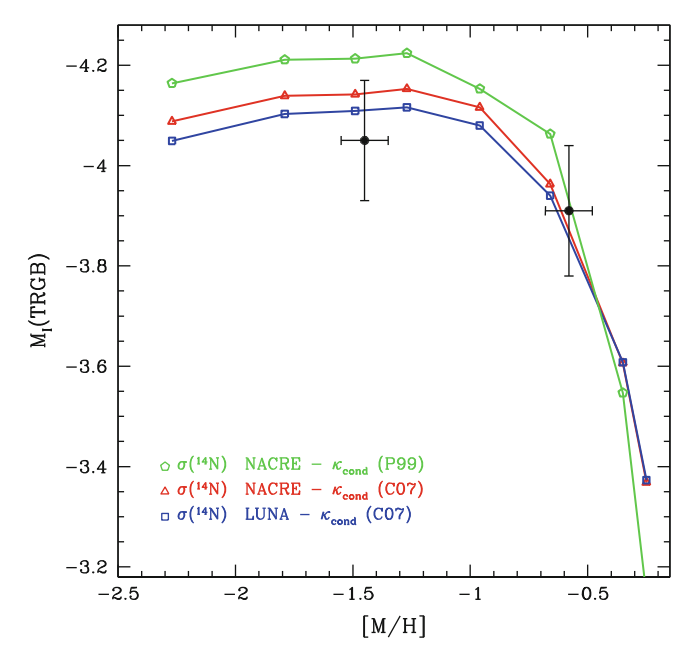


**Fig. 4** The I-band TRGB magnitude: a comparison among GGCs data and model predictions based on various assumptions on the conductive opacity and/or an updated  $^{14}N(p,\gamma)^{15}O$  reaction rate

Due to its relevance as standard candle, it is worthwhile showing a comparison between theoretical predictions about the I-Cousins magnitude of the TRGB and empirical data. This comparison is displayed in Fig. 4, where we show the data for the GGCs  $\omega$  Cen. and 47 Tuc (Bellazzini et al. 2004), and theoretical calibrations of  $M_I^{TRGB}$  as a function of the metallicity based on our own stellar models by using various assumptions concerning the conductive opacity and the rate for the nuclear reaction  $^{14}N(p,\gamma)^{15}O$  (see Pietrinferni et al. 2010, for details). The calibrations based on the most updated physics are in fine agreement with the empirical evidence.

#### 4 Conclusions

We have shown that theoretical predictions on stellar models are affected by sizeable uncertainties, a clear proof being the occurrence of not-negligible differences between results provided by different theoretical groups. From the point of view of stellar models users, the best approach to be used for properly accounting for these uncertainties, is to not use evolutionary results with an uncritical approach and, also

to adopt as many as possible independent theoretical predictions in order to have an idea of the uncertainty existing in the match between theory and observations.

On the other hand, stellar model makers should continue their effort of continuously updating their models in order to account for the "best" physics available at any time, and consider the various empirical constraints as a benchmark of their stellar models. This represents a fundamental step for obtaining as much as possible accurate and reliable stellar models.

**Acknowledgements** We warmly thank the LOC and the SOC for organizing this interesting meeting.

#### References

Alexander, D.R., Ferguson, J.W.: ApJ 437, 879 (1994)

Bellazzini, M., Ferraro, F.R., Sollima, A., Pancino, E., Origlia, L.: A&A 424, 199 (2004)

Böhm-Vitense, E.: ZAp **46**, 108 (1958)

Canuto, V.M., Goldman, I., Mazzitelli, I.: ApJ 473, 550 (1996)

Cassisi, S.: Astronomical Society of the Pacific Conference Series. In: Kurtz, D.W., Pollard, K.R. (eds.) IAU Colloq. 193: Variable Stars in the Local Group, vol. 310, p. 489 (2004)

Cassisi, S., Salaris, M.: MNRAS 285, 593 (1997)

Cassisi, S., degl'Innocenti, S., Salaris, M.: MNRAS 290, 515 (1997)

Cassisi, S., Castellani, V., degl'Innocenti, S., Weiss, A.: A&AS 129, 267 (1998)

Cassisi, S., Castellani, V., degl'Innocenti, S., Salaris, M., Weiss, A.: A&AS 134, 103 (1999)

Cassisi, S., Salaris, M., Bono, G.: ApJ 565, 1231 (2002)

Cassisi, S., Salaris, M., Irwin, A.W.: ApJ 588, 862 (2003)

Cassisi, S., Potekhin, A.Y., Pietrinferni, A., Catelan, M., Salaris, M.: ApJ 661, 1094 (2007)

Castellani, V., degl'Innocenti, S.: A&A **344**, 97 (1999)

Catelan, M.: Ap&SS 320, 261 (2009)

Chaboyer, B.: ApJ 444, L9 (1995)

Christensen-Dalsgaard, J., Proffitt, C.R., Thompson, M.J.: ApJ 403, L75 (1993)

Di Cecco, A., Bono, G., Stetson, P.B., et al.: ApJ 712, 527 (2010)

Ferguson, J.W., Alexander, D.R., Allard, F., et al.: ApJ 623, 585 (2005)

Girardi, L., Bressan, A., Bertelli, G., Chiosi, C.: A&AS 141, 371 (2000)

Irwin, A.W.: FreeEOS, http://freeeos.sourceforge.net (2005)

Kippenhahn, R., Weigert, A.: In: Kippenhahn, R., Weigert, A. (eds.) Stellar Structure and Evolution, XVI, **468** pp. 192 (1990)

Krishna Swamy, K.S.: ApJ 145, 174 (1966)

Kurucz, R.L.: Astronomical Society of the Pacific Conference Series. In: Dworetsky, M.M., Castelli, F., Faraggiana, R. (eds.) IAU Colloq. 138: Peculiar versus Normal Phenomena in A-type and Related Stars, vol. 44, p. 87 (1993)

Montalbán, J., Kupka, F., D'Antona, F., Schmidt, W.: A&A370, 982 (2001)

Pedersen, B.B., Vandenberg, D.A., Irwin, A.W.: ApJ 352, 279 (1990)

Pietrinferni, A., Cassisi, S., Salaris, M.: A&A **522**, A76 (2010)

Potekhin, A.Y.: A&A 351, 787 (1999)

Renzini, A., Fusi Pecci, F.: ARA&A 26, 199 (1988)

Rogers, F.J., Nayfonov, A.: ApJ 576, 1064 (2002)

68 S. Cassisi

Salaris, M., Cassisi, S.: In: Salaris, M., Cassisi, S. (eds.) Evolution of Stars and Stellar Populations, pp. 400. ISBN 0-470-09220-3. Wiley-VCH (2005)

Salaris, M., Cassisi, S.: A&A 487, 1075 (2008)

Salaris, M., Weiss, A.: A&A 335, 943 (1998)

Salaris, M., Cassisi, S., Weiss, A.: PASP 114, 375 (2002)

Silvestri, F., Ventura, P., D'Antona, F., Mazzitelli, I.: ApJ 509, 192 (1998)

Thomas, H.-C.: ZAp **67**, 420 (1967)

VandenBerg, D.A., Swenson, F.J., Rogers, F.J., Iglesias, C.A., Alexander, D.R.: ApJ 532, 430 (2000)

VandenBerg, D.A., Edvardsson, B., Eriksson, K., Gustafsson, B.: ApJ 675, 746 (2008)

Yi, S., Demarque, P., Kim, Y.-C., et al.: ApJS 136, 417 (2001)

# Convection Modelling and the Morphology of RGBs in Stellar Clusters

Paolo Ventura, Roberta Carini, and Marcella Di Criscienzo

**Abstract** Convection modelling in stellar interiors proves essential for a number of topics, particularly in the cases where, due to the scarce efficiency of the convective modality of transporting energy, a given degree of overadiabaticity is required. The convective envelopes of red giants are the typical example of such a situation, because the whole thermodynamic structure of the outermost layers, and consequently the radius of the star, are strongly interfaced with the treatment of the convective instability. In this contribution we analyze how the colors of RGB stars depend on the convective model adopted, and underline the differences found in the attempts of modelling the morphology of the RGBs of globular clusters, and of high metallicity clusters.

#### 1 Introduction

The treatment of the convective instability put a serious challenge to the predictive power of stellar evolution theories. The lack of any robust and general solution of the Navier–Stokes equations pushed astrophysicists to look for parametrizations, to be easily implemented into stellar evolution codes. The procedure adopted in most simulations is to look for the border separating the radiatively stable regions from the convective zones via the classic Schwarzschild criterium, and to model the temperature gradient within the instability regions via some ad hoc, local assumptions, in which the typical scale of the convective phenomenology in a given layer of the star is parametrized as a function of the local values of some thermodynamic variables. This description proves to be highly incomplete in

P. Ventura (⋈) · R. Carini · M. Di Criscienzo

INAF – Osservatorio Astronomico di Roma, via Frascati 33, 00040 Monte Porzio Catone (RM), Italy

e-mail: paolo.ventura@oa-roma.inaf.it; roberta.carini@oa-roma.inaf.it; marcella.dicriscienzo@oa-roma.inaf.it

P. Ventura et al.

particular in the regions close to the convection borders, where the phenomenon is expected to be non local, i.e. the temperature gradient in a given layer will depend on the physical environment experienced by the convective eddies during the distance travelled before dissolving.

Despite some admirable attempts (Canuto 1992; Xiong 1986), devoted to develop a self-consistent theoretical model to consider non locality, and produce the temperature gradient and the true extension of the convective zone, with no need of free parameters, the physical description of convection in the modern evolution codes still relies on local models, and is therefore sensitive to the choices made for the free parameters entering these treatments.

The results obtained in terms of the temperature gradients can be considered safe and reliable in the zones where convection is very efficient in carrying the energy demanded by the conservation of the total flux condition, because the stratification will be very close to adiabaticity. Conversely, in the zones where a given degree of overadiabaticity is required, the steepness of the temperature profile will increase when a low-efficiency convection model is used, and will be flatter otherwise.

Red Giant Branch (hereinafter RGB) stars are the classic example of such a situation, because their outermost layers are convective, but the densities are so small that a narrow overadiabaticity peak is developed. The height and the width of this peak will depend on the convection model adopted, and this will influence the effective temperature at a given evolutionary stage (normally represented by the location of the CNO burning shell, or by the total luminosity of the star). Unlike main sequence stars, whose external convective zones, if any, are very thin, the RGB stars radii are extremely dependent on the convective model adopted.

In this contribution we will show how the choice of the convective model influences the temperature of the RGBs of low-mass stars, and thus the RGBs locii of stellar clusters. We will treat separately the case of globular clusters and the problems associated to the interpretation of the RGBs of high-metallicity clusters.

# 2 Convection Modelling in a Local Framework

A detailed description of the transport of energy within regions unstable to convection demands to solve the Navier–Stokes equations, for which a general solution has not been found yet. This is the reason why stellar astrophysicists have traditionally used local approaches.

The simplest model, still implemented in the vast majority of the stellar evolution codes, is the Mixing Length Theory (hereinafter MLT) of convection (Vitense 1953): the whole eddy distribution is modelled via a simple delta function, and the typical size of the eddy considered (l) is assumed to equal the distance travelled before dissolving (the mixing length,  $\Lambda$ ). Being these quantities unknown, the following parametrization is introduced:

$$l = \Lambda_{MLT} = \alpha \times H_p \tag{1}$$

where  $H_p$  is the pressure scale height, given by  $H_p = p/g\rho$ .

A more recent approach was developed by Canuto and Mazzitelli (Canuto and Mazzitelli 1991, 1992). For what concerns the size of the convective bubbles, in this treatment the whole spectrum of the eddies dimensions is accounted for the evaluation of the convective flux, which leads to the FST (Full Spectrum of Turbulence) terminology (see Fig. 1 in Canuto and Mazzitelli 1991). Also, the mixing length is assumed to equal z, the distance to the nearest convective border. This choice allows a fit of the solar radius within a few percents, although the necessity of reproducing the solar radius with a much higher precision suggested the introduction of an additional term in the expression for the mixing length, that includes  $H_p^{top}$ , the value that the pressure scale height assumes at the border of the convective region. The full expression is:

$$\Lambda_{FST} = z + \beta \times H_p^{\text{top}} \tag{2}$$

The physical meaning and the relevance of the parameters in the expressions (1) and (2) are deeply different:  $\alpha$  determines the mixing length in the whole convective zone, whereas  $\beta$  is relevant only in the very proximities of the convective borders, the only regions where the additional term in (2) is not negligible compared to z.

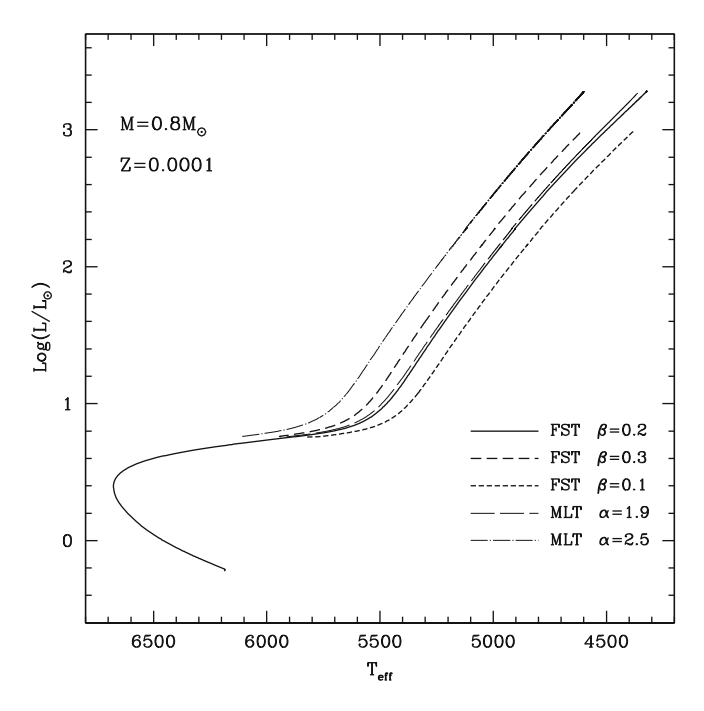


Fig. 1 Evolutionary tracks on the theoretical HR plane for a popII model of  $0.8M_{\odot}$ . The three heavier lines refer to models calculated with the FST description for turbulent convection, whereas the two lighter lines indicate MLT models with different choices for the free parameter  $\alpha$ . The values  $\alpha=1.9$  and  $\beta=0.2$ , corresponding to the long-dashed and the solid lines, allows to fit the solar radius

The inclusion of the whole eddy spectrum renders the convective flux evaluated according to the FST prescription higher that MLT, with the exception of the regions where the efficiency of convection is low, in which case the MLT flux is larger (see Fig. 5 in Canuto and Mazzitelli 1991).

# 3 FST vs. MLT Convection Modelling: The RGB of Population II Stars

RGB stars possess an extended convective mantle, that encompasses the whole region from the CNO burning shell to the surface. In most of this region convection is rather efficient, such that the convective gradient is quite close to the adiabatic value. In the outermost layers the situation is different, because the drop in the density when approaching the surface makes the true gradient to deviate from the adiabatic value. The degree of overadiabaticity depends on the convective model adopted. When this latter is scarcely efficient, the temperature gradient will be steeper, therefore the star will be cooler and redder.

We show in Fig. 1 the theoretical tracks of a  $0.8 \rm M_{\odot}$  model with metallicity  $Z=10^{-4}$ ; this is the typical mass currently populating the RGB of Globular Clusters. The various evolutionary paths shown in Fig. 1 were obtained by changing the convective model; all the other physical and chemical inputs were left unchanged. The range of values for  $\alpha$  and  $\beta$  cluster around  $\alpha=1.9$  and  $\beta=0.2$ , the values needed to fit the Sun. The tracks are practically overimposed in the Main Sequence (MS) and the Sub Giant branch (SGB), before an extended convective envelope is formed. As expected on the basis of the previous discussion, the tracks become progressively hotter when either  $\alpha$  or  $\beta$  are increased; in fact, any increase in the mixing length determines a higher efficiency of convection. The different relevance of  $\alpha$  and  $\beta$  on the color of the tracks can be deduced by the change in the effective temperature when these parameters are changed: a 100% change in  $\beta$  determines a shift in  $T_{\rm eff}$  of  $\sim$ 200 K, whereas a smaller change of  $\alpha$ , of the order of 25%, determines a difference in  $T_{\rm eff}$  of the order of  $\sim$ 250 K.

The range of effective temperatures spanned by the two sets of tracks (MLT and FST) are rather similar, despite the difference in the convection modelling. This finding can be understood on the basis of the left panel of Fig. 2, that shows the overadiabaticity in the outer regions of the star at four different evolutionary stages during the RGB evolution, in the MLT and FST cases. The models on the tracks were analyzed at luminosities  $\log(L/L_{\odot})=1,1.5,2,3$ , this latter corresponding to the curves on the right in the two panels of Fig. 2. We note that the two sets of curves diverge in the interior, where the FST overadiabaticity is sistematically smaller, whereas the situation is reversed in the proximities of the surface, where the FST models develop a higher and narrower overadiabaticity peak. This behaviour is a mere consequence of the larger efficiency of the FST model in the regions of higher density, and of the larger fluxes predicted by the MLT description in the regions where the density is very small, such as the external zone.

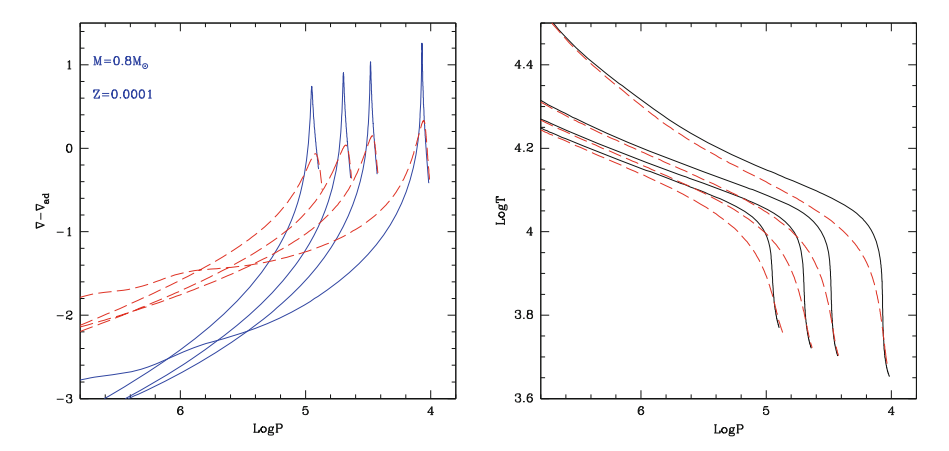


Fig. 2 Left: The profile of the overadiabaticity in the external layers of two models whose tracks are shown in Fig. 1, calculated with the FST model for convection (solid lines), and the MLT scheme (dashed lines). The free parameters were chosen in agreement with the values that allow to fit the Sun, i.e.  $\alpha=1.9$  and  $\beta=0.2$ . For each model we show four lines, that refer to various stages during the RGB evolution (see text for details). Right: The symbols are the same as in the right panel, but in this case the temperatures are shown

In the run of temperature versus pressure (see the right panel of Fig. 2), these two behaviours are seen to compensate each other, which is the reasons why the effective temperatures of the two sets of models almost coincide, within the uncertainties associated to the choice of the free parameters.

#### 4 The RGB of Metal Rich Clusters

The similarity between the shapes of the RGB predicted by the FST and MLT descriptions found in the analysis of PopII stars does not hold at higher metallicities. Figure 3, in which two tracks of  $1.2\,\mathrm{M}_\odot$  at Z=0.04 are plotted together, shows a huge difference in the effective temperatures (the FST model being hotter up to  $\sim\!500\,\mathrm{K}$ ), and also in the morphology of the RGBs, whose slopes are very different for most of the track.

Some ad hoc changes in the free parameters  $\alpha$  and  $\beta$  would possibly help reducing the differences in the effective temperatures, but would not eliminate the differences in the morphology of the RGBs.

To investigate the reasons for such discrepant behaviours, we show in the two panels of Fig. 4 the run of the overadiabaticity and of the adiabatic gradient in the external regions of the two sets of models, in four distinct evolutionary stages during the RGB evolution, at the same luminosities as in Fig. 2. We note the same trend as in previous case: the FST models attain a smaller overadiabaticity in the interior, and develop a higher and narrower overadiabaticity peak in the proximities

74 P. Ventura et al.

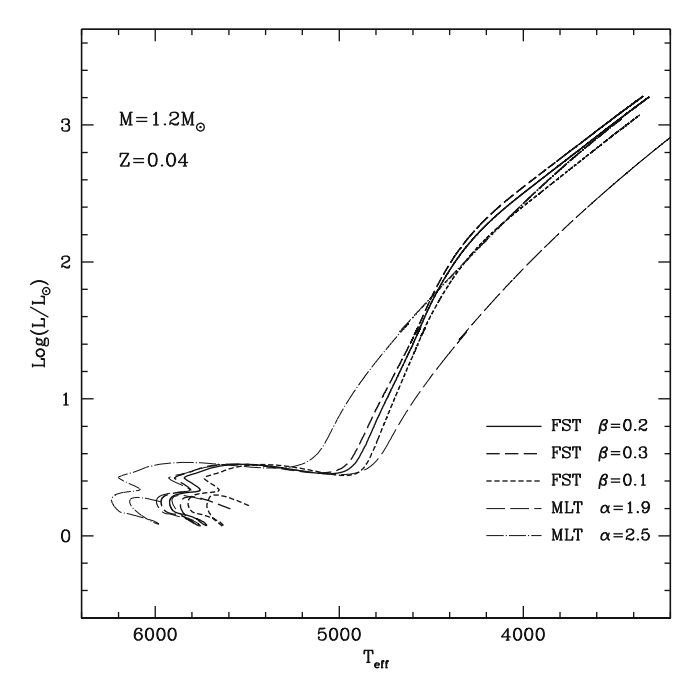


Fig. 3 Theoretical excursions in the HR plane of models of a star of mass  $M=1.2\,{\rm M}_\odot$  and metallicity Z=0.04, for various choices regarding the treatment of convection. The heavier lines refer to the FST treatment, whereas the lighter lines indicate the MLT models

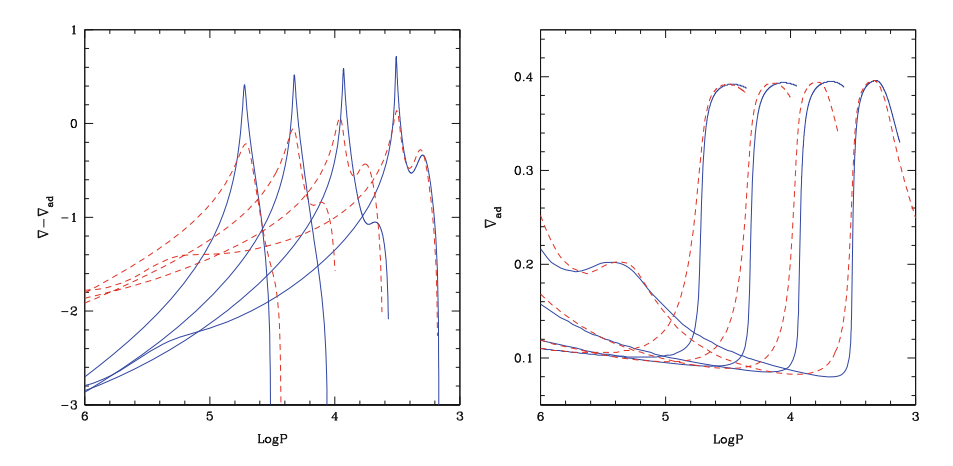


Fig. 4 Left: The degree of overadiabaticity in the external layers within two models of  $M=1.2M_{\odot}$  and metallicity Z=0.04. The models differ in the treatment of convection, either FST (solid lines) or MLT (dashed). The four lines for each model indicate different evolutionary stages during the RGB evolution. Right: the value of the adiabatic gradient in the outer layers of the same models shown in the right panel. Note the decrease of  $\nabla_{ad}$  for decreasing pressure in the MLT models, which is the reason for the differences in the morphology of the tracks in the RGB zone (see text for details)

of the surface. Differently from the previous case, we note in the MLT case the presence of a local maximum in  $(\nabla - \nabla_{ad})$ , which is found in the FST case only in the last model, when the evolution approaches the helium flash. It is this local maximum that is the ultimate reason for the difference in the tracks, because the MLT temperature profile, after approaching the FST counterpart, steepens again, which leads to a much smaller surface temperature. This effect is cancelled once the FST temperature profile develops the local maximum too, although the difference in temperature persists, and the two RGBs run parallel.

The right panel of Fig. 4 provides a physical explanation for these differences, showing the behaviour of the adiabatic gradient in the external regions, in the same four evolutionary stages. The dashed lines, indicating the MLT models, decline in the outer regions after reaching a local maximum. This behaviour is found in the FST case only in the last model. It is this decrease in the adiabatic gradient that, via an increase in  $(\nabla_{rad} - \nabla_{ad})$ , determines a secondary peak in the overadiabaticity, and leads to the gap in the effective temperature between FST and MLT models. This behaviour of  $\nabla_{ad}$  is due to the cool temperatures that characterize the RGBs of high metallicity clusters, that favour molecular dissociation; the MLT models, being cooler in their interiors, achieve this condition earlier during the RGB phase.

To conclude this discussion, we stress that the whole region involving the overadiabaticity peak and the following decline in the adiabatic gradient is at optical depths  $\tau < 10$ . Before these results are confirmed, it is therefore essential to compare these findings, based on a grey-like atmosphere, with a non grey treatment, extended at least to  $\tau \sim 20$ . This investigation is mandatory, to rule out the possibility that the whole thermodynamic stratification in the external regions, and consequently the temperature of the star, is a mere result of the simplified treatment of the atmospheric layers.

#### 5 Conclusions

We analyzed the morphology of the RGBs of metal poor and high-Z stellar clusters, and how the relative predictions change according to the description of the convective regions. We focused on the two mostly used local models available, i.e. the MLT and the FST treatments, and to the role of the free parameters entering the expression for the mixing length, i.e.  $\alpha$  (MLT) and  $\beta$  (FST). We first showed that  $\beta$  plays only a modest role in determining the effective temperature of the stars during the RGB phase, because it provides a not negligible contribution only in the regions close to the border of the convective region; conversely, in the MLT scheme, the mixing length is proportional to  $\alpha$ , which has a much stronger influence on the thermodynamic stratification of the whole convective zone.

In Pop II stars the RGBs predicted by adopting the solar calibrated parameters for the MLT and FST models are very close each other, and lead to similar effective temperatures at a given luminosity, due to a counterbalance between the internal P. Ventura et al.

zones, where the FST predicts a smaller overadiabaticity, and the outermost layers, where the situation is completely reversed, due to the small densities.

The situation is completely different in the Pop I stars, where the FST models are systematically hotter, and the slope of the RGB is steeper with the only exception of the phases immediately preceding the helium flash. The reasons for this discrepancy, that cannot be cancelled even by playing with the free parameters, is that the temperatures of high-metallicity giants are so small that the MLT models (which in the interior are cooler than their FST counterparts) enter the region of molecular dissociation, where the adiabatic gradient declines while approaching the surface; this favours a higher degree of overadiabaticity, and a smaller effective temperature.

A comparison of these results with models based on a non grey treatment of the atmospheric layers is essential before these results are confirmed.

#### References

Canuto, V.M.: ApJ392, 218 (1992)

Canuto, V.M., Mazzitelli, I.: ApJ**370**, 295 (1991) Canuto, V.M., Mazzitelli, I.: ApJ**389**, 724 (1992)

Vitense, E.: ZA **32**, 135 (1953) Xiong, D.R.: A&A**167**, 239 (1986)

# **Helium Burning in Moderate-Mass Stars**

**Achim Weiss** 

**Abstract** The evolution of low- and intermediate mass stars at the onset and during core helium burning is reviewed. Particular emphasis is laid on structural differences, which may allow to identify a star's nature and evolutionary phase in spite of the fact that it is found in a region of the Hertzsprung-Russell-Diagram objects from both mass ranges may populate. Seismic diagnostics which are sensitive to the temperature and density profile at the border of the helium core and outside of it may be the most promising tool.

### 1 Mass Ranges

In this talk I will be concerned with stellar models in the mass ranges usually called *low* and *intermediate*. While these two ranges are separated by a physical effect—the ignition of helium under degenerate plasma conditions—stars in both ranges share some properties, but within each mass range they also differ in others. Here, we are concentrating on stars which

- Are massive enough to ignite helium and had the time to reach the heliumburning stage within a Hubble-time, and
- At helium ignition are not brighter than the tip of the red giant branch, i.e., have approximately  $\log L/L_{\odot} < 3.5$ .

These requirements limit the mass range of interest to about  $0.7 < M/M_{\odot} < 7$ ; exact numbers, which are not needed here, would depend on composition. I call this mass range that of *moderate-mass* stars.

78 A. Weiss

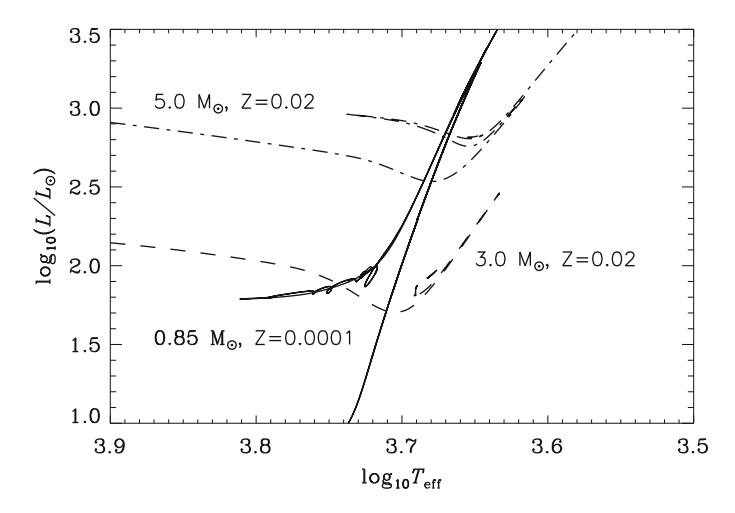


**Fig. 1** Parts of the evolutionary tracks in the Hertzsprung-Russell-diagram for a low-mass  $(0.85\,M_\odot)$  star with Z=0.0001 (*solid line*), and two stars with solar-like metallicity (Z=0.02) and 3 (*dashed line*) and 5  $M_\odot$  (*dash-dotted line*)

Before and during helium burning moderate-mass stars may be confused, as is demonstrated by the example of Fig. 1, which shows stars of 0.85, 3.0, and 5.0  $M_{\odot}$  before and during core helium burning. If the metallicity is not known accurately enough, a low-mass star (LMS) on its ascent on the RGB occupies roughly the same effective temperature and luminosity as a more metal-rich intermediate-mass star (IMS) of  $3 M_{\odot}$  during core helium burning. Close to the tip of the RGB it crosses the evolution of a  $5 M_{\odot}$  star before and shortly after helium ignition and again during early helium shell burning. In the following I will discuss the structural differences between such models, which occupy similar regions in the HRD.

#### 2 Low-Mass Stars: The Core Helium Flash

All of the following is based on traditional 1-dimensional, hydrostatic stellar evolution models, which have been calculated through their full evolution from the main-sequence into and past core helium burning; in particular the core helium flash is followed completely, which is possible with the GARSTEC code (Weiss and Schlattl 2008) which I used. One should keep in mind that these models are still approximations to the real evolution, which is dynamic and multi-dimensional. Such models will be presented by M. Mocak (these proceedings).

The stability of nuclear burning depends mainly on the thermodynamic properties of the plasma, as can be shown with very simple arguments (following Kippenhahn and Weigert 1990). If we denote a small perturbation to physical quantities by an index 1, we can write the equation of state in the following standard way

$$\frac{\rho_1}{\rho} = \alpha \frac{P_1}{P} - \delta \frac{T_1}{T} \tag{1}$$

with  $\alpha$  and  $\delta$  being the usual logarithmic derivatives with respect to P and T of density. For the energy generation rate we assume a power law,  $\epsilon = \epsilon_0 \rho^n T^{\nu}$ , and define

$$\xi = \frac{4\delta}{4\alpha - 3}, \qquad \eta = \alpha \xi - \delta = \frac{3\delta}{4\alpha - 3}.$$
 (2)

With

$$A = \frac{\epsilon_0 (n\eta + \nu)}{c_P T_0 (1 - \nabla_{ad} \xi)} \tag{3}$$

one can show that  $T_1/T \sim \exp(At)$ , i.e., if A < 0, nuclear burning is stable, while for A > 0 it is unstable, and an exponential runaway will take place for small perturbations.

For a main-sequence star with almost ideal gas conditions,  $\alpha=\delta=1, n=1$ , and thus  $\xi=4$  and  $\eta=3$ , such that A<0. However, for a LMS near helium ignition, the helium electron gas is (non-relativistically) degenerate and dominating the equation of state. Therefore,  $\alpha=3/5$  and  $\delta\ll1$ .  $\xi$  and  $\eta$  are thus  $\approx0$  and A>0; helium ignition is thermally unstable and a runaway takes place. This is the reason for the *core helium flash*.

In spite of its name, the flash starts very slowly and quite early on the RGB. Figure 2 demonstrates how the helium luminosity increases from values of  $10^{-8}$   $L_{\odot}$  at  $\log L/L_{\odot}=2.45$  to peak values of  $10^{10}$   $L_{\odot}$  (and above) at the tip. While the star needs 18 Myr from the first to the second point ( $\log L_{\rm He}/L_{\odot}=-3$ ) at  $\log L/L_{\odot}=3.12$ , already 3.3 Myr later  $\log L_{\rm He}/L_{\odot}=3$  is reached (basically at the tip), and a mere 180 years later the peak luminosity of  $10^{10}$   $L_{\odot}$  is reached (the two final diamond symbols in Fig. 2 are at almost the same position). In this final phase the exponential runaway truly takes place.

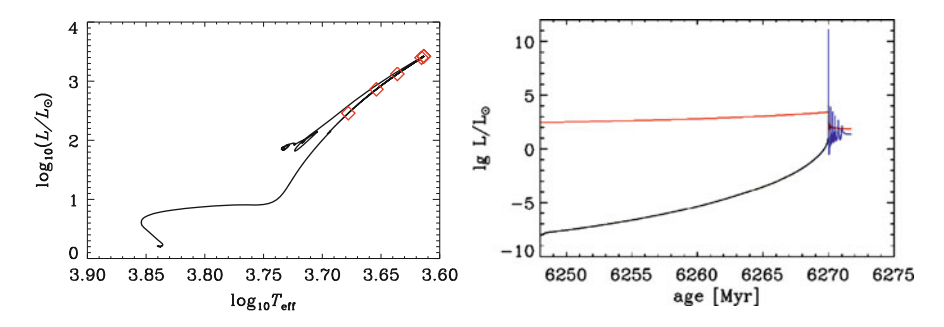
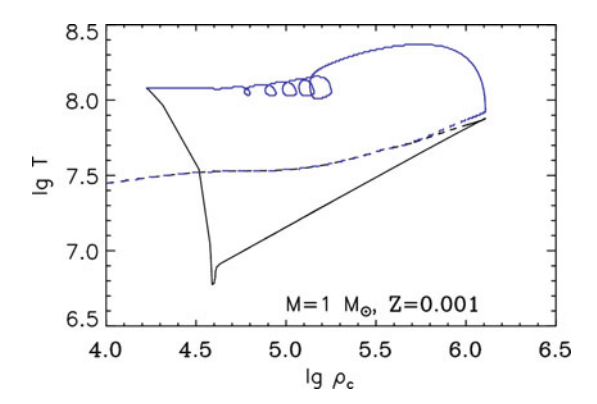


Fig. 2 Left: Evolution of a star of  $1\,M_\odot$  star with Z=0.001 from the main-sequence through the core helium flash to the horizontal branch. Along the RGB the diamonds indicate points where the helium luminosity  $L_{\rm He}/L_\odot$  has reached levels of  $10^{-8}$ ,  $10^{-5}$ ,  $10^{-3}$ ,  $10^{0}$ , and  $10^{10}\,L_\odot$ . The last two points are almost at the same location. Right: The rise of  $L_{\rm He}$  (blue line) with time in comparison with the almost constant total luminosity L during the final stages of the helium flash and the approach to the HB

A. Weiss

Fig. 3 Evolution of central  $(T_c; black, lower curve)$  and maximum  $(T_{max}; blue, upper curve)$  density and temperature during the core helium flash in the same model as in Fig. 2. The evolution proceeds first from left to right, where both curves separate during the flash, then move to the left as the core is expanding and finally meet again after the secondary flashes are over



The right panel shows how  $\log L_{\rm He}/L_{\odot}$  increases during the final stages of the helium flash in comparison to the almost constant total luminosity. The approach to the horizontal branch (HB) is characterized by secondary flashes in the course of the heating of the core and the progression of helium burning from the off-centre ignition shell to the centre. These correspond to the small loops visible in the left plot of the same figure.

The ignition of helium happens off-centre because of three combined effects: (1) the helium core being inert, to first order it is isothermal, and its temperature defined by the hydrogen shell surrounding it. At the tip of the RGB, the shell temperature is  $\log T \approx 7.9$ ; (2) as the core is growing in mass due to the progression of the hydrogen shell, thermal energy is released, since the core, being degenerate, is shrinking in radius and thereby matter is compressed; this creates a positive T-gradient towards the centre; (3) emission of plasma neutrinos is increasingly cooling the core, with two effects: the maximum temperature in the core is limited and helium ignition delayed, and the centre is cooler than outer regions of the core. In consequence, the temperature maximum is at some place outside the centre (typically around a relative mass of 0.1...0.2), but detached from the hydrogen shell. For higher masses, the core being not degenerate, T is increasing towards the centre, and helium is ignited centrally, and at much lower helium core mass because of the lack of efficient neutrino cooling. The evolution of density and temperature at the centre and at the location of maximum temperature during the core helium flash is shown in Fig. 3.

The evolution along the RGB is, for LMSs, determined by the mass of the helium core. Simple homology considerations lead to the global relations

$$L \sim M_c^7; \qquad T \sim M_c; \qquad L \sim \mu^7.$$
 (4)

More detailed considerations, which include M-R-relations for degenerate structures lead to slightly different exponents. These qualitative relations are confirmed by numerical models. The consequence of (4) is that independent of total mass, all LMSs reach helium ignition temperatures at virtually the same core mass and

therefore identical luminosities. This is the reason that the RGB-tip can serve as a standard candle.

On closer inspection,  $M_c$  and L at the RGB-tip do depend slightly on stellar parameters, but also on the input physics, and even on the numerical code used. Salaris and Cassisi (2005) give the following gross dependencies: (1) the core helium mass decreases with increasing metallicity Z by about  $0.001-0.01\,M_\odot$ , and with increasing total mass M by  $0.01\,M_\odot$  (taking a typical range in Z and M for old halo stars); (2) the luminosity  $\log L/L_\odot$  increases with Z by about 0.1 dex and to a lower degree with decreasing mass (0.05 dex). Raffelt and Weiss (1992) give analytical fits to their numerical results:

$$M_c = 0.475 - 0.22(Y_e - 0.25) - 0.01(3 - \log Z) - 0.025(M/M_{\odot} - 0.8)$$
  

$$M_{\text{bol,tip}} = -3^m.27 + 1.1(Y_e - 0.25) - 0.21(3 - \log Z) + 0.30(M/M_{\odot} - 0.8), \quad (5)$$

( $Y_e$  being the helium mass fraction in the envelope). These relations include the effect of mass loss along the RGB.

Recently, Cassisi (2009) showed model comparisons between different codes. The bolometric tip brightness differed by about 0.2 mag for a wide range of metallicities. With the input physics predefined, differences are about half as large, as Weiss (same meeting) demonstrated. Nevertheless, they are at least as important as the global stellar parameters mentioned above.

Updates in input physics have also been the reason for changes in the core mass and luminosity at the RGB-tip. Cassisi et al. (2007) investigated the influence of new conductive opacities and found an almost metallicity-independent decrease in  $\log L/L_{\odot}$  of 0.03 dex for the TRGB, and 0.02 dex for the ZAHB (zero-age HB), when using the new opacities. New nuclear rates for the  $3\alpha$  and  $^{14}{\rm N}(p,\gamma)^{15}{\rm O}$  reactions were tested by Weiss et al. (2005), both rates being now lower than older values. In the first case, luminosity increases by a small amount of  $\approx$ 0.01 dex (helium igniting later), while in the case of the CNO-bottleneck reaction it decreases by  $\approx$ 0.05 dex. This is one of the largest influences on tip quantities found so far.

An open question concerns the possibility of significant mixing episodes besides that by the convective envelope. C. Charbonnel reports about thermohaline mixing between the lower boundary of the convective envelope and the outer regions of the hydrogen burning shell, and M. Mocak (both these proceedings) about the possibility of mixing between core and envelope during the helium flash. So far, such mixing episodes were found only in extreme situations: either in metal-free LMSs (e.g., Schlattl et al. 2002) or in ordinary Pop. II stars with extremely thin envelopes (Cassisi et al. 2003).

After the core helium flash the next phase of low-mass stellar evolution is the (zero-age) horizontal branch, where the core helium burning takes place. The ZAHB luminosity is, within the errors, in agreement with observations, but differs between codes and depending on the implemented physics by about 0.05–0.1 dex in  $\log L/L_{\odot}$  (Cassisi 2009).

82 A. Weiss

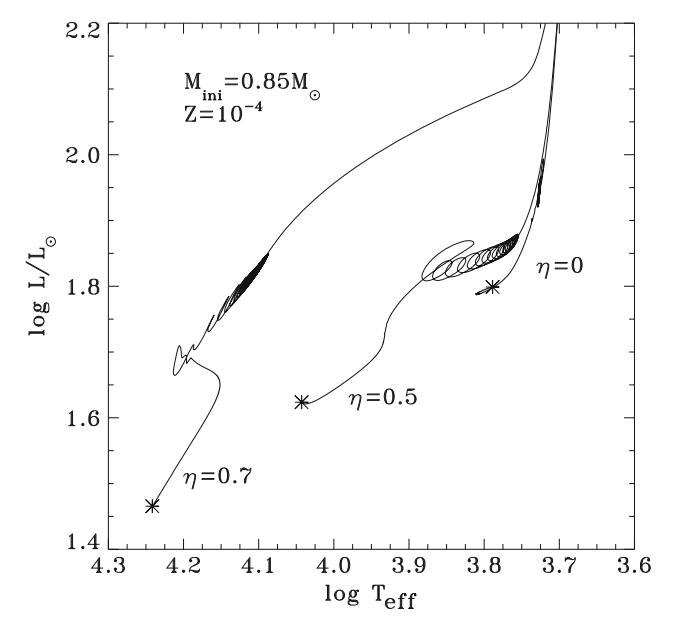


Fig. 4 Horizontal branch evolution for three stellar models (initial mass  $M=0.85\,M_\odot$ ; Z=0.0001), which were followed up the RGB and through the core helium flash with different values of  $\eta$ , the parameter in the Reimers mass loss formula. The tracks start at the ZAHB, indicated by the asterisk

The stars burn helium in a convective core, and evolve, with increasing central CO-abundance and thus molecular weight, to higher luminosities. Whether  $T_{\rm eff}$  inor decreases initially, depends on the contribution of H- and He-burning to the total luminosity. At core helium exhaustion the tracks always turn towards cooler temperatures and up to start the early AGB evolution, unless the envelope mass is extremely low. I show three cases in Fig. 4, taken from Serenelli and Weiss (2005), which are the result of full flash calculations with different degrees of mass loss (according to the Reimers formula, characterized by the parameter  $\eta$ ) along the RGB. With increasing mass loss, the envelope mass on the HB decreases and the stars settle down at increasingly hotter  $T_{\rm eff}$ . The cases shown have HB masses of 0.847, 0.657, and 0.563  $M_{\odot}$ , but, as we saw above, the same core mass. Complications arise due to the retreating convective core, which leaves behind a region of varying molecular weight, which gives rise to semiconvection, an illunderstood secular mixing process. Salaris and Cassisi (2005) describe a method how to treat this in stellar evolution programs. In the case shown in Fig. 4, standard convection and the Schwarzschild-criterion for convective stability was used. This treatment leads to so-called breathing pulses, which are episodes of convection outside the core that result in mixing of fresh helium into the core and the loops visible in the figure. These are most likely artificial effects which disappear, for example, when the Ledoux-criterion for convection is used, since this tends to inhibit convection.

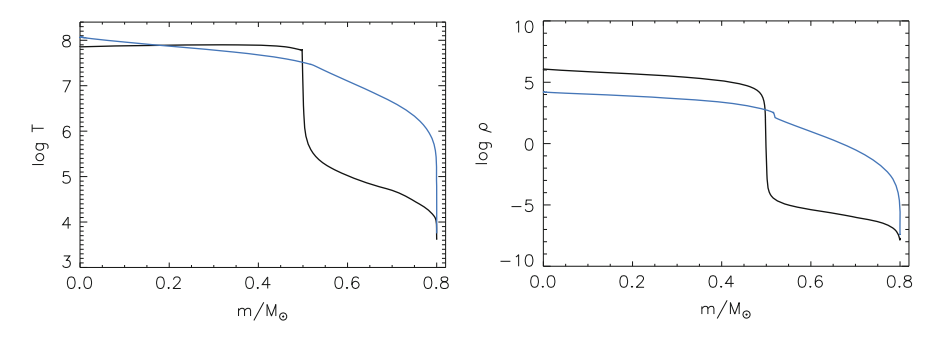


Fig. 5 Temperature (*left*) and density (*right*) profiles in a star of  $0.8 M_{\odot}$  and Z = 0.001 before (*black*) and after (*blue*) the core helium flash

The chemical profile hardly changes from the pre- to the post-flash phase. The helium core increases by at most a few  $1/100~M_{\odot}$ , with a very steep composition gradient being kept. The central carbon abundance increases to levels of 3-5% due to the  $3\alpha$ -reactions taking place during the  $\approx 10^6$  yrs it takes the star to settle down on the ZAHB. Stellar models, which are not followed through the flash, but where the calculations are stopped at the RGB-tip and resumed on the ZAHB, need to change the chemical composition in this respect to be reasonable approximations to full flash calculations (Serenelli and Weiss 2005).

Since the main effect of the core helium flash is the lifting of degeneracy in the core by expansion and heating (see Fig. 3), the T- and  $\rho$ -profiles before and after ignition differ drastically (Fig. 5): Both are now monotonically decreasing and the very steep gradient at the helium core boundary has vanished almost completely (a small step in density is still discernible). Together with the change of a radiative to an adiabatic temperature gradient at the convective core boundary, seismology should be able to detect these differences, and therefore be able to discriminate between pre- and post-flash structures.

# 3 Intermediate-Mass Stars: Quiescent Helium Ignition

Figure 6 (left panel) displays the evolution of luminosities during the helium ignition in a 3  $M_{\odot}$  star. In contrast to LMSs,  $L_{\rm He}$  rises only to moderate levels, which, after some adjustment phase are of the same order as those during the burning phase. The decrease in total luminosity L, which is visible in the HRD of Fig. 1, is solely due to the reduction of the luminosity produced in the H-shell. The rise of  $\log L_{\rm He}/L_{\odot}$  from -2 to 0.6 during ignition takes 2 Myrs in this model. If one compares helium core sizes and luminosities during core helium burning between the 0.85 and 3  $M_{\odot}$  stars of Fig. 1, one finds that they differ by only 0.13  $M_{\odot}$  resp. 0.8 dex. The general run of these quantities with mass can be found in Fig. 5.19 of Salaris and Cassisi (2005): Almost independent of metallicity  $M_c$  it is nearly constant for  $M < 2M_{\odot}$ 

84 A. Weiss

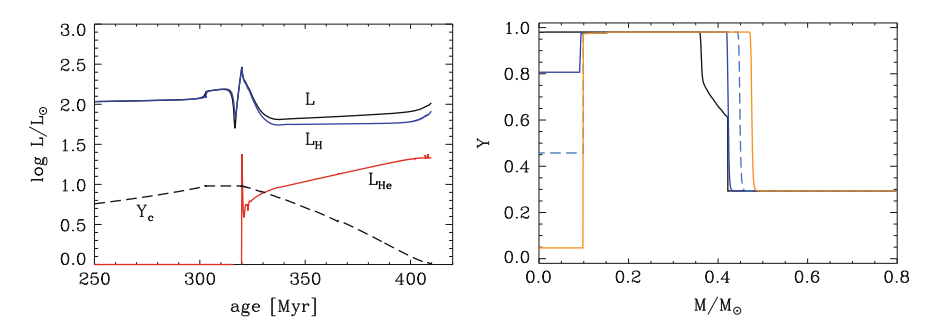
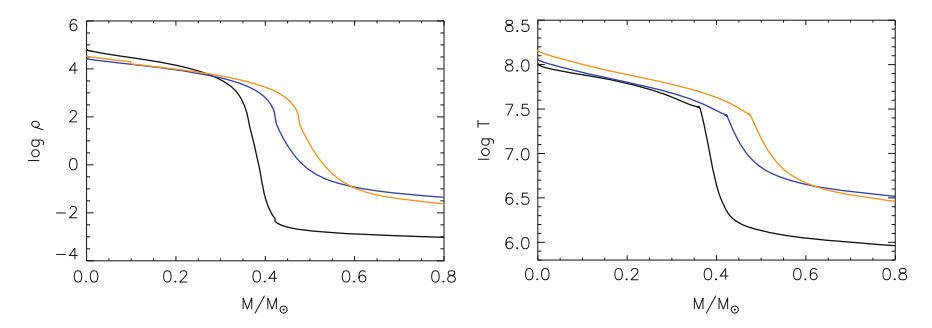


Fig. 6 Left: Total, hydrogen- and helium-luminosity during the ignition of core helium burning in a 3  $M_{\odot}$  star (Z=0.02). The central helium content  $Y_c$  is also shown. Right: Helium abundance inside the core of the same model for four different stages during core helium burning



**Fig. 7** Temperature (*left*) and density (*right*) profiles within the same star as in Fig. 6 before (at the tip of the first RGB ascent; *black line*), during the early (*blue*) and the very late (*red*) phases of core helium burning

(as discussed in Sect. 2), then drops over a rather narrow mass interval to values of about  $0.3\,M_\odot$ . The location and width of the drop depends on metallicity. With increasing mass it then increases almost linearly, reaching the low-mass values again around  $4\,M_\odot$ . Luminosity behaves in a very similar way, but low-mass values are reached again only at much higher mass. This is the reason why at the brightness level of the upper RGB only LMSs are to be expected.

The right panel of Fig. 6 shows the helium profile in the inner  $0.8\,M_\odot$  of the same model for four stages (lines from top to bottom at left edge: black solid, blue solid, cyan dashed, orange solid): before ignition ( $Y_c=0.98$ ), at  $Y_c=0.804$  and 0.458, and finally close to exhaustion ( $Y_c=0.047$ ). The burning core is slightly growing in mass (the calculations were done without overshooting and with the Schwarzschild criterion), while the hydrogen shell is advancing by  $0.12\,M_\odot$  and steepening the chemical profile. In the HRD these phases are at the tip of the red giant phase, during the lower end of the short loop, and on the second red giant ascent.

The temperature and density structure of the same model before, during and at the end of core helium burning is shown in Fig. 7, and should be compared to Fig. 5. The change is not as drastic as in the LMS, and the pre-ignition drop is much less

pronounced. During and after core helium burning the profiles are more similar, but the curvature is different, and the IMS has a broader hydrogen shell. Note that in these figures the same mass range in absolute mass is shown. The outer parts of the  $4 M_{\odot}$  star are not depicted.

A particular feature of IMSs during core helium burning are the *blue loops*, during which they cross the Cepheid intstability strip. These are very sensitive to the detailed structure of the star, in particular of the chemical profile, which is established during the main-sequence (Kippenhahn and Weigert 1990). Differences in the appearance and extension of the loops arise from the treatment of overshooting, semiconvection and rotation.

Figure 8 demonstrates this for a 9  $M_{\odot}$  star and two different chemical compositions. Cases with overshooting included have generally higher luminosities during helium burning (as is the case also during the MS phase), but the loops tend to be reduced, which is quite obvious in the X=0.66, Z=0.03 case. Ignoring overshooting and employing the Schwarzschild criterion for convective instability it may happen that during the final phases of core helium burning regions outside the convective core become convective, too, and fresh helium is mixed into the core, rejuvenating the core and leading to a secondary loop in the HRD. There is an indication of this along the dashed line in the Z=0.03 case, but it is quite evident

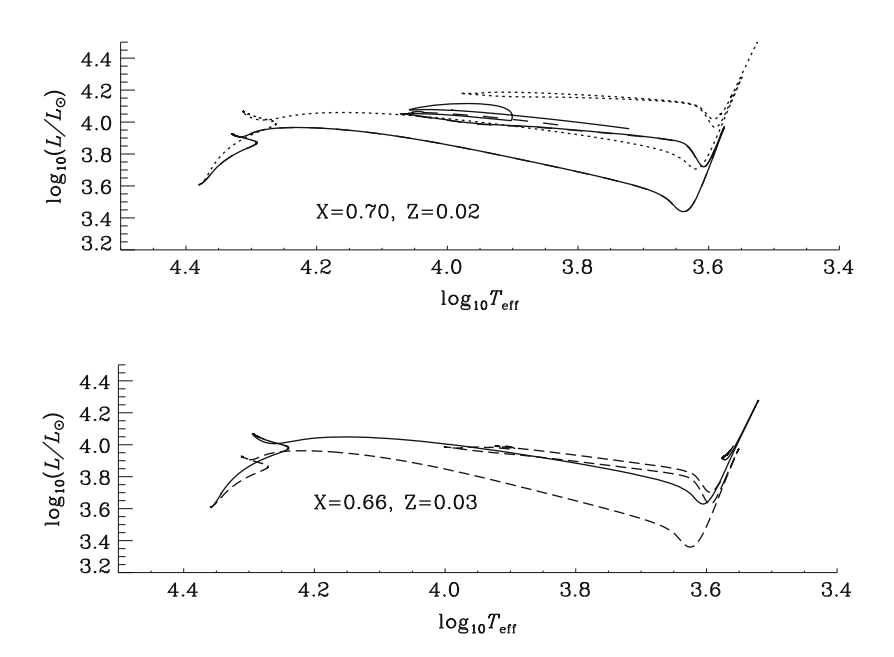


Fig. 8 A star of  $9\,M_{\odot}$  and two different chemical compositions followed from the zero-age main sequence until the end of core helium burning with different treatments of convection. Upper panel (Z=0.02): the solid and dashed line are without overshooting, and a reduced spatial resolution in the latter case, while the dotted line is with overshooting included. Lower panel (Z=0.03): without (dashed) and with (solid) overshooting

86 A. Weiss

in the solid-line track of the upper panel. Here, the "rejuvenation" was provoked by a reduced spatial resolution in the calculation. Notice that apart from this phase during the loop the two tracks with higher and lower numerical resolutions are indistinguishable. A general problem in up-to-date models is that below  $\approx 4\,M_\odot$  they do not display blue loops (see Fig. 1), while observed Cepheids, which can be identified with this phase, have luminosities as low as is appropriate for such masses. There is clearly improvement in the modeling of IMSs before and during helium burning.

#### 4 Summary

Low- and intermediate-mass stars populate similar regions in the HRD before, during and after core helium burning. If  $T_{\rm eff}$  and composition are accurately known, the LMSs can be identified as the cooler objects. If these parameters are not known, low-metallicity pre-flash LMSs may be confused with helium-burning IMSs of higher metallicity. During helium burning LMSs on the HB may also be found in the same HRD-region that is occupied by blue loops of IMSs.

The interior structure at the helium core boundary is clearly different between stars in these two mass ranges, with LMSs generally showing much steeper T and  $\rho$  gradients. This is particularly true for pre-flash objects. This opens the possibility for seismology to discriminate between them. If a LMS and an IMS occupy a similar position in the HRD, their masses should be quite different, such that also first-order seismic scaling laws should be able to discriminate between them. And finally, the IMS will have a convective core, while the low-mass pre-flash star will have a degenerate core.

**Acknowledgements** This work was supported by the Cluster of Excellence EXC 153 "Origin and Structure of the Universe", Garching (http://www.universe-cluster.de).

#### References

Cassisi, S.: Workshop on The Giant Branches. Lorentz Center, Leiden, The Netherlands (2009); www.lorentzcenter.nl

Cassisi, S., Schlattl, H., Salaris, M., Weiss, A.: ApJ Lett. 582, 43 (2003)

Cassisi, S., Potekhin, A.Y., Pietrinferni, A., Catelan, M., Salaris, M.: ApJ 661, 1094 (2007)

Kippenhahn, R., Weigert, A.: Stellar Structure and Evolution. A&A Library. Springer, Heidelberg (1990)

Raffelt, G.G., Weiss, A.: A&A 264, 536 (1992)

Salaris, M., Cassisi, S.: Evolution of Stars and Stellar Populations. Wiley, Chichester (2005)

Schlattl, H., Salaris, M., Cassisi, S., Weiss, A.: A&A 395, 77 (2002)

Serenelli, A., Weiss, A.: A&A 442, 1041 (2005)

Weiss, A., Schlattl, H.: Ap&SS **316**, 99 (2008)

Weiss, A., Serenelli, A., Kitsikis, A., Schlattl, H.: A&A 441, 1129 (2005)

# **Hydrodynamic Simulations of Shell Convection** in Stellar Cores

Miroslav Mocák, Ewald Müller, and Lionel Siess

Abstract Shell convection driven by nuclear burning in a stellar core is a common hydrodynamic event in the evolution of many types of stars. We encounter and simulate this convection (1) in the helium core of a low-mass red giant during core helium flash leading to a dredge-down of protons across an entropy barrier, (2) in a carbon-oxygen core of an intermediate-mass star during core carbon flash, and (3) in the oxygen and carbon burning shell above the silicon-sulfur rich core of a massive star prior to supernova explosion. Our results, which were obtained with the hydrodynamics code HERAKLES, suggest that both entropy gradients and entropy barriers are less important for stellar structure than commonly assumed. Our simulations further reveal a new dynamic mixing process operating below the base of shell convection zones.

#### 1 Introduction

Our knowledge of stellar core convection stems from one-dimensional stellar evolutionary calculations assuming a hydrostatic stellar structure and describing dynamic processes (like, e.g., convection) by local and linear theories (Weiss et al. 2004). This approach is computationally feasible and predicts observables. However, it involves some degeneracy due to necessary utilization of observationally constrained free parameters (Montalbán et al. 2004), which may vary during the star's evolution, and from star to star. One way to check the 1D results is by means

M. Mocák (⋈) · L. Siess

Institute of Astronomy and Astrophysics at the Université Libre de Bruxelles, 1050 Bruxelles, Belgium

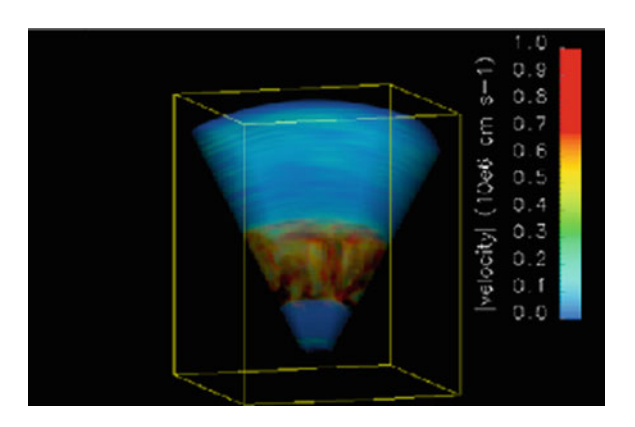
e-mail: mmocak@ulb.ac.be; siess@astro.ulb.ac.be

E. Müller

Max-Planck-Institut für Astrophysik, 85748 Garching bei München, Germany e-mail: ewald@mpa-garching.mpg.de

88 M. Mocák et al

Fig. 1 3D volume rendering of the velocity amplitude of shell convection (red/yellow/green) enclosed between two stable layers (blue) in the helium core during core helium flash



of hydrodynamic simulations which are based on the solution of the Navier-Stokes equations and are essentially parameter free. This approach is computationally demanding, and in our case does not yet predict any observables. Nevertheless, our simulations provide some important insight into intrinsically multidimensional processes connected to core shell convection, like convective overshooting, and mixing across entropy barriers. In particular, they revealed a potentially very important, new mixing process operative below the base of such convection zones.

#### 2 Shell Convection in Stellar Cores

Shell convection in stellar cores occurs in a sandwich-like structure where a dynamically unstable zone sustained by nuclear burning is enclosed by two stable regions above and below (Fig. 1). Besides mixing of chemical species the convective shell redistributes the energy released by nuclear burning and keeps the stellar core in quasi-hydrostatic equilibrium. Such convection typically occurs for instance during:

- 1. Core helium flashes in low-mass red giants (Mocák et al. 2008, 2009, 2010)
- 2. Core carbon flashes of "super-AGB" stars (Siess et al. 2002)
- 3. Shell nuclear burning in massive stars (Meakin and Arnett 2007)
- 4. Thermal pulses of AGB stars (Herwig 2005)

We simulated the first three cases mostly in two but also in three spatial dimensions (2D and 3D simulations, respectively) using initial core structures of metal-rich  $1.25\,M_\odot$  (Mocák et al. 2008),  $9.3\,M_\odot$  star (Siess 2006), and  $23\,M_\odot$  (Meakin and Arnett 2007) stars. None of these simulations led to a violent hydrodynamic event. Initially convection occurred in regions which are unstable according to the Schwarzschild criterion. The convective velocities found in our 3D simulations are close to those predicted by mixing-length theory (MLT). However, our simulations showed an additional non-radial instability at the boundaries of the convection zone,

which allowed convection to penetrate inexorably into the adjacent stable layers, thereby increasing the width of the convection zone on a dynamical timescale. Consequently, core convection driven by nuclear burning covers likely larger regions than predicted by MLT theory.

#### 3 Turbulent Entrainment and Entropy Gradients

Convection is able to generate mixing in neighboring stable layers by convective plumes, which can move into these regions due to their momentum. This process is typically called overshooting and refers to localized events. However, if the frequency of these events is high, entropy can change in the affected stable layers. Hence, we can speak of penetration (Brummell et al. 2002). This occurs due to extensive heat exchange between the penetrating convective plumes and the stable layers. Actually, processes at the edges of convection zones appear to be a combination of both overshooting and penetration. We prefer to call them turbulent entrainment (Fernando 1991) which is well described by the divergence of the buoyancy flux at convection boundaries (Meakin and Arnett 2007). We find turbulent entrainment to operate at convection boundaries in all our hydrodynamic models. We thus conclude that convection zones grow in size during dynamic nuclear flashes (nuclear burning in semi-degenerate gas) when entropy gradients given by canonical 1D stellar calculations cannot withstand turbulent entrainment of stable layers. A direct implication of this result for the core helium flash is the occurrence of a hydrogen injection flash, because the entrainment rates found for the convection zone driven by helium burning in our models are of the order of meters per second. Thus, the upper boundary of the convective shell would reach the overlying hydrogen shell within weeks. This is not predicted for solar metallicity stars (Campbell and Lattanzio 2008) as our initial model. The implications of enlarged convection zones for the core carbon flash in intermediate-mass stars remain unexplored, and the case of the oxygen burning shell in massive stars was studied by Meakin and Arnett (2006, 2007).

### 4 Hydrogen Injection Flash and Mixing Across an Entropy Barrier

Hydrogen injection during the core helium flash is predicted by canonical 1D stellar evolution calculations only for Pop III and extremely metal-poor stars with intrinsic metallicities [Fe/H] < -4]. A similar hydrogen injection phase also occurs:

 At the beginning of the thermally pulsing AGB phase of metal-poor intermediatemass stars (Chieffi et al. 2001; Siess et al. 2002; Iwamoto et al. 2004) 90 M. Mocák et al

• In "Late Hot Flasher" stars experiencing strong mass loss on the RGB (Brown et al. 2001; Cassisi et al. 2003)

We refer to these events as "dual flashes" (Campbell and Lattanzio 2008), since they all experience simultaneous hydrogen and helium flashes. These events often lead to a "splitting" of the initial convection zone driven by helium burning due to dredge-down of material from the above-lying hydrogen-rich envelope and rapid CNO burning.

In order to study this episode by means of hydrodynamic simulations, we designed a special stellar model from the helium core of a metal-rich  $1.25 M_{\odot}$ , where we shifted the hydrogen-rich layers down to the upper edge of the already present helium-burning convection zone. This immediately causes hydrogen to be dredged-down to the hotter layers of the underlying helium-burning convection zone. The results of this first 3D simulation of a dual core flash being driven by hydrogen injection into hot layers of helium-burning convection zone (Fig. 2) are the following:

- Dredge-down of protons across an entropy barrier between the helium-rich layers and the hydrogen shell
- Subtle retreat of the helium-burning convection zone (CVZ-1 in Fig. 2) to smaller radii, and the appearance of a hydrogen-burning convection zone (CVZ-2 in Fig. 2) just above it
- Non-existence of stable radiative layer preventing mixing between the two convection zones, which is in contradiction to 1D stellar evolutionary calculations
- Appearance of the 2nd temperature peak at the base of the hydrogen-burning convection zone, in agreement with 1D stellar evolutionary calculations

We think these results should be qualitatively similar to all dual flash events and to thermal pulses occurring during AGB phase of stars. Hydrodynamic simulations of a thermal pulse with hydrogen mixing into the helium-burning convection zone has already led to improvements in our understanding of Sakurai's object (Herwig et al. 2011).

# 5 A New Dynamic Mixing Process Below the Base of Shell Convection Zones

In our 2D and 3D hydrodynamic models of the core helium and carbon flash, we discovered unreported dynamic mixing process operating at the base of convection zones. The mixing manifests itself by cold and over-dense blobs sinking in the direction of gravity, leaving traces of material with higher mean molecular weight  $\mu$  (Fig. 3). Blobs originate from a layer situated just below the lower edge of the convection zone. We do not see any mixing in our oxygen burning shell models. The driving mechanism of the mixing remains unclear. Possible explanations for the appearance of the sinking cold and dense blobs range from:

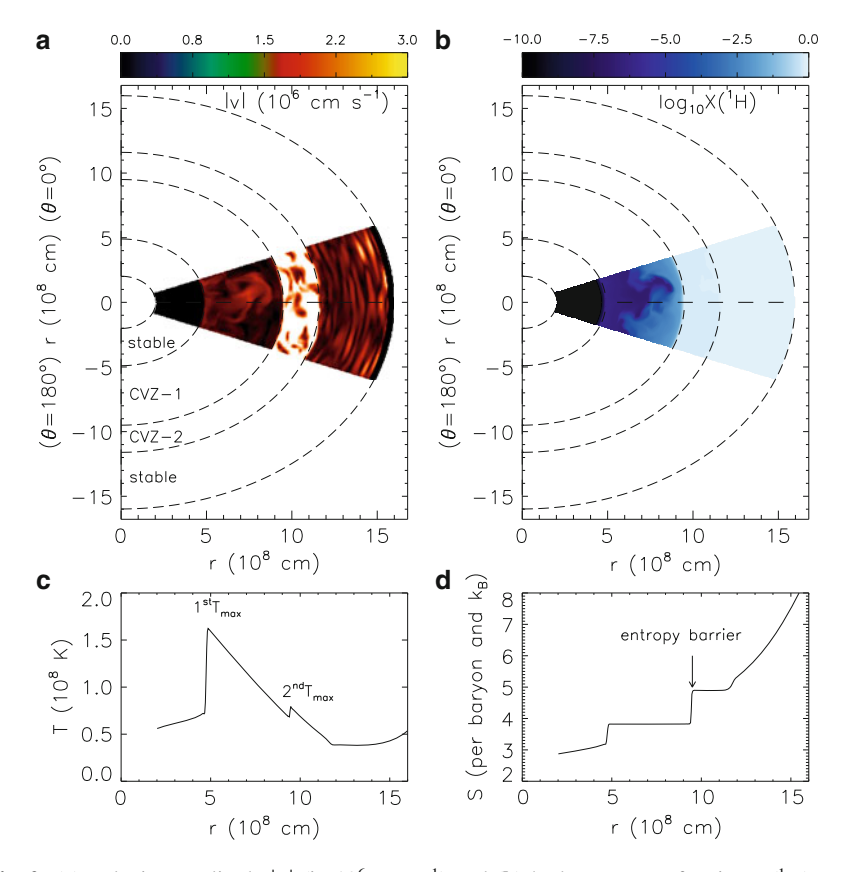


**Fig. 2** (a) Velocity amplitude  $|\mathbf{v}|$  (in  $10^6$  cm s<sup>-1</sup>) and (b) hydrogen mass fraction  $X(^1\mathrm{H})$  at the onset of the hydrogen injection flash in a meridional plane of a 3D simulation. Panels (c) and (d) show the angle-averaged radial distributions of temperature and entropy, respectively, at the same time. The two temperature maxima are denoted as  $1^{\mathrm{st}}T_{max}$  and  $2^{\mathrm{nd}}T_{max}$ , and the entropy barrier is marked by a vertical arrow. Dashed lines enclose distinguished layers, where "CVZ-1" is the convection zone driven by helium burning, "CVZ-2" the convection zone driven by hydrogen burning, and "stable" denotes dynamically stable layers

- The presence of a steep negative mean molecular gradient  $\nabla_{\mu} < 0$  with  $\nabla_{\mu} \equiv d \ln \mu / d \ln P$  (i.e., the molecular weight  $\mu$  decreases in direction of gravity) destabilizing the layers where the mixing starts
- A strong shear creating peculiar turbulence at the convection boundary due to trapped gravity waves excited by convection in the zone above and indicated by a large value of the square of the Brunt-Väisälä frequency N<sup>2</sup>
- A weak dynamic stability of the layers below the convection zone indicated by
  a relatively small positive value of N<sup>2</sup>, which is larger in case of the oxygen
  burning shell model, and hence mixing is effectively suppressed

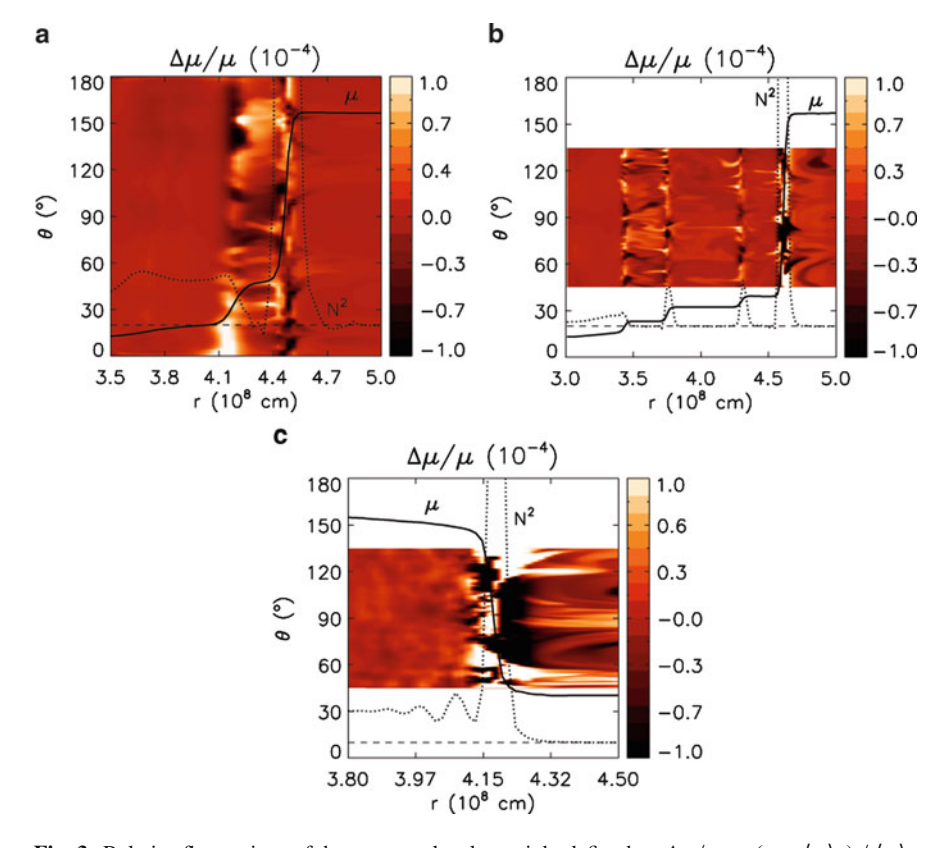


Fig. 3 Relative fluctuations of the mean molecular weight defined as  $\Delta\mu/\mu=(\mu-\langle\mu\rangle_{\theta})/\langle\mu\rangle_{\theta}$  (taken from 2D simulations) below the base of shell convection zones during the (a) core helium flash, (b) core carbon flash, and (c) oxygen burning shell shown together with the radial distributions of the mean molecular weight  $\mu$  (solid) and the square of the Brunt-Väisälä frequency  $N^2$ . The horizontal dashed line corresponds to  $N^2=0$ , and  $\langle \rangle_{\theta}$  denotes the horizontal average at a given radius

 A "turbulence" imitating heat transfer or grid scale diffusion removing heat from patches of gas at the convection zone boundary, hence making some blobs colder and heavy

# 6 Summary

We investigated convection driven by shell nuclear burning during core helium flash in a low-mass star, core carbon flash in an intermediate-mass star, and in the oxygen burning shell in a massive star using data from 2D and 3D hydrodynamic simulations. We find that all convection zones are growing on a dynamic timescale due to turbulent entrainment. This either implies that the convection zones become enlarged or that the physical conditions at the convection zone boundaries inherited from the initial 1D stellar evolutionary models are inconsistent with real conditions in stars. The enlargement of the helium-burning shell convection zone during the core helium flash may lead to a dual core flash by injection of hydrogen into deeper hot layers of the helium core. With our specifically designed initial model for a hydrogen injection flash we show that such an event is possible and the entropy barrier does not prevent mixing of material from the hydrogen shell into the underlying hot helium-burning convection zone. These findings imply that the stabilizing entropy gradients are less important in stars during flash events. In the hydrogen injection flash simulation, we observe the appearance of a second hydrogen-burning shell residing above the already existing helium-burning convection zone. Radiative stable layers separating the two convection shells are not observed. We think, that these finding should be generally valid for all dual flashes. We also found a new dynamic mixing process below the base of shell convection zones manifesting itself by cold and dense blobs sinking in direction of gravity creating eventually finger-like structures. The origin of this mixing is still under investigation.

**Acknowledgements** The simulations were performed at the Rechenzentrum Garching of the Max Planck Society. The authors want to thank Casey Meakin for providing us with an initial model of the oxygen burning shell and valuable discussions. Miroslav Mocák acknowledges financial support from the Communauté française de Belgique – Actions de Recherche Concertées.

#### References

Brown, T.M., Sweigart, A.V., Lanz, T., Landsman, W.B., Hubeny, I.: ApJ 562, 368 (2001)

Brummell, N.H., Clune, T.L., Toomre, J.: ApJ 570, 825 (2002)

Campbell, S.W., Lattanzio, J.C.: A&A 490, 769 (2008)

Cassisi, S., Schlattl, H., Salaris, M., Weiss, A.: ApJ 582, L43 (2003)

Chieffi, A., Domínguez, I., Limongi, M., Straniero, O.: ApJ 554, 1159 (2001)

Fernando, H.J.S.: Ann. Rev. Fluid Mech. 23, 455 (1991)

Herwig, F.: ARA&A 43, 435 (2005)

Herwig, F., Pignatari, M., Woodward, P.R., et al.: ArXiv e-prints (2011)

Iwamoto, N., Kajino, T., Mathews, G.J., Fujimoto, M.Y., Aoki, W.: ApJ 602, 377 (2004)

Meakin, C.A., Arnett, D.: ApJ 637, L53 (2006)

Meakin, C.A., Arnett, D.: ApJ 667, 448 (2007)

Mocák, M., Müller, E., Weiss, A., Kifonidis, K.: A&A 490, 265 (2008)

Mocák, M., Müller, E., Weiss, A., Kifonidis, K.: A&A 501, 659 (2009)

Mocák, M., Campbell, S.W., Müller, E., Kifonidis, K.: A&A 520, A114+ (2010)

Montalbán, J., D'Antona, F., Kupka, F., Heiter, U.: A&A 416, 1081 (2004)

Siess, L.: A&A 448, 717 (2006)

Siess, L., Livio, M., Lattanzio, J.: ApJ 570, 329 (2002)

Weiss, A., Hillebrandt, W., Thomas, H.-C., Ritter, H.: Cox and Giuli's Principles of Stellar Structure. Gardners Books, East Sussex (2004)

# Impact of Rotational Mixing on the Global and Asteroseismic Properties of Red Giants

Patrick Eggenberger, Nadège Lagarde, and Corinne Charbonnel

Abstract The influence of rotational mixing on the global parameters and asteroseismic properties of red giant stars is reviewed. While red giants are generally characterised by low surface rotational velocities, they may have been rotating much more rapidly during the main sequence, so that the rotational history of a star has a large impact on its properties during the red giant phase. For stars massive enough to ignite helium burning in non-degenerate conditions, rotational mixing leads to a significant increase of the stellar luminosity and shifts the location of the core helium burning phase to a higher luminosity in the HR diagram. This results in a change of the seismic properties of red giants and of the fundamental parameters of a red giant star as determined by performing an asteroseismic calibration. For red giants with a lower mass that undergo the helium flash, rotational mixing decreases the luminosity of the bump at solar metallicity changing thereby the global and asteroseismic properties of these stars.

#### 1 Introduction

The wealth of information obtained about the internal structure of the Sun by the observation and interpretation of solar oscillation modes stimulated various attempts to detect solar-like oscillations on other stars. Consequently, many instruments have

P. Eggenberger  $(\boxtimes) \cdot N$ . Lagarde

Observatoire de Genève, Université de Genève, 51 ch. des Maillettes, 1290 Sauverny,

Switzerland

e-mail: patrick.eggenberger@unige.ch; nadege.lagarde@unige.ch

C. Charbonnel

Observatoire de Genève, Université de Genève, 51 ch. des Maillettes, 1290 Sauverny, Switzerland

Laboratoire d'Astrophysique de Toulouse-Tarbes, CNRS UMR 5572, Université de Toulouse, 14 av. E. Belin 31400 Toulouse, France

e-mail: corinne.charbonnel@unige.ch

96 P. Eggenberger et al.

been recently developed to perform such asteroseismic studies. From the ground, the stabilized spectrographs have reached the accuracy needed to detect and characterise solar-like oscillations on stars other than the Sun, while space missions have been recently designed to perform very high accuracy photometric measurements of these oscillation modes. Solar-like oscillations are not restricted to solar-type stars, but are expected in any star exhibiting a convective envelope able to stochastically excite pressure modes of oscillations. In the case of red giants, solar-like oscillations have been first detected for a few stars (see e.g. Frandsen et al. 2002; Barban et al. 2004; De Ridder et al. 2006; Barban et al. 2007), while clear identifications of non-radial oscillations have then been obtained for a large number of red giant stars with the CoRoT space mission (De Ridder et al. 2009) and the Kepler satellite (Bedding et al. 2010). These observations stimulated population studies aiming at reproducing the distribution of global asteroseismic properties of red giant stars (Miglio et al. 2009a,b), as well as the theoretical study of the asteroseismic properties of red giants and of the effects of various physical processes on the modelling of these stars (Dupret et al. 2009; Eggenberger et al. 2010c; Montalbán et al. 2010). Rotation being one of the key processes that has an important impact on stellar physics and evolution (Maeder 2009), we briefly review here its effects on the global and asteroseismic properties of red giants.

#### 2 Effects of Rotation on Evolutionary Tracks

Stellar models computed with and without the inclusion of shellular rotation (Zahn 1992) are compared in order to discuss the influence of rotation on the evolution and global properties of red giant stars. We discuss first the evolution of stars massive enough to start helium burning in non-degenerate conditions, and then the evolution of low mass red giants undergoing the helium flash.

#### 2.1 Intermediate-Mass Stars

The effects of rotation on the global properties of red giants massive enough to ignite He burning in non-degenerate conditions are illustrated by computing the evolution of a 3  $M_{\odot}$  star with and without rotation using the Geneva stellar evolution code (Eggenberger et al. 2008). The solar chemical composition given by Grevesse and Noels (1993) is used together with a solar calibrated value for the mixing-length parameter. No overshooting from the convective core into the surrounding radiatively stable layers is included. Figure 1 compares the evolutionary track of the non-rotating model with that of a rotating model computed with exactly the same input parameters except for an initial velocity of  $150\,\mathrm{km\,s^{-1}}$  on the zero age main sequence (ZAMS).

We see that evolutionary tracks in the HR diagram are significantly affected when rotational effects are taken into account. During the main sequence, we first note a slight decrease of the luminosity for the rotating model compared to the model without rotation at the beginning of the main-sequence evolution, while the increase of the luminosity of the rotating model becomes more and more pronounced as evolution proceeds. In particular, the model including rotation has a larger luminosity than the standard one during the post-main sequence phase of evolution. The location of the core helium-burning phase, which is the phase during which the star spends most of its lifetime as a red giant, is then shifted to larger luminosity when rotational effects are included.

We recall here that rotational effects can be basically divided in two main categories: (1) the effects resulting from changes in the chemical and internal structure induced by rotational mixing and (2) the effects resulting from hydrostatic corrections due to the centrifugal force. At the beginning of the main sequence, only hydrostatic effects of rotation are observed. The effective gravity of the rotating model is then slightly reduced compared to the non-rotating model so that the resulting evolutionary track is similar to the one of a non-rotating star computed with a slightly lower initial mass. This explains the small decrease in luminosity and effective temperature observed near the ZAMS for the model including rotation in Fig. 1. As the star evolves on the main sequence, the effects related to rotational mixing plays however a more and more important role by bringing fresh hydrogen fuel in the stellar core and transporting helium and other H-burning products in the radiative zone. Rotational mixing thus increases the size of the convective core and changes the chemical composition profiles in the radiative zone. This induces an increase of the luminosity together with a widening of the main sequence when rotation is included in the computation (see Fig. 1). The changes observed in the

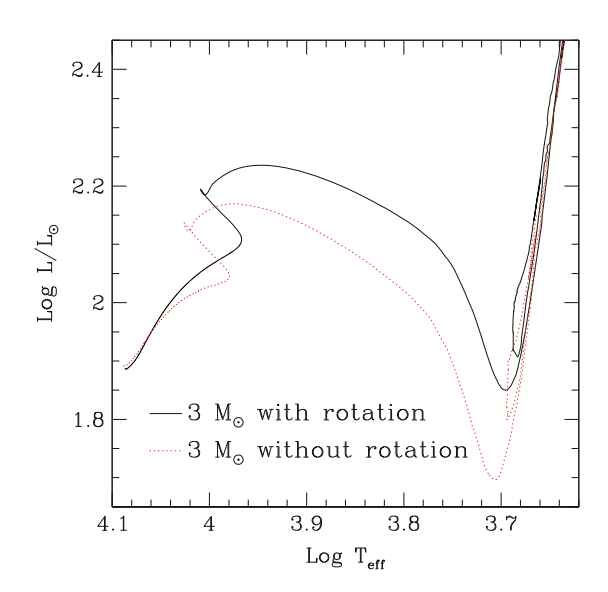


Fig. 1 Evolutionary tracks in the HR diagram for 3 M<sub>☉</sub> models computed with (*continuous line*) and without (*dotted line*) shellular rotation

98 P. Eggenberger et al.

tracks are thus mainly due to rotational mixing with only a very limited contribution from the effects of the centrifugal force at the very beginning of the main sequence. This can be explained by recalling that the kinetic rotational energy of the  $3 \, \mathrm{M}_{\odot}$  star is much lower than its gravitational energy.

Rotational mixing has also an important influence on stellar ages. The value of the central abundance of hydrogen at a given age is indeed larger for the rotating model than for the non-rotating one. This is due to the transport of hydrogen in the deep stellar layers, which leads to an enhancement of the main-sequence lifetime for rotating models compared to standard models. For the  $3\,M_\odot$  model considered here with an initial velocity of  $150\,km\,s^{-1}$ , this corresponds to an increase of the age of about 10%.

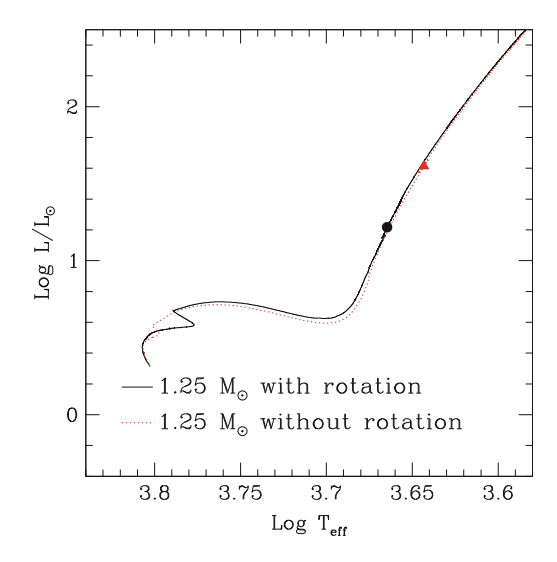
As far as the evolution of the surface rotational velocity is concerned, a slow decrease is first obtained during the main sequence; starting with an initial velocity of  $150\,\mathrm{km\,s^{-1}}$  on the ZAMS, a velocity of  $115\,\mathrm{km\,s^{-1}}$  is reached at the end of the main sequence for the  $3\,\mathrm{M}_\odot$  star presented here. A very rapid decrease of the surface velocity then occurs when the star crosses the Hertzsprung gap. The exact value of the surface velocity during the red giant phase is sensitive to the assumption made on the rotation law in the extended convective envelope of the star. By assuming solid body rotation or uniform specific angular momentum in the external convective zone, a mean value of the surface rotational velocity of about 6 and  $0.3\,\mathrm{km\,s^{-1}}$  is respectively found during the red giant phase. For both limiting assumptions on the rotation law in the external convective zone, a model computed with a significant value for the initial rotational velocity on the ZAMS thus exhibits a low surface rotational velocity as a red giant. This shows that a slowly rotating red giant may have been rotating much more rapidly during the main sequence and that its global properties depend on its rotational history.

#### 2.2 Low-Mass Stars

The impact of rotational mixing on low-mass red giants that undergo the helium flash at the RGB tip is now briefly discussed by comparing  $1.25\,M_\odot$  models with and without rotation. These models are computed with the evolution code STAREVOL (Charbonnel and Lagarde 2010) at solar metallicity, with an initial velocity on the ZAMS of  $110\,\mathrm{km\,s^{-1}}$  for the rotating case. The corresponding evolutionary tracks are shown in Fig. 2.

During the evolution on the main sequence, the inclusion of rotational effects results in slightly larger effective temperatures and luminosities. For these models with a lower mass and a small convective core, this shift is mainly due to the fact that rotational mixing counteracts the effects of atomic diffusion in the external layers of the star (Eggenberger et al. 2010b). Larger values of helium abundance are then found at the surface of models including rotation, which leads to a decrease of the opacity in the external layers of the star. As for the more massive  $3\,M_{\odot}$  models described above, the influence of rotational mixing is not restricted to the

Fig. 2 Evolutionary tracks in the HR diagram for  $1.25\,\mathrm{M}_\odot$  models computed with (continuous line) and without (dotted line) shellular rotation. The dot and triangle indicate the location of the bump for the rotating and non-rotating model, respectively



external layers of the star, since the properties of the central layers are changed due to the transport of fresh hydrogen fuel into the stellar core. Consequently, the main-sequence lifetime is larger when rotation is accounted for. Contrary to the case of intermediate-mass red giants discussed in Sect. 2.1, the location in the HR diagram of the core helium burning phase is now very similar for models computed with and without rotational effects. However, rotational mixing has a large impact on the location of the bump. At solar metallicity, the inclusion of rotation leads indeed to a significant decrease of the luminosity of the star at the bump and to an increase of its effective temperature (see Fig. 2 and Charbonnel and Lagarde 2010).

## 3 Effects of Rotation on Asteroseismic Properties of Red Giants

Red giant stars are characterised by deep convective envelopes and dense cores. From an asteroseismic point of view, the large density near the center of the star leads to huge values of the Brunt-Väisälä frequency in the central layers. Consequently, oscillation modes of mixed p-mode and g-mode properties are expected. In addition to purely acoustic radial modes, a large number of non-radial modes are then found, which are in most cases dominated by the g-mode behaviour and have therefore a high inertia. However, for non-radial modes trapped in the acoustic cavity the inertia becomes similar to the one of radial modes. For  $\ell=2$  modes, the separation between the p- and g-mode region is sufficient to obtain oscillation modes which in terms of inertia are very similar to purely acoustic modes. This results in trapped  $\ell=2$  modes with a dominant amplitude close to every radial mode, which define the small separation between  $\ell=0$  and  $\ell=2$  modes

P. Eggenberger et al.

(see e.g. Christensen-Dalsgaard 2004). This basic description of the properties of oscillation modes in red giant stars is solely based on inertia consideration and does not take into account the problem of excitation and damping of these modes (see e.g. Dziembowski et al. 2001; Dupret et al. 2009).

#### 3.1 Intermediate-Mass Stars

We now discuss the effects of rotation on the properties of the oscillation modes of these stars. This is first done by comparing the asteroseismic properties of rotating and non-rotating models at the same evolutionary phase computed with the same input parameters (except for the inclusion of shellular rotation). A rotating model of  $3\,\mathrm{M}_\odot$  computed with an initial velocity of  $150\,\mathrm{km\,s^{-1}}$  on the ZAMS and situated in the middle of the core helium-burning phase ( $Y_c=0.355$ ) is then compared to the corresponding non-rotating red-giant model. The theoretical low- $\ell$  frequencies of both models are computed and the values of the large and small frequency separations are obtained. The values of the large separation are calculated from the radial modes, while the small separations between  $\ell=0$  and  $\ell=2$  modes are determined by considering only  $\ell=2$  modes well trapped in the acoustic cavity.

Rotational effects lead to a significantly lower value of the mean large separation. The rotating model exhibits indeed a mean large separation that is about 20% lower that the one of the non-rotating model. The mean large separation being mainly proportional to the square root of the star's mean density, this difference is directly related to the larger radius of the rotating model (both models share the same mass of  $3 \, \mathrm{M}_{\odot}$ ). This larger radius is a direct consequence of the significant increase of the luminosity discussed in the preceding sections when rotational mixing is included in the computation. The value of the mean small frequency separation between radial modes and  $\ell=2$  modes trapped in the acoustic cavity of the star is also found to be significantly reduced when rotational effects are taken into account. For stars evolving on the main sequence, the ratio of the small to large separation is sensitive to the conditions in the central regions of the star (Roxburgh and Vorontsov 2003; Roxburgh 2005). In the case of red giant models, the decrease of the values of the small and large separation when rotation is included is similar, so that the ratio between the small and large separation remains approximately the same for rotating and non-rotating models. This shows that the decrease of the small separation between  $\ell = 0$  and trapped  $\ell = 2$  modes observed for rotating models is mainly due to the change of the global stellar properties and not to a change in the structure of the central regions of the star (Eggenberger et al. 2010c; Montalbán et al. 2010).

In addition to the comparison between rotating and non-rotating models computed with the same initial parameters, it is also interesting to discuss the impact of rotation on the determination of the fundamental stellar parameters and asteroseismic properties for red giants sharing the same location in the HR diagram. This is done by computing another model with approximately the same luminosity as the non-rotating red giant stars of  $3\,\mathrm{M}_\odot$  during the core helium-burning phase. Since rotational mixing increases the stellar luminosity, such a rotating model is obtained

for a lower mass of  $2.7\,M_{\odot}$ . The lower initial mass of models including rotation leads to a large increase of the age determined for a red giant. This illustrates how rotational mixing changes the global stellar parameters needed to reach the same location in the HR diagram for core helium-burning stars.

The change of the global stellar parameters induced by rotation also results in differences in the asteroseismic properties between rotating and non-rotating models of red giants sharing the same location in the HR diagram. The rotating 2.7  $M_{\odot}$  model is then characterised by a lower value of the mean large separation than the  $3\,M_{\odot}$  non-rotating model. This directly reflects the different masses of both models, which lead to different mean densities and hence mean large frequency separations. The mean small frequency separation between radial and  $\ell=2$  modes trapped in the acoustic cavity of the star is also found to decrease when rotational effects are taken into account. As mentioned above, this is mainly due to the change of the global stellar properties (the stellar mass in this case) for models computed with rotation compared to non-rotating models and not to differences in the structure of the central stellar layers.

#### 3.2 Low-Mass Stars

The global asteroseismic properties of a rotating (initial velocity of 110 km s<sup>-1</sup> on the ZAMS) 1.25 M<sub>☉</sub> red-giant model at the bump and the corresponding nonrotating model situated at the same evolutionary stage are finally compared. As noted above, the values of the large separation are calculated from the radial modes, while the small separations between  $\ell = 0$  and  $\ell = 2$  modes are determined by considering only  $\ell = 2$  modes well trapped in the acoustic cavity of the star. For lowmass red giants at the bump, the inclusion of rotation results in a large increase of the mean value of the large separation, which is directly related to the smaller radius of the rotating model. As seen in Sect. 2.2, a rotating model of 1.25 M<sub>☉</sub> at solar metallicity is characterised by a lower luminosity and a larger effective temperature at the bump than a model without rotation. This leads to a smaller radius and hence a larger mean density and large frequency separation when rotational effects are taken into account. As for more massive red giant models, this change of the global stellar properties also results in a change of the mean small frequency separation between radial modes and trapped  $\ell=2$  modes with a significant increase of the small separation for rotating red giants.

### 4 Summary

The surface rotation velocity of a red giant star is generally low, but the star may have been rotating much more rapidly during the main sequence. The evolution in the red giant phase is then sensitive to the rotational history of the star, because P. Eggenberger et al.

rotation significantly changes its internal structure and global properties during the main sequence. Rotational mixing is the main driver of the changes of the evolutionary tracks in the HR diagram, with only a very limited contribution from hydrostatic corrections induced by rotation. For red giants massive enough to ignite He burning in non-degenerate conditions, rotational mixing shifts the location of the core helium burning phase to higher luminosity in the HR diagram, while for low-mass red giants undergoing the helium flash the luminosity at the bump is significantly reduced when rotation is included in the computation. This of course results in different global asteroseismic properties for red giant models with and without rotation and changes the values of the fundamental stellar parameters (in particular the mass and age of the star) determined from an asteroseismic calibration. In addition to these effects of rotation on the global asteroseismic properties, it will be interesting to study in detail the effects of rotational mixing on asteroseismic observables that are more sensitive to changes in the structure near the central core like the small separation between radial and dipole modes (Montalbán et al. 2010). Asteroseismic data coming from ground-based observations and space missions are thus particularly valuable to provide us with new insight into transport processes in stellar interiors like rotation, magnetic fields (e.g. Eggenberger et al. 2010a), and internal gravity waves (e.g. Charbonnel and Talon 2005).

**Acknowledgements** Part of this work is supported by the Swiss National Science Foundation and by the French Programme National de Physique Stellaire (PNPS) of CNRS/INSU.

#### References

```
Barban, C., de Ridder, J., Mazumdar, A., et al.: ESA Special Publication. In: Danesy, D. (ed.) SOHO 14 Helio- and Asteroseismology: Towards a Golden Future, vol. 559, p. 113 (2004)
```

Barban, C., Matthews, J.M., de Ridder, J., et al.: A&A 468, 1033 (2007)

Bedding, T.R., Huber, D., Stello, D., et al.: ApJ 713, L176 (2010)

Charbonnel, C., Lagarde, N.: A&A 522, A10 (2010)

Charbonnel, C., Talon, S.: Science 309, 2189 (2005)

Christensen-Dalsgaard, J.: Sol. Phys. 220, 137 (2004)

De Ridder, J., Barban, C., Carrier, F., et al.: A&A 448, 689 (2006)

De Ridder, J., Barban, C., Baudin, F., et al.: Nature **459**, 398 (2009)

Dupret, M., Belkacem, K., Samadi, R., et al.: A&A 506, 57 (2009)

Dziembowski, W.A., Gough, D.O., Houdek, G., Sienkiewicz, R.: MNRAS 328, 601 (2001)

Eggenberger, P., Meynet, G., Maeder, A., et al.: Ap&SS 316, 43 (2008)

Eggenberger, P., Maeder, A., Meynet, G.: A&A 519, L2 (2010a)

Eggenberger, P., Meynet, G., Maeder, A., et al.: A&A 519, A116 (2010b)

Eggenberger, P., Miglio, A., Montalban, J., et al.: A&A 509, A72 (2010c)

Frandsen, S., Carrier, F., Aerts, C., et al.: A&A 394, L5 (2002)

Grevesse, N., Noels, A.: In: Prantzos, N., Vangioni-Flam, E., Casse, M. (eds.) Origin and evolution of the elements: Proceedings of a symposium in honour of H. Reeves, Paris, 22–25 June 1992,

p. 14. Cambridge University Press, Cambridge (1993)

Maeder, A.: Physics, Formation and Evolution of Rotating Stars. Springer, Berlin (2009)

Miglio, A., Montalbán, J., Baudin, F., et al.: A&A 503, L21 (2009a)

Miglio, A., Montalbán, J., Eggenberger, P., Hekker, S., Noels, A.: American Institute of Physics Conference Series, vol. 1170, In: Guzik, J.A., Bradley, P.A. (eds.) American Institute of Physics Conference Series, pp. 132–136 (2009b)

Montalbán, J., Miglio, A., Noels, A., Scuflaire, R., Ventura, P.: ApJ 721, L182 (2010)

Roxburgh, I.W.: A&A 434, 665 (2005)

Roxburgh, I.W., Vorontsov, S.V.: A&A 411, 215 (2003)

Zahn, J.-P.: A&A 265, 115 (1992)

# **3D Picture of the Convective Envelope of a Rotating RGB Star**

Ana Palacios

**Abstract** We present here a brief review of the efforts made in the last years to understand the interplay between rotation and convection in the deep envelopes of red giant stars via 3D hydrodynamical simulations.

#### 1 Introduction

Rotational data collected across the HR diagram in the form of  $\upsilon \sin i$  or rotation periods suggest that the angular momentum distribution changes in stars as they evolve. The evolution of angular momentum distribution in stellar interiors affects that of the nuclides through the transport processes that develop in rotating fluids. This, in turn, can have a non-negligible impact on the nucleosynthesis and evolution of stars (Maeder 2009). Understanding the global picture of stellar evolution thus implies that of the angular momentum evolution at each evolutionary phase.

The best way to constrain the distribution of angular momentum would be to have direct information on the internal angular velocity profile at all stages, as can be given by seismology. Such information is already available down to the core edge in the Sun (García et al. 2011), but all other stars, and stellar evolutionary phases are yet to be investigated.

A phase of particular interest for the evolution of low- and intermediate-mass stars is the red giant phase. At this stage the convective envelope may occupy more than 90% of the total stellar radius, that will reach several hundreds of the solar radius. Numerous abundance anomalies (Lattanzio and Tout 2006), complex

A. Palacios (⋈)

LUPM, Université Montpellier 2 cc 72 – Place Eugène Bataillon – 34095 Montpellier cedex, France

CEA/DSM/IRFU/SAp, L'Orme des Merisiers bât 709, 91191 Gif-sur-Yvette, France e-mail: ana.palacios@univ-montp2.fr

nuclesoynthesis (see Mowlavi 2002, for a review) and usually slow rotation (de Medeiros 2004) characterize the red giants on the RGB and on the AGB, that trace internal mixing processes, hence the importance of a good understanding and modelling of the transport of angular momentum in the convective envelopes of these stars.

As of today, the mixing length theory with a parameter calibrated on the Sun and solid-body rotation is assumed in 1D stellar evolution models of red giants, and very few work has been devoted to 3D simulations of their extended convective regions (Woodward et al. 2003; Steffen and Freytag 2007; Palacios and Brun 2007; Brun and Palacios 2009).

In the following we will present a brief summary of the recent work published on the description of convection in deep stellar convective envelopes with special emphasis on the results obtained with the ASH code by Brun and Palacios (2009).

#### 2 Astrophysical Context

As mentioned in the introduction, there are several observational hints of the redistribution of angular momentum within the stars as they evolve through the red giant phase. On the main sequence, low and intermediate-mass stars exhibit a large panel of rotation velocities according to their mass and evolutionary status. The more massive (A-F type) and less evolved stars (G-type) present surface  $v \sin i$  in the range 50 km s<sup>-1</sup> to about 150 km s<sup>-1</sup>, and the low-mass more evolved stars (Gtype older than 1 Gyr) all exhibit lower rotation, as can be seen from data collected in open clusters (Meibom et al. 2011). Later on the first ascent of the red giant branch, the large increase of the radius and modest mass loss should lead to a dramatic decrease of the surface velocity, which is actually observed for most of the stars at all metallicities (de Medeiros 2004; Cortés et al. 2009). Further on, for those stars experiencing central He burning (red clump and horizontal branch stars),  $v \sin i$  as high as  $40 \,\mathrm{km \, s^{-1}}$  have been observed in the red horizontal branch of globular clusters and the field at low metallicity, while such rapid rotators do not exist for  $T_{eff} > 11,000 \,\mathrm{K}$  (Recio-Blanco et al. 2004; Cortés et al. 2009). Stars in more advanced evolutionary stages exhibit slow rotation, in particular white dwarfs (Berger et al. 2005) indicating that transport and losses of angular momentum shall have occurred in the previous phases (Charpinet et al. 2009).

All these points reveal a complex evolution of the distribution of angular momentum inside low- and intermediate-mass stars, and the evolution inside metal-poor RGB stars is of particular interest considering the puzzling distribution of surface velocities among horizontal branch stars. On this point, Sills and Pinsonneault (2000) proposed that in order to reproduce the rotation velocity of HB stars considering that the progenitors of these stars on the red giant branch had almost zero surface rotation, a large amount of angular momentum should be retained in the inner part of the stars during the RGB ascension. This can be achieved if RGB convective envelopes rotate differentially (Chanamé et al. 2005).

Differential rotation in RGB convective envelopes should also have an impact on the rotation profile in the underlying radiative zone, and this will affect the efficiency of transport processes associated with rotation in this region (Palacios et al. 2006). In the absence of direct observational constraints and/or clear theoretical prescriptions (solid-body rotation and uniform specific angular momentum have been proposed as equally justified by Tayler 1973), 3D hydrodynamical simulations may bring some important clues.

#### 3 The Simulations

#### 3.1 Existing Non-Rotating Hydrodynamical Simulations

The study of turbulent convection in rotating media requires global 3-D simulations of convection in spherical geometry, which is both computationally very demanding and difficult to achieve due to the large number of scales that have to be represented. It is only in the last two decades that such an approach was made possible, in particular thanks to the development of massively parallel computer architectures. Concerning the convection realized in extended envelopes of red giant stars, 3-D hydrodynamical simulations of the convection in a red supergiant star (Freytag et al. 2002, "star-in-a-box" experiment; hereafter FSD02) and in AGB stars (e.g., FSD02, Woodward et al. 2003, hereafter WPJ03) have been performed using fully compressible codes. These simulations do not include rotation and present as a common feature the development of pulsations without any  $\kappa$ -mechanism. The convective pattern presents a dipolar configuration in WPJ03 (see Fig. 1) and Steffen and Freytag (2007), hereafter SF07, which is also present in simulations of non-rotating fully-convective white dwarfs (Kuhlen et al. 2006). This dipolar nature can be related to the fact that in a convective shell, the  $\ell=1$  mode is for

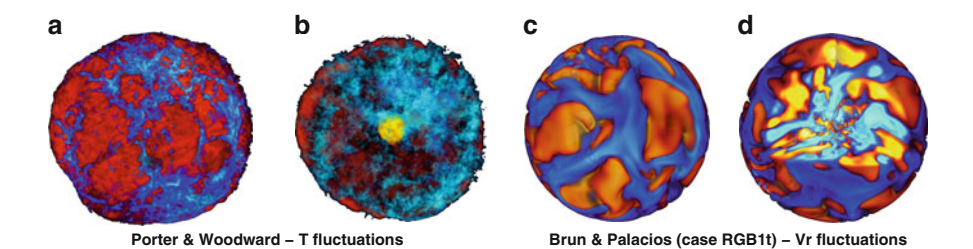


Fig. 1 3D rendering of the convective patterns in terms of of the temperature perturbations  $(\mathbf{a} - \text{full view} \text{ and } \mathbf{b} - \text{meridional cut})$  and convective radial velocity fluctuations  $(\mathbf{c} - \text{full view})$  and  $\mathbf{d} - \text{with extracted octant})$  in 3D hydrodynamical simulations of a non-rotating red giant by Porter and Woodward (unpublished) and of a moderately rotating RGB star (case RGB1t in Brun and Palacios 2009) respectively. *Reddish color* is for warm upgoing flows and blueish for cool downgoing flows

108 A. Palacios

small aspect ratio, one of the most unstable modes to excite, as first emphasized by Chandrasekhar (1961).

In all these non-rotating simulations, the convective pattern achieved consists of a small number of large cells covering the surface, the number of which increases with resolution: large warm up-going flows are surrounded by narrow cooler down-going structures.

## 3.2 Simulations of the Rotating Convective Envelope of an RGB Star

SF07 also presented rotating "star-in-a-box" experiments. They use scaling relations to mimic the rotation of the red supergiant Betelgeuse that exhibits a rotation period of about 17 years for a radius of about 1,750  $R_{\odot}$ . They find no striking difference in the convective pattern compared to their non-rotating case. Concerning rotation, they find a strong differential rotation (see Fig. 2), which is anti-solar in latitude, and very strong meridional circulation flows, comparable to typical convective velocities.

Parallel to this work Palacios and Brun (2007) and Brun and Palacios (2009) used the ASH code (Brun and Toomre 2002; Miesch et al. 2006; Browning et al. 2004)

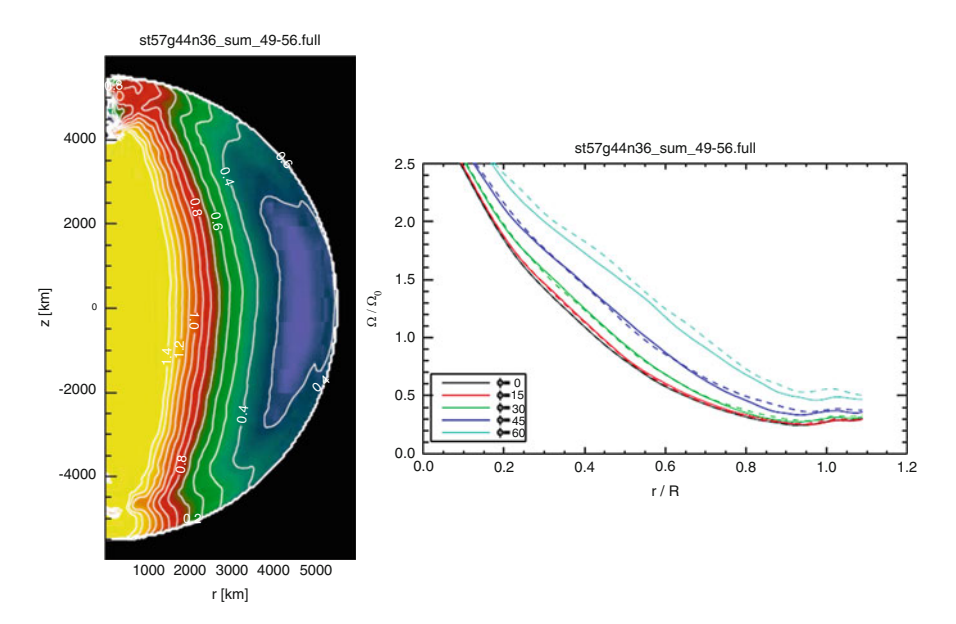


**Fig. 2** Differential rotation for the fully convective rotating min-sun experiment from Steffen and Freytag (2007). Color displays  $\Omega(s, z)$  overplotted with  $\Omega$  contours while the *right panel* shows the  $\Omega$  radial profile at several latitudes. Adapted from Steffen and Freytag (2007)

to compute the first direct hydrodynamical simulations of the inner half (density contrast of 100, aspect ratio of 10 in radius) of the extended convective envelope of a low-mass metal-poor RGB star ( $R_{\star}=39R_{\odot},\,L=425L_{\odot}$ ), based on the thermodynamical structure as computed by a 1D stellar evolution code (see Brun and Palacios 2009 for details). They considered four different cases: two different bulk rotations (case A @ 1/10th solar and case B @ 1/50th solar) and for each of these, two different values for the Reynolds number (300 or 800) in order to test the stability of their results against this parameter.

#### 3.2.1 Convection: Energy Budget and Patterns

Whatever the bulk rotation considered, the convective instability sets in during the first 100 days of the simulation and then undergoes non-linear saturation. It subsequently reaches a statistical equilibrium that is maintained over the later evolution of the simulation. The simulations are thus considered to be relaxed (even though the model is still marginally evolving toward complete thermal equilibrium). The convective patterns that develop are shown in Fig. 3 after respectively 10 and 6 rotation periods of overall evolution for the moderatly rotating (A) and slowly rotating (B) cases.

The turbulent convection achieved in these simulations is characterized by large warm up-flows surrounded by cool narrower downflows at the top edge of the computational domain similar to that observed in the non-rotating simulations previously described (see also Fig. 1). In case of very slow rotation (1/50th solar corresponding to  $2 \, \mathrm{km \, s^{-1}}$  at the stellar surface) the number of cells is considerably reduced, and convection is strongly bipolar, with a warm and a cool side that are clearly distinct. This pattern resembles that obtained in non-rotating simulations

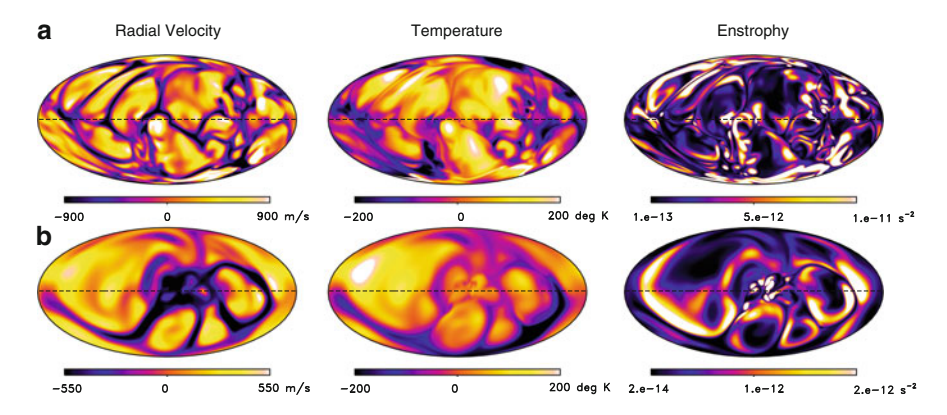


Fig. 3 Convective patterns represented by the radial velocity  $V_r$  (left column), the temperature T (central column) and the enstrophy (right column) variations at the top edge of the computational domain ( $R = 19 \, \mathrm{R}_{\star}$ ) for cases A (first row) and B (second row)

110 A. Palacios

(Woodward et al. 2003; Kuhlen et al. 2006), indicating that for such slow rotation rates, rotation is not efficient in stabilizing the convection.

In both cases, the strong correlation between radial velocity and temperature variations appearing in the maps results in an outward transport of heat. Due to the large luminosity of the star, the velocity and temperature fluctuations are very large (at least one order of magnitude larger than those found in the simulations of the solar convective envelope) as can be seen on Fig. 3. The even larger fluctuations that appear in slowly rotating case (lower row in Fig. 3) underline the stabilizing role of rotation (when significant) that leads to a less vigorous convective flow.

The convective luminosity is found to be significantly larger than the star's luminosity. This is to compensate a negative kinetic energy luminosity that can represent up to 120% of the total energy flux. This negative kinetic energy flux results from the strong asymmetry between up-flows and downflows in the bulk of the domain. This is an important result that contradicts the assumption of the mixing length theory, that assumes that the total and convective luminosity are equal.

In the bulk of our simulations, the kinetic energy density (KE) is dominated by convection, and the meridional circulation contributes significantly to the total energy (about 10% in both cases). This is clearly different than for the solar case, where the contribution of meridional circulation to the averaged total KE is less than 1%. When the kinetic energy in the meridional circulation (MCKE) is smaller than that in the differential rotation (DRKE), the meridional circulation pattern consists of one poleward cell per hemisphere. In case of very slow bulk rotation, MCKE > DRKE and this pattern changes turns into a unique cell crossing the equator, and being equatorward in the northern hemisphere. In that case, the slow rotation leads to a reduced rotational constrain on the flow. Forming axisymmetric averages around the axis of rotation may, in this case, lead to large fluctuation in the resulting averaged quantity by the simple misalignment of the large scale flow with respect to that axis (i.e the meridional flow may drift in latitude and longitude making it difficult to project into the meridional plane). The typical amplitudes of these large-scale circulations are one or two orders of magnitude larger than what is found in the Sun (about 20 m s<sup>-1</sup> at the solar surface). The turnover time for the meridional circulation in both cases is much longer that the typical convection turnover time (3.5 years vs. 150 days for mildly rotating case).

## 4 Angular Momentum

In this extended convective envelope, our choice of stress-free velocity boundaries ensures that no torque is applied to the system, and that angular momentum is conserved in the convective shell. In turbulent convection zones, the angular momentum is redistributed by various physical processes, which are in turn, viscous diffusion, Reynolds stresses, and mean large scale circulations. We may identify the contribution to the transport of angular momentum of each process by considering the mean radial  $(\mathcal{F}_r)$  and latitudinal  $(\mathcal{F}_\theta)$  angular momentum fluxes.

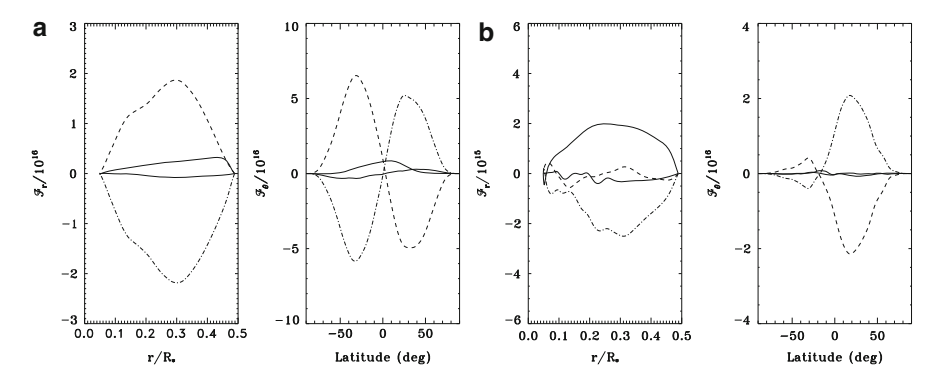
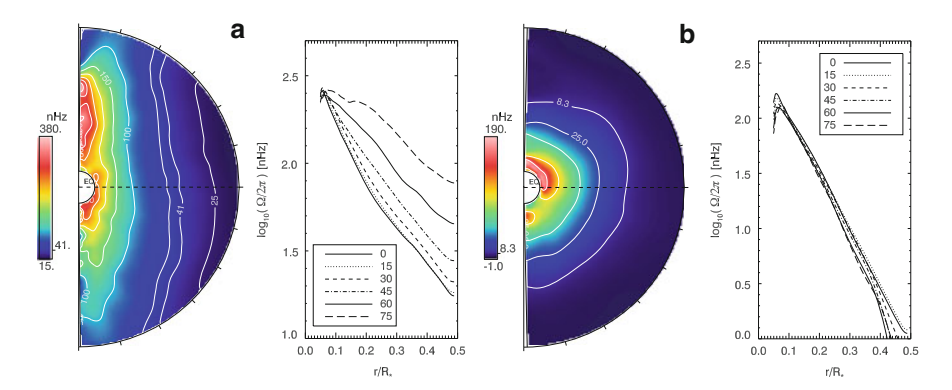


Fig. 4 Time average of latitude line integral of the angular momentum flux  $\mathscr{F}_r$  and of the radial line integral of the angular momentum  $\mathscr{F}_\theta$  for cases A (*left panels*) and B (*right panels*). Viscous (*dashed-triple-dotted*), Reynolds stresses (*dashed-dotted*) and meridional circulation (*dashed*) contributions are represented together with the total fluxes (*solid*). Positive values indicate outward radial flux and northward latitudinal flux. Averages are over 12 and 6 rotation periods for cases A and B respectively

The expressions of these fluxes are given in Brun and Toomre (2002). Figure 4 presents these integrated averaged fluxes along co-latitude and radius for case A and case B respectively. We may first note the good quality of the angular momentum balance characterized by the solid lines, that is very close to zero (e.g. no net flux) when averaging over the entire length of the simulations. In the latitudinal direction, the meridional circulation flux compensates that of the Reynolds stresses, with a poleward transport in the northern hemisphere. The viscous transport is negligible. In the radial direction, the pictures differs in both cases. In the slowly rotating case (B) meridional circulation and Reynolds stresses are of opposite sign, but the viscous flux has the same amplitude and sign as meridional circulation flux, and plays an important role in the flux balance. This is associated with a shellular rotation achieved in this case (see Fig. 5). In the mildly rotating case (A), the balance in the radial directions resembles that in latitudinal direction: meridional circulation acts to transport the angular momentum outward, and is compensated by the Reynolds stresses (associated with  $< v_r'v_\phi' >$ ). The viscous flux is negligible in this case.

The redistribution of angular momentum in the convective shell results in a strong departure from the initial solid-body rotation regime. The rotation achieved is substantially different according to the bulk angular velocity adopted as can be seen in Fig. 5. This behaviour has also been reported by Steffen and Freytag (2007) in their rotating "star-in-a-box" experiments that mimic Betelgeuse.

For case A,  $\Omega_0$  corresponds to the largest value observed for red giant stars (namely  $7\,\mathrm{km\,s^{-1}}$ , this being a maximum value for the  $v\sin i$  measured in RGB tip stars de Medeiros 2004). A strong differential rotation is found in both radial and latitudinal directions ( $\Delta\Omega/\Omega_0$  between 0° and 60° near the top of the domain close to 60%). The poles rotate faster than the equator (anti-solar rotation) and the inner and outer regions rotate in opposite directions.  $\Omega$  contours are aligned with the



**Fig. 5** 2D plots Temporal and longitudinal average of the angular velocity profile in cases A (*left*) and B (*right*). *1D plots* Radial profiles for selected latitudes (0,15,30,45,60,75 degrees) for cases A and B

rotation axis, resulting in an almost cylindrical pattern that might be attributed to the mild degree of turbulence of the simulation or to the absence of a strong latitudinal entropy contrast (Miesch et al. 2006).

For a slower bulk rotation (B) better characterizing the actual rotation velocities determined in RGB stars, a strong shellular rotation is found: shells rotating as solid-bodies pile-up with increasing radial velocity towards the center. This leads to the large viscous transport found in the radial direction and to a more subtle balance of angular momentum. *Independently of their latitudinal angular velocity profiles both models possess a strong radial differential rotation*.

## 5 Conclusions and Perspectives

In order to clarify the distribution of angular momentum in the deep convective envelopes of red giant stars, we have performed direct 3D hydrodynamical simulations of the inner part of the convective envelope of a low-mass RGB star. We have explored the parameter space by considering two bulk rotation rates and different degrees of turbulence for the convection, two of these models are presented here. The rotation rate appears to be crucial in determining both the convective pattern and the angular momentum redistribution. The convective patterns obtained for the slower case are comparable to those obtained for non-rotating simulations by Woodward et al. (2003) and Steffen and Freytag (2007), presenting a strong bipolar character. For an associated surface rotation velocity of about  $2\,\mathrm{km\,s^{-1}}$ , the angular momentum redistribution leads to shellular rotation in the spherical shell, with a strong differential rotation in the radial direction. When rotation rate is increased (as in case A), the  $\ell=1$  mode does not dominate turbulent convection anymore, and the convective pattern becomes more complex. In this case, we observe the development and maintenance of a large cylindrical differential rotation within the

inner part of the convective envelope of the RGB star. *This regime contradicts the assumption of solid body rotation assumed in stellar evolution modeling*. It could be of great importance for the global redistribution of angular momentum and chemical species in the underlying radiative region.

Due to the natural limitation of such simulations as far as the characteristics of the flow are concerned (Reynolds Re and Prandtl Pd numbers in particular), and to difficulty to explore the parameter space at length because of the greed of such computations, the results presented here, and in particular the quantitative values should be considered cautiously. However, the finding of similar configurations for the distribution of the angular momentum by two distinct approaches (CO5BOLD and ASH codes) is very encouraging and qualitatively supports the results.

Much work remains to be done from the simulation point of view, and much is expected from observational constraints that are becoming available. Zeeman-Doppler Imaging and latitudinal differential rotation reconstruction via spectropolarimetry on one hand, and asteroseismic constraints on the other hand are to give much anticipated constraints in the near future.

#### References

Berger, L., Koester, D., Napiwotzki, R., Reid, I.N., Zuckerman, B.: A&A 444, 565 (2005)

Browning, M.K., Brun, A.S., Toomre, J.: ApJ 601, 512 (2004)

Brun, A.S., Palacios, A.: ApJ 702, 1078 (2009)

Brun, A.S., Toomre, J.: ApJ 570, 865 (2002)

Chanamé, J., Pinsonneault, M., Terndrup, D.M.: ApJ 631, 540 (2005)

Chandrasekhar, S. (ed.): Hydrodynamic and hydromagnetic stability (1961)

Charpinet, S., Fontaine, G., Brassard, P.: Nature 461, 501 (2009)

Cortés, C., Silva, J.R.P., Recio-Blanco, A., et al.: ApJ **704**, 750 (2009)

de Medeiros, J.R.: IAU Symposium. In: Maeder, A., Eenens, P. (eds.) Stellar Rotation, vol. 215, p. 144 (2004)

Freytag, B., Steffen, M., Dorch, B.: Astron. Nachr. 323, 213 (2002)

García, R.A., Salabert, D., Ballot, J., et al.: J. Phys. Conf. Ser. 271, 012046 (2011)

Kuhlen, M., Woosley, S.E., Glatzmaier, G.A.: ApJ 640, 407 (2006)

Lattanzio, J.C., Tout, C.A.: EAS Publications Series. In: Montmerle, T., Kahane, C. (eds.) EAS Publications Series, vol. 19, pp. 189–197 (2006)

Maeder, A. (ed.): Physics, Formation and Evolution of Rotating Stars (2009)

Meibom et al. ApJ **733**, 115 (2011)

Miesch, M.S., Brun, A.S., Toomre, J.: ApJ 641, 618 (2006)

Mowlavi, N.: IAU Symposium. In: Nomoto, K., Truran, J.W. (eds.) Cosmic Chemical Evolution, vol. 187, pp. 57–69 (2002)

Palacios, A., Brun, A.S.: Astron. Nachr. 328, 1114 (2007)

Palacios, A., Charbonnel, C., Talon, S., Siess, L.: A&A 453, 261 (2006)

Recio-Blanco, A., Piotto, G., Aparicio, A., Renzini, A.: A&A 417, 597 (2004)

Sills, A., Pinsonneault, M.H.: ApJ 540, 489 (2000)

Steffen, M., Freytag, B.: Astron. Nachr. 328, 1054 (2007)

Tayler, R.J.: MNRAS 165, 39 (1973)

Woodward, P.R., Porter, D.H., Jacobs, M.: Astronomical Society of the Pacific Conference Series. In: Turcotte, S., Keller, S.C., Cavallo, R.M. (eds.) 3D Stellar Evolution, vol. 293, p. 45 (2003)

# **Effects of Rotation and Thermohaline Mixing** in Red Giant Stars

Corinne Charbonnel, Nadège Lagarde, and Patrick Eggenberger

**Abstract** Thermohaline mixing has been recently identified as the probable dominating process that governs the photospheric composition of low-mass bright giant stars [Charbonnel and Zahn, A&A467, L15 (2007)]. Here we present the predictions of stellar models computed with the code STAREVOL including this mechanism together with rotational mixing. We compare our theoretical predictions with recent observations.

#### 1 Introduction

The standard theory of stellar evolution predicts that the convective envelope of low-mass stars deepens in mass during the contraction of the degenerate He-core after the main sequence turnoff, and engulfes hydrogen-processed material (the so-called first dredge-up, hereafter 1dup). This induces a decrease of the surface  $^{12}$ C/ $^{13}$ C ratio and of the Li and  $^{12}$ C abundances, while  $^{14}$ N and  $^{3}$ He abundances increase. After the 1dup, the convective envelope retracts and the hydrogen burning shell (HBS) moves outward (in mass). According to the standard theory, no further change of the surface chemical properties is expected after the 1dup on the Red Giant Branch (RGB). However, spectroscopic observations (Gilroy 1989; Gilroy and Brown 1991; Luck 1994; Gratton et al. 2000; Tautvaišiene et al. 2000; Tautvaišiene et al. 2005;

Observatoire de Genève, Université de Genève, 51 ch. des Maillettes 1290 Versoix, Switzerland

Laboratoire d'Astrophysique de Toulouse-Tarbes, CNRS UMR 5572, Université de Toulouse, 14 av. E.Belin 31400 Toulouse, France e-mail: Chabonnel.Corinne@unige.ch

N. Lagarde · P. Eggenberger

Observatoire de Genève, Université de Genève, 51 ch. des Maillettes, 1290 Versoix, Switzerland Lagarde.Nadege@unige.ch; Patrick.Eggenberger@unige.ch

C. Charbonnel (⋈)

116 C. Charbonnel et al.

Smith et al. 2002; Shetrone 2003; Pilachowski et al. 2003; Geisler et al. 2005; Spite et al. 2006; Recio-Blanco and de Laverny 2007; Smiljanic et al. 2009) show clear signatures of "extra-mixing" on the upper RGB in low-mass stars, when the HBS crosses the discontinuity left behind by the 1dup at the bump luminosity. More specifically, the carbon isotopic ratio and the C and Li abundances drop again as the stars move across the bump. Different processes have been proposed to explain these abundance anomalies. Here we recall the potential impact of rotation-induced mixing and thermohaline instability on the RGB.

#### 2 Rotation-Induced Mixing

Rotation-induced mixing has an impact on the internal abundance profiles of chemicals involved in hydrogen-burning while the stars are on the main sequence (Talon and Charbonnel 1998, 2010; Charbonnel and Talon 1999; Palacios et al. 2003; Pasquini et al. 2004; Smiljanic et al. 2009; Charbonnel and Lagarde 2010). This can be seen in Fig. 1 where we present the chemical structure at the end of the main sequence for  $1.25 \ M_{\odot}$  stellar models computed assuming different initial rotation velocities. In the rotating models, the abundance gradients are smoothed out compared to the standard (i.e., non-rotating) case:  $^{3}$ He,  $^{13}$ C,  $^{14}$ N, and  $^{17}$ O diffuse outwards, while  $^{12}$ C and  $^{18}$ O diffuse inwards. After the turnoff, this reflects in different post-dredge up predictions for the surface abundances that agree well with observations in low-luminosity red giant stars (see Fig. 2). However, rotation-induced mixing does not explain the abundance anomalies observed in low-mass red giants brighter than the bump (Chanamé et al. 2005; Palacios et al. 2006).

## 3 Thermohaline Mixing

Charbonnel and Zahn (2007) identified thermohaline mixing as the process that governs the photospheric composition of low-mass stars above the bump on the RGB. At this evolutionary phase, this double diffusive instability is induced by the <sup>3</sup>He(<sup>3</sup>He; 2p)<sup>4</sup>He reaction (Eggleton et al. 2006) that creates an inversion of mean molecular weight (Ulrich 1971). Here we use the following prescription for the turbulent diffusivity coefficient (Ulrich 1972; Kippenhahn et al. 1980):

$$D_{t} = C_{t} K\left(\frac{\varphi}{\delta}\right) \frac{-\nabla_{\mu}}{(\nabla_{ad} - \nabla)} \quad \text{for } \nabla_{\mu} < 0, \tag{1}$$

$$C_t = \frac{8}{3}\pi^2\alpha^2,\tag{2}$$

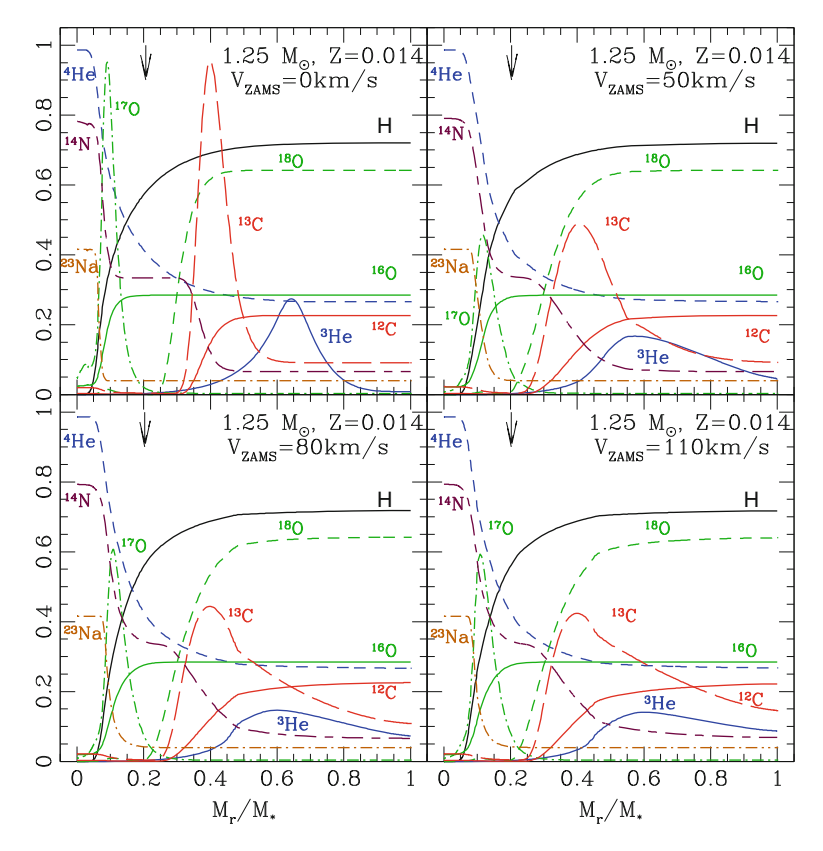


**Fig. 1** Chemical structure at the turnoff of a 1.25  $M_{\odot}$  star computed for different initial rotation velocities as indicated. The mass fractions are multiplied by 100 for  $^{3}$ He,  $^{12}$ C, and  $^{14}$ N, by 2,500 for  $^{13}$ C, by 50, 900, and 5×10<sup>4</sup> for  $^{16}$ O,  $^{17}$ O, and  $^{18}$ O respectively, and by 1,500 for  $^{23}$ Na. The *vertical arrows* show, in all cases, the maximum depth reached by the convective envelope at its maximum extent during the 1dup. Figure from Charbonnel and Lagarde (2010)

with K the thermal diffusivity and  $\alpha = 5$  the aspect ratio of salt fingers (Ulrich 1972). At the RGB bump and above, the thermohaline diffusion coefficient is several order of magnitudes higher than the total diffusion coefficient related to rotation-induced processes (Charbonnel and Lagarde 2010).

## 4 Model Predictions and Comparisons to Observations

The results shown in this section are presented and discussed in detail in Charbonnel and Lagarde (2010) and have been computed with the code STAREVOL including rotation-induced processes and thermohaline mixing. Here we briefly discuss the

118 C. Charbonnel et al.

effects of rotation-induced mixing and thermohaline mixing on carbon isotopic ratio, lithium and <sup>3</sup>He.

#### 4.1 Carbon Isotopic Ratio

In Fig. 2 we compare the evolution of the theoretical surface carbon isotopic ratio for 1.25  $M_{\odot}$  models with observations in M67 stars by Gilroy and Brown (1991). We note that rotation-induced mixing on the main sequence slightly lowers the post-dredge-up  $^{12}C/^{13}C$  value (see Sect. 2). On the other hand, thermohaline mixing leads to further decrease of the carbon isotopic ratio at the luminosity of the bump  $(\log(L/L_{\odot}) \sim 2)$ , in excellent agreement with M67 data.

In Fig. 3 we show the predictions for the surface <sup>12</sup>C/<sup>13</sup>C ratio at the tip of the RGB and at the end of second dredge-up (black and blue lines respectively) for models over a large mass range and compare them with observations in stars belonging to open clusters of various turnoff masses. We see that in stars with

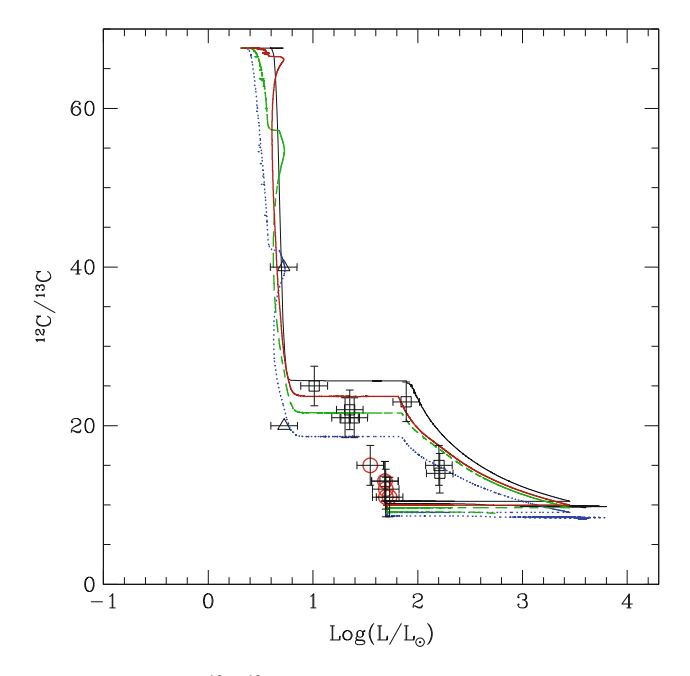


Fig. 2 Evolution of the surface  $^{12}$ C/ $^{13}$ C ratio as a function of stellar luminosity for models of 1.25 M $_{\odot}$  stars. Different tracks are for different initial rotation velocities (non-rotating case, 50, 80, and 110 km s $^{-1}$  respectively in *black, red, green*, and *blue*). Observations by Gilroy and Brown (1991) in evolved stars of the open cluster M67 (turnoff mass  $\sim$ 1.2 M $_{\odot}$ ) are also shown (*triangle, squares*, and *circles* for subgiant, RGB, and clump stars respectively). Figure from Charbonnel and Lagarde (2010)

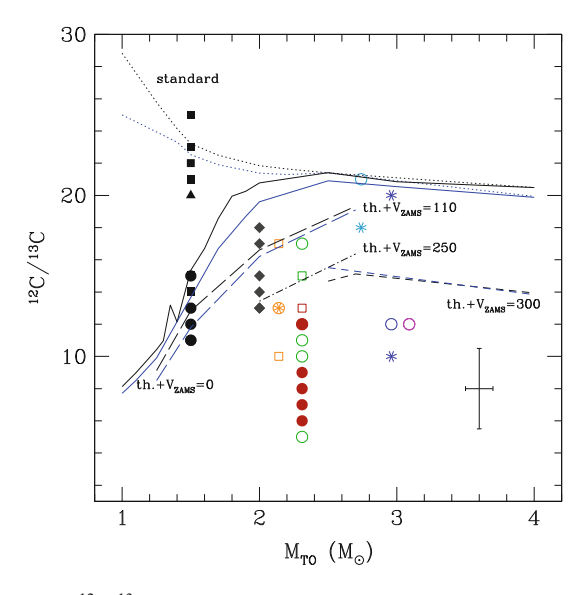


Fig. 3 Observations of  $^{12}C/^{13}C$  in evolved stars of Galactic open clusters by Smiljanic et al. (2009), Gilroy (1989), Gilroy and Brown (1991), and Mikolaitis et al. (2010) as a function of the turnoff mass of the corresponding host cluster. Squares, circles, and asterisks are for RGB, clump, and early-AGB stars respectively, while diamonds are for stars from Gilroy (1989) sample with doubtful evolutionary status; triangles are for lower limits. A typical error bar is indicated. Theoretical predictions are shown at the tip of the RGB and after completion of the second dredge-up (black and blue lines respectively). Standard models (no thermohaline nor rotation-induced mixing) are shown as dotted lines, models with thermohaline mixing only ( $V_{\rm ZAMS} = 0$ ) as solid lines, and models with thermohaline and rotation-induced mixing for different initial rotation velocities as indicated as long-dashed, dot-dashed, and dashed lines. Figure from Charbonnel and Lagarde (2010)

masses below  $\sim\!2\,M_\odot$ , thermohaline mixing is the main physical process governing the photospheric composition of evolved giants, although the final carbon isotopic ratio also slightly depends on rotation-induced mixing on the main sequence. In intermediate-mass stars that do not reach the bump on the RGB and do not undergo thermohaline mixing at that phase, rotation is necessary to explain the data and accounts for star-to-star abundance variations at a given evolutionary status. Overall, the present models explain very well the observed abundance patterns over the considered mass range.

#### 4.2 Lithium

In Fig. 4 we present lithium data for field red giant stars with metallicities around solar and precise determination of their evolutionary status, and compare them to predictions for models of various masses. Contrary to the standard case, rotation-induced mixing leads to Li depletion on the main sequence (see e.g. Talon and

120 C. Charbonnel et al.

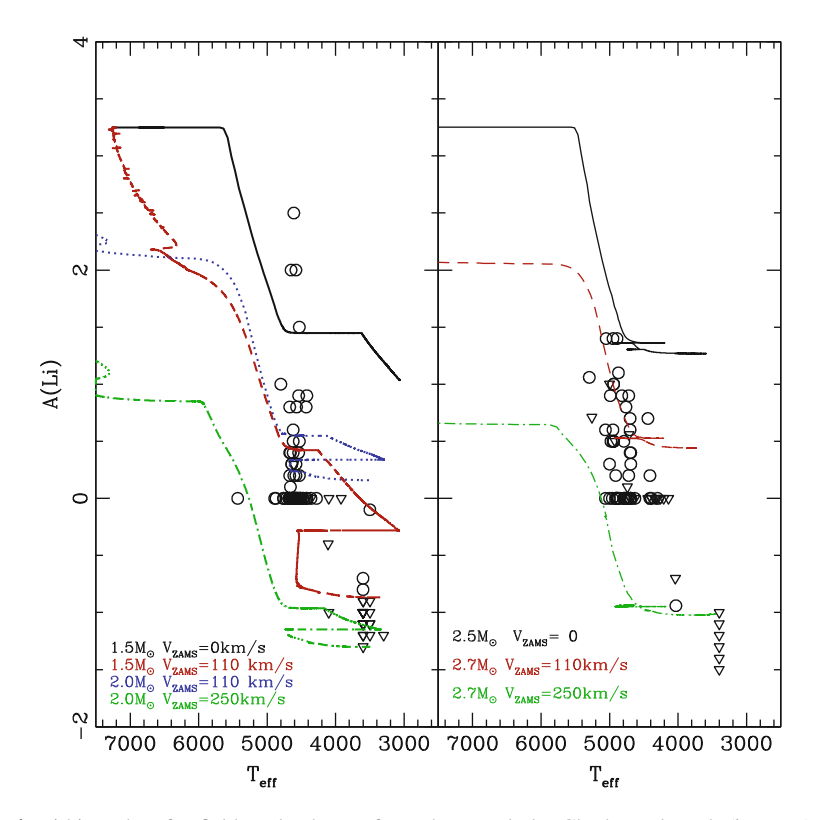
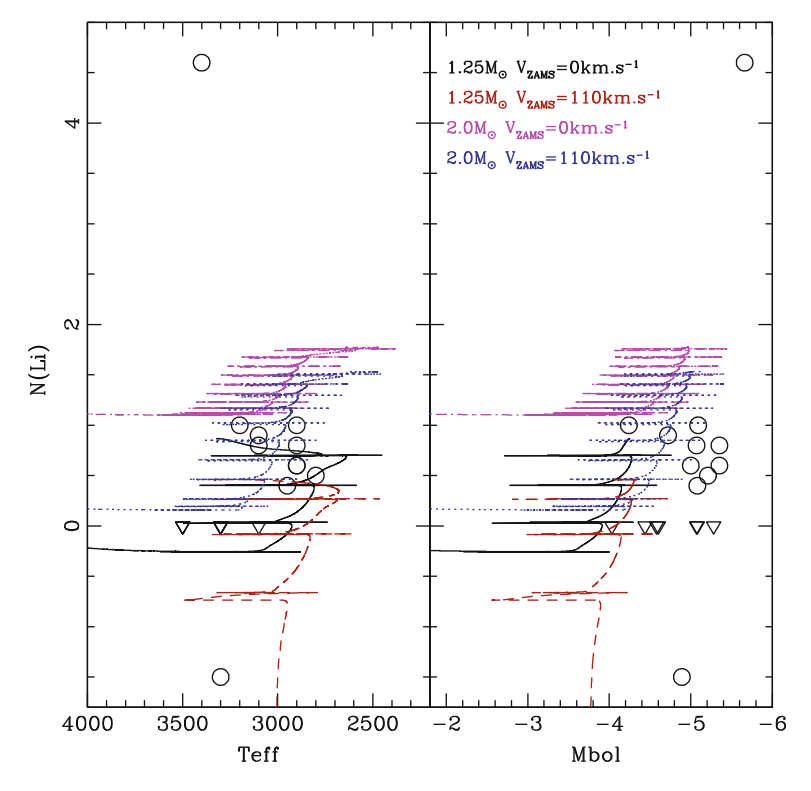


Fig. 4 Lithium data for field evolved stars from the sample by Charbonnel et al. (in prep.) that are segregated according to their mass (*left* and *right panels* include respectively sample stars with masses lower and higher than  $2\,M_\odot$ ; Li detections and upper limits are shown as *circles* and *triangles* respectively). Theoretical lithium evolution is shown from the ZAMS up to the end of the early-AGB. Various lines correspond to predictions for stellar models of different masses computed without or with rotation as indicated, and with thermohaline mixing in all cases

Charbonnel 1998, 2010; Palacios et al. 2003). After the 1dup, the surface Li abundance remains constant until the stars reach the bump luminosity where thermohaline mixing becomes efficient and destroys Li. Later on the star reaches the RGB tip, and finally the second dredge-up decreases again Li at the surface. Models are in perfect agreement with observations.

We have computed a few models along the TP-AGB, and found that thermohaline mixing leads to non negligible fresh lithium production, as shown in Fig. 5. There we present the evolution of the surface lithium abundance as a function of both effective temperature and bolometric magnitude for TP-AGB models of 1.25 and  $2.0\,M_\odot$  stars. Theoretical predictions are compared with observations of the sample of low-mass oxygen-rich AGB variables belonging to the Galactic disk studied by Uttenthaler and Lebzelter (2010), and are found to fit very nicely the observed Li



**Fig. 5** Lithium observations in oxygen-rich variables belonging to the Galactic disk as a function of effective temperature and bolometric magnitude (Uttenthaler and Lebzelter 2010); *circles* and *triangles* are for abundance determinations and upper limits respectively. Theoretical lithium evolution is shown from the early-AGB up to the end of the TP-AGB. Various lines correspond to predictions for stellar models of different masses computed without or with rotation as indicated, and with thermohaline mixing in all cases. Figure from Charbonnel and Lagarde (2010)

behaviour. Let us note that despite the strong production of fresh Li at that phase, the total stellar yields remain negative for this element.

#### 4.3 Helium 3

On the main sequence, a  ${}^{3}$ He peak builds up due to pp-reactions inside low-mass stars (Iben 1967), and is engulfed in the stellar envelope during the 1dup. As a consequence the surface abundance of  ${}^{3}$ He strongly increases on the lower RGB as can be seen in Fig. 6 which presents the evolution of  ${}^{3}$ He mass fraction at the surface of  ${}^{1}$ M $_{\odot}$  model at solar metallicity in the standard case and in the case with thermohaline mixing (black solid and red dotted lines respectively). After the bump, thermohaline mixing transports  ${}^{3}$ He from the convective envelope down to

122 C. Charbonnel et al.

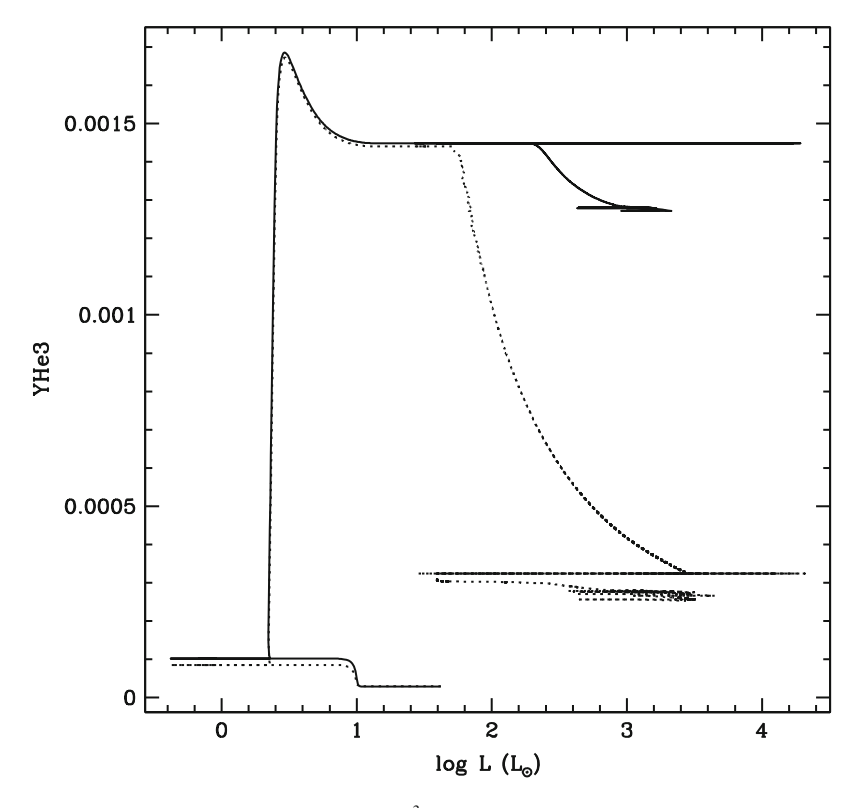


Fig. 6 Evolution of the surface abundance of  $^3$ He (in mass fraction) from the pre-main sequence up to the AGB tip for  $1M_{\odot}$  models at solar metallicity. The *black solid line* and the *red dotted-line* correspond to the standard and thermohaline cases respectively

the hydrogen-burning shell where it burns. This leads to a rapid decrease of the surface abundance (and thus of the corresponding yield) of this element as can be seen in Fig. 6. We are presently computing similar stellar models over a large range in stellar mass and metallicity in order to quantify the actual contribution of low-mass stars to Galactic <sup>3</sup>He (Lagarde et al., in preparation). We are confident that the corresponding <sup>3</sup>He yields will help reconciling the primordial nucleosynthesis with measurements of <sup>3</sup>He/H in Galactic HII regions (Charbonnel 2002).

#### 5 Conclusions

An inversion of molecular weight created by the <sup>3</sup>He(<sup>3</sup>He; 2p)<sup>4</sup>He reaction is at the origin of thermohaline instability in low-mass RGB stars brighter than the bump. The associated mixing explains very well observations of <sup>12</sup>C/<sup>13</sup>C and Li in these objects. Rotation-induced mixing, coupled with thermohaline mixing, allows us to

explain the <sup>12</sup>C/<sup>13</sup>C and Li data in giant stars over a large mass range. Thermohaline mixing has also an effect during the TP-AGB phase, where it leads to fresh lithium production. Finally, this process helps reconciling stellar yields predictions with the Galactic evolution of <sup>3</sup>He as constrained by the data in Galactic HII regions.

**Acknowledgements** We acknowledge financial support from the Swiss National Science Foundation (FNS) and from the french Programme National Program (PNPS) of CNRS/INSU.

#### References

Chanamé, J., Pinsonneault, M., Terndrup, D.M.: ApJ 631, 540 (2005)

Charbonnel, C.: Nature 415, 27 (2002)

Charbonnel, C., Lagarde, N.: A&A 522, A10 (2010)

Charbonnel, C., Talon, S.: A&A 351, 635 (1999)

Charbonnel, C., Zahn, J.-P.: A&A 467, L15 (2007)

Eggleton, P.P., Dearborn, D.S.P., Lattanzio, J.C.: Science 314, 1580 (2006)

Geisler, D., Smith, V.V., Wallerstein, G., Gonzalez, G., Charbonnel, C.: AJ 129, 1428 (2005)

Gilrov, K.K.: ApJ 347, 835 (1989)

Gilroy, K.K., Brown, J.A.: ApJ 371, 578 (1991)

Gratton, R.G., Sneden, C., Carretta, E., Bragaglia, A.: A&A 354, 169 (2000)

Iben, I. Jr.: ApJ 147, 624 (1967)

Kippenhahn, R., Ruschenplatt, G., Thomas, H.-C.: A&A 91, 175 (1980)

Luck, R.E.: ApJS 91, 309 (1994)

Mikolaitis, Š., Tautvaišienė, G., Gratton, R., Bragaglia, A., Carretta, E.: MNRAS 407, 1866 (2010)

Palacios, A., Talon, S., Charbonnel, C., Forestini, M.: A&A 399, 603 (2003)

Palacios, A., Charbonnel, C., Talon, S., Siess, L.: A&A 453, 261 (2006)

Pasquini, L., Bonifacio, P., Randich, S., Galli, D., Gratton, R.G.: A&A 426, 651 (2004)

Pilachowski, C., Sneden, C., Freeland, E., Casperson, J.: AJ 125, 794 (2003)

Recio-Blanco, A., de Laverny, P.: A&A 461, L13 (2007)

Shetrone, M.D.: ApJ **585**, L45 (2003)

Smiljanic, R., Gauderon, R., North, P., et al.: A&A 502, 267 (2009)

Smith, V.V., Hinkle, K.H., Cunha, K., et al.: AJ 124, 3241 (2002)

Spite, M., Cayrel, R., Hill, V., et al.: A&A 455, 291 (2006)

Talon, S., Charbonnel, C.: A&A 335, 959 (1998)

Talon, S., Charbonnel, C.: In: Charbonnel, C., Tosi, M., Primas, F., Chiappini, C. (eds.) IAU Symposium, vol. 268 pp. 365–374 (2010)

Tautvaišiene, G., Edvardsson, B., Tuominen, I., Ilyin, I.: A&A 360, 499 (2000)

Tautvaišienė, G., Edvardsson, B., Puzeras, E., Ilyin, I.: A&A 431, 933 (2005)

Ulrich, R.K.: ApJ **168**, 57 (1971)

Ulrich, R.K.: ApJ 172, 165 (1972)

Uttenthaler, S., Lebzelter, T.: A&A 510, A62 (2010)

## **3D Model Atmospheres of Red Giant Stars**

Hans-Günter Ludwig and Matthias Steffen

**Abstract** We provide a brief overview of the modelling of the atmospheres of red giant stars with the 3D radiation-hydrodynamics code CO5BOLD. We emphasize aspects where 3D modelling provides additional insight beyond standard hydrostatic 1D models, and comment on present modelling challenges.

#### 1 Introduction

Modelling of three-dimensional (3D) atmospheres of cool stars is an active field of development (e.g. Nagendra et al. 2009), and particularly 3D models of atmospheres of red giant (RG) stars are just on the verge of becoming available for application to astrophysical problems. In an early application, Kučinskas et al. (2005) used a 3D RG model to estimate color corrections due to thermal inhomogeneities; Collet et al. (2007) considered a set of eight giant models to investigate the impact on line formation and abundances. More recently, Freytag and Höfner (2008) developed model atmospheres of AGB stars and their winds, Dupret et al. (2009) derived the energy input to solar-like oscillations in giants from 3D models, Ramírez et al. (2010) studied convective line-shifts in the metal-poor RG HD 122563 and compared them to a 3D model, Chiavassa et al. (2011) applied global 3D models to assess effects of photometric and related astrometric variability, and Pasquini et al. (2011) took recourse to 3D dwarf and RG models to correct for convective blueshifts in high-precision, spectroscopic radial velocity measurements. While fairly exhaustive, the

H.-G. Ludwig (⊠)

Zentrum für Astronomie der Universität Heidelberg, Landessternwarte, Königstuhl 12, 69117 Heidelberg, Germany

e-mail: H.Ludwig@lsw.uni-heidelberg.de

M. Steffen

Astrophysikalisches Institut Potsdam, An der Sternwarte 16, 14482 Potsdam, Germany msteffen@aip.de

list of examples is still quite short, but illustrates already the variety of possible applications of 3D RG models. At the moment efforts are under way to cover the Hertzsprung-Russell diagram with 3D model atmospheres including stars in the redgiant branch (Ludwig et al. 2009a; Trampedach and Stein 2011).

In the following we are going to focus on aspects related to abundances from 3D models, and the theoretical calibration of the mixing-length parameter  $\alpha_{MLT}$  from 3D model atmospheres. Here, we are not so much presenting results as rather pointing out problems which are still lingering. We finally add some comments about predictions of the photometric micro-variability which are of interest in the context of high-precision photometry missions like CoRoT.

### 2 Our Model Atmosphere Codes

#### 2.1 3D Model Atmospheres: CO5BOLD

Our 3D model atmospheres were calculated with the radiation-hydrodynamics code CO5BOLD (Freytag et al. 2002; Wedemeyer et al. 2004; Freytag et al. 2011). The code solves the time-dependent equations of compressible hydrodynamics coupled to radiative transfer in a constant gravity field in a Cartesian computational domain which is representative of a volume located at the stellar surface. The equation of state takes into consideration the ionization of hydrogen and helium, as well as the formation of H<sub>2</sub> molecules according to Saha-Boltzmann statistics. Relevant thermodynamic quantities—in particular gas pressure and temperature are tabulated as a function of gas density and internal energy. The multi-group opacities used by CO5BOLD are based on monochromatic opacities stemming from the MARCS stellar atmosphere package (Gustafsson et al. 2008) provided as function of gas pressure and temperature with high wavelength resolution. The opacities have been calculated assuming solar elemental abundances according to Grevesse and Sauval (1998), with the exception of CNO for which values close to the recommendation of Asplund (2005) are adopted (specifically, A(C) = 8.41, A(N) = 7.80, A(O) = 8.67). The metal abundances were scaled according to overall metallicity of the model assuming an enhancement of the  $\alpha$ -elements by  $+0.4\,\mathrm{dex}$ at metallicities [M/H] < -1.

In our RG models we typically use a number of  $140 \times 140 \times 150-160 \times 160 \times 200$  points for the hydrodynamical grid. The decision about the resolution primarily hinges on the effective temperature of the model, hotter models usually require a higher resolution. The wavelength dependence of the radiation field is represented by 5 multi-group bins in the case of solar metallicity, and 6 bins at sub-solar metallicities, following the procedures laid out by Nordlund (1982), Ludwig (1992), Ludwig et al. (1994), Vögler et al. (2004). For test purposes we have calculated a few models with more bins. Since it is of relevance for the discussion later, we emphasize that all opacity sources—including scattering opacities—are treated as

true absorption. The sorting into wavelength groups is done applying thresholds in logarithmic Rosseland optical depth  $\{+\infty,0.0,-1.5,-3.0,-4.5,-\infty\}$  for the 5-bin, and  $\{+\infty,0.1,0.0,-1.0,-2.0,-3.0,-\infty\}$  for the 6-bin schemes. In all but one bin a switching between Rosseland and Planck averages is performed at a band-averaged Rosseland optical depth of 0.35; in the bin gathering the largest line opacities, the Rosseland mean opacity is used throughout. The decisions about number of bins, and sorting thresholds are motivated by comparing radiative fluxes and heating rates obtained by the binned opacities in comparison to the case of high wavelength resolution.

#### 2.2 1D Stellar Atmospheres: LHD

Due to still present limitations in the realism (e.g. by the limited wavelength resolution) of 3D model atmospheres it is often advantageous to work differentially, and express 3D effects relative to a 1D comparison structure. To this end we developed a 1D stellar atmosphere code called LHD which employs the same opacities and equation-of-state as the 3D code CO5BOLD. The convective energy transport is modelled in the framework of mixing-length theory as described in Mihalas (1978). The resulting 1D stratifications are in hydrostatic and radiative-convective equilibrium. See Caffau et al. (2007) for more details on our approach of deriving abundance corrections.

### 3 RG Abundances and the Issue of Scattering

Collet et al. (2007) presented 3D-1D abundance corrections for RG models at effective temperatures of around 5,000 K,  $\log g = 2.2$ , and metallicities ranging from solar to [M/H] = -3, using the 3D code of Stein and Nordlund (1998). Two similar studies were presented by Dobrovolskas et al. (2010) and Ivanauskas et al. (2010) who used CO5BOLD and LHD models at about  $T_{\rm eff} = 5,000$  K,  $\log g = 2.5$ , with metallicities down to [M/H] = -3 to derive 3D-1D abundance corrections. While the two later studies confirm the results of Collet and collaborators, showing that generally the magnitude of 3D-1D abundance corrections becomes larger towards lower metallicity, the quantitative agreement is not satisfactory. The CO5BOLD-based abundance corrections are usually noticeably smaller in magnitude, in particular at the lowest metallicities. Obviously, this is an unfortunate situation, and one would like to see a higher degree of consistency among results from different 3D codes.

In a recent paper, Collet et al. (2011) suggested the treatment of scattering in the simulations as the reason for the discrepant abundance corrections for RGs at low metallicity. The main scattering process is Rayleigh scattering by neutral hydrogen. This is perhaps the simplest case of scattering and can be modelled as coherent

isotropic scattering in the continuum. Collet and collaborators implemented a proper treatment of this kind of scattering in 3D. They also put forward an approximate treatment of scattering by simply leaving out scattering contributions in the binned opacities in the optically thin regions. They showed that this approximate treatment provides results in close agreement with the exact treatment. They further performed a comparison with the case where scattering is treated as true absorption—as is the case in the CO5BOLD models. Their models of 2007 used the approximate treatment of scattering. The models show a sensitive dependence of the resulting temperature stratification on the treatment of scattering. In their [M/H] = -3 RG model, the difference amounts to 600 K at optical depth  $\log \tau_{Ross} = -4$  in the sense that a proper treatment of scattering leads to cooler structures in comparison to treating scattering opacities as true absorption.

It appears plausible that the differing 3D-1D abundance corrections are a consequence of the different thermal structures resulting from the different treatment of scattering in the CO5BOLD and Nordlund-Stein class of models. To test this idea, we calculated a RG model with the same atmospheric parameters as before but with the approximate treatment of scattering as suggested by Collet et al. (2011). Figures 1 and 2 illustrate the outcome. The most striking aspect is that our models

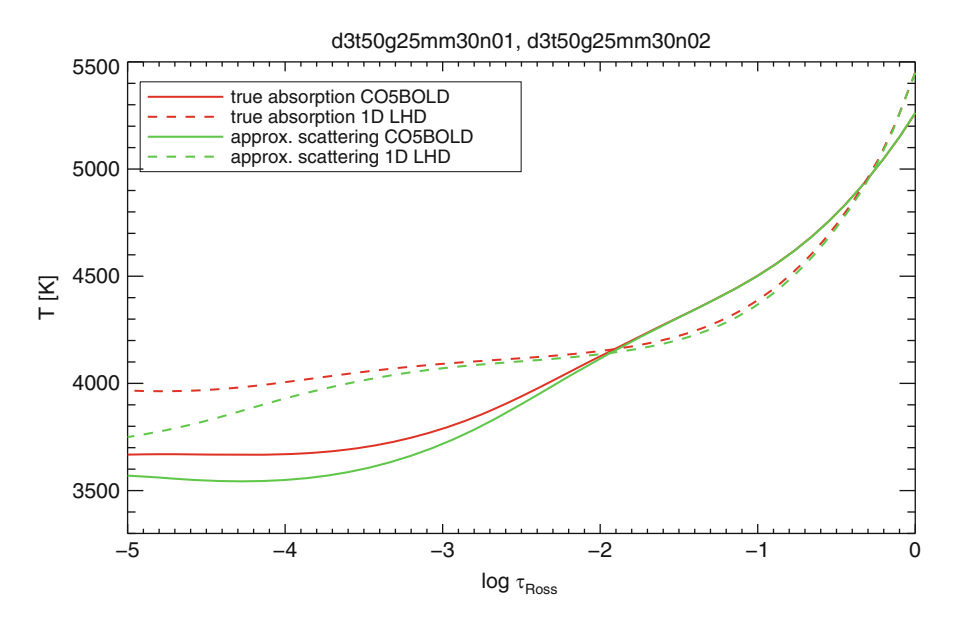


**Fig. 1** Comparison of the mean temperature structures of two different 3D CO5BOLD hydrodynamical model atmospheres (*solid*) and associated 1D LHD models (*dashed*), computed with a different treatment of radiative transfer. In the first case (*dark [red] curves*), the continuum scattering opacity is treated as true absorption opacity, while in the second case (*light [green] curves*), the continuum scattering opacity is ignored in the optically thin layers. For the 3D models, averaging was performed on surfaces of constant Rosseland optical depth and over 70 equidistant snapshots covering a total of 140,000 s

show a very much reduced sensitivity to the treatment of scattering in comparison to the models of Collet and co-workers. The approximate treatment of scattering leads to a structure which is only 120 K cooler at log  $\tau_{Ross} = -4$ , in comparison to  $\approx\!600\,\mathrm{K}$  found by Collet et al. (2011). This also carries over to the temperature fluctuations which are little affected by the treatment of scattering (see Fig. 2). We already emphasized the importance of a differential approach, and Fig. 1 also shows the effects on the associated 1D LHD models. Temperature differences between the 1D and 3D models at given optical depth are changing even less. While we did not perform spectrum synthesis calculations yet to derive new abundance corrections, we consider it as unlikely that the modest changes in the thermal structure can change our abundance corrections so much that they become consistent with the values of Collet et al. (2007).

The situation remains puzzling. The very different sensitivity to the treatment of scattering is difficult to explain. We only can hint at the differences in the calculation of the band-averaged opacities in the various codes: Collet and collaborators use intensity-averaged opacities in the optically thin regions, while we use Planck-averages—except for the band collecting the strongest lines where a Rosseland average is used throughout. We speculate that these choices, together with the definition of the opacity bins, may have a significant influence on the resulting thermal structures and their sensitivity to the treatment of scattering.

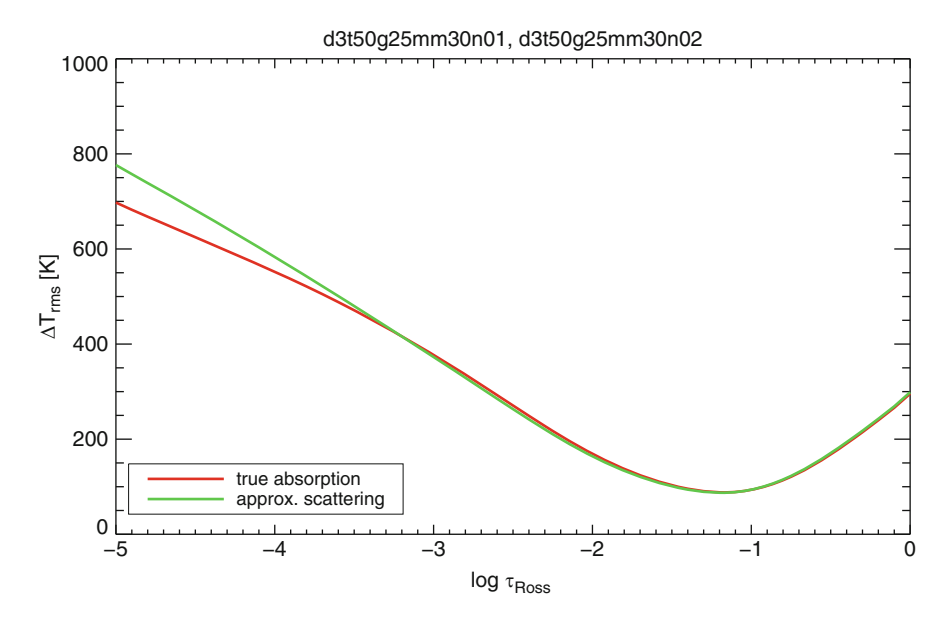


Fig. 2 Total rms temperature fluctuation  $\Delta T_{\rm rms,tot}$  as a function of Rosseland optical depth for the two 3D models shown in Fig. 1, computed as  $\Delta T_{\rm rms,tot} = \sqrt{\langle T^2 \rangle_{x,y,t} - \langle T \rangle_{x,y,t}^2}$ , where  $\langle . \rangle_{x,y,t}$  denotes horizontal averaging over surfaces of constant Rosseland optical depth and over time. We have verified that the amplitude of the total temperature fluctuation is completely dominated by the spatial temperature variations:  $\Delta T_{\rm rms,tot} \approx \Delta T_{\rm rms,xy} = \left(\sqrt{\langle T^2 \rangle_{x,y} - \langle T \rangle_{x,y}^2}\right)_t$ 

#### 4 The Calibration of $\alpha_{MLT}$ and Turbulent Pressure

It is well known from the theory of stellar structure that convection is generally an efficient means of transporting energy, and that it establishes a thermal structure close to adiabatic. Only in the vicinity of the boundaries of convective regions noticeable deviations from adiabaticity occur. In convective envelopes of latetype stars the upper boundary of the convective envelope—usually located close to or even in the optically thin layers—constitutes the bottle-neck for the energy transport through the stellar envelope assigning a special role to it. Despite its small geometrical extent and low mass, it largely determines the properties of the convective envelope as a whole. It is the value of the entropy of the adiabatically stratified bulk of the convective s<sub>env</sub> which is most important from the point of view of stellar structure since it influences the resulting radius and effective temperature of a stellar model. senv is controlled by the efficiency of convective and radiative energy transport in the thin, superadiabatically stratified surface layers. 3D model atmospheres can be applied to model this region, and allow to quantify the mutual efficiency of the convective and radiative energy transport, and to predict senv. Comparing the model predictions to standard 1D models based on mixing-length theory (MLT) the value of s<sub>env</sub> can be translated into a corresponding mixing-length parameter  $\alpha_{MLT}$  (Trampedach et al. 1999; Ludwig et al. 1999, 2008).

In stellar evolution calculations the free mixing-length parameter is usually calibrated against the Sun. However, it is unclear whether mixing-length theory provides a suitable scaling of the convective efficiency at constant  $\alpha_{\text{MLT}}$  across the Hertzsprung-Russell diagram. The depth of the surface convective envelope and the related  $\alpha_{\text{MLT}}$  can be constraint by asteroseismology. However, degeneracies with other parameters often make it difficult to obtain a unique solution (e.g. Goupil et al. 2011). Hence, it would be useful to have an independent estimate available which 3D models can provide in principle.

In main-sequence models turbulent pressure plays generally only a minor role but becomes relatively more important towards lower gravities—and causes trouble when one is interested in a well-defined calibration of the mixing-length parameter. Figure 3 shows the average temperature profile of a 3D red giant model ( $T_{\rm eff} \approx 3,600~{\rm K},\log g=1.0,[{\rm M/H}]=0.0$ ) in comparison to standard 1D model atmospheres of the same atmospheric parameters. While the turbulent pressure  $P_{\rm turb}$  is naturally included in the 3D models, it is modelled in a ad-hoc fashion in 1D models, assuming a parameterisation  $P_{\rm turb} = f_{\rm turb} \rho v_{\rm c}^2$ , where  $f_{\rm turb}$  is a free parameter of order unity,  $\rho$  the mass density and  $v_{\rm c}$  the convective velocity according MLT.

Figure 3 shows that it is essentially impossible to reproduce the mean thermal profile of the 3D model with any of the 1D models—irrespective of the choice of  $\alpha_{\text{MLT}}$  and  $f_{\text{turb}}$ . The failure is related to the local nature of MLT confining the action of the turbulent pressure gradients strictly to the convectively unstable regions. While formally one can still match  $s_{\text{env}}$  of the 3D model by a 1D profile with suitably chosen  $\alpha_{\text{MLT}}$  and/or  $f_{\text{turb}}$  such a match becomes physically little motivated, and is unlikely to provide a robust scaling with changing atmospheric parameters.

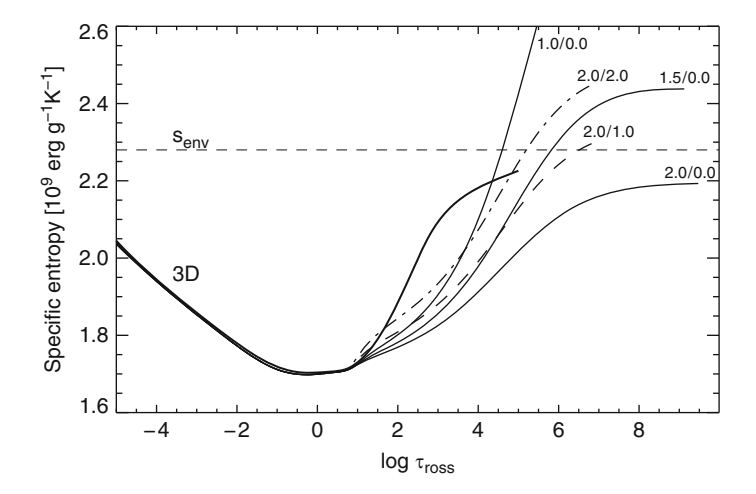
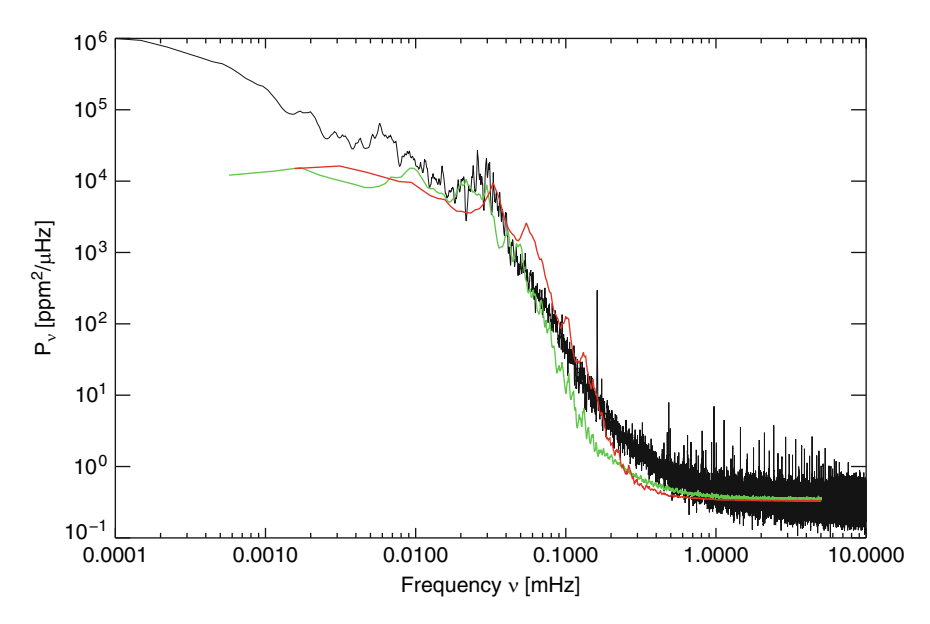


Fig. 3 Entropy-optical depth profiles (horizontal and temporal average) of a 3D red giant model (thick solid line) in comparison to 1D stellar atmosphere models of different  $\alpha_{MLT}$  leaving out (thin solid lines) or including (dashed and dashed-dotted lines) turbulent pressure. The lines are labeled with values  $\alpha_{MLT}/f_{turb}$  (details see text). The horizontal dashed line indicates the value of  $s_{env}$  as predicted by the 3D model

An improved 1D convection description including non-local effects like overshooting is clearly desirable to handle this situation. Empirical calibrations of  $\alpha_{MLT}$  using giants are likely to suffer from ambiguities related to the way turbulent pressure is treated in the 1D models. One may take the result as an indication that taking recourse to 1D models is not warranted, and one may give up the benefits of a differential approach by relating 3D to 1D structures. Alternatively, one may take the absolute entropy of the convective envelope (perhaps translated to equivalent pressure-temperature pairs) as predicted by the 3D model as constraint to be matched in 1D stellar structure models.

## 5 Granulation-Related Photometric Micro-Variability

High-precision photometry of satellite missions (foremost Most, CoRoT, *Kepler*) allow the detection of stellar variability associated with the random changes of the granulation pattern on the surfaces of late-tape stars—by asteroseismologists usually referred to as "granular background noise". 3D model atmospheres represent the granulation pattern in detail and allow to predict the power spectrum of the variability signal (Trampedach et al. 1998; Svensson and Ludwig 2005; Ludwig 2006). Despite this possibility, no comprehensive theoretical study has been conducted so far. One of the reasons is that long time series need to be calculated to collect sufficient statistics, which is computationally demanding. The F-dwarf HD 49933—a prominent CoRoT-target—is an exception for which Ludwig et al.



**Fig. 4** Comparison of power spectra of photometric variability. *Black line*: HD 181907 as observed by CoRoT. The predicted power spectra from two 3D models are depicted with *light [green]* ( $T_{\rm eff} = 4,500 \, {\rm K}$ ) and *dark grey [red]* ( $T_{\rm eff} = 5,000 \, {\rm K}$ ) lines. Further details see text

(2009b) performed an analysis. However, the growing body of observational data in particular for giant stars should motivate further efforts in this direction. Recently, Kjeldsen and Bedding (2011) suggested a new scaling relation for the amplitude of solar-like oscillations, and also discuss the scaling of the granulation background signal. It would be interesting to see whether 3D model atmospheres can lend further support to the suggested relations.

To illustrate the feasibility, we show in Fig. 4 a rough comparison of the photometric variability between the RG HD 181907 (HR 7349) and predictions from two 3D models. The plot focuses on the frequency region where the granulation-related signal is expected. CoRoT acquired a high-quality time series for HD 181907; Carrier et al. (2010) give atmospheric parameters  $4780 \pm 80/2.78 \pm 0.16/-0.08 \pm 0.10$  ( $T_{\rm eff}/\log g/[{\rm M/H}]$ ). The two 3D models have atmospheric parameters 4,500/2.5/0.0 and 5,000/2.5/0.0, bracketing the star in effective temperature, as well as having comparable surface gravity and metallicity. Although no dedicated modelling was performed, the spectra appear quite similar.

## 6 Concluding Remarks

3D model atmospheres of cool stars, including red giants, have reached a level of realism which allows a direct confrontation with observations. In some areas they allow to make predictions beyond the capabilities of classical 1D models. However,

as we have seen there still exist modelling challenges, and last but not least quite some work is still necessary to fully exploit the potential of such models.

#### References

Asplund, M.: ARA&A 43, 481 (2005)

Caffau, E., Faraggiana, R., Bonifacio, P., Ludwig, H.-G., Steffen, M.: A&A 470, 699 (2007)

Carrier, F., Morel, T., Miglio, A., et al.: Ap&SS 328, 83 (2010)

Chiavassa, A., Pasquato, E., Jorissen, A., et al.: A&A 528, A120 (2011)

Collet, R., Asplund, M., Trampedach, R.: A&A 469, 687 (2007)

Collet, R., Hayek, W., Asplund, M., et al.: A&A 528, A32 (2011)

Dobrovolskas et al.: Nuclei in the Cosmos, p. 288 (2010)

Dupret, M., Belkacem, K., Samadi, R., et al.: A&A 506, 57 (2009)

Freytag, B., Höfner, S.: A&A 483, 571 (2008)

Freytag, B., Steffen, M., Dorch, B.: Astron. Nachr. 323, 213 (2002)

Freytag et al.: Journal of Computational Physics 231, 919

Goupil, M.J., Lebreton, Y., Marques, J.P., et al.: J. Phys. Conf. Ser. 271, 012032 (2011)

Grevesse, N., Sauval, A.J.: Space Sci. Rev. 85, 161 (1998)

Gustafsson, B., Edvardsson, B., Eriksson, K., et al.: A&A 486, 951 (2008)

Ivanauskas, A., Kucinskas, A., Ludwig, H.G., Caffau, E.: Nuclei in the Cosmos, p. 290 (2010)

Kjeldsen, H., Bedding, T.R.: A&A 529, L8 (2011)

Kučinskas, A., Hauschildt, P.H., Ludwig, H.-G., et al.: A&A 442, 281 (2005)

Ludwig, H.-G.: PhD thesis, University of Kiel (1992)

Ludwig, H.-G.: A&A 445, 661 (2006)

Ludwig, H.-G., Jordan, S., Steffen, M.: A&A 284, 105 (1994)

Ludwig, H.-G., Freytag, B., Steffen, M.: A&A 346, 111 (1999)

Ludwig, H.-G., Caffau, E., Kučinskas, A.: In: Deng, L., Chan, K.L. (eds.) IAU Symposium, vol. 252, pp. 75–81 (2008)

Ludwig, H.-G., Caffau, E., Steffen, M., et al.: Mem. Soc. Astron. Italiana 80, 711 (2009a)

Ludwig, H.-G., Samadi, R., Steffen, M., et al.: A&A 506, 167 (2009b)

Mihalas, D.: Stellar Atmospheres, 2nd edn. (1978)

Nagendra, K.N., Bonifacio, P., Ludwig, H.-G.: Mem. Soc. Astron. Italiana 80, 601 (2009)

Nordlund, A.: A&A 107, 1 (1982)

Pasquini, L., Melo, C., Chavero, C., et al.: A&A 526, A127 (2011)

Ramírez, I., Collet, R., Lambert, D.L., Allende Prieto, C., Asplund, M.: ApJ 725, L223 (2010)

Stein, R.F., Nordlund, A.: ApJ 499, 914 (1998)

Svensson, F., Ludwig, H.-G.: ESA Special Publication. In: Favata, F., Hussain, G.A.J., Battrick, B. (eds.) 13th Cambridge Workshop on Cool Stars, Stellar Systems and the Sun, vol. 560, p. 979 (2005)

Trampedach, R., Stein, R.F.: ApJ **731**, 78 (2011)

Trampedach, R., Christensen-Dalsgaard, J., Nordlund, A., Stein, R.F.: In: Kjeldsen, H., Bedding, T.R. (eds.) The First MONS Workshop: Science with a Small Space Telescope, vol. 59, p. 59 (1998)

Trampedach, R., Stein, R.F., Christensen-Dalsgaard, J., Nordlund, Å.: In: Gimenez, A., Guinan, E.F., Montesinos, B. (eds.) Astronomical Society of the Pacific Conference Series, Stellar Structure: Theory and Test of Connective Energy Transport, vol. 173, p. 233 (1999)

Vögler, A., Bruls, J.H.M.J., Schüssler, M.: A&A 421, 741 (2004)

Wedemeyer, S., Freytag, B., Steffen, M., Ludwig, H.-G., Holweger, H.: A&A 414, 1121 (2004)

## Part III Stellar Populations in the Milky Way

## Structure and Evolution of the Milky Way

Ken Freeman

**Abstract** This review discusses the structure and evolution of the Milky Way, in the context of opportunities provided by asteroseismology of red giants. The review is structured according to the main Galactic components: the thin disk, thick disk, stellar halo, and the Galactic bar/bulge. The review concludes with an overview of Galactic archaeology and chemical tagging, and a brief account of the upcoming HERMES survey with the AAT.

#### 1 The Thin Disk: Formation and Evolution

Here are some of the issues related to the formation and evolution of the Galactic thin disk:

- Building the thin disk: Its exponential radial structure, and the role of mergers.
- The star formation history: Chemical evolution and continued gas accretion.
- Evolutionary processes in the disk: Disk heating, radial mixing.
- The outer disk: Chemical properties and chemical gradients.

Many of the basic observational constraints on the properties of the Galactic disk are still uncertain. At this time, we do not have reliable information about the star formation history of the disk. We do not know how the metallicity distribution and the stellar velocity dispersions in the disk have evolved with time. One might have expected that these observational questions were well understood by now, but this is not yet so. The basic observational problem is the difficulty of measuring ages for individual stars.

138 K. Freeman

The younger stars of the Galactic disk show a clear abundance gradient of about  $0.07 \, \text{dex kpc}^{-1}$ , outlined nicely by the cepheids (Luck et al. 2006). In the outer disk, for the older stars, the abundance gradient appears to be even stronger: the abundance gradient (and the gradient in the ratio of alpha-elements to Fe) have flattened with time towards the solar values. A striking feature of the radial abundance gradient in the Galaxy is that it flattens for  $R > 12 \, \text{kpc}$  at an [Fe/H] value of about -0.5 (Carney et al. 2005). A similar flattening of the abundance gradient is seen in the outer regions of the disk of M31 (Worthey et al. 2005).

The relation between the stellar age and the mean metallicity and velocity dispersion are the fundamental observables that constrain the chemical and dynamical evolution of the Galactic thin disk. The age-metallicity relation (AMR) in the solar neighborhood is still uncertain. Different authors find different relations, ranging from a relatively steep decrease of metallicity with age from Rocha-Pinto et al. (2004) to almost no change of mean metallicity with age from Nordström et al. (2004). Much of the earlier work indicated that a large scatter in metallicity was seen at all ages, which was part of the motivation to invoke large-scale radial mixing of stars within the disk. This mixing, predicted by Sellwood and Binney (2002), is generated by resonances with the spiral pattern, and is able to move stars from one near-circular orbit to another. It would bring stars from the inner and outer disks, with their different mean abundances, into the solar neighborhood. Radial mixing is potentially an important feature of the evolution of the disk. At this stage, it is a theoretical concept, and it is not known how important it is in the Galactic disk. We are not aware of any strong observational evidence at this stage for the existence of radial mixing. More recent results on the AMR (e.g. Wylie de Boer et al., unpublished) indicate that there is a weak decrease of mean metallicity with age in the Galactic thin disk, but that the spread in metallicity at any age is no more than about 0.10 dex. If this is correct, then radial mixing may not be so important for chemically mixing the Galactic disk.

The age-velocity dispersion relation (AVR) is also not well determined observationally. The velocity dispersion of stars appears to increase with age, and this is believed to be due to the interaction of stars with perturbers such as giant molecular clouds and transient spiral structure. But there is a difference of opinion about the duration of this heating. One view is that the stellar velocity dispersion  $\sigma$  increases steadily for all time,  $\sim t^{0.2-0.5}$ , based on Wielen (1977)'s work using chromospheric ages and kinematics for the McCormick dwarfs. Another view (e.g. Quillen and Garnett 2001), based on the data for subgiants from Edvardsson et al. (1993) is that the heating takes place for the first  $\sim$ 2 Gyr, but then saturates when  $\sigma \approx 20 \, \mathrm{km \, s^{-1}}$ because the stars of higher velocity dispersion spend most of their orbital time away from the Galactic plane where the sources of heating lie. Data from Soubiran et al. (2008) support this view. Again, much of the difference in view goes back to the difficulty of measuring stellar ages. Accurate ages from asteroseismology would be very welcome. Accurate ages and distances for a significant sample of red giants would allow us to measure the AMR and AVR out to several kpc from the Sun. This would be a great step forward in understanding the chemical and dynamical evolution of the Galactic disk.

#### 2 The Formation of the Thick Disk

Most spiral galaxies, including out Galaxy, have a second thicker disk component. For example, the thick disk and halo of the edge-on spiral galaxy NGC 891, which is much like the Milky Way in size and morphology, has a thick disk nicely seen in star counts from HST images (Mouhcine et al. 2010). Its thick disk has scale height  $\sim 1.4 \, \text{kpc}$  and scalelength  $\sim 4.8 \, \text{kpc}$ , much as in our Galaxy. The fraction of baryons in the thick disk is typically about 10-15% in large systems like the Milky Way, but rises to about 50% in the smaller disk systems (Yoachim and Dalcanton 2008).

The Milky Way has a significant thick disk, discovered by Gilmore and Reid (1983). Its vertical velocity dispersion is about  $40 \, \mathrm{km \, s^{-1}}$ ; its scale height is still uncertain but is probably about 1,000 pc. The surface brightness of the thick disk is about 10% of the thin disk's, and near the Galactic plane it rotates almost as rapidly as the thin disk. Its stars are older than 10 Gyr and are significantly more metal poor than the stars of the thin disk; most of the thick disk stars have [Fe/H] values between about -0.5 and -1.0 and are enhanced in alpha-elements relative to Fe. This is usually interpreted as evidence that the thick disk formed rapidly, on a timescale  $\sim 1 \, \mathrm{Gyr}$ . From its kinematics and chemical properties, the thick disk appears to be a discrete component, distinct from the thin disk. Current opinion is that the thick disk shows no vertical abundance gradient (e.g. Gilmore et al. 1995; Ivezić et al. 2008).

The old thick disk is a very significant component for studying Galaxy formation, because it presents a kinematically and chemically recognizable relic of the early Galaxy. Secular heating is unlikely to affect its dynamics significantly, because its stars spend most of their time away from the Galactic plane.

How do thick disks form? Several mechanisms have been proposed, including:

- Thick disks are a normal part of early disk settling, and form through energetic early star forming events, e.g. in gas-rich mergers (Samland and Gerhard 2003; Brook et al. 2004)
- Thick disks are made up of accretion debris (Abadi et al. 2003). From the mass-metallicity relation for galaxies, the accreted galaxies that built up the thick disk of the Galaxy would need to be more massive than the SMC to get the right mean [Fe/H] abundance (~ 0.7). The possible discovery of a counter-rotating thick disk (Yoachim and Dalcanton 2008) in an edge-on galaxy would favor this mechanism.
- Thick disks come from the heating of the thin disk via disruption of its early massive clusters (Kroupa 2002). The internal energy of large star clusters is enough to thicken the disk. Recent work on the significance of the high redshift clump structures may be relevant to the thick disk problem: the thick disk may originate from the merging of clumps and heating by clumps (e.g. Bournaud et al. 2009). These clumps are believed to form by gravitational instability from turbulent early disks: they appear to generate thick disks with scale heights that are radially approximately uniform, rather than the flared thick disks predicted from minor mergers.

140 K. Freeman

• Thick disks come from early partly-formed thin disks, heated by accretion events such as the accretion event which is believed to have brought omega Centauri into the Galaxy (Bekki and Freeman 2003). In this picture, thin disk formation began early, at z = 2-3. The partly formed thin disk is partly disrupted during the active merger epoch which heats it into thick disk observed now, The rest of the gas then gradually settles to form the present thin disk, a process which continues to the present day.

 A recent suggestion is that stars on more energetic orbits migrate out from the inner galaxy to form a thick disk at larger radii where the potential gradient is weaker (Schönrich and Binney 2009)

How can we test between these possibilities for thick disk formation? Sales et al. (2009) looked at the expected orbital eccentricity distribution for thick disk stars in different formation scenarios. Their four scenarios are:

- A gas-rich merger: The thick disk stars are born in-situ
- The thick disk stars come in from outside via accretion
- The early thin disk is heated by accretion of a massive satellite
- The thick disk is formed as stars from the inner disk migrate out to larger radii.

Preliminary results from the observed orbital eccentricity distribution for thick disk stars may favor the gas-rich merger picture (Wilson et al. 2011). This is a potentially powerful approach for testing ideas about the origin of the thick disk. Because it depends on the orbital properties of the thick disk sample, firm control of selection effects is needed in the identification of which stars belong to the thick disk. Kinematical criteria for choosing the thick disk sample are clearly not ideal.

To summarize this section on the thick disk: Thick disks are very common in disk galaxies. In our Galaxy, the thick disk is old, and is kinematically and chemically distinct from the thin disk. It is important now to identify what the thick disk represents in the galaxy formation process. The orbital eccentricity distribution of the thick disk stars will provide some guidance. Chemical tagging will show if the thick disk formed as a small number of very large aggregates, or if it has a significant contribution from accreted galaxies. This is one of the goals for the upcoming AAT/HERMES survey: see Sect. 5.

#### 3 The Galactic Stellar Halo

The stars of the Galactic halo have [Fe/H] abundances mostly less than -1.0. Their kinematics are very different from the rotating thick and thin disks: the mean rotation of the stellar halo is close to zero, and it is supported against gravity primarily by its velocity dispersion. It is now widely believed that much of the stellar halo comes from the debris of small accreted satellites (Searle and Zinn 1978). There remains a possibility that a component of the halo formed dissipationally during the

Galaxy formation process (Eggen et al. 1962; Samland and Gerhard 2003). Halobuilding accretion events continue to the present time: the disrupting Sgr dwarf is an example in our Galaxy, and the faint disrupting system around NGC 5907 is another example of such an event (Martínez-Delgado et al. 2010). The metallicity distribution function (MDF) of the major surviving satellites around the Milky way is not like the MDF in the stellar halo (e.g. Venn and Hill 2008) but the satellite MDFs may have been more similar long ago. We note that the fainter satellites are more metal-poor and are consistent with the Milky Way halo in their [ $\alpha$ /Fe] behaviour.

Is there a halo component that formed dissipationally early in the Galactic formation process? Hartwick (1987) showed that the metal-poor RR Lyrae stars delineate a two-component halo, with a flattened inner component and a spherical outer component. Carollo et al. (2010) identified a two-component halo and the thick disk in a sample of 17,000 SDSS stars, mostly with [Fe/H] < -0.5. They described the kinematics well with these three components:

```
Thick disk: (\bar{V}, \sigma, [\text{Fe/H}]) = (182, 51, -0.7)
Inner halo: (\bar{V}, \sigma, [\text{Fe/H}]) = (7, 95, -1.6)
Outer halo: (\bar{V}, \sigma, [\text{Fe/H}]) = (-80, 180, -2.2)
```

Here [Fe/H] is the mean abundance for the component,  $\bar{V}$  and  $\sigma$  are its mean rotation velocity relative to a non-rotating frame, and velocity dispersion, in kilometer per second. The outer halo appears to have retrograde mean rotation. As we look at subsamples at greater distances from the Galactic plane, we see that the thick disk dies away and the retrograde outer halo takes over from the inner halo. With the above kinematic parameters, the equilibrium of the inner halo is a bit hard to understand. It may not yet be in equilibrium. From comparison with simulations, Zolotov et al. (2009) argue that the inner halo has a partly dissipational origin, while the outer halo is made up from debris of faint metal-poor accreted satellites.

Recently Nissen and Schuster (2010) studied a sample of 78 halo stars with [Fe/H] > -1.6 and find that they show a variety of  $[\alpha/Fe]$  enhancement. Their sample shows high and low  $[\alpha/Fe]$  groups, and the low  $[\alpha/Fe]$  stars are mostly in high energy retrograde orbits. The high  $[\alpha/Fe]$  stars could be ancient halo stars born in situ and possible heated by satellite encounters. The low-alpha stars may be accreted from dwarf galaxies.

How much of the halo comes from accreted structures? An ACS study by Ibata et al. (2009) of the halo of NGC 891 (a nearby edge-on galaxy like the Milky Way) shows a spatially lumpy metallicity distribution, indicating that its halo is made up largely of accreted structures which have not yet mixed away. This is consistent with simulations of stellar halos by Font et al. (2008), Gilbert et al. (2009) and Cooper et al. (2010).

To summarize this section on the Galactic stellar halo: the stellar halo is probably made up mainly of the debris of small accreted galaxies, although there may be an inner component which formed dissipatively.

142 K. Freeman

## 4 The Galactic Bar/Bulge

The boxy appearance of the Galactic bulge is typical of galactic bars seen edge-on. These bar/bulges are very common: about 2/3 of spiral galaxies show some kind of central bar structure in the infra-red. Where do these bar/bulges come from?

Bars can arise naturally from the instabilities of the disk. A rotating disk is often unstable to forming a flat bar structure at its center. This flat bar in turn is often unstable to vertical buckling which generates the boxy appearance. This kind of bar/bulge is not generated by mergers but follows simply from the dynamics of a flat rotating disk of stars. The maximum vertical extent of boxy or peanut-shaped bulges occurs near the radius of the vertical and horizontal Lindblad resonances, i.e. where

$$\Omega_h = \Omega - \kappa/2 = \Omega - \nu_z/2.$$

Here  $\Omega$  is the circular angular velocity,  $\Omega_b$  is the pattern speed of the bar,  $\kappa$  is the epicyclic frequency and  $\nu_z$  is the vertical frequency of oscillation. We note that the frequencies  $\kappa$  and particularly  $\nu_z$  depend on the amplitude of the oscillation. Stars in this zone oscillate on 3D orbits which support the peanut shape.

We can test whether the Galactic bulge formed through this kind of bar-buckling instability of the inner disk, by comparing the structure and kinematics of the bulge with those of N-body simulations that generate a boxy/bar bulge (e.g. Athanassoula 2005). The simulations show an exponential structure and near-cylindrical rotation: do these simulations match the properties of the Galactic bar/bulge?

The stars of the Galactic bulge appear to be old and enhanced in  $\alpha$ -elements. This implies a rapid history of star formation. If the bar formed from the inner disk, then it would be interesting to know whether the bulge stars and the stars of the adjacent disk have similar chemical properties. This is not yet clear. There do appear to be similarities in the  $\alpha$ -element properties between the bulge and the thick disk in the solar neighborhood (e.g. Meléndez et al. 2008).

The bar-forming and bar-buckling process takes 2–3 Gyr to act after the disk settles. In the bar-buckling instability scenario, the bulge *structure* is probably younger than the bulge *stars*, which were originally part of the inner disk. The alpha-enrichment of the bulge and thick disk comes from the rapid chemical evolution which took place in the inner disk before the instability acted. In this scenario, the stars of the bulge and adjacent disk should have similar ages: accurate asteroseismology ages for giants of the bulge and inner disk would be a very useful test of the scenario.

We are doing a survey of about 28,000 clump giants in the Galactic bulge and the adjacent disk, to measure the chemical properties (Fe, Mg, Ca, Ti, Al, O) of stars in the bulge and adjacent disk: are they similar, as we would expect if the bar/bulge grew out of the disk? We use the AAOmega fiber spectrometer on the AAT, to acquire medium-resolution spectra of about 350 stars at a time, at a resolution  $R \sim 12,000$ .

The central regions of our Galaxy are not only the location of the bulge and inner disk, but also include the central regions of the Galactic stellar halo. Recent

simulations (e.g. Diemand et al. 2005; Moore et al. 2006; Brook et al. 2007) indicate that the *metal-free* (population III) stars formed until redshift  $z \sim 4$ , in chemically isolated subsystems far away from the largest progenitor. If its stars survive, they are spread throughout the Galactic halo. If they are not found, then it would be likely that their lifetimes are less than a Hubble time which in turn implies a truncated IMF. On the other hand, the *oldest* stars form in the early rare high density peaks that lie near the highest density peak of the final system. They are not necessarily the most metal-poor stars in the Galaxy. Now, these oldest stars are predicted to lie in the central bulge region of the Galaxy. Accurate asteroseismology ages for metal-poor stars in the inner Galaxy would provide a great way to tell if they are the oldest stars or just stars of the inner Galactic halo. This test would require a  $\sim 10\%$  precision in age.

Our data so far indicate that the rotation of the Galactic bulge is close to cylindrical (see also Howard et al. 2009). Detailed analysis will be needed to see if there is any evidence for a small classical merger generated bulge component, in addition to the boxy/peanut bar/bulge which probably formed from the disk. We also see a more slowly rotating metal-poor component in the bulge region. The problem now is to identify the *first* stars from among the expected metal-poor stars of the inner halo.

## 5 Galactic Archaeology

The goals of Galactic Archaeology are to find signatures or fossils from the epoch of Galaxy assembly, to give us insight into the processes that took place as the Galaxy formed. A major goal is to identify observationally how important mergers and accretion events were in building up the Galactic disk, bulge and halo of the Milky Way. CDM simulations predict a high level of merger activity which conflicts with some observed properties of disk galaxies, particularly with the relatively common nature of large galaxies like ours with small bulges (e.g. Kormendy et al. 2010).

The aim is to reconstruct the star-forming aggregates and accreted galaxies that built up the disk, bulge, and halo of the Galaxy. Some of these dispersed aggregates can still be recognized kinematically as stellar moving groups. For others, the dynamical information was lost through heating and mixing processes, but their debris can still be recognized by their chemical signatures (chemical tagging). We would like to find groups of stars, now dispersed, that were associated at birth either

- Because they were born together and therefore have almost identical chemical abundances over all elements (e.g. De Silva et al. 2009), or
- Because they came from a common accreted galaxy and have abundance patterns
  that are clearly distinguished from those of the Galactic disk (e.g. Venn and Hill
  2008).

144 K. Freeman

The galactic disk shows kinematical substructure in the solar neighborhood: groups of stars moving together, usually called moving stellar groups. Some are associated with dynamical resonances (e.g. the Hercules group): in such groups, we do not expect to see chemical homogeneity or age homogeneity (e.g. Bensby et al. 2007). Others are the debris of star-forming aggregates in the disk (e.g. the HR1614 group and Wolf 630 group). They are chemically homogeneous, and such groups could be useful for reconstructing the history of the galactic disk. Yet others may be debris of infalling objects, as seen in CDM simulations (e.g. Abadi et al. 2003).

The stars of the HR 1614 group appear to be the relic of a dispersed star-forming event. These stars have an age of about 2 Gyr and [Fe/H] = +0.2, and they are scattered all around us. This group has not lost its dynamical identity despite its age. De Silva et al. (2007) measured accurate differential abundances for many elements in HR 1614 stars, and found a very small spread in abundances. This is encouraging for recovering dispersed star forming events by chemical tagging.

Chemical studies of the old disk stars in the Galaxy can help to identify disk stars which came in from outside in disrupting satellites, and also those that are the debris of dispersed star-forming aggregates like the HR 1614 group (Freeman and Bland-Hawthorn 2002). The chemical properties of surviving satellites (the dwarf spheroidal galaxies) vary from satellite to satellite, but are different in detail from the overall chemical properties of the disk stars.

We can think of a chemical space of abundances of elements: O, Na, Mg, Al, Ca, Mn, Fe, Cu, Sr, Ba, Eu for example. Not all of these elements vary independently. The dimensionality of this space chemical space is probably between about 7 and 9. Most disk stars inhabit a sub-region of this space. Stars that come from dispersed star clusters represent a very small volume in this space. Stars which came in from satellites may have a distribution in this space that is different enough to stand out from the rest of the disk stars. With this chemical tagging approach, we hope to detect or put observational limits on the satellite accretion history of the galactic disk.

Chemical studies of the old disk stars in the Galaxy can identify disk stars that are the debris of common dispersed star-forming aggregates. Chemical tagging will work if

- Stars form in large aggregates, which is believed to be true
- Aggregates are chemically homogenous
- Aggregates have unique chemical signatures defined by several elements or element groups which do not vary in lockstep from one aggregate to another.
   We need sufficient spread in abundances from aggregate to aggregate so that chemical signatures can be distinguished with accuracy achievable (~0.05 dex differentially)

De Silva's work on open clusters was aimed at testing the last two conditions: they appear to be true. See De Silva et al. (2009) for more on chemical tagging.

We should stress here that chemical tagging is not just assigning stars chemically to a particular population, like the thin disk, thick disk or halo. Chemical tagging is intended to assign stars chemically to substructure which is no longer detectable kinematically. We are planning a large chemical tagging survey of about a million stars, using the new HERMES multi-object spectrometer on the AAT. The goal is to reconstruct the dispersed star-forming aggregates that built up the disk, thick disk and halo within about 5 kpc of the sun.

HERMES is a new high resolution multi-object spectrometer on the AAT. Its spectral resolution is about 28,000, with a high resolution mode with R=50,000. It is fed by 400 fibers over a 2-degree field, and has 4 non-contiguous wavelength bands covering a total of about 1,000 Å. The four wavelength bands were chosen to include measurable lines of elements needed for chemical tagging. HERMES is scheduled for first light in late 2012. The HERMES chemical tagging survey will include stars brighter than V=14 and has a strong synergy with Gaia: for the dwarf stars in the HERMES sample, the accurate (1%) parallaxes and proper motions will be invaluable for more detailed studies.

The fractional contribution of the different Galactic components to the HERMES sample will be about 78% thin disk stars, 17% thick disk stars and about 5% halo stars. About 70% of the stars will be dwarfs within about 1,000 pc and 30% giants within about 5 kpc. About 9% of the thick disk stars and about 14% of the thin disk stars pass within our 1 kpc dwarf horizon. Assume that all of their formation aggregates are now azimuthally mixed right around the Galaxy, so that all of their formation sites are represented within our horizon. Simulations (Bland-Hawthorn and Freeman 2004) show that a complete random sample of about a million stars with V < 14 would allow detection of about 20 thick disk dwarfs from each of about 4,500 star formation sites, and about 10 thin disk dwarfs from each of about 35,000 star formation sites. These estimates depend on the adopted mass spectrum of the formation sites. In combination with Gaia, HERMES will give the distribution of stars in the multi-dimensional{position, velocity, chemical} space, and isochrone ages for about 200,000 stars with V < 14. We would be interested to explore further what the HERMES survey can contribute to asteroseismology.

Some authors have argued that the thick disk may have formed from the debris of the huge and short-lived star formation clumps observed in disk galaxies at high redshift (e.g. Bournaud et al. 2009; Genzel et al. 2011). If this is correct, then only a small number of these huge building blocks would have been involved in the assembly of the thick disk, and their debris should be very easy to identify via chemical tagging techniques.

Chemical tagging in the inner regions of the Galactic disk will be of particular interest. We expect about 200,000 survey giants in the inner region of the Galaxy. The surviving old (> 1 Gyr) open clusters are all in the outer Galaxy, beyond a radius of 8 kpc. Young open clusters are seen in the inner Galaxy, but do not appear to survive the disruptive effects of the tidal field and giant molecular clouds in the inner regions. We expect to find the debris of many broken open and globular clusters in the inner disk. These will be good for chemical tagging recovery using the HERMES giants. The radial extent of the dispersal of individual broken clusters will provide an acute test of radial mixing theory within the disk. Another opportunity comes from the Na/O anomaly, which is unique to globular clusters, and may help to identify the debris of disrupted globular clusters.

146 K. Freeman

#### References

Abadi, M.G., Navarro, J.F., Steinmetz, M., Eke, V.R.: ApJ 597, 21 (2003)

Athanassoula, E.: MNRAS 358, 1477 (2005)

Bekki, K., Freeman, K.C.: MNRAS 346, L11 (2003)

Bensby, T., Oey, M.S., Feltzing, S., Gustafsson, B.: ApJ 655, L89 (2007)

Bland-Hawthorn, J., Freeman, K.C.: PASA 21, 110 (2004)

Bournaud, F., Elmegreen, B.G., Martig, M.: ApJ 707, L1 (2009)

Brook, C.B., Kawata, D., Gibson, B.K., Freeman, K.C.: ApJ 612, 894 (2004)

Brook, C., Richard, S., Kawata, D., Martel, H., Gibson, B.K.: ApJ 658, 60 (2007)

Carney, B.W., Yong, D., Teixera de Almeida, M.L., Seitzer, P.: AJ 130, 1111 (2005)

Carollo, D., Beers, T.C., Chiba, M., et al.: ApJ **712**, 692 (2010)

Cooper, A.P., Cole, S., Frenk, C.S., et al.: MNRAS 406, 744 (2010)

De Silva, G.M., Freeman, K.C., Bland-Hawthorn, J., Asplund, M., Bessell, M.S.: AJ 133, 694 (2007)

De Silva, G.M., Freeman, K.C., Bland-Hawthorn, J.: PASA 26, 11 (2009)

Diemand, J., Madau, P., Moore, B.: MNRAS 364, 367 (2005)

Edvardsson, B., Andersen, J., Gustafsson, B., et al.: A&A 275, 101 (1993)

Eggen, O.J., Lynden-Bell, D., Sandage, A.R.: ApJ 136, 748 (1962)

Font, A.S., Johnston, K.V., Ferguson, A.M.N., et al.: ApJ 673, 215 (2008)

Freeman, K., Bland-Hawthorn, J.: ARA&A 40, 487 (2002)

Genzel, R., Newman, S., Jones, T., et al.: ApJ 733, 101 (2011)

Gilbert, K.M., Font, A.S., Johnston, K.V., Guhathakurta, P.: ApJ 701, 776 (2009)

Gilmore, G., Reid, N.: MNRAS 202, 1025 (1983)

Gilmore, G., Wyse, R.F.G., Jones, J.B.: AJ 109, 1095 (1995)

Hartwick, F.D.A.: In: Gilmore, G., Carswell, B. (eds.) NATO ASIC Proc. 207: The Galaxy, pp. 281–290 (1987)

Howard, C.D., Rich, R.M., Clarkson, W., et al.: ApJ 702, L153 (2009)

Ibata, R., Mouhcine, M., Rejkuba, M.: MNRAS 395, 126 (2009)

Ivezić, Ž., Sesar, B., Jurić, M., et al.: ApJ **684**, 287 (2008)

Kormendy, J., Drory, N., Bender, R., Cornell, M.E.: ApJ 723, 54 (2010)

Kroupa, P.: MNRAS 330, 707 (2002)

Luck, R.E., Kovtyukh, V.V., Andrievsky, S.M.: AJ 132, 902 (2006)

Martínez-Delgado, D., Gabany, R.J., Crawford, K., et al.: AJ 140, 962 (2010)

Meléndez, J., Asplund, M., Alves-Brito, A., et al.: A&A 484, L21 (2008)

Moore, B., Diemand, J., Madau, P., Zemp, M., Stadel, J.: MNRAS 368, 563 (2006)

Mouhcine, M., Ibata, R., Rejkuba, M.: ApJ **714**, L12 (2010)

Nissen, P.E., Schuster, W.J.: A&A 511, L10 (2010)

Nordström, B., Mayor, M., Andersen, J., et al.: A&A 418, 989 (2004)

Quillen & Garnett: Galaxy Disks and Disk Galaxies230, ASP Conf Series 87, p. 87 (2001)

Rocha-Pinto, H.J., Flynn, C., Scalo, J., et al.: A&A 423, 517 (2004)

Sales, L.V., Helmi, A., Abadi, M.G., et al.: MNRAS 400, L61 (2009)

Samland, M., Gerhard, O.E.: A&A 399, 961 (2003)

Schönrich, R., Binney, J.: MNRAS **399**, 1145 (2009)

Searle, L., Zinn, R.: ApJ 225, 357 (1978)

Sellwood, J.A., Binney, J.J.: MNRAS 336, 785 (2002)

Soubiran, C., Bienaymé, O., Mishenina, T.V., Kovtyukh, V.V.: A&A 480, 91 (2008)

Venn, K.A., Hill, V.M.: The Messenger 134, 23 (2008)

Wielen, R.: A&A 60, 263 (1977)

Wilson, M.L., Helmi, A., Morrison, H.L., et al.: MNRAS 413, 2235 (2011)

Worthey, G., España, A., MacArthur, L.A., Courteau, S.: ApJ 631, 820 (2005)

Yoachim, P., Dalcanton, J.J.: ApJ 682, 1004 (2008)

Zolotov, A., Willman, B., Brooks, A.M., et al.: ApJ **702**, 1058 (2009)

## Red Giant Stars: Probing the Milky Way Chemical Enrichment

Cristina Chiappini

Abstract Many ongoing (SDSS-SEGUE, SDSS-APOGEE, RAVE) and future (HERMES, 4MOST) surveys have the main goal to map the complex kinematical and chemical substructures of the Milky Way, with the final aim to constrain its assembly history. The combination of asteroseismic information from *Kepler* and CoRoT satellites for giant stars, for which abundance and kinematical information are provided by ground-based spectroscopic surveys opens a new and powerful way to study our Galaxy. Indeed the asteroseismology plus abundance information can be potentially translated into stellar ages for large samples of stars. Here, I give a brief overview of what are the main open questions in the field of Galactic Archaeology—from the study of the First Stars to enrich the Universe, to the Galaxy assembly history—and how could CoRoT and *Kepler* make a definitive contribution to those questions.

## 1 The Oldest Stars in Our Galaxy

## 1.1 What is the Nucleosynthesis of the Most Metal-Poor Halo Stars Telling Us? Are These the Oldest Stars in the Galaxy?

One of the key open problems in Astrophysics is how the initially metal-free Universe was enriched in chemical elements up to the present time. An important piece in the puzzle of the chemical enrichment of the Universe is the study of the nature of the first stars born after the Big Bang. In other words, whether the very different primordial environment produced noticeable effects with respect to their properties, and what was their impact on subsequent stellar generations and on the

Leibniz-Institut für Astrophysik Potsdam (AIP), An der Sternwarte 16 14482, Potsdam, Germany e-mail: cristina.chiappini@aip.de

C. Chiappini (⋈)

148 C. Chiappini

re-ionization of the Universe. The massive first stars are long dead, and even though efforts to directly observe them in high-redshift galaxies are underway (Bouwens et al. 2011) this might still take many years. An alternative is to search for the imprints of the first stellar generations left on the oldest stars in our Galaxy. Lowmass stars with  $M \leq 0.8$  of the solar mass have lifetimes comparable to the age of the Universe, and in their atmospheres, the elemental abundances of the gas at the time of their birth are mostly preserved. The search for a large number of these fossil records of the history of the Universe constitutes the goal of several planned and ongoing ambitious surveys, and red giants play a crucial role here as being a luminous tracer.

Recently, a burst of new information on cosmic abundances, provided by high-resolution spectra of stars in the halo, bulge, thick and thin disks of the MW and its satellites has considerably fuelled debate in the field. In particular, thanks to the ESO/VLT Large Program First Stars (Cayrel et al. 2004), very metal-poor (most probably old) normal halo giant stars below the luminosity bump were found to show striking C, N, O (Spite et al. 2005, 2006). In a series of papers (Chiappini et al. 2006, 2008; Ekström et al. 2008) we have shown that rotating models of massive stars are, at present, the only ones that can successfully account for some of these puzzling observations, such as the high N/O and C/O ratios and low  $^{12}$ C/ $^{13}$ C ratio in very-metal poor stars (see details in the caption of Fig. 1). Fast rotating stars could also be the explanation for the anomalous abundances observed in the most metal-poor CEMPs, especially for those for which a binary companion have not been identified, which is for instance the case of the two most metal-poor stars known to date (Meynet et al. 2010, and references therein).

# 1.2 Are Bulge Stars with 1/10th the Metallicity of the Sun Sampling the Same Ages as the Most Metal-Poor Halo Stars?

Efforts to look for the first stars signatures have concentrated so far in the Galactic halo, where the most metal-poor stars were found. However, the first galactic component to have formed was most probably the bulge. The search for the first stars signatures in the Galactic bulge is now one important goal of infrared surveys such as SDSS-APOGEE.

In particular, the bulge metal-poor globular cluster NGC 6522 is among the oldest objects in the Galaxy. Despite its iron-content being 1/10th of the one in the Sun, this cluster is around 1-2 Gyrs older than the oldest cluster in the halo (Barbuy et al.

 $<sup>^1</sup>$  Around 20% of stars with [Fe/H]  $\leq -2.0$  show extremely high C abundance, with [C/Fe]  $\geq +1.0$ . These stars are named C-Enhanced Metal Poor Stars (CEMP). Part of them also show enhancement in s-process elements (CEMP-s stars), which is attributed to AGB mass-transfer episodes. The remaining 80% stars are called normal metal-poor stars.

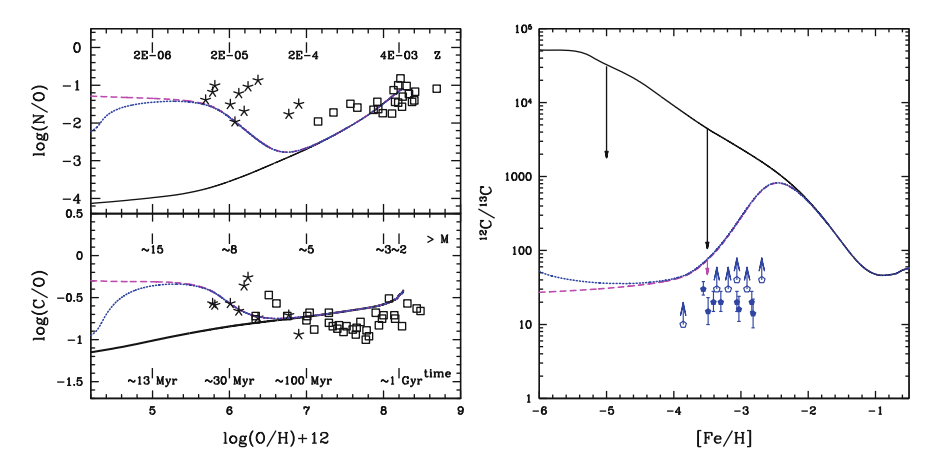


Fig. 1 Left Panel: Evolution of the N/O and C/O ratios in the halo of the MW. Solid (black) curve: the chemical evolution predictions obtained with the stellar yields of slow rotating  $(300 \,\mathrm{km} \,\mathrm{s}^{-1})$  stellar models. Dashed (magenta) line includes the contribution of fast rotating stars at very low metallicities. Dotted (blue) lines show what is obtained upon the inclusion of population III (Z=0) stars. Fast rotation enhances nitrogen in the early phases of the Galactic enrichment by 3 orders of magnitude! (Figure taken from Ekström et al. 2008)—Right Panel: Predicted evolution of the  $^{12}C/^{13}C$  ratio (curves are labelled as in left panel). The data are the metal-poor unmixed giants of (Spite et al. 2006). The arrows indicate the final  $^{12}C/^{13}C$  observed in giants after the first dredge-up. In this framework, the low  $^{12}C/^{13}C$  ratios can be attributed to the contribution to  $^{13}C$  by fast rotating massive stars, before AGBs had time to enrich the early interstellar medium. It would be very important to extend the isotopic ratio measurements to turnoff stars, something possibly feasible with the ELT. (Figure taken from Chiappini et al. 2008)

2009), and hence most probably samples the same early epoch of the very-metal poor halo stars discussed above. We thus expect to see the signatures of the first stars in this object despite its larger metallicity with respect to the very metal-poor stars found in the Galactic halo. Which signatures are we looking for? The production of primary <sup>22</sup>Ne has an important impact on the s-process nucleosynthesis in fast rotating massive stars compared to non-rotating stars, increasing by orders of magnitude the s-process yields (Pignatari et al. 2008), hence large quantities of s-process elements in very old objects could be a signature left by the first stellar generations.

Interestingly, eight stars in NGC6522, were found to have surface abundances consistent with the gas from which they formed being enriched by massive stars (that is, with oversolar [ $\alpha$ /Fe] and [Eu/Fe] ratios). However, the same stars have high [Ba/Fe] and [La/Fe] ratios,which usually arises through nucleosynthesis in low-mass stars (via the slow-neutron-capture process, or s-process). In a recent paper we (Chiappini et al. 2011) reanalysed the earlier spectra of the NGC 6522 giants and found that Y and Sr are also overabundant with respect to Fe, showing a large scatter similar to that observed in extremely metal-poor halo stars. These stars have [C/Fe]  $\leq 0$ . This pattern is best explained as originating in metal-poor fast-rotating massive stars and might constitute a signature of the first stellar generations now found also in the Galactic Bulge.

150 C. Chiappini

## 1.3 CoRoT and Kepler in This Context

The main question mark to the above results, is if the halo stars with [Fe/H] < -2.5 and, the bulge stars with  $[Fe/H] \sim -1$  sample the same earliest phases of the Galaxy chemical enrichment. In other words, are these stars old enough so that AGB stars, would not have had time to contribute to the enrichment of the ISM from which these stars formed? If the answer is yes, then the implication is that massive stars in the early Universe should be able to make enough  $^{14}N$ ,  $^{13}C$ , and a s-process elements themselves (provided that late AGB mass transfer episodes could be discarded). This would imply that the early generation of massive stars were fast rotators. This in turn could have important implications for the reionization of the Universe, or the expected rates of long-Gamma-ray bursts in the early Universe, among others (Chiappini et al. 2011).

Asteroseismology could make a crucial contribution in constraining the chemical evolution timescales. It would be very important if asteroseismology could provide an (independent) age estimate to the most metal-poor bulge giants (probably with CoRoT), and the very metal-poor halo stars (probably with Kepler). The Kepler field will probe stars around the solar vicinity but with large heights above the plane, probing the low metallicity regime. Currently, CoRoT probes the disk fields, with one of them toward the center of the Galaxy. In case CoRoT would define a new field (for instance, during its extension period) then the bulge could provide an interesting option. Indeed, as suggested in Chiappini et al. (2011), it is probable that halo stars with metallicities  $[Fe/H] \le -3$  have similar ages than bulge stars with metallicities  $\sim$ -1. If this turns out to be true, it would mean that the inner parts of the Galaxy were enriched faster, and that the hunt for the imprints of the first stellar generations of the Universe should not only consider the most metal-poor halo stars but also look into the metal-poor tail of the bulge metallicity distribution (which seems to be around [Fe/H] = -1, see Freeman this book). Current CoRoT fields offer a powerful tool to study the formation of the disk of our Galaxy (see next section).

## 2 The Thick and Thin Disks at the Solar Vicinity

Many are the proposed scenarios for the formation of the thick disk of the Milky Way, going from the merger with smaller galaxies to fast gas accretion in the early Universe (see Sales et al. 2009; Bournaud 2011, for more details). Crucial information on which was the dominant mechanism for the formation of the thick disk and other Galactic components is encoded in the chemical properties of their stars. By comparing the chemical properties of bulge, thick and thin disk stars one can address the question of which, among the competing processes of dissipation, satellite accretion and radial migration, play the dominant role in the formation of the different Galactic components. Star formation and accretion histories of the distinct Galactic components can in principle be inferred by a comparison

of predicted and observed abundance patterns in each of these components. This method shows promise to be extremely robust in view of the large amounts of high spectral resolution abundance data now available in the literature.

We have shown (Meléndez et al. 2008; Cescutti et al. 2009) that a homogeneous and differential analysis of bulge, thick and thin disk stars confirmed the well-established differences for [O/Fe] (at a given metallicity) between the local thin-disk and bulge stars, while no chemical distinction between the bulge and the local thick disk was found, which is in contrast to previous studies (see also Alves-Brito et al. 2010). We concluded that the bulge and local thick disk experienced short formation timescales and share a similar initial mass function.

For stars with Hipparcos parallaxes, a kinematic separation between thick and thin disk is observed (although not free from important biases). This has revealed a clear distinction between the abundance patterns of these two populations, particularly in the alpha elements with respect to iron suggesting a different origin for each of these galactic components and imposing strong constraints on galaxy formation models and stellar yields. We found (Chiappini 2009) that a model, in which the thick disk forms on a much shorter timescale than the thin disk (with a larger star formation efficiency than that in the thin disk) can account for the observed abundance ratio shifts of several chemical elements between thick and thin disk stars (see Fig. 2). Moreover, the lack of scatter in the abundance ratio patterns of both the thick and thin disks and their smooth metallicity dependency, suggest both components to have been formed in situ by gas accretion and not by mergers of smaller stellar systems. For the thick disk, this last constraint gains importance if its metallicity extends to, at least, solar (something still debated in the literature). The thick disk properties we infer from our galactic Archeology approach remind us of those of the recently discovered disks around redshift of 2, and have formation timescales compatible with those inferred by some high-z simulations of the bulge thick-disk formation by smooth gas accretion (Bournaud et al. 2009 and references therein).

Note that in Fig. 2, the thin disk curves (solid red) do not extend to oxygen abundances above  $\sim 0.05$  dex, whereas the stars classified as thin disk stars (based on kinematical criteria) reach metallicities as high as 0.2 dex. The reason why the model predictions for the thin disk do not extend to larger metallicities is because these models are also constrained by several other observables, among which the present metallicity of the ISM, which is solar (see Asplund et al. 2009 for a discussion on this point). This suggests the stars more metal rich than the Sun to have been formed at inner radii and then scattered out to the solar position, as a clear manifestation of the radial migration process (as already suggested by Grenon 1999). In fact, for some of these so-called Super Metal Rich Stars for which Hipparcos data is available, it is found that the turnoff of this population indicates an age of 10–12 Gyrs suggesting the thin disk close to the bulge as the probable their birthplace (see Barbuy et al. 2010 and references therein). In addition, Haywood (2008) analyzed the orbital parameters of local samples of stars in the thin disk and found that stars in the metal-poor ( $[Fe/H] < -0.3 \,\text{dex}$ ) and metal-rich ([Fe/H]) > +0.2 dex) tails of the thin disk have orbital parameters significantly different from 152 C. Chiappini

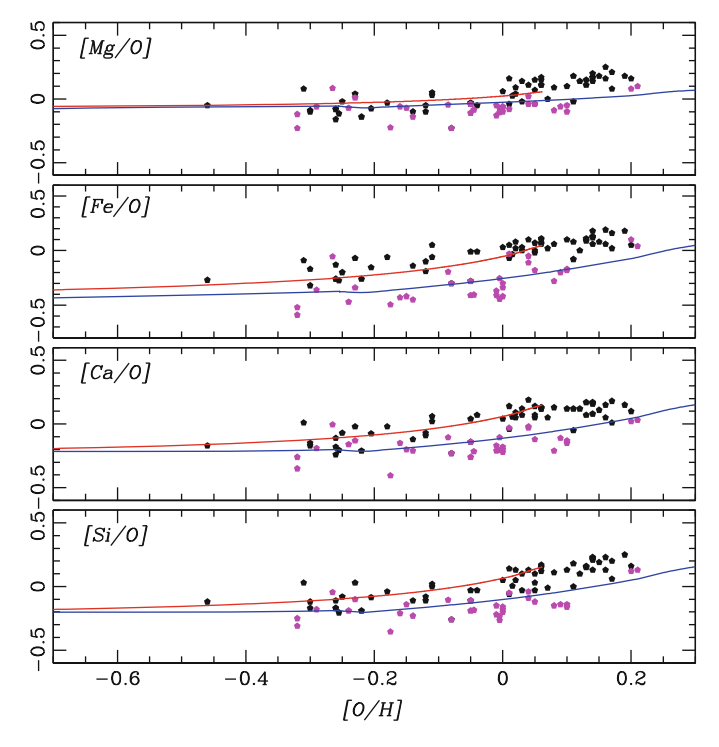


**Fig. 2** Predicted [X/O] vs. [O/H] relationships for *thin* (*red curve*) and *thick* (*blue curve*) disk evolution. The *dotted curve* shows a model for the thick disk where the contribution from Type Ia supernovae has been suppressed. The data points are from Feltzing and collaborators (*black* for *thin disk*, and *magenta* for *thick disk stars*)

the main population suggesting an origin in the outer and inner galactic regions, respectively.

If stellar mixing phenomenon is really important, it could imply that the "hiatus" between the thick and thin disk stars observed in Fig. 3 would not be an effect of local chemical evolution, but would be artificially created by biased selected samples, as a consequence of radial stellar mixing (Schönrich and Binney 2009). In addition, it would have important consequences for the other three important observational constraints for chemical evolution models, namely: the G-dwarf metallicity distribution, the age-metallicity relation and the abundance gradients. So far few authors have tried to estimate the impact of stellar mixing on the local kinematics and chemistry (Schönrich and Binney 2009). Moreover, even if a real chemical discontinuity between the thick and thin disks has been challenged by Schönrich and Binney (2009), these two components seem to show discontinuities not only in some of their kinematical properties (as shown by Veltz et al. 2008, with RAVE data), but also in their ages (Fuhrmann 2011, and references therein).

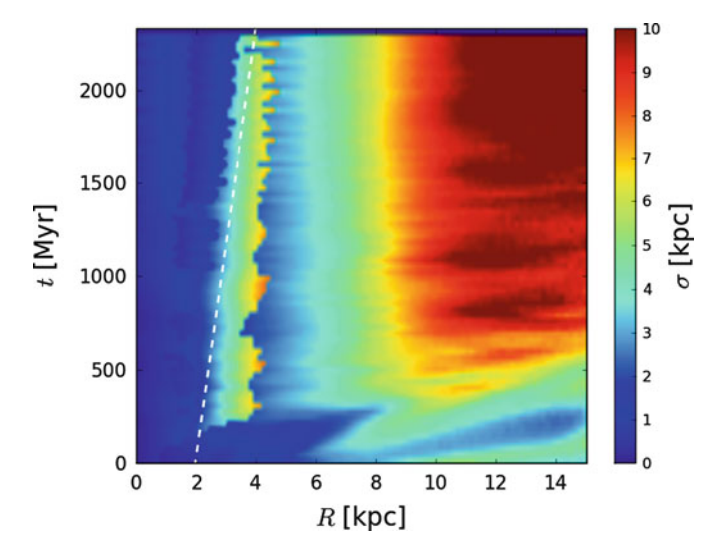


**Fig. 3** Contour maps of the radial dispersion in a cold disk. If the disk is sufficiently cold, the radial dispersion is high near the corotation region of the bar (indicated by the *dashed line*), where it can recurrently assume values of the order of  $\sigma \sim 6$  kpc. This implies that internal stars can recurrently be forced by the activity of the bar to migrate in the external region of the disk. At an intermediate radius, such as R = 6 kpc, the radial dispersion is of the order of  $\sigma \sim 3$  kpc and it increases in the external less dense regions where the pattern m = 1 dominates. (Figure adapted from Brunetti et al. 2011)

The mechanisms driving radial diffusion and heating are still hotly debated, and in many cases the role of the bar is not taken into account. In order to include the effect of radial migration in chemical evolution models and to gain a global (chemical and kinematic) understanding of the processes at play in the galactic disks, many dynamical aspects need to be further investigated, and in particular the role of the bar, that is the strongest non-axisymmetric component in disk galaxies (Minchev et al. 2011; Brunetti et al. 2011). For instance, Brunetti et al. (2011) find that spatial diffusion is not constant in time and strongly depends on the activity of the bar, which can move stars all over the disk recurrently (see Fig. 3), concluding that to realistically study the impact of radial migration on the chemical evolution modeling of the Milky Way the role of the bar has to be taken into account.

## 2.1 CoRoT and Kepler in This Context

Given the intrinsic theoretical difficulties in quantifying the importance of radial migration, asteroseismologic ages would offer a completely independent and powerful way to answer questions that would help us better constraining these complex processes, namely: what is the age of the most metal rich thin disk stars at the solar

154 C. Chiappini

vicinity? Is there an age gap between the thick and thin disk? What is the agemetallicity relation in the two CoRoT fields? Does this gives a consistent scatter to what is seen in samples where ages were obtained by isochrone fitting? Is it possible to determine the abundance gradients in the disk as a function of age? Is the thick/thin disk discontinuity observed also at other radii? Are stars towards the outer disk predominantly older as predicted by some radial-mixing models (e.g. Roškar et al. 2008)?

Answers to these questions and others, with CoRoT and *Kepler* samples, for which abundances and hence ages are known, couSld be our only hope to better quantify how important was stellar mixing in the formation of the Milky Way, and hence, how valid is the Galactic Archaeology approach as a tool to understand the formation of our Galaxy.

**Acknowledgements** I thank the organizers for the invitation to give this review, and for the wonderful hospitality of the Academia Belgica in Rome.

#### References

Alves-Brito, A., Meléndez, J., Asplund, M., Ramírez, I., Yong, D.: A&A 513, A35 (2010)

Asplund, M., Grevesse, N., Sauval, A.J., Scott, P.: ARA&A 47, 481 (2009)

Barbuy, B., Zoccali, M., Ortolani, S., et al.: A&A 507, 405 (2009)

Barbuy, B., Trevisan, M., Gustafsson, B., et al.: In: Charbonnel, C., Tosi, M., Primas, F., Chiappini, C. (eds.) IAU Symposium, vol. 268, pp. 325–326 (2010)

Bournaud, F.: In: Alves, J., Elmegreen, B.G., Girart, J.M., Trimble, V. (eds.) IAU Symposium, vol. 270, pp. 491–498 (2011)

Bournaud, F., Elmegreen, B.G., Martig, M.: ApJ 707, L1 (2009)

Bouwens, R.J., Illingworth, G.D., Labbe, I., et al.: Nature 469, 504 (2011)

Brunetti et al.: A&A **534**, 75 (2011)

Cayrel, R., Depagne, E., Spite, M., et al.: A&A 416, 1117 (2004)

Cescutti, G., Matteucci, F., McWilliam, A., Chiappini, C.: A&A 505, 605 (2009)

Chiappini, C.: Andersen, J., Bland-Hawthorn, J., Nordström, B. (eds.) IAU Symposium, vol. 254, pp. 191–196 (2009)

Chiappini, C., Hirschi, R., Meynet, G., et al.: A&A 449, L27 (2006)

Chiappini, C., Ekström, S., Meynet, G., et al.: A&A 479, L9 (2008)

Chiappini, C., Frischknecht, U., Meynet, G., et al.: Nature 472, 454 (2011)

Ekström, S., Meynet, G., Chiappini, C., Hirschi, R., Maeder, A.: A&A 489, 685 (2008)

Fuhrmann, K.: MNRAS 414, 2893 (2011)

Grenon, M.: Ap&SS 265, 331 (1999)

Haywood, M.: MNRAS 388, 1175 (2008)

Meléndez, J., Asplund, M., Alves-Brito, A., et al.: A&A 484, L21 (2008)

Meynet, G., Hirschi, R., Ekstrom, S., et al.: A&A 521, A30 (2010)

Minchev, I., Famaey, B., Combes, F., et al.: A&A 527, A147 (2011)

Pignatari, M., Gallino, R., Meynet, G., et al.: ApJ 687, L95 (2008)

Roškar, R., Debattista, V.P., Stinson, G.S., et al.: ApJ **675**, L65 (2008)

Sales, L.V., Helmi, A., Abadi, M.G., et al.: MNRAS 400, L61 (2009)

Schönrich, R., and Binney, J.: MNRAS 396, 203 (2009)

Spite, M., Cayrel, R., Plez, B., et al.: A&A 430, 655 (2005)

Spite, M., Cayrel, R., Hill, V., et al.: A&A 455, 291 (2006)

Veltz, L., Bienaymé, O., Freeman, K.C., et al.: A&A 480, 753 (2008)

## **Chemical Abundances of Giants** in Globular Clusters

Raffaele G. Gratton, Angela Bragaglia, Eugenio Carretta, Valentina D'Orazi, and Sara Lucatello

Abstract A large fraction of stars form in clusters. According to a widespread paradigma, stellar clusters are prototypes of single stellar populations. According to this concept, they formed on a very short time scale, and all their stars share the same chemical composition. Recently it has been understood that massive stellar clusters (the globular clusters) rather host various stellar populations, characterized by different chemical composition: these stellar populations have also slightly different ages, stars of the second generations being formed from the ejecta of part of those of an earlier one. Furthermore, it is becoming clear that the efficiency of the process is quite low: many more stars formed within this process than currently present in the clusters. This implies that a significant, perhaps even dominant fraction of the ancient population of galaxies formed within the episodes that lead to formation the globular clusters.

#### 1 Globular Clusters and the Galactic Halo

Current cosmological models (White and Rees 1978; Moore et al. 1999) predict that the Milky Way's stellar halo was assembled from many smaller systems. This building up can be probed using the fossil records left, such as the composition and dynamics of the most metal-poor stellar components: the old globular clusters, and the galactic halo, thick disk and bulge field populations. Globular clusters are particularly useful, both because they are observable to large distances and because many properties (e.g. ages, chemical composition and kinematics) can be quite easily determined. For instance, Figure 1 shows the age-metallicity relation for galactic

R.G. Gratton (🖾) · A. Bragaglia · E. Carretta · V. D'Orazi · S. Lucatello INAF-Osservatorio Astronomico di Padova, Vicolo dell'Osservatorio 5, 35122 Padova, Italy e-mail: raffaele.gratton@oapd.inaf.it; angela.bragaglia@oabo.inaf.it; eugenio.carretta@oabo.inaf.it; valentina.dorazi@oapd.inaf.it; sara.lucatello@oapd.inaf.it

R.G. Gratton et al.

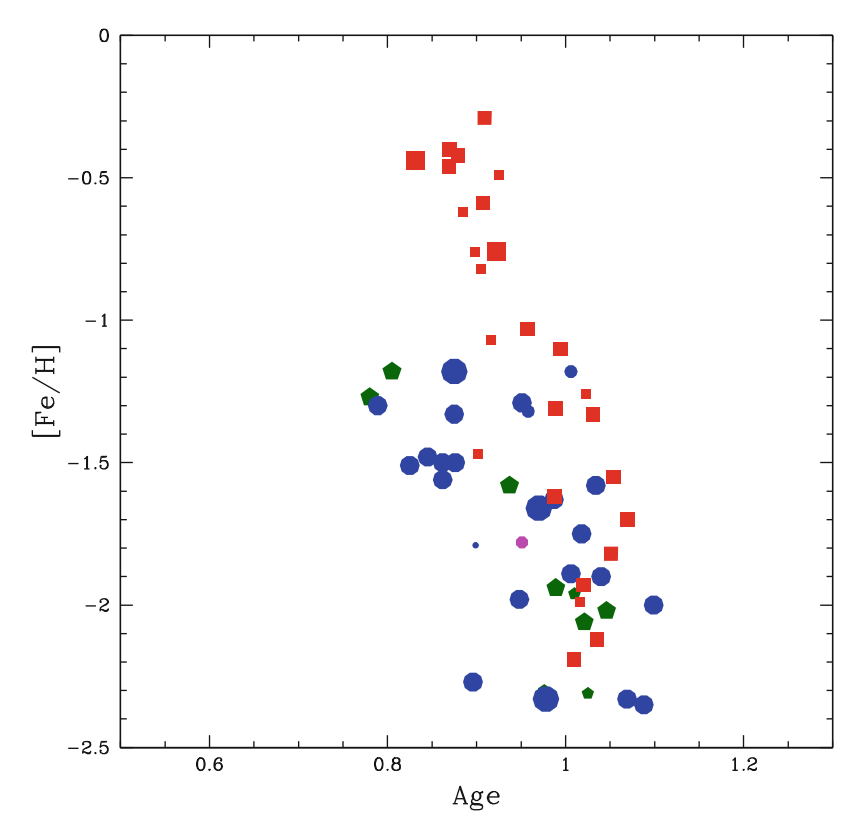


Fig. 1 Age-metallicity relation for different groups of globular clusters: outer halo clusters (green pentagons), inner halo clusters (blue circles), disk/bulge clusters (red squares). Magenta circles are globular clusters associated to dwarf Spheroidals. Different symbol sizes are used for clusters of different luminosity

globular clusters (from Gratton et al 2010a): various families of globular clusters display different and well defined age-metallicity relations. For similar reasons, globular clusters have been extensively used as ideal laboratories to study stellar evolution and have been fundamental benchmarks for population synthesis models, under the hypothesis that they are composed of simple stellar populations (see however below for a revision of this concept). If the connection between formation of globular clusters and halo stars were clear, it could be possible to use such a diagram to reconstruct the early phase of the Milky Way.

Unfortunately, this connection is not well known at present. Globular clusters presently make up some 1.2% of the stellar halo, but a large fraction of stars should have been lost by globular clusters in the very initial phases due to violent relaxation following gas expulsion and mass loss from the most massive stars (see e.g. Baumgardt et al. 2008). On a much longer timescale a significant fraction of stars should have evaporated because of two-body encounters and other mechanisms

(e.g. disk shocking: see e.g. Aguilar et al. 1988) move a number of stars outside the tidal radius. A substantial fraction of the original globular cluster mass should then have been lost, this loss being more efficient among smaller globular clusters. There is ample evidence that this is indeed the case for many globular clusters, e.g. from the presence of tidal tails (see e.g. Odenkirchen et al. 2003) or the deficiency of low mass stars, which are preferentially lost if energy equipartition holds (Henon 1969; Richer et al. 1991; de Marchi and Pulone 2007). Since these processes may lead to cluster dissolution on a timescale comparable to the lifetime of the globular clusters (see e.g. Lamers et al. 2005), current globular clusters are the survivors of a potentially larger initial population. The lack of knowledge about the properties of the original distribution of globular clusters and the subtleties of models of mass loss from globular clusters (see e.g. Kruijssen 2009) prevent an accurate estimate of the original total mass of globular clusters (see however Baumgardt et al. 2008). for an attempt to reconstruct these values from observed distributions). Up to now, data adequate to study the connection between the halo and globular clusters was insufficient.

On the other hand, various authors proposed scenarios for the formation of globular clusters (Peebles and Dicke 1968; Searle and Zinn 1978; Fall and Rees 1985; Cayrel 1986; Freeman 1990; Brown et al. 1991, 1995; Ashman and Zepf 1992; Murray and Lin 1992; Bromm and Clarke 2002; Kravtsov and Gnedin 2005; Saitoh et al. 2006; Bekki and Chiba 2002, 2007; Bekki et al. 2007; Hasegawa et al. 2009; Marcolini et al. 2009; Hartwick 2009). While very suggestive and intriguing, these scenarios either do not reproduce in a completely convincing way the whole spectrum of observations or are likely incomplete, describing only part of the sequence of events that lead to globular cluster formation or only a subset of them. We still lack a clear understanding of the globular cluster phenomenon.

Recent progresses are opening new promising perspectives. Very extensive surveys of field stars are now available, mainly (but not uniquely) thanks to 2MASS and the Sloan Digital Sky Survey and following surveys (see e.g. Carollo et al. 2008; Jurić et al. 2008; Martell and Grebel 2010), providing chemical and dynamical data for thousands of halo stars. In a few years, much more additional data are expected from projects like e.g. Pan-Starrs, HERMES, APOGEE, and GAIA, with spectroscopy, photometry and astrometry for millions of stars. With these large surveys, there is even the hope of tagging populations of field stars derived from individual globular clusters, at least in a few cases. On the other hand, the advent of efficient multi-object spectrographs on 8-m telescopes has overcome the main difficulty of gathering high quality, high resolution spectra to derive reliable abundances of several elemental species in globular clusters. As a result, extensive surveys providing detailed chemical composition of globular cluster stars are now routinely performed (see e.g. Gratton et al. 2007; Carretta et al. 2009a,b). These studies permit a much better insight into the properties of globular clusters.

158 R.G. Gratton et al.

## 2 Multiple Populations in Globular Clusters

Since almost forty years we know that large star-to-star abundance variations for several light elements are present in globular clusters (see Gratton et al. 2004 for a recent review). Regarded for long time as intriguing abundance anomalies restricted to some cluster stars, this observed peculiar chemical composition was only recently explicitly understood as a universal phenomenon in globular clusters, likely related to their very same nature/origin (Carretta et al. 2006, 2009a,b, 2010; see Figs. 2 and 3). The observational pattern of Li, C, N, O, Na, Al, Mg in cluster stars is currently well assessed (Gratton et al. 2004), thanks to several important milestones:

Abundance variations of the heavier species (O, Na, Mg, Al) are restricted to the
denser cluster environment. The signature for lighter elements (Li, C, N) may be
reproduced by assuming a mixture of primordial composition plus evolutionary
changes, both in low mass Pop II field stars and in their cluster analogues

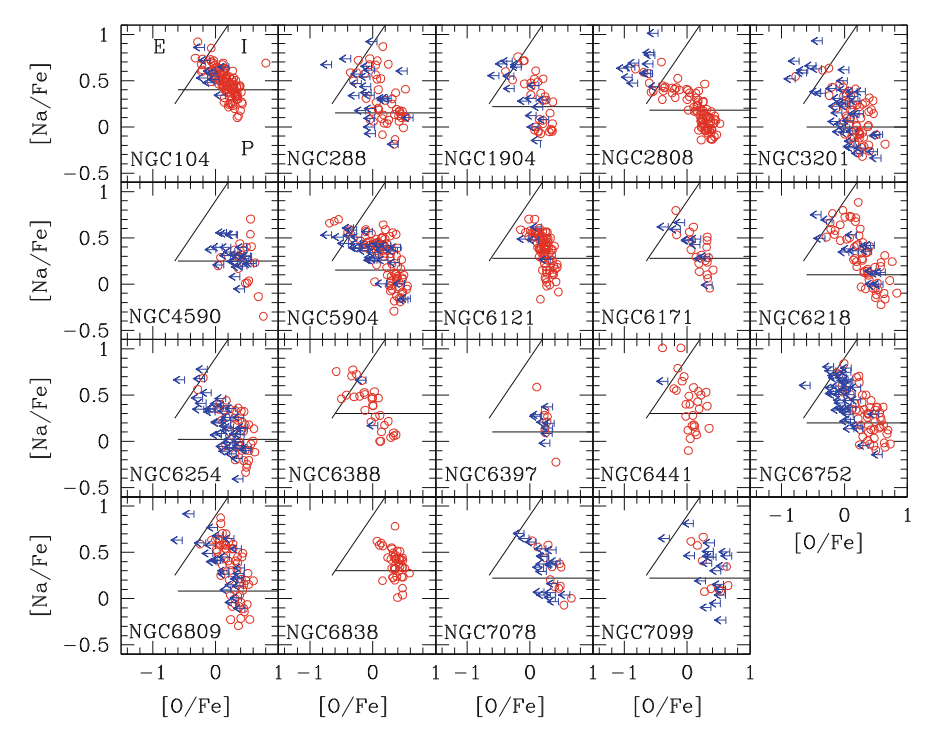


**Fig. 2** Summary of the Na-O anticorrelation observed in the 19 globular clusters. *Arrows* indicate upper limits in oxygen abundances. The two lines in each panel separate the Primordial component (located in the Na-poor/O-rich region, the only one present in Pop II field stars), the Na-rich/O-poor Extreme component, and the Intermediate component in-between (called P, E, and I, respectively as indicated only in the first panel). From Carretta et al. (2010)

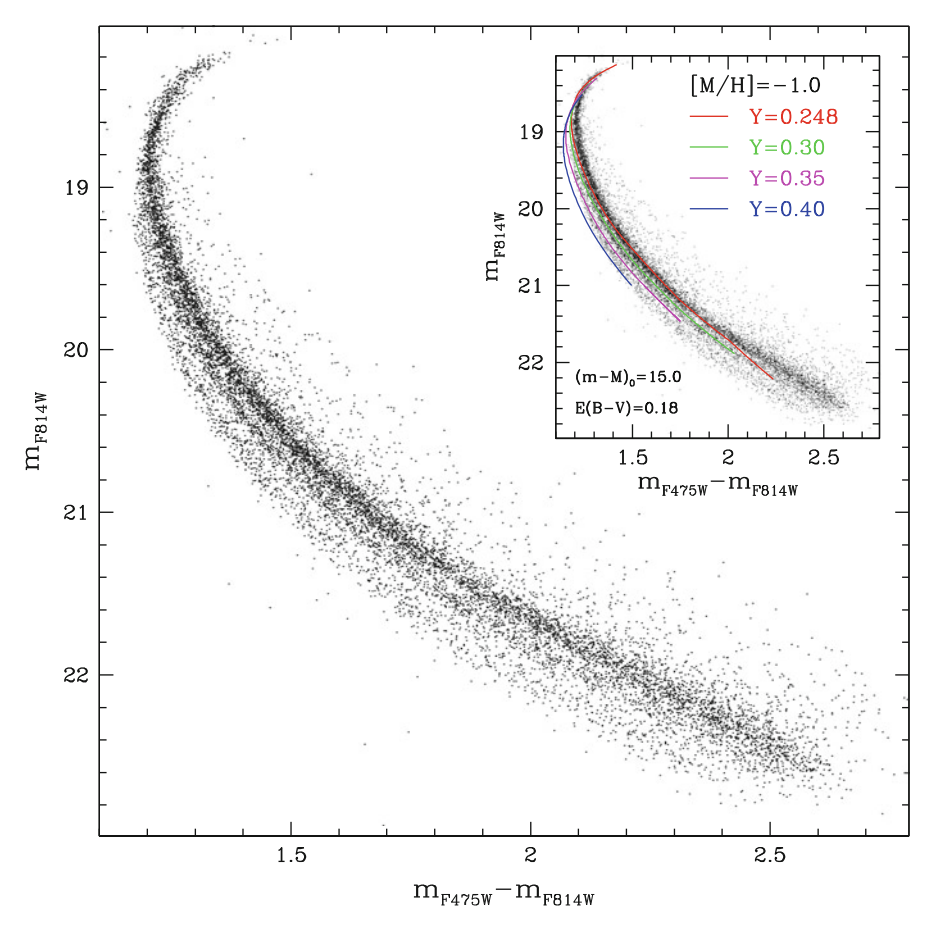


**Fig. 3** The triple main sequence of the globular cluster NGC2808 (from Piotto et al. 2007). The best explanation for this peculiar feature is a different He abundance, with *bluer stars* having an increased He abundance (Y 0.3–0.4) compared to the redder ones (with a standard Y 0.25)

(Charbonnel et al. 1998; Gratton et al. 2000; Smith and Martell 2003; see also the presentation by Charbonnel at this meeting).

- The observed pattern of abundance variations is established in proton-capture reactions of the CNO, NeNa and MgAl chains during H-burning at high temperature (Denisenkov and Denisenkova 1989; Langer et al. 1993);
- The variations are found also among unevolved stars currently on the main-sequence of globular clusters (Gratton et al. 2001; Ramírez and Cohen 2002; Carretta et al. 2004; D'Orazi and Marino 2010). This unequivocally implies that this composition has been imprinted in the gas by a previous generation of stars. The necessity of this conclusion stems from the fact that low-mass main sequence stars are unable to reach the high temperatures required for the nucleosynthesis

R.G. Gratton et al.

chains to produce the observed inter-relations between the elements (in particular the Mg-Al anticorrelation).

This calls for a class of now extinct stars, more massive than the low-mass ones presently evolving in globular clusters, as the site for the nucleosynthesis. Unfortunately, we do not know yet what kind of stars produced the pollution. The most popular candidates are either intermediate-mass asymptotic giant branch (AGB) stars (e.g., D'Antona and Ventura 2007) or fast rotating massive stars (FRMS, e.g., Decressin et al. 2007).

The observed abundance variations are also connected to the helium abundance, since He is the main outcome of H-burning (i.e., Na-rich, O-poor stars should also be He-rich). However, the relation between He abundance variations and the light element abundance pattern may be quite complicated. Multiple main sequences, attributed to populations with different He fraction Y, have been recently found in some globular clusters (ω Cen, NGC 2808: Bedin et al. 2004 and Piotto et al. 2007, respectively; see Fig. 3). There is a clear indication that Na-rich and Na-poor stars in NGC6218 and NGC6752 have slightly different red giant branch bump luminosities (Carretta et al. 2007), as expected from models of cluster sub-populations with different He content (Salaris et al. 2006). Gratton et al. (2010a) and Bragaglia et al. (2010a,b) examined in more detail the relation between He and light element abundance variations from evidence based on horizontal branch, red giant branch, and main sequence.

In summary, globular clusters are not exactly a single stellar population: they must harbour at least two stellar generations, as explained above, clearly distinct by their chemistry. These populations may be separated, provided data of adequate quality are available (and more easily with spectroscopy than with photometry). The patterns of anti-correlated Na-O, Mg-Al and, partly, C-N, Li-Na (and associated correlations) must be regarded as the fingerprints of these different sub-populations, and may be used to obtain insights into the early phases of formation and evolution of globular clusters, which are still obscure. The time scale for the release of matter processed by H-burning at high temperature is of the order of 10<sup>7</sup> yr if it comes from FRMS, and a few times longer if it comes from massive AGB stars. Thus, whatever the candidate producers, the observed patterns were already in place within some 10<sup>8</sup> yr after the start of cluster formation. These processes occurred on time-scales less than 1% of the typical total age of a globular cluster. The dynamical evolution that occurred in the remaining 99% of the cluster lifetime, while likely important, did not completely erase these fingerprints. Their fossil record is still recognisable in the chemical compositions of the low mass stars.

#### 3 A Scenario for the Formation of Globular Clusters

To decipher the relevant information we need large and homogeneous data sets, like the one recently gathered by Carretta et al. (2009a,b). Using this dataset, Carretta et al. (2010) were able to place the properties of different stellar generations

and global cluster parameters into a general framework for the formation of globular clusters. The presence of the Na-O anticorrelation may be used to separate globular clusters from smaller (open) clusters (see Fig. 4), globular clusters were then divided according to their kinematics and location in the Galaxy in three populations: disk/bulge, inner halo, and outer halo. The luminosity function of bona fide globular clusters (that is, those which exhibit the Na-O anticorrelation) is fairly independent of their population. This suggests that it is imprinted by the formation mechanism, and only marginally affected by the following evolution. The evidence of different generations within globular clusters given by their chemistry was then used considering separately the composition of the primordial population and of the second generation. A large fraction of the primordial population should have been lost by the proto-globular clusters. The fraction of primordial population stars lost by globular clusters may make up the main component of halo field stars (see also Martell and Grebel 2010; Conroy 2011; Schaerer and Charbonnel 2011). Arguments in favour include the total number of stars, the metallicity, kinematics and density distribution, and the chemistry. In addition, the extremely low Al abundances found for the primordial population of massive globular clusters is an indication of a very fast enrichment process before the formation of the primordial population. This suggests a scenario for the formation of globular clusters including at least three main phases: (a) the formation of a precursor population (likely due to the interaction with the early Galaxy or with other cosmological structures similar to those that led to the formation of dwarf Spheroidals, but residing at smaller

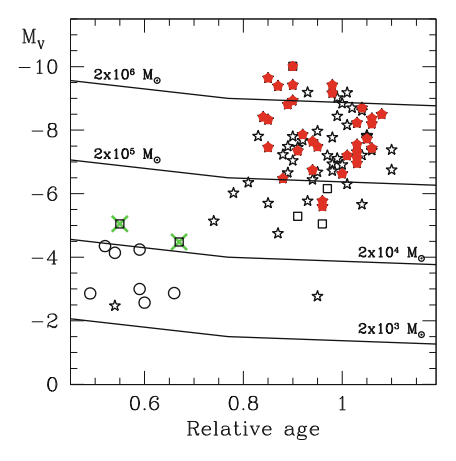


Fig. 4 Relative Age parameter vs absolute magnitude  $M_V$  for globular and old open clusters. Red filled pentagons and triangles are globular clusters where Na-O anticorrelation has been observed, in the Milky Way or the Large Magellanic Cloud respectively; green squares are clusters which do not show evidence for O-Na anticorrelation, both members of Sagittarius dwarf spheroidal. Open stars and triangles mark clusters for which not enough data is available, in the Milky Way or the Large Magellanic Cloud respectively. Open circles are old open clusters. Superimposed are lines of constant mass (light solid lines). The heavy blue solid line (at a mass of  $4 \times 10^4 \, \mathrm{M}_{\odot}$ ) is the proposed separation between globular and open clusters

galactocentric distances), (b) which triggers a large episode of star formation (the primordial population), and (c) then the formation of the current globular cluster, mainly within a cooling flow formed by the slow winds of a fraction of this primordial population. Some stars of the primordial population remain trapped in the newly forming cluster, producing the primordial component still observed in globular clusters. The precursor population is very effective in raising the metal content in massive and/or metal-poor (mainly halo) clusters, while its role is minor in small and/or metal rich (mainly disk) ones.

The proposed scenario for the origin of globular clusters offers a first framework to interpret the increasing information coming from spectroscopy and photometry of globular clusters, and suggests several tests that can be performed. Some are currently undertaken by our and other groups. For instance, Gratton et al. (2010a,b) showed that using this approach is possible to reproduce the observed features of the HB and AGB in term of the fundamental parameters mass, metallicity, and age, solving most of the aspects related to the long standing second parameter problem.

## 4 Open Points

However, in spite of the corroborating evidence coming from these studies, several issues are still dramatically open and/or poorly explored. These include:

- The nature of the polluters and their precise yields. There are two requisites: (1) the temperature must be high enough; and (2) the stars must be able to give back the nucleosynthesis products to the intracluster material at a velocity low enough that it can be kept within the cluster (a few tens of km s<sup>-1</sup>), possibly to be subsequently mixed with some pristine material (Prantzos and Charbonnel 2006). Two possible nucleosynthesis sites have been identified: (1) Massive  $(M > 25 \,\mathrm{M}_{\odot})$  rotating stars, before becoming Wolf-Rayet stars might lose mass through a low-velocity wind exposing regions where complete CNO-cycle has occurred (Decressin et al. 2007). (2) The most massive  $(4 < M < 8 \,\mathrm{M}_{\odot})$  of the intermediate mass stars, that undergo hot bottom burning during their AGB phase (Ventura et al 2001). These two mechanisms act on different timescales ( $< 10^7$ and several 10<sup>7</sup> yr, respectively) and then correspond to different hydrodynamical situations. Both solutions have assets and problems. In the massive star scenario it is not easy to avoid mixing O-poor, Na-rich material with that rich in heavy elements produced by the supernovae. On the other hand, producing the right pattern of abundances from massive AGB stars seems to require considerable fine tuning of models.
- The mass range where this scenario applies. This includes definition of both
  the low-mass (separating globular from open clusters) and the upper (relation
  between massive globular clusters, Ultra-Compact Dwarf galaxies and nuclear
  star clusters) ends. The low-mass end is likely related to the ability to retain the
  content of the slow winds discussed above (see Conroy 2011). The upper mass

end is very fuzzy and not well understood (for a recent discussion, see Forbes and Kroupa 2011).

- A full hydrodynamical treatment of the formation and evolution of globular clusters. Models developed up to now mainly concern the AGB scenario. In these models, it is not so obvious that secondary star formation can occur within globular clusters, given their shallow gravitational potential wells and the small mass fraction of AGB ejecta. Therefore, secondary star formation processes within clusters must be investigated by numerical simulations. 1-D models were first presented by D'Ercole et al. (2008). However, their models have limitations in predicting 3-D structures and kinematics of final stellar systems. 3-D stellar and gas dynamical numerical simulations with a plausible model for star formation were considered by D'Ercole et al. (2010) and Bekki (2011). A number of simplifications in these computations (e.g. that all mass is lost by AGB stars at the same time) make them not completely realistic. New more realistic models are required. Furthermore, the observational counterparts of young globular clusters are urgently required to constrain these models.
- The relation between globular clusters and field halo. Since globular clusters form under very special conditions, requiring large overdensities likely occurring during accretion episodes, this would link the formation of the halo to these peculiar phases.

#### References

```
Aguilar, L., Hut, P., Ostriker, J.P.: ApJ 335, 720 (1988)
Ashman, K.M., and Zepf, S.E.: ApJ 384, 50 (1992)
Baumgardt, H., Kroupa, P., Parmentier, G.: MNRAS 384, 1231 (2008)
Bedin, L.R., Piotto, G., Anderson, J., et al.: ApJ 605, L125 (2004)
Bekki, K.: MNRAS 412, 2241 (2011)
Bekki, K., Chiba, M.: ApJ 566, 245 (2002)
Bekki, K., Chiba, M.: ApJ 665, 1164 (2007)
Bekki, K., Campbell, S.W., Lattanzio, J.C., Norris, J.E.: MNRAS 377, 335 (2007)
Bragaglia, A., Carretta, E., Gratton, R., et al.: A&A 519, A60 (2010a)
Bragaglia, A., Carretta, E., Gratton, R.G., et al.: ApJ 720, L41 (2010b)
Bromm, V., Clarke, C.J.: ApJ 566, L1 (2002)
Brown, J.H., Burkert, A., Truran, J.W.: ApJ 376, 115 (1991)
Brown, J.H., Burkert, A., Truran, J.W.: ApJ 440, 666 (1995)
Carollo, D., Beers, T.C., Lee, Y.S., et al.: Nature 451, 216 (2008)
Carretta, E., Gratton, R.G., Bragaglia, A., Bonifacio, P., Pasquini, L.: A&A 416, 925 (2004)
Carretta, E., Bragaglia, A., Gratton, R.G., et al.: A&A 450, 523 (2006)
Carretta, E., Bragaglia, A., Gratton, R.G., Lucatello, S., Momany, Y.: A&A 464, 927 (2007)
Carretta, E., Bragaglia, A., Gratton, R., Lucatello, S.: A&A 505, 139 (2009a)
Carretta, E., Bragaglia, A., Gratton, R.G., et al.: A&A 505, 117 (2009b)
Carretta, E., Bragaglia, A., Gratton, R.G., et al.: A&A 516, A55 (2010)
Cayrel, R.: A&A 168, 81 (1986)
Charbonnel, C., Brown, J.A., Wallerstein, G.: A&A 332, 204 (1998)
Conroy, C.: ArXiv e-prints (2011)
D'Antona, F., Ventura, P.: MNRAS 379, 1431 (2007)
```

R.G. Gratton et al.

de Marchi, G., Pulone, L.: A&A 467, 107 (2007)

Decressin, T., Meynet, G., Charbonnel, C., Prantzos, N., Ekström, S.: A&A 464, 1029 (2007)

Denisenkov, P.A., Denisenkova, S.N.: Astron. Tsirkulyar 1538, 11 (1989)

D'Ercole, A., Vesperini, E., D'Antona, F., McMillan, S.L.W., Recchi, S.: MNRAS 391, 825 (2008)

D'Ercole, A., D'Antona, F., Ventura, P., Vesperini, E., McMillan, S.L.W.: MNRAS 407, 854 (2010)

D'Orazi, V., Marino, A.F.: ApJ 716, L166 (2010)

Fall, S.M., Rees, M.J.: ApJ 298, 18 (1985)

Forbes, D.A., Kroupa, P.: PASA 28, 77 (2011)

Freeman, K.C.: In: Gustafsson, B., Nissen, P.E. (eds.) Astrophysics: Recent Progress and Future Possibilities, pp. 187–194 (1990)

Gratton, R.G., Sneden, C., Carretta, E., Bragaglia, A.: A&A 354, 169 (2000)

Gratton, R.G., Bonifacio, P., Bragaglia, A., et al.: A&A 369, 87 (2001)

Gratton, R., Sneden, C., Carretta, E.: ARA&A 42, 385 (2004)

Gratton, R.G., Lucatello, S., Bragaglia, A., et al.: A&A 464, 953 (2007)

Gratton, R.G., Carretta, E., Bragaglia, A., Lucatello, S., D'Orazi, V.: A&A 517, A81 (2010a)

Gratton, R.G., D'Orazi, V., Bragaglia, A., Carretta, E., Lucatello, S.: A&A 522, A77 (2010b)

Hartwick, F.D.A.: ApJ 691, 1248 (2009)

Hasegawa, K., Umemura, M., Kitayama, T.: MNRAS 397, 1338 (2009)

Henon, M.: A&A 2, 151 (1969)

Jurić, M., Ivezić, Ž., Brooks, A., et al.: ApJ 673, 864 (2008)

Kravtsov, A.V., Gnedin, O.Y.: ApJ 623, 650 (2005)

Kruijssen, J.M.D.: A&A 507, 1409 (2009)

Lamers, H.J.G.L.M., Gieles, M., Portegies Zwart, S.F.: A&A 429, 173 (2005)

Langer, G.E., Hoffman, R., Sneden, C.: PASP 105, 301 (1993)

Marcolini, A., Gibson, B.K., Karakas, A.I., Sánchez-Blázquez, P.: MNRAS 395, 719 (2009)

Martell, S.L., Grebel, E.K.: A&A 519, A14 (2010)

Moore, B., Ghigna, S., Governato, F., et al.: ApJ **524**, L19 (1999)

Murray, S.D., Lin, D.N.C.: ApJ 384, 177 (1992)

Odenkirchen, M., Grebel, E.K., Dehnen, W., et al.: AJ 126, 2385 (2003)

Peebles, P.J.E., Dicke, R.H.: ApJ 154, 891 (1968)

Piotto, G., Bedin, L.R., Anderson, J., et al.: ApJ 661, L53 (2007)

Prantzos, N., Charbonnel, C.: A&A 458, 135 (2006)

Ramírez, S.V., Cohen, J.G.: AJ 123, 3277 (2002)

Richer, H.B., Fahlman, G.G., Buonanno, R., et al.: ApJ 381, 147 (1991)

Saitoh, T.R., Koda, J., Okamoto, T., Wada, K., Habe, A.: ApJ 640, 22 (2006)

Salaris, M., Weiss, A., Ferguson, J.W., Fusilier, D.J.: ApJ 645, 1131 (2006)

Schaerer, D., Charbonnel, C.: MNRAS 413, 2297 (2011)

Searle, L., Zinn, R.: ApJ 225, 357 (1978)

Smith, G.H., Martell, S.L.: PASP 115, 1211 (2003)

White, S.D.M., Rees, M.J.: MNRAS 183, 341 (1978)

## TRILEGAL, a TRIdimensional modeL of the GALaxy: Status and Future

Léo Girardi, Mauro Barbieri, Martin A.T. Groenewegen, Paola Marigo, Alessandro Bressan, Helio J. Rocha-Pinto, Basílio X. Santiago, Julio I.B. Camargo, and Luiz N. da Costa

L. Girardi (⊠)

Osservatorio Astronomico di Padova - INAF, Padova, Italy

Laboratório Interinstitucional de e-Astronomia – LIneA, Rio de Janeiro, RJ, Brazil

e-mail: leo.girardi@oapd.inaf.it

M. Barbieri

Observatoire Côte d'Azur, Nice, France

e-mail: mauro.barbieri@oca.eu

M.A.T. Groenewegen

Koninklijke Sterrenwacht van Belgium, Brussels, Belgium

e-mail: marting@oma.be

P. Marigo

Dipartimento di Astronomia, Università di Padova, Padova, Italy

e-mail: paola.marigo@unipd.it

A. Bressan

SISSA-ISAS, International School for Advanced Studies, Trieste, Italy

e-mail: alessandro.bressan@sissa.it

Osservatorio Astronomico di Padova - INAF, Padova, Italy

H.J. Rocha-Pinto

Universidade Federal do Rio de Janeiro, Observatório do Valongo, Rio de Janeiro, RJ, Brazil

e-mail: helio@iagusp.usp.br

Laboratório Interinstitucional de e-Astronomia - LIneA, Rio de Janeiro, RJ, Brazil

B.X. Santiago · J.I.B. Camargo

Universidade Federal do Rio Grande do Sul, Porto Alegre, RS, Brazil

e-mail: santiago@if.ufrgs.br; camargo@on.br

Laboratório Interinstitucional de e-Astronomia - LIneA, Rio de Janeiro, RJ, Brazil

L.N. da Costa

Observatório Nacional, Rio de Janeiro, RJ, Brazil

Laboratório Interinstitucional de e-Astronomia – LIneA, Rio de Janeiro, RJ, Brazil

e-mail: ldacosta@eso.org

A. Miglio et al. (eds.), *Red Giants as Probes of the Structure and Evolution of the Milky Way*, Astrophysics and Space Science Proceedings, DOI 10.1007/978-3-642-18418-5\_17, © Springer-Verlag Berlin Heidelberg 2012

L. Girardi et al.

**Abstract** We briefly describe TRILEGAL, a TRIdimensional modeL of thE GALaxy, and its more recent developments. Particularly relevant is the recent inclusion of a kinematical module to the code, and the present efforts to provide a more solid calibration of Milky Way parameters based on 2MASS and SDSS data.

#### 1 Introduction

Star count models find a wide range of applications in modern astrophysics. Since 2000 we have developed the TRIdimensional modeL of thE GALaxy (TRILEGAL), a Milky Way (MW) star counts model based on the population synthesis approach. It was initially conceived as a tool for the science verification of the ESO Imaging Survey, and especially to verify the reliability of the star counts provided by the EIS-deep surveys in several passbands and down to the limit in which galaxy counts largely surpass the stellar ones (Groenewegen et al. 2002). Present applications of TRILEGAL are quite varied, going from the direct determination of structural parameters of the MW (e.g. Vanhollebeke et al. 2009) to the forecast of the stellar content in future wide-area surveys (e.g. Kerber et al. 2009; Rossetto et al. 2011, Girardi et al. in prep.). It is also being extensively used to model external galaxies (e.g. Rubele et al., in prep.), to calibrate uncertain phases of stellar evolution, like the TP-AGB (Girardi and Marigo 2007; Girardi et al. 2010) and hot white dwarfs (Bianchi et al. 2011), or to test different subsamples of evolutionary tracks (Girardi et al. 2011).

The basic idea behind TRILEGAL, in its "MW mode", is very simple: it builds a geometric model for the MW, including main components such as the thin and thick disks, halo and bulge, each one containing a particular stellar population. The latter are defined by means of a star formation rate and age—metallicity relation. The main geometric parameters of the MW components are then calibrated using wide-area data for several lines-of-sight and for magnitudes at which the reddening is small and at magnitudes for which problems such as photometric incompleteness and stargalaxy separation are not an issue. Then, this simple model is applied everywhere in the MW, for different filters, and at deeper magnitudes, making the implicit assumption that the several MW components (but for the interstellar dust) are smoothly distributed and quite uniform in their distributions of ages/metallicities.

## 2 Simulating Photometric Catalogues

TRILEGAL is thoroughly described in Girardi et al. (2005). Figure 1 presents an updated scheme of the code in its version 1.3, which is available online. It allows

http://stev.oapd.inaf.it/trilegal.

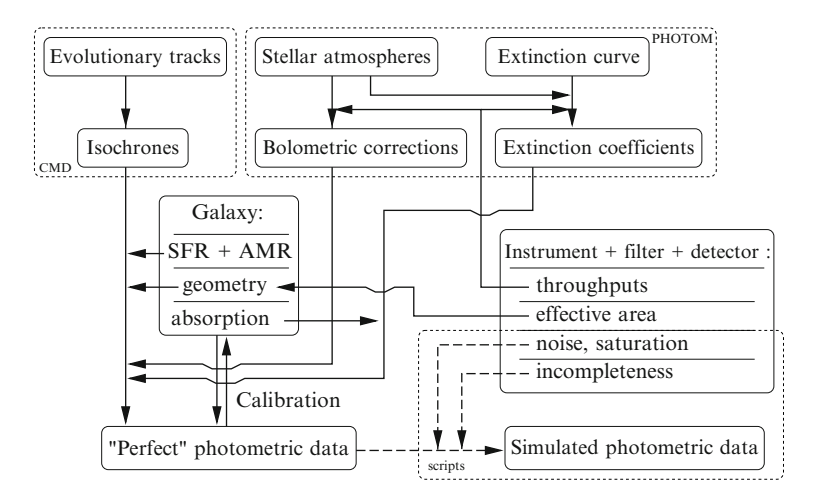


Fig. 1 The photometry part of TRILEGAL version 1.3, available via the web form http://stev.oapd.inaf.it/trilegal. This scheme does not include the kinematics module, which was developed successively

the simulation of catalogues for more than 20 photometric systems, going from the UV (e.g. GALEX and WFC3/UVIS) to the IR (e.g. Spitzer/MIPS and AKARI).

The calibration of version 1.3 is described on both Girardi et al. (2005), for the thin disk and halo, and Vanhollebeke et al. (2009) for the bulge. This latter work introduces an optimization method to refine the set of parameters that describes the triaxial bulge. In short, these parameters are varied by a BFGS optimization algorithm, that turns out to maximize the likelihood that the observations come from the density distribution given by the model. A wide set of 2MASS and OGLE data has been used to this aim.

We have been applying the same optimization algorithm, with minimal changes, to recalibrate the parameters for the disk(s)+halo in TRILEGAL, using 2MASS and SDSS data for 50 lines-of-sight almost evenly distributed across the sky. An improved solution has been reached, showing discrepancies in the star counts of the order of  $\sim 17\%$ , bin-per-bin, and in all  $ugrizJHK_c$  filters, over the entire magnitude range covered by these surveys. This new solution will be available from version 1.6 of TRILEGAL.

## 3 Simulating Kinematics

We have recently added a kinematical module to TRILEGAL, in order to simulate 3D velocities and proper motions for every model star. For each simulated star, we randomly pick a velocity from the Schwarzschild velocity distribution. Velocity ellipsoids are taken from the literature (Chiba and Beers 2000; Robin et al. 2003;

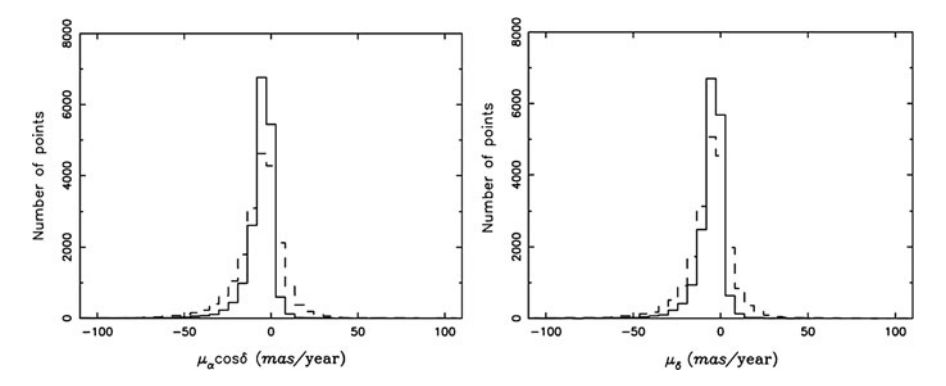


**Fig. 2** A comparison between the proper motions simulated by TRILEGAL (*continuous lines*) and the observed ones (*dashed lines*) in a well-defined subsample of UCAC3. The figure is taken from Rossetto et al. (2011)

Holmberg et al. 2009), and separately for the thin and thick disk, halo, and bulge. The model is admittedly very simple: for instance, cylindrical symmetry is adopted for all velocity ellipsoids, although we know that such an approximation cannot hold for large distances from the Sun. An empirical rotation curve from Dias and Lépine (2005) is adopted for the thin disk.

Rossetto et al. (2011) use this kinematical module to simulate the proper motions to be measured by the Dark Energy Survey (DES). The kinematical model is validated via a comparison with UCAC3 data (Zacharias et al. 2010), with excellent results, as can be appreciated in Fig. 2.

## 4 Perspectives from Spectroscopy and Asteroseismology

Star count models suffer from a significant drawback: there are degeneracies between stellar ages, metallicities and distances, that hamper the main goal of such models: deriving the full distance distribution of stars along the observed lines of sight. The best example of degeneracies is provided by Reylé and Robin (2001), who show that essentially the same thick disk star counts can be obtained with different combinations of local density and scale height. Our recalibration work for the MW disks (Girardi et al., in prep.), using more elaborate models and various sources of data, just reconfirms their results. In practice, there is no hope of obtaining a well-constrained thick disk geometry unless we have additional chemical and kinematical information for huge samples of stars. Data from surveys such as RAVE, SEGUE and SEGUE-2 (Steinmetz et al. 2006; Yanny et al. 2009; Eisenstein et al. 2011) are invaluable in this sense, although their potential for calibrating star count models are still largely unexplored (with a few notable exceptions, for instance Jurić et al. 2008; de Jong et al. 2010; Just et al. 2011, and Girardi et al., in prep.).

The perspectives of exploring galactic structure at large, across the MW disks and bulge, will improve dramatically with APOGEE (Eisenstein et al. 2011) with its near-infrared spectroscopy.

In this context of *removing degeneracies via the analysis of new observables*, the release of asteroseismic information for a large number of targets represents another major opportunity to MW star count models. Indeed, with CoRoT and *Kepler* we have, for the first time, direct access to *reliable* information about the distributions of stellar masses, radii (and hence distances), along a few lines of sights. The new potential of such kind of data is beautifully demonstrated by Chaplin et al. (2011), who show not only that TRILEGAL provides a good general description of the mass and radius distributions of dwarfs observed by *Kepler*, but also find a statistically significant discrepancy in the the distribution of stellar masses at  $\sim 1~M_{\odot}$ .

## 5 Closing Remarks

TRILEGAL is a very versatile code for the simulation of deep and/or widearea surveys. Its utility goes from the simple interpretation of already-existing data in terms of the properties of the observed stars, to the simulation of future surveys. Although the code has been calibrated mainly in optical and near-infrared passbands (DMS, EIS-deep, and 2MASS), the photometry can be simulated in a seemingly realistic way from the ultra-violet (e.g. GALEX) to the mid-infrared (e.g. Spitzer/MIPS and AKARI). In this way we can study exactly in the same way the star counts from classical and shallow surveys such as 2MASS, to those in newly-designed deep surveys such as DES. The addition of a kinematics module in TRILEGAL allows to greatly expand its range of applications, so as to explore the improved spectroscopic (e.g. RAVE, SEGUE and SEGUE-2) and astrometric (e.g. Tycho and UCAC3) data nowadays available. TRILEGAL is also being expanded to take advantage of the rich spectroscopic data that is about to be collected by APOGEE for giants all across the Galaxy. Last but not least, we are already exploring the completely new constraints provided by CoRoT and Kepler, which will hopefully be expanded over wide areas of the sky by PLATO.

**Acknowledgements** Funding for the SDSS-III Brazilian Participation Group has been provided by the Ministério de Ciência e Tecnologia (MCT), Fundação Carlos Chagas Filho de Amparo à Pesquisa do Estado do Rio de Janeiro (FAPERJ), Conselho Nacional de Desenvolvimento Científico e Tecnológico (CNPq), and Financiadora de Estudos e Projetos (FINEP).

This research was made possible by the Laboratório Interinstitucional de e-Astronomia (LIneA) operated jointly by the Centro Brasileiro de Pesquisas Físicas (CBPF), the Laboratório Nacional de Computação Científica (LNCC) and the Observatório Nacional (ON) and funded by the Brazilian Ministry of Science and Technology (MCT).

L.G. acknowledges the hospitality of ON-Rio during several visits. His travels have been partially funded by the PRIN INAF07 project CRA 1.06.10.03.

170 L. Girardi et al.

#### References

Bianchi, L., Efremova, B., Herald, J., et al.: MNRAS 411, 2770 (2011)

Chaplin, W.J., Kieldsen, H., Christensen-Dalsgaard, J., et al.: Science 332, 213 (2011)

Chiba, M., Beers, T.C.: AJ 119, 2843 (2000)

de Jong, J.T.A., Yanny, B., Rix, H.-W., et al.: ApJ 714, 663 (2010)

Dias, W.S., Lépine, J.R.D.: ApJ **629**, 825 (2005)

Eisenstein, D.J., Weinberg, D.H., Agol, E., et al.: AJ 142, 72 (2011)

Girardi, L., Marigo, P.: Astronomical Society of the Pacific Conference Series. In: Kerschbaum, F., Charbonnel, C., Wing, R.F. (eds.) Why Galaxies Care About AGB Stars: Their Importance as Actors and Probes, vol. 378, p. 20 (2007)

Girardi, L., Groenewegen, M.A.T., Hatziminaoglou, E., da Costa, L.: A&A 436, 895 (2005)

Girardi, L., Williams, B.F., Gilbert, K.M., et al.: ApJ 724, 1030 (2010)

Girardi, L., Eggenberger, P., Miglio, A.: MNRAS 412, L103 (2011)

Groenewegen, M.A.T., Girardi, L., Hatziminaoglou, E., et al.: A&A 392, 741 (2002)

Holmberg, J., Nordström, B., Andersen, J.: A&A **501**, 941 (2009)

Jurić, M., Ivezić, Ž., Brooks, A., et al.: ApJ **673**, 864 (2008)

Just, A., Gao, S., Vidrih, S.: MNRAS 411, 2586 (2011)

Kerber, L.O., Girardi, L., Rubele, S., Cioni, M.-R.: A&A 499, 697 (2009)

Reylé, C., Robin, A.C.: A&A 373, 886 (2001)

Robin, A.C., Reylé, C., Derrière, S., Picaud, S.: A&A 409, 523 (2003)

Rossetto, B.M., Santiago, B.X., Girardi, L., et al.: AJ 141, 185 (2011)

Steinmetz, M., Zwitter, T., Siebert, A., et al.: AJ 132, 1645 (2006)

Vanhollebeke, E., Groenewegen, M.A.T., Girardi, L.: A&A 498, 95 (2009)

Yanny, B., Rockosi, C., Newberg, H.J., et al.: AJ 137, 4377 (2009)

Zacharias, N., Finch, C., Girard, T., et al.: AJ 139, 2184 (2010)

## The Besançon Model of Stellar Population Synthesis of the Galaxy

Annie C. Robin, Céline Reylé, Douglas J. Marshall, and Mathias Schultheis

Abstract We present the most recent developments of the Besançon Galaxy model and results obtained from analysis of near-infrared large scale surveys and a new 3D map of the extinction. Giants are the main tracers and are used to characterized the large scale structures in the outer disc and in the inner regions. The warp has been found to be asymmetric and weaker than the HI warp. In the central region, the dust lanes associated with the bar have been detected, characterized and compared with the dust lanes in CO. The nuclear bar is also detected. An improved model of the bulge/bar has been established and the discovery of an in-plane overdensity which could be interpreted as either a second long thin bar, or a merger residual.

#### 1 Introduction

The main objective of Galactic astronomy today is to understand the overall scheme of the formation of galaxies and the physical processes involved. The big questions to answer are: What is the mass distribution? How is the mass cycled through the Galaxy? What is the merging history? Is the Galaxy consistent with the standard cosmological model? Which stars have been formed where and when? The population synthesis approach is dedicated to simulate the stellar content in the Galaxy based on a scenario of formation of the Galaxy. It is a useful tool to

A.C. Robin  $(\boxtimes) \cdot C$ . Reylé  $\cdot$  M. Schultheis

Institut Utinam, CNRS UMR6213, Université de Franche-Comté, Observatoire de Besançon, Besançon, France

e-mail: annie.robin@obs-besancon.fr; celine@obs-besancon.fr; mathias@obs-besancon.fr

D.I. Marshall

Université de Toulouse, UPS-OMP, IRAP, 31028 Toulouse cedex 4, France

CNRS, Institut de Recherche en Astrophysique et Planétologie, 9 Av. colonel Roche, BP 44346, 31028 Toulousecedex 4, France

e-mail: douglas.marshall@cesr.fr

172 A.C. Robin et al.

test various scenarii of formation by comparing the simulations with existing data coming from surveys at different wavelengths. In the following sections we shall describe the inputs and hypothesis done in the Besançon Galaxy model, then show comparisons with large scale surveys, and results concerning galactic structure and evolution, and conclude with the perspectives of this approach.

## 2 Scheme of the Population Synthesis Model

The population synthesis approach aims at assembling current scenarios of galaxy formation and evolution, theories of stellar formation and evolution, models of stellar atmospheres and dynamical constraints, in order to make a consistent picture explaining currently available observations of different types (photometry, astrometry, spectroscopy) at different wavelengths. The validity of any Galactic model is always questionable, as it describes a smooth galaxy, while inhomogeneities exist, either in the disc or the halo. The issue is not to make a perfect model that reproduces the known Galaxy at any scale. Rather one aims to produce a useful tool to compute the probable stellar content of large data sets and therefore to test the usefulness of such data to answer a given question in relation to Galactic structure and evolution. Modelling is also an effective way to test alternative scenarii of galaxy formation and evolution.

The originality of the Besançon model, as compared to a few other population synthesis models presently available for the Galaxy, is the dynamical self-consistency. The Boltzmann equation allows the scale height of an isothermal and relaxed population to be constrained by its velocity dispersion and the Galactic potential Bienaymé et al. (1987). The use of this dynamical constraint avoids a set of free parameters quite difficult to determine: the scale height of the thin disc at different ages. It gives the model an improved physical credibility. However this constraint is only applied at the solar position and perpendicular to the plane. A more fully consistent dynamical model would apply self-consistency constraints at any position in the Galaxy.

The main scheme of the model is to reproduce the stellar content of the Galaxy, using some physical assumptions and a scenario of formation and evolution. We essentially assume that stars belong to four main populations: the thin disc, the thick disc, the stellar halo (or spheroid), and the outer bulge. The modelling of each population is based on a set of evolutionary tracks, assumptions on density distributions, constrained either by dynamical considerations or by empirical data, and guided by a scenario of formation and evolution, that is to say assumptions on initial mass function (IMF) and star formation rate (SFR) for each population. A detailed description is given in Robin et al. (2003).

The Galactic model has been developed to return results in the near-infrared and visible filters, but has also been extended to predict the stellar content in the X-ray domain (Guillout et al. 1996). More recently, a new study of the bulge region has led

to revisions of the parameters of this population and the discovery of an overdensity in the plane (Robin et al. 2011).

The main characteristics of each populations in the latest version of the Besançon Galaxy model are described below.

## 2.1 The Thin Disc Population

A standard evolution model is used to produce the disc population, based on a set of evolutionary tracks, a constant star formation rate (hereafter SFR) over 10 Gyr and a two-slope Initial Mass Function  $\phi(M) = A \times M^{-\alpha}$  with  $\alpha = 1.6$  for M<  $1M_{\odot}$  and  $\alpha = 3.0$  for M> $1M_{\odot}$ . The preliminary tuning of the disc evolution parameters against relevant observational data was described in Haywood et al. (1997a,b) and further changes are explained in Robin et al. (2003).

Using the evolution model we populate the thin disc dividing it into seven age components. For each subcomponent the distribution in absolute magnitude and effective temperature is obtained, assuming a star formation history constant over the last 10 Gyr. The star counts are computed using the standard equation of stellar statistics from the distribution in  $M_V$  and a spatial density distribution. Hence it is equivalent to assume that the SFR is roughly the same all over the thin disc.

The thin disc density distribution model follows the Einasto (1979) law: the distribution of each disc component (except for the very young one of age less than 150 million years which is not important here) is described by an axisymmetric ellipsoid with an axis ratio depending on the age; the density law of the ellipsoid is described by the subtraction of two functions:

$$\rho_d = \rho_{d_0} \times \left[ \exp(-\sqrt{0.25 + (\frac{a}{R_d})^2}) - \exp(-\sqrt{0.25 + (\frac{a}{R_h})^2}) \right]$$

with 
$$a^2 = R^2 + \left(\frac{Z}{\epsilon}\right)^2$$
, where:

- R and Z are the cylindrical Galactocentric coordinates.
- $\epsilon$  is the axis ratio of the ellipsoid. Values of  $\epsilon$  as a function of age and local normalisation are given in Robin et al. (2003).
- $R_d$  is the scale length of the disc up to the disc edge (see below). This value has been redetermined to be 2.5 kpc in Robin et al. (2011).
- $R_h$  is the scale length of the hole. It is also fitted to the value of 0.9 kpc. However the hole might not be symetrical and could be larger at negative longitudes than at positive ones. The maximum density of the disc population is approximately at 2 kpc from the centre.
- The normalization  $\rho_{d_0}$  is deduced from the local luminosity function (Jahreiß et al, CNS3, private communication), assuming that the Sun is located at  $R_{\odot} = 8$  kpc and  $Z_{\odot} = 15$  pc.

In the external disc, the exponential is truncated following several studies which have shown that the edge of the disc is detected at a galactocentric distance of about 14 kpc (Robin et al. 1992; Ruphy et al. 1996). The disc is also warped and flared and all stellar components in the disc have the same warp and flare. The warp and flare parameters have been studied by comparison of simulated star counts with 2MASS data (Reylé et al. 2009). They concluded that the warp in stars is not symmetric (as observed for the HI warp) but is less pronounced than the HI or the dust warp. The warp is found to start at about the sun galactocentric distance (as the flare), and to have a linear slope of 0.09, as a first approximation, in the first and second quadrant. At negative longitudes, the warp is distorted: it does not follow the classical S shape, neither does it follow the complex shape of the HI warp, as modelled by Levine et al. (2006). Its shape has still to be investigated in detail.

#### 2.2 The Thick Disc

The thick disc formation scenario that drives the model characteristics is a formation by a merger event (or several merger events) at the beginning of the life of the thin disc. This scenario well explains the observed properties of this population: The accretion body heats the stellar population previously formed in the disc making a thicker population with larger velocity dispersions. Due to the epoch of this event, the thick disc abundances are intermediate between the stellar halo and the present thin disc. We have adopted an age of 11 Gyr for this population. This is just slightly older than the thin disc, and is younger than the stellar halo in agreement with Fuhrmann (1998). The choice of the slightly different age (by 1 Gyr) would not significantly change wide band photometric star counts.

In order to model this population, a single epoch of star formation (that is a period of formation negligible compared to the age of the Galaxy) is assumed. Oxygen enhanced evolutionary tracks have been taken from Bergbush and VandenBerg (1992). The horizontal branch (HB) has been added following models from Dorman (1992). Stars of effective temperature between 7,410 and 6,450 K are assumed to be RRLyrae. There is no blue horizontal branch, as in metal rich globular clusters. The position of the HB is assumed to be 3.54 visual magnitudes brighter than the main sequence turnoff.

The thick disc density law has often been assumed in the literature to be exponentially decreasing perpendicular to the Galactic plane. Tests of various laws have been performed by comparing data with model predictions in various directions. At present time, it does not seem possible to obtain detailed constraints on the true shape, either exponential or  $\operatorname{sech}^2$ , because the distances are not known with sufficient accuracy. Moreover the contribution of nearby stars to the star counts is often negligible due to the small volume where they are counted. We have assumed that the thick disc shape is a truncated exponential along the z axis: at large distances the law is exponential, at short distances it is a parabola. This option

ensures the continuity and derivability of the density law in the plane, to ease the computation of the thick disc contribution to the potential.

The density law parameters and IMF adopted are constrained by the analysis of deep wide field and near-infrared star counts at high and intermediate Galactic latitudes (Reylé and Robin 2001). The best fit model has a scale length  $h_R = 2,500 \pm 500\,\mathrm{pc}$ , a scale height  $h_z = 800 \pm 50\,\mathrm{pc}$  with  $x_l = 400\,\mathrm{pc}$ , and a local density  $\rho_0 = 1.36 \times 10^{-3}\,\mathrm{stars}\,\mathrm{pc}^{-3}$  for  $\mathrm{M}_V \leq 8$ , corresponding to 8.8% of the thin disc local density. These values are being reinvestigated using the SDSS3 survey.

#### 2.3 The Stellar Halo

The spheroid, or stellar halo, is essentially an old and metal poor population. The stellar halo should be considered distinct from the dark matter halo, which is probably mainly non baryonic, although a small part of it can be formed of stellar remnants. Our standard model assumes a homogeneous population of spheroid stars with a short period of star formation. We do not assume any stream and sub-structure but we model a smooth halo. Comparisons with true data should then, by contrast, help finding existing streams. Bergbush and VandenBerg (1992) oxygen enhanced models are used assuming a Gaussian metallicity distribution of mean -1.78 and dispersion 0.5 dex. The age of the spheroid is assumed to be 14 Gyr, a value which may be slightly high, as constrained by the analysis of the WMAP experiment (Bennett et al. 2003). However, a change by 0.5 Gyr would have no effects on star count predictions.

The density law and IMF of the spheroid were constrained using deep star counts at high and medium Galactic latitudes (Robin et al. 2000). This global adjustment of the spheroid shape has led to the following values: the density law is characterized by a power law index n = 2.44, a flattening  $\epsilon = 0.76$  and a local density  $\rho_0 = 4.87 \times 10^{-5} \,\mathrm{pc}^{-3}$  including all red dwarfs down to the hydrogen burning limit, but not the white dwarfs. This local density has been computed with an IMF  $dN/dm \propto m^{-0.5}$ , similar to the globular clusters and to the thick disc population. The relative density of the spheroid to the disc is about 0.09% for stars at  $M_V < 8$ . At fainter magnitudes the luminosity function is not well constrained. In Robin and Reylé (2007) and Robin et al. (2007) a new study of the halo shape and density was attempted using Cosmos data up to magnitudes I = 24, and a set of shallower data towards various directions. Using the density at the turnoff, a new fit suggests a larger exponent for the power law, close to the standard value of n=3. A new investigation is now being conducted using the latest release of the SDSS3 data (SDSS-III collaboration: Aihara et al. 2011), covering a much larger portion of the sky, hence providing better constraints on the shape of the halo, and the possible existence of a dual halo.

176 A.C. Robin et al.

## 2.4 The Bulge Region

In Picaud and Robin (2004) we investigated characteristics of the outer bulge stellar populations, studying its density and luminosity function by fitting model parameters to a set of 100 windows in the outer bulge. The bulge stellar population was taken from a single burst population of age varying between 6 and 10 Gyr. The favoured combinations between age and evolution model was from Girardi et al. (2002) with an age of 7.94 Gyr (log(age) = 9.9). It appears that the  $K_s$  band counts are not very sensitive to the age and a proper estimation of the age and age range of the populations in the bulge would require complementary data.

Since then a number of studies have shown very different results concerning the bulge, its shape and orientation. Exploring the bulge region of our Galaxy is an interesting but challenging quest, because of the complex structure and the highly variable extinction in this region. The apparent orientation of the bulge seems to vary depending on the range of longitude and latitude considered. This is why we have investigated the bulge population using a full 3D map of the inner Galaxy.

## 3 Taking into Account the Extinction

The interstellar extinction is a major problem when trying to study the stellar populations close to the Galactic plane. This is why we have developed a 3D map of the extinction which allows us to simulate realistic stellar distributions even in regions of high extinction. In order to produce this map, we used the 2MASS colour distributions and compared in every line of sight with simulations coming from the Galaxy model, assuming a first estimate based on a smooth extinction distribution. An iterative process was then applied to modify the extinction in order to reproduce quantitatively the J-K distribution. The algorithm was described in detail in Marshall et al. (2006). It has been shown to give very satisfactory results, and to correlate very well with the CO map density (see Fig. 1) from Dame et al. (2001), as well as with 2D maps obtained with different methods (Schultheis et al. 1999; Dutra et al. 2003; Drimmel et al. 2003).

The detailed description of the extinction distribution in the bulge region has allowed for the first time to detect the dust lanes related to the bar. In Marshall et al. (2008) we have compared the position and shape of these dust lanes with the position as determined from CO data using the Fux (1999) model. The dust lanes looks very similar in both tracers and are found to be out of the Galactic plane, appearing at negative latitudes for  $l > 0^{\circ}$  and at positive latitudes for  $l < 0^{\circ}$ . However, even though there is substantial overlap between the two components, they are offset from one another with the dust appearing to lie closer to the  $b = 0^{\circ}$  plane.

In Robin et al. (2011) we re-analysed photometric near-infrared data in order to solve the problem of the shape and characteristics of the populations in the bulge region. The study used the Besançon Galaxy Model to provide a scheme for

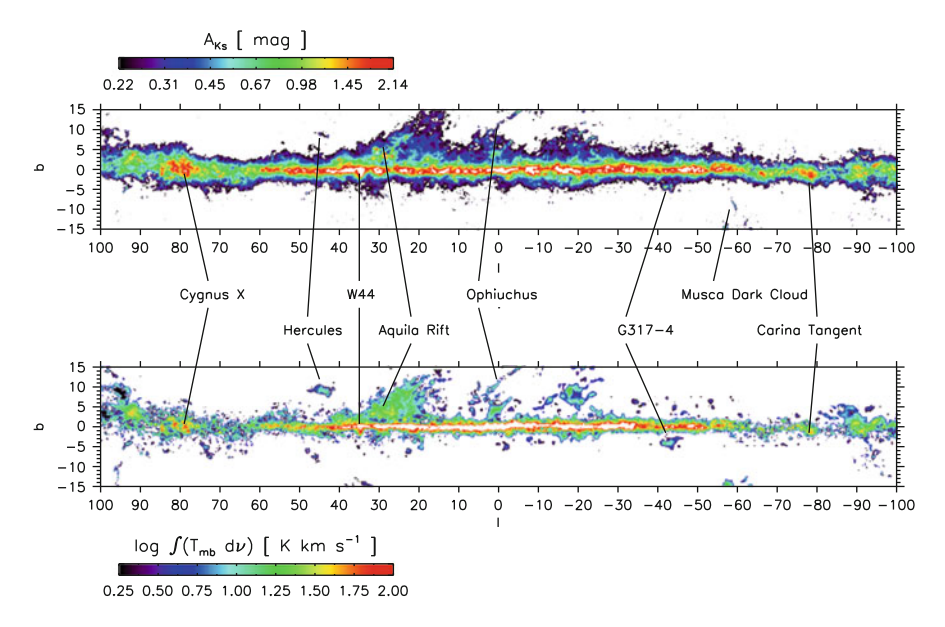


**Fig. 1** *Top*: total extinction integrated along the line of sight. *Bottom*: CO velocity integrated spatial map by Dame et al. (2001). The units of the two maps are different; they are put here to compare their respective interpretation of the large scale structure of the Galaxy. The coordinates are expressed in degrees (l, b)

parameter fitting of the structural characteristics of the bulge region. The fitting process allows the determination of the global shape of the bulge main structure but also suggests the presence of a new structure lying between us and the bulge. The results show that, on top of a quite standard triaxial boxy bulge with an orientation of about 17° with regard to the Sun-centre direction, a second population is seen preferentially at  $|l| < 4^\circ$  in the in-plane region. It is a structure elongated along the sun-centre axis. Our study does not show whether this structure is dominated by a young or old population. It may be related to a thin in-plane bar, as seen for example in M83 galaxy, or may be due to an on-going merger in the plane of the Milky Way. This stellar structure can have been missed by many studies due to the intrinsic difficulty in exploring the in-plane region in the presence of high extinction. The inclusion of this structure in the process of model fitting allows a better estimate of the shape of the central bulge, and it also reveals the presence of the nuclear bar near the Galactic centre.

New model star count predictions compare well with 2MASS star counts in the  $K_s$  band. Figure 2 shows maps of star counts in the Galactic plane in the  $K_s$  band up to magnitude 12 from 2MASS (top) and in the new model (middle panel). The bottom panel shows the residuals  $(N_{model}-N_{observed})/N_{observed}$  of the same quantities. It shows that in most of the regions the model is in good agreement with 2MASS star counts. Although, significant discrepancies still exists in specific regions, like in the outer disc, due to an asymmetric warp for which no satisfactory formula was

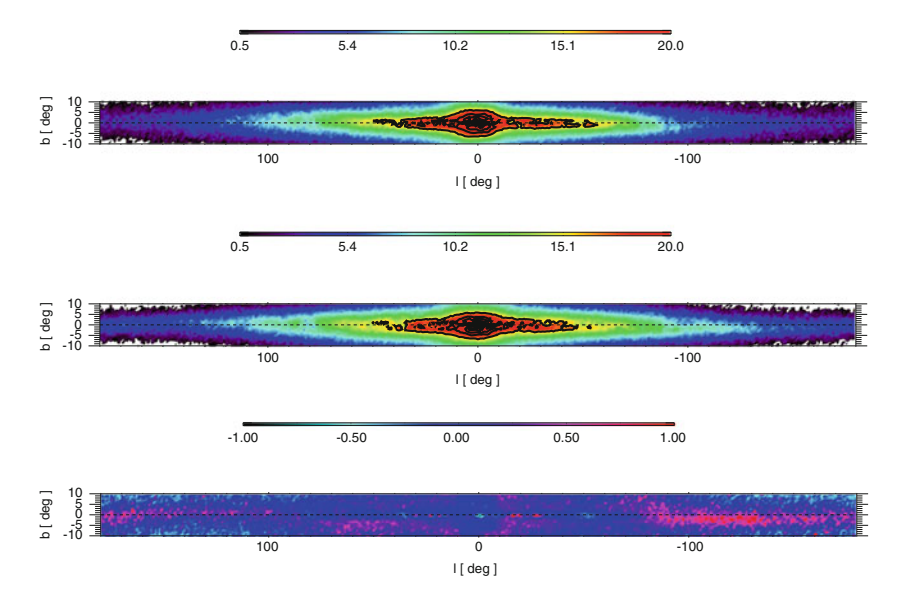
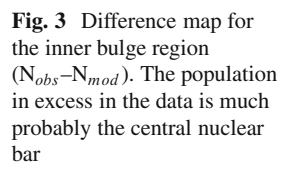
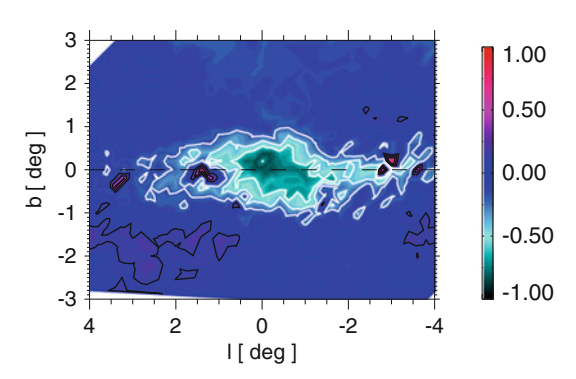


Fig. 2 Maps of star counts in the  $K_s$  band up to magnitude 12 from 2MASS (top), the new model (middle panel) in the galactic plane, and residuals  $(N_{model} - N_{observed})/N_{observed}$  (bottom panel)





found. This is also the case in a few regions in the plane, in particular in regions where we expect significant contributions from giant star formation regions related to spiral arms (which are not included there) at longitudes  $26^{\circ}$  and  $-50^{\circ}$ , and in the Galactic center. For example Fig. 3 shows a more detailed view of the difference map for the inner bulge region ( $N_{obs}$ – $N_{mod}$ ). The population in excess in the data is much probably the central nuclear bar. However it is not straightforward to deduce the properties of this structure from the present study because the 3D map saturates at about  $A_K = 3$  which leads to an overestimation in the model of the stellar density. It is clear that the nuclear bar is a population which should be added in the model in the near future.

## 4 Perspectives

Modelling the Galaxy through its stellar populations is a very challenging but fruitful task. It helps the understanding and testing of scenarii for the formation of the Milky Way, which will also give new insight in galaxy formation in general. With forthcoming large scale surveys like Gaia, PanStarrs, LSST and many others, the challenge will be raised again and new methods will be needed to exploit the data and to interpret them in terms of galactic evolution. Stellar population models will continue to be useful tools and new statistical methods will be developed to compare model simulations with the data in the many observable space, and to fit the model parameters. One of our goals is to develop a dynamical model based on this approach implying a dynamically consistent description of the stellar motions which will be constrained by astrometric data, in particular from the Gaia mission. The second aim will be to include a comprehensive chemical evolution model, which will be able to help the interpretation of new chemical abundances surveys like HERMES and APOGEE.

Acknowledgements This publication makes use of data products from the Two Micron All Sky Survey, which is a joint project of the University of Massachusetts and the Infrared Processing and Analysis Center/California Institute of Technology, funded by the National Aeronautics and Space Administration and the National Science Foundation. The CDSClient package was used for the remote querying of the 2MASS dataset. Simulations have been executed on computers from the Utinam Institute of the Université de Franche-Comté, supported by the Région de Franche-Comté and Institut des Sciences de l'Univers (INSU).

#### References

Bennett, C.L., Halpern, M., Hinshaw, G., Jarosik, N., Kogut, A., Limon, M., Meyer, S.S., Page, L., Spergel, D.N., Tucker, G.S., Wollack, E., Wright, E.L., Barnes, C., Greason, M.R., Hill, R.S., Komatsu, E., Nolta, M.R., Odegard, N., Peirs, H.V., Verde, L., Weiland, J.L.: preprint astro-ph/0302207 ApJS 148,1 (2003)

Bergbush, P.A., VandenBerg, D.A.: ApJS 81, 163 (1992)

Bienaymé, O., Robin, A. C., Creze, M.: A&A 186, 359 (1987)

Dame, T.M., Hartmann, D., Thaddeus, P.: ApJ 547, 792 (2001)

Dorman, B.: ApJS 81, 221 (1992)

Drimmel, R., Cabrera-Lavers, A., López-Corredoira, M.: A&A 409, 205 (2003)

Dutra, C.M., Santiago, B.X., Bica, E.L.D., Barbuy, B.: MNRAS 338, 253 (2003)

Einasto, J.: IAU Symp., vol. 84. In: Burton, W.B. (ed.) The Large Scale Characteristics of the Galaxy (1979)

Furhmann, K.: A&A 338, 161 (1998)

Fux, R.: A&A 345, 787 (1999)

Girardi, L., Bertelli, G., Bressan, A., Chiosi, C., Groenewegen, M.A.T., Marigo, P., Salasnich, B., Weiss, A.: A&A 391, 195 (2002)

Guillout, P., Haywood, M., Motch, C., Robin, A.C.: A&A 316, 89 (1996)

Haywood, M., Robin, A.C., Crézé, M.: A&A **320**, 428–439 (1997)

Haywood, M., Robin, A.C., Crézé, M.: A&A 320, 440-459 (1997)

Levine, E.S., Blitz, L., Heiles, C.: ApJ 643, 881 (2006)

180 A.C. Robin et al.

Marshall, D.J., Robin, A.C., Reylé, C., Schultheis, M., Picaud, S.: A&A 453, 635 (2006)

Marshall, D.J., Fux, R., Robin, A.C., Reylé, C.: A&A 477, 21 (2008)

Picaud, S., Robin, A.C.: A&A 428, 891 (2004)

Reylé, C., Robin, A.C.: A&A 373, 886 (2001)

Reylé, C., Marshall, D.J., Robin, A.C., Schultheis, M.: A&A 495, 819 (2009)

Robin, A.C., Reylé, C.: In: de Boer, K.S., Kroupa, P. (eds.) The Milky Way Halo – Stars and Gas, http://www.astro.uni-bonn.de/~mwhalo/proceedings/mwh-t03-robin.pdf (2007)

Robin, A.C., Crézé, M., Mohan, V.: ApJ 400, L25 (1992)

Robin, A.C., Reylé, C., Crézé, M.: A&A 359, 103 (2000)

Robin, A.C., Reylé, C., Derrière, S., Picaud S.: A&A 409, 523 (2003)

Robin, A.C., et al.: ApJS 172, 545 (2007)

Robin, A.C., Marshall, D.J., Schultheis, M., Reyle, C.: arXiv:1111.5744 (2011)

Ruphy, S., Robin, A.C., Epchtein, N., Copet, E., Bertin, E., Fouqué, P., Guglielmo, F.: A&A 313, L21 (1996)

Schultheis, M., Ganesh, S., Simon, G., et al.: A&A 349, L69 (1999)

Aihara, H., Allende Prieto, C., An, D., et al.: ApJS 195, 26 (2011)

## **Index**

Atmospheres

1D models, 130–132 3D models, 125–132	Kepler, 4–6, 11, 14, 15, 19, 20, 28–31, 40, 45, 96, 131, 150, 153–154, 169
granulation, 131–132	90, 131, 130, 133–134, 109
Atomic diffusion, 55, 59, 64, 98	
	2MASS, 157, 167, 169, 174, 176–178
	Mass loss, 12, 14, 47, 48, 55, 81, 82, 90, 106,
Convection	156, 157
2D and 3D models, 88, 90	The Milky Way
full spectrum of turbulence (FST), 59, 71–76	age-metallicity relation (AMR), 138, 152, 155, 156
Ledoux criterion, 54, 82	age-velocity dispersion relation (AVR), 138
mixing length theory (MLT), 36, 50, 59,	bulge, 142–143, 148–151
70–76, 88, 89, 126, 130–131	halo, 139–145
overshooting, 55, 60, 85, 88, 89, 96, 131	initial mass function (IMF), 143, 151 star formation history, 137
penetration, 89	thick disk, 139–142, 144, 145, 150–152
Schwarzschild criterion, 50, 59, 82, 84, 85, 88	thin disk, 137–140, 144, 145, 148, 150–154
semiconvection, 50, 82, 85	
shell convection, 87–93	
superadiabatic convection, 60, 62	4MOST, 147
	4MOST, 147 OGLE, 4, 167
superadiabatic convection, 60, 62	
superadiabatic convection, 60, 62 CoRoT, 4–6, 8, 9, 11–16, 19, 20, 28–31, 38,	OGLE, 4, 167
superadiabatic convection, 60, 62 CoRoT, 4–6, 8, 9, 11–16, 19, 20, 28–31, 38, 40, 45, 96, 126, 131, 132, 150,	OGLE, 4, 167  Photospheric abundances, 119
superadiabatic convection, 60, 62 CoRoT, 4–6, 8, 9, 11–16, 19, 20, 28–31, 38, 40, 45, 96, 126, 131, 132, 150, 153–154, 169	OGLE, 4, 167  Photospheric abundances, 119 PLATO, 20, 169
superadiabatic convection, 60, 62 CoRoT, 4–6, 8, 9, 11–16, 19, 20, 28–31, 38, 40, 45, 96, 126, 131, 132, 150,	OGLE, 4, 167  Photospheric abundances, 119 PLATO, 20, 169 Pulsations
superadiabatic convection, 60, 62 CoRoT, 4–6, 8, 9, 11–16, 19, 20, 28–31, 38, 40, 45, 96, 126, 131, 132, 150, 153–154, 169	OGLE, 4, 167  Photospheric abundances, 119 PLATO, 20, 169 Pulsations adiabatic, 23, 35
superadiabatic convection, 60, 62 CoRoT, 4–6, 8, 9, 11–16, 19, 20, 28–31, 38, 40, 45, 96, 126, 131, 132, 150, 153–154, 169  DMS, 169	Photospheric abundances, 119 PLATO, 20, 169 Pulsations adiabatic, 23, 35 gravity modes (g modes), 24–26, 34, 99
superadiabatic convection, 60, 62 CoRoT, 4–6, 8, 9, 11–16, 19, 20, 28–31, 38, 40, 45, 96, 126, 131, 132, 150, 153–154, 169  DMS, 169  EIS-deep, 166, 169	Photospheric abundances, 119 PLATO, 20, 169 Pulsations adiabatic, 23, 35 gravity modes (g modes), 24–26, 34, 99 mode inertia, 24, 26, 34
superadiabatic convection, 60, 62 CoRoT, 4–6, 8, 9, 11–16, 19, 20, 28–31, 38, 40, 45, 96, 126, 131, 132, 150, 153–154, 169  DMS, 169	Photospheric abundances, 119 PLATO, 20, 169 Pulsations adiabatic, 23, 35 gravity modes (g modes), 24–26, 34, 99
superadiabatic convection, 60, 62 CoRoT, 4–6, 8, 9, 11–16, 19, 20, 28–31, 38, 40, 45, 96, 126, 131, 132, 150, 153–154, 169  DMS, 169  EIS-deep, 166, 169 ESO/VLT, 148	Photospheric abundances, 119 PLATO, 20, 169 Pulsations adiabatic, 23, 35 gravity modes (g modes), 24–26, 34, 99 mode inertia, 24, 26, 34 mode lifetimes, 35, 36, 38
superadiabatic convection, 60, 62 CoRoT, 4–6, 8, 9, 11–16, 19, 20, 28–31, 38, 40, 45, 96, 126, 131, 132, 150, 153–154, 169  DMS, 169  EIS-deep, 166, 169 ESO/VLT, 148	Photospheric abundances, 119 PLATO, 20, 169 Pulsations adiabatic, 23, 35 gravity modes (g modes), 24–26, 34, 99 mode inertia, 24, 26, 34 mode lifetimes, 35, 36, 38 non-adiabatic, 36
superadiabatic convection, 60, 62 CoRoT, 4–6, 8, 9, 11–16, 19, 20, 28–31, 38, 40, 45, 96, 126, 131, 132, 150, 153–154, 169  DMS, 169  EIS-deep, 166, 169 ESO/VLT, 148 Extinction, 176–178  GAIA, 19, 20, 145, 157, 179	Photospheric abundances, 119 PLATO, 20, 169 Pulsations adiabatic, 23, 35 gravity modes (g modes), 24–26, 34, 99 mode inertia, 24, 26, 34 mode lifetimes, 35, 36, 38 non-adiabatic, 36 period spacing, 34 pressure modes (p modes), 24–26, 28–30, 34, 59, 99
superadiabatic convection, 60, 62 CoRoT, 4–6, 8, 9, 11–16, 19, 20, 28–31, 38, 40, 45, 96, 126, 131, 132, 150, 153–154, 169  DMS, 169  EIS-deep, 166, 169 ESO/VLT, 148 Extinction, 176–178  GAIA, 19, 20, 145, 157, 179 Galactic archaeology, 143–145, 151, 154	Photospheric abundances, 119 PLATO, 20, 169 Pulsations adiabatic, 23, 35 gravity modes (g modes), 24–26, 34, 99 mode inertia, 24, 26, 34 mode lifetimes, 35, 36, 38 non-adiabatic, 36 period spacing, 34 pressure modes (p modes), 24–26, 28–30, 34, 59, 99 radiative damping, 36, 39–41
superadiabatic convection, 60, 62 CoRoT, 4–6, 8, 9, 11–16, 19, 20, 28–31, 38, 40, 45, 96, 126, 131, 132, 150, 153–154, 169  DMS, 169  EIS-deep, 166, 169 ESO/VLT, 148 Extinction, 176–178  GAIA, 19, 20, 145, 157, 179	Photospheric abundances, 119 PLATO, 20, 169 Pulsations adiabatic, 23, 35 gravity modes (g modes), 24–26, 34, 99 mode inertia, 24, 26, 34 mode lifetimes, 35, 36, 38 non-adiabatic, 36 period spacing, 34 pressure modes (p modes), 24–26, 28–30, 34, 59, 99

HERMES, 140, 145, 157, 179

A. Miglio et al. (eds.), *Red Giants as Probes of the Structure and Evolution of the Milky Way*, Astrophysics and Space Science Proceedings, DOI 10.1007/978-3-642-18418-5, © Springer-Verlag Berlin Heidelberg 2012

182 Index

stochastic excitation, 37	main sequence (MS), 6, 12–15, 24, 26, 28,
time-dependent convection, 36	29, 31, 33, 40, 41, 46, 47, 55, 62,
	64, 70, 72, 78, 79, 85, 96–102, 106,
RAVE, 152, 168, 169	115, 116, 118, 119, 121, 122, 130,
Rotation	159, 160, 174
angular momentum transport, 105, 106,	red giant branch (RGB)
110	bump, 47, 48, 53–56, 63, 117
in convective envelopes, 130	tip, 47, 81, 83, 98, 111, 120
hydrodynamical simulations, 109	sub-giant branch (SGB), 72
meridional circulation, 108, 110, 111	thermal pulses-AGB (TP-AGB), 48, 88, 90
rotational mixing, 55, 95–102	Stellar models
	boundary conditions, 50, 55, 58, 60–62
	conductive opacity, 64, 66, 81
SDSS-APOGEE, 19, 148	equation of state (EOS), 57, 60, 78, 79,
SDSS-SEGUE, 147	126, 127
Stellar clusters	neutrino losses, 48, 49
globular clusters, 57, 70, 106, 145, 148,	nuclear reactions, 48-50, 66
155–163, 174, 175	radiative opacity, 60–61
multiple populations, 158–160	Stellar parameters
open clusters, 19, 57, 106, 118, 119, 144,	age, 28, 60, 81, 96, 98, 102, 138, 144, 150,
145, 161, 162	153, 156, 161, 162, 166, 172
Stellar evolution	mass, 13, 14, 16, 24–28, 32, 34, 46, 47, 59,
asymptotic giant branch (AGB)	64, 72, 81, 101
early AGB, 48, 51–53, 56, 82, 119–121	radius, 12, 16, 18, 24-26, 31, 35, 71, 80,
blue loops, 85, 86	92, 100, 101, 105, 106, 108, 109,
breathing pulses, 50, 82	111, 130, 142, 145, 153
core helium burning	surface gravity, 12, 132
red clump (RC), 46, 47, 106	Stellar populations
dredge up, 53, 55, 63, 115, 116, 118–120,	population seismology, 3–9, 11–20
149	population synthesis, 156, 166, 171–179
helium flash, 78–83	
horizontal branch (HB), 63, 79–82, 86, 106,	
160, 162, 174	Thermohaline mixing, 55, 81, 115–123